MULTIDIMENSIONAL HYBRID NANOMATERIAL APPROACHES FOR THERAPEUTIC AND DIAGNOSTIC APPLICATIONS

By

SY-TSONG DEAN CHUENG

A dissertation submitted to the

School of Graduate Studies

Rutgers, The State University of New Jersey

In partial fulfillment of the requirements

For the degree of

Doctor of Philosophy

Graduate Program in Chemistry and Chemical Biology

Written under the direction of

Ki-Bum Lee

And approved by

_____

_____

_____

_____

New Brunswick, New Jersey

January, 2019

ABSTRACT OF THE DISSERTATION

MULTIDIMENSIONAL HYBRID NANOMATERIAL APPROACHES FOR THERAPEUTIC AND DIAGNOSTIC APPLICATIONS

by SY-TSONG DEAN CHUENG

Dissertation Director: Ki-Bum Lee

Nanomaterials are highly versatile and allow us to effectively and dynamically control a myriad of biomedical application from stem cell differentiation to diagnostics and translational therapeutics. While the scientific community has made tremendous strides in understanding disease and treatments, the complexities of disease and injuries still undermine the full realization of therapies. To this end, this dissertation will focus on the approaches within the novel nanotechnology toolbox for addressing multiple challenges in the field of regenerative medicine with the ultimate goal to regrow and reform damaged tissues and organs. Specifically, this dissertation addresses the regeneration of neural tissues within the central nervous system as the regeneration of such tissue is extremely challenging in the first two decades of the 21^{st} century. The first part of the dissertation will focus on the innovative insoluble extracellular approaches for controlling the differentiation of neural stem cells (NSCs) into neurons and supporting cells such as oligodendrocytes. Traditionally, biologists have focused on introducing exogenous materials such as proteins and chemical factors to induce specific stem cell differentiation. The goal of our novel insoluble nanomaterial approaches is to uncover the interaction between cells and their surrounding environments for differentiation. The second part of

the thesis will focus on the clinical translational approaches of nanomaterials. Through a novel, non-viral transient gene manipulation method developed by Prof. Lee research laboratory, NanoScript, a nanoparticle-based synthetic transcription factor was tasked to regenerate axon in spinal cord injury. This demonstration is tremendous progress in regenerative medicine as it holds a promise for the regulation of every gene expression in a living biological system. Finally, this dissertation will focus on the development of highly sensitive, selective, real-time, and non-invasive characterizations of stem cell differentiation. The development of such an approach will have a significant impact in cell-based therapy. By overcoming the destructive nature of traditional cellular characterization methods, the clinicians can confirm the mature differentiation of stem cells before transplantation to completely avoid potential tumor formation. As such, more cell-based therapies will find their ways into clinical applications. Altogether, this dissertation covers the widely collaborative nanomaterial-based approaches from guiding the differentiation of stem cell, biosensing, and non-viral nanoparticle for gene expression regulation, to the transplantable nanofiber-nanomaterial hybrid scaffold with the foundation of nanochemistry with well-defined biochemical, chemical, and physical compositions, shapes, and properties.

Acknowledgements

We never walk alone. The start of my Ph.D. was accidental. Now, near the end of this road, I can finally say the process was full of rewarding surprises. This journey, along the way, has many supportive individuals I need to be thankful to. To me, the Ph.D. training is more than the knowledge I have acquired for my chosen field of study. It also gave me extraordinary leadership and communication training opportunities. First, I thank my parents. Born as the first son of the first son in a scholar-oriented Hakka family, I was fortunate to receive a tremendous amount of responsibilities and expectation. Throughout my life, my parents have always given me unreserved love and support. My father, a successful civil engineer who has designed nuclear power plants around the world for his entire career, has always taught me the importance of being a team player and a team leader. He also taught me the importance of the fundamentals of any careers. My mother, a strong family oriented woman, taught me the value of family in addition to interpersonal and business skills. I want to specially thank my grandparents from both side of the family who taught me through their life stories. I learned that no matter the hardship, the adverse environment, one should never succumb to mediocrity. Although I cannot tell them in person anymore, I know they will always be proud. Furthermore, I thank my brothers. Growing up in a house with three boys was the best I could ask for. I am proud to have a twin and a younger brother, Roy and Steven. As fate has it, Roy and I shared the same schools all the way from pre-kindergarten to Rutgers University Master. Now, Roy is an excellent electrical engineer. Steven, the youngest brother, also has a background in biomedical engineering and is pursuing a path in medicine. I remember our time growing up together fondly. I thank my family for all the love and support and pushing me to always believe in me to do my best. Next, I thank my Ph.D. advisor and career mentor, Prof. KiBum Lee, for providing me the golden opportunity to foster under his

tutelage. I remember at the end of our introductory meeting; he asked me "Are you interested in an academic job or industrial job?" I replied, "Industrial job, because I don't think I would like to be a professor." For which Prof. Lee replied, "Hey Dean, I'm not your friend!" At that time, of course, I was naive, and had no idea what I wanted to do. However, given my biomedical engineering background, my career goal has always been real-life applications to innovative sciences. Throughout my Ph.D. career, Prof. Lee has guided and pushed me to pursue not only high caliber science but also high caliber entrepreneur skills. I was entrusted to more than just leading science in our lab; Prof. Lee trusted me with the KBLEE Group. I am even more grateful for having an advisor who fully allows me to achieve and pursuit scientific and career goals. Together, we will continue our professional relationship with our business venture, NanoScript Biotech, to transfer our technology developed in the academic laboratory to commercialization. Prof. Lee showed me how to be a diligent, kind, and effective leader. I also thank my committee members Prof. John Brennan, Prof. Eric Garfunkel, and Prof. Wise Young for all their great guidance. Prof. Brennan and Prof. Garfunkel have been on my committee since pre-qualifying and have seen my transition from the beginning for my Ph.D. path by providing key insights throughout the years to enhance my research. I also offer a tremendous appreciation to Prof. Young over the last few years for providing a collaborative research environment for me to conduct translational research for the treatment of spinal cord injuries in his laboratory, the W.M. Keck Center for Collaborative Neuroscience. Especially, I would like to thank Xiaowen "Charles" Qiu who is my surgeon on the NanoScript-PTEN project for helping me collect and conduct the animal experiments. I would also like to thank Prof. Dongming Sun at Prof. Young's laboratory for coordinating all the experiments and inputs for this collaboration. We believe at the KBLEE group that "Good Science comes from Good Citizen." I truly appreciate all the group members, past, present, and the future, from the KBLEE group. I would like to thank everyone who has been a part of the KBLEE family. Without you, the journey of my Ph.D. would not be as colorful. For my earlier days, I specifically thank Dr. Aniruddh Solanki who was a great friend and laboratory mentor and role model from my early days in the KBLEE

group. He helped me established myself in the laboratory and showed the creative ways of conspiring research ideas. For my intermediate days, I would like to thank the examples set by Dr. Shreyas Shah, Dr. Sahishnu Patel, and Dr. Perry Yin who showed me the tremendous work ethic required to be a successful Ph.D. student. I always admire Dr. Shah's wit and the approachable attitude he has for everyone, Dr. Patel's optimistic tactic when facing any obstacles, and Dr. Yin's bold and critical approach in general. During my senior phase, I would like to thank the junior members of the group Hudifah Rabie, Christopher Rathnam, Thanapat Pongkulapa, Jeffery Luo, and Brian Conley for their efforts and help for day-to-day KBLEE operations. Additionally, I would like to thank the other two Ph.D. students who started at the same year as me: Letao Yang, and Yixiao Zhang. Both of them are outstanding Chemists who gave me different perspectives and being my council throughout my time. Furthermore, I am grateful to Dr. Tae-Hyung Kim, Dr. Cheol-Heon Yee, Dr. Hyeon-Yeol Cho, Dr. Jin-Ho Lee, and Dr. Jin-Ha Choi for their help and advice for all the research projects I am fortunately involved in.

Dedication

I dedicate my Ph.D. thesis to my family, to my grandparents who are before me and to my children will come after me. Embracing the core value of Hakka, we have worked hard and stayed humble no matter the environment. As a family of immigrants, we have all done our best for the next generation. We may not speak the same language or live on the same land, but we are the same people. I am proud to be a Hakka.

Table of Contents

List of Tables

List of Figures

Chapter 1

Introduction

Current stem cell therapy suffers low efficiency in giving rise to differentiated cell lineages, which can replace the original damaged cells [1]. Through the use of Nanomaterials, we can provide unique physical size, surface chemistry, conductivity, and topographical microenvironment to control and modulate stem cell differentiation [2]. With rational design, we can fully take advantage of the multidimensional approach of nanotechnology to facilitate gene delivery, cell-cell, and cell-ECM interactions for both therapeutic and diagnostic purposes. Overall, we can categorize the nanotechnology toolbox for regnerative medicine in three approaches: 1) soluble microenvironmental factors; 2) insoluble physical microenvironment; and 3) nano-topographical features. With these three distinct disciplines, this dissertation will focus on the synergistic approaches to demonstrate synergistic nanomaterials to guide selective stem cell differentiation, cellular therapies, and diagnostics [3].

As the pioneer of the field of nanotechnology, Nobel Prize winnder Richard Feymann famously conspired the idea of developing molecular machines in 1959. Since then, the field of nanotechnology has reach every aspect of the human life today. Simply put, we now have the ability to assemble materials at the atomic level with fine control at the nanoscale. At this level, nanomaterials possesses unique properties compared to elemental bulk counterpart in electronic, optical, magnetic, and structural properties. In this regard, biology oriented scientists have explored biological phenomena through various innovative techniques. Since nanomaterials can be designed to interact with proteins and subcellular organelles, they are the best tool we have for biomedical applications. To begin, we will explore the type of commonly used nanomaterials and their biomedical applications.

1.1 Nanomaterial Toolbox

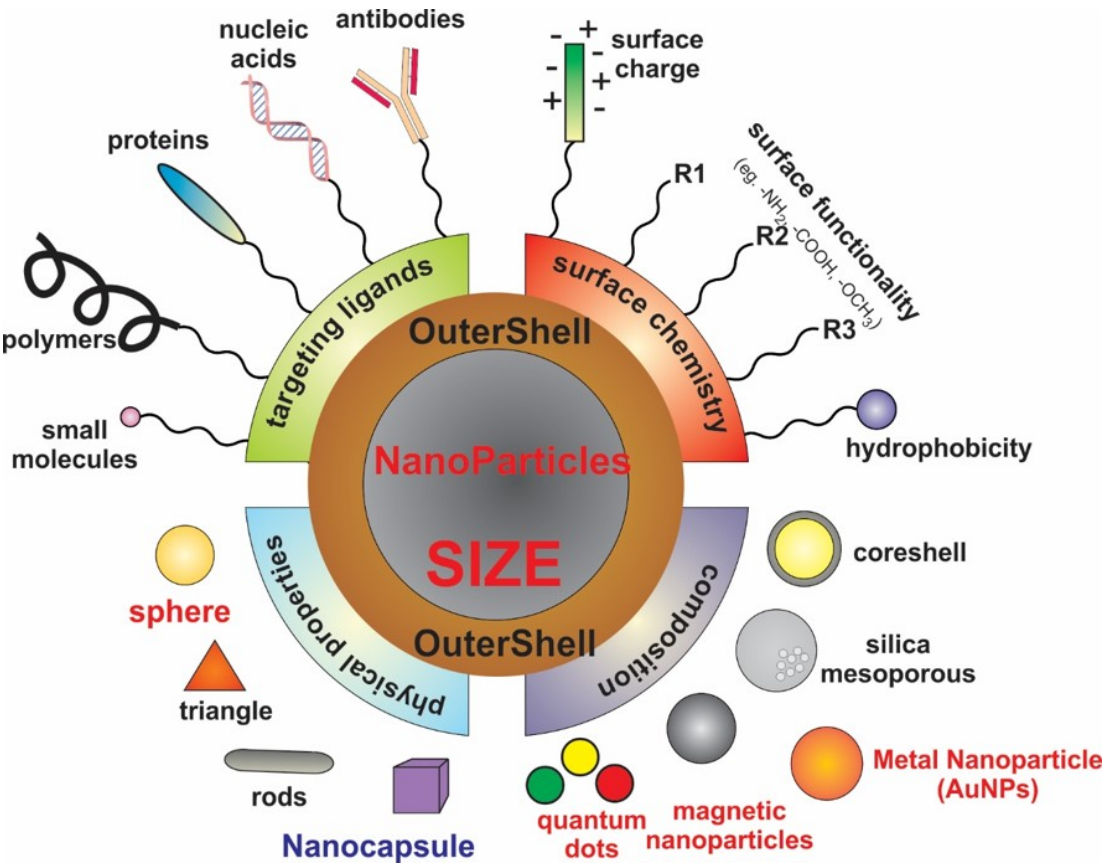

Figure 1.1: Simple Schematic Diagram of Nanoparticles and their Biomedical Functionalization

1.1.1 Quantum Dots

Quantum dots (QDs) have significant biological, catalysis, photovoltaic, photodetector, light emitting diodes, and display application potential due to their semiconducting nanocrystal nature [4]. With strong and narrow fluorescent emitting properties, QDs have a very broad absorption spectra, they are ideal for cell labeling, cell tracking, cell imaging [5]. Compared to their organic counterpart, QDs have a significant advantage in high signal to noise ratio, do not suffer photobleaching which allows for extended excitation exposure indispensable for time-lapse application [6]. Typically, QDs range from 2-3 nm to less than 10 nm. To control their optoelectronic properties, the methods typically involve the change of diameter size and composition. For example, a well-reported CdSe QD emits orange to red light at a diameter of 5-6nm whereas a 2-3 nm

CdSe QD emits at blue light. Other type of QDs change their emissions by changing its composition as a function of each element makeup [7]. For example, in ZnS-$AgInS_2$ QD, the change of Zn faction can change the emission from red (0.0 composition/mole) to blue (1.0 composition/mole ratio) [8]. Due to their their highly tunable properties, QDs are of wide interest.

Specifically in bio-application, quantum dots are not only brighter but also more photo-stable compared to tranditional organic fluorescent dyes [9]. This has enabled the acquisition of reconstructive high-resolution three-dimensional images. Researches have explores application such as real-time tracking of molecules and cells over a long period of time measure in months. Furthermore, QDs can also be used as a drug delivery vehicle for antibodies, antibiotics, peptides, DNA,RNA, etc. These type of works have a strong significance in stem cell and cancer research [10, 11].

The synthesis of QDs have also come a long way for biomedical applications. Traditional QD synthesis uses organometallic method were done in high-temperature, air-free, and organic solvents. Typically, the formation steps follow nucleation, growth, and termination. After the formation, these QDs were then undergo ligand exchange with amphipathic polymers or nano-shell to become water soluble for practical purpose [5]. Biomolecules are then added to tailor the nanoparticles for their specific applications through covalent bioconjugation methods. Since then, aqueous solution-based, mild synthetic conditions have arise using thiol-containing molecules. There has also been demonstration where QDs were synthesized inside a living organism in yeast and E. coli using glutathion and QD binding peptide [8]. Going forward, we expect to see commercialization of robust QDs for *in vivo* and clinical applications.

Figure 1.2: Quantum dots emission at different wavelengths under the same UV light source in a particle size dependent fashion. Photo by Allison Dennis (aldennis@bu.edu) at Boston University.

1.1.2 Gold Nanoparticles

Gold nanoparticles, also known as colloidal gold, are typically red in color when suspended in water [12]. Scientists have been studying gold nanoparticles in depth and found that their optical and electronic properties vary with size and shape such as sphere, star, and rod. There has also demonstration in the fabrication of gold nanocages and hollow nanospheres for their excellent plasmonic activities from this type of physical structures. With promise in various research field, gold nanoparticles are one of the stables in nanomedicine. Due to the different size, shape, and surface properties of gold nanoparticles, they can be easily modified for specific therapeutic purposes. They are the anchoring scaffold of many great technology.

Interestingly, gold nanoparticless was said to cure various diseases during the Middle Ages where doctors at the time would prescribe gold nanoparticle solution as potions [13]. Modern advances with many tools and methods have made the synthesis of gold nanoparticles to be very precise and simple. Furthermore, gold nanoparticles are extremely stable with long shelf-life, they are very practical in a wide range of applications. For example, in the field of regenerative medicine, gold nanoparticles (AuNPs) have been widely used for delivering payloads such as small molecules, peptides, protiens, DNAs, and RNAs into the biological system [14]. Worth noting, the

inert and non-toxic nature of AuNP has already been approved by the FDA for imaging purpose [15]. Furthermore, the well-established gold-thiol reaction allows for very easy and robust surface functionalization of AuNPs. To this end, not only do they have extensive applications in therapeutic applications, they are widely use in the application of diagnostic and biosensing as well. Focusing on the applications of AuNP in diagnostics and therapeutics, we will briefly introduce the current common use of AuNPs.

The synthesis of AuNP are typically done through the use of Choroauric acid ($H[AuCl_4]$) and cetyltrimethylammonium bromide (CTAB) stabilizing agent with very robust and simple preparation procedure. There are four critical physical and chemical properties for the use of AuNP for biomedical applications: i) chemical inertness, ii) surface properties, iii) electronic structure, and (iv) optical properties. Using the robust thiol ligands, AuNPs can form self-assembling monolayer (SAM) at the substrate surface. This in terms have given rise to interesting macromolecular structures [16].

The currently common uses for AuNP is photothermal therapy (PTT) [17]. Using light as the energy source, PTT delivers local cytotoxic hyperthermia on cancer cells. Based on their unique optical properties and biologically inert nature, AuNPs have been used as photothermal contrast agents in clinical and preclinical trials for cancer treatment to denature proteins, disrupt enzymes and metabolic signaling pathways to induce cancer apoptosis. Interestingly, AuNP can also be used in radiotherapy to effectively the dosage of X-ray radiation without compromise in efficacy. This is advantageous for the surrounding normal tissue [18].

Gold nanoparticles, because of their different sizes and shapes offer a multitude of opportunities for their use in biomedical applications. The variety of synthetic methods for obtaining particles provides a versatile toolbox for producing conjugates with Gold nanoparticles with appropriate ligand conjugation with higher affinity for cell receptors, efficient cell and tumor internalization, and long circulation half-life. The physicochemical properties of AuNPs pave ways for better imaging and enhanced radiotherapy and PTT for cancer, development of novel vaccines, efficient methods for gene therapy, and enhanced LTDD-based chemotherapies. Even though gold is less toxic, health problems

may arise from the relatively low rate of clearance from circulation and tissues and because of this approaches that increase the specific targeting of diseased cells must be standardized before AuNPs find their application for routine human use [19].

1.1.3 Magnetic Nanoparticles

Magnetic nanoparticles are an interesting class of its own as it allows for remote manipulation through the use of external magnetic field which is tremendous in biomedical application [20]. Typically, magnetic particles consist of iron, nickel, and cobalt with doping agent to increase their magnetic functionalities. Their size can range from 1-100 nm to up to 500 μm. Because of their unique properties, magnetic nanoparticles see a wide range of applications from nanomaterial-based catalysts, to tissue targeting, magnetic resonance imaging, and data storage [21]. While mostly superparamagnetic, the physical and chemical properties of magnetic nanoparticles depend on the synthesis method greatly.

Specifically for biomedical applications, magnetic nanoparticles have been used quite extensively in magnetic hyperthermia treatment under high frequency (100-500 kHz) alternative magnetic field (AMF) [22]. Magnetic hyperthermia have shown a great promise as a therapeutic technique for cancer treatment. As an alternative and complementary approach to traditional anti-cancer drug, magnetic nanoparticle can be deliberately delivered to the targeted tumor, the internalized particles can then deliver cargo and respond to external AMF to heat up and disrupt and eliminate tumor [23]. Interestingly, due to their cellular membrane properties, cancerous tissues are more sensitive to heat damage due to the insufficient heat dissipation. Even though there are other means of heat delivery in the clinic, such as RF, microwave, ultrasound, these methods do not provide any spatiotemporal control for cancer treatment. Although chemotherapy is still the current standard-of-care, the added modalities from magnetic nanoparticles can further advance cancer treatment [24].

Furthermore, magnetic nanoparticle has also shown promise in targeting circulating tumor cells. By attaching magnetic nanoparticls to free-floating cells through particle surface fictionalization, scientists can capture and extract these circulating tumor

cells through the use of constant magnetic field [25]. This kind of capturing through magnetic field strategy has also been used as cancer detection methods. By targeting cancer-associated biomolecules, cancer markers can be easily identified and concentrated through magnetic field for early non-invasive diagnostic through blood samples [26].

Although we mentioned the classical applications of magnetic nanoparticles here, many recent application showed the promise of magnetic particles towards anti-inflammatory, tissue growth, anti-bacterial, and bacterial detection as well [27]. Additionally, there has also been commercially available products to compete against the well-established fluorescence activated cell sorting (FACS). These magnetic particle-based system conjugate antibodies of interest onto magnetic particle for cell characterization as fraction of the costs compared to the fluorescence counterpart [28].

In short, we can still expect continual exciting prospects from these nanoparticles in the field of biomedical application from disease detection, prevention, to treatment and fundamental research related tools. As part of the theme of this dissertation, the future of magnetic nanoparticle involves the multifunctionality we the scientists and engineers find to integrate into any current system with new knowledge gained from the ongoing research.

1.1.4 Silica Nanoparticles

Silica nanoparticles (SiNPs) are made up by the most and second most abundant element on earth: oxygen and silicon. Silicon dioxide (SiO_2) are most commonly found as quartz and exists in many living organisms [29]. As the most abundant material, Silica is still extremely complex. Currently, silica is commonly used in structural materials, microelectronics, and food/pharmaceutical additives. Due to their easy preparation, highly biocompatibility, and low cost nature, SiNPs have seen a wide adaptation for their use in biomedical application. Specifically, their specific surface characteristics, porosity and capacity for functionalization make them invaluable tools from biosensing to drug delivery use [30].

Compare to other inorganic nanoparticles introduced in this dissertation, SiNPs do not seem to have any unique characteristics that one will chose over other materials.

However, the truth is quite the opposite. SiNPs have an unmatched role in providing high specific surface area, low density, adsorption capacity, encapsulation capacity, and biodegradability [30]. These properties make SiNP a dominant force in biomedical application. Specifically, intensive research has been performed to use SiNPs in diverse biomedical applications such as biosensors, enzyme supporters, controlled drug release and delivery, and cellular uptake. With its rich history in the design of advanced tools for bioapplication, SiNPs also play an incredible role as auxiliary materials. For example, silica shells are highly efficient for protecting imaging agents and increase their efficacy. SiNPs have also been use as additive to improve mechanical properties of powders in the pharmaceutical industry. Due to their unique characteristics, SiNPs are among the most important materials for understanding and promoting biomedical applications.

From the synthetic point of view, SiNPs can be precisely controlled in terms of particle size, porosity, crystallinity, and shape to fine tune the structure for applications. The precise control of surface chemistry of SiNPs also lead to modulation of drug/chemical loading, nanoparticle dispersity, *in vivo* circulation, and targeting strategy. As shown in Figure 1.3, SiNP synthesis typically uses sol-gel processing at room temperature (25°C). Commonly started from tetraethyl orthosilicate (TEOS), the dissolution process can fine tune the final structure of SiNPs. The various synthetic techniques and structures that can be achieved with silica nanoparticles have helped to facilitate the innovation and investigation into many biomedical applications [31].

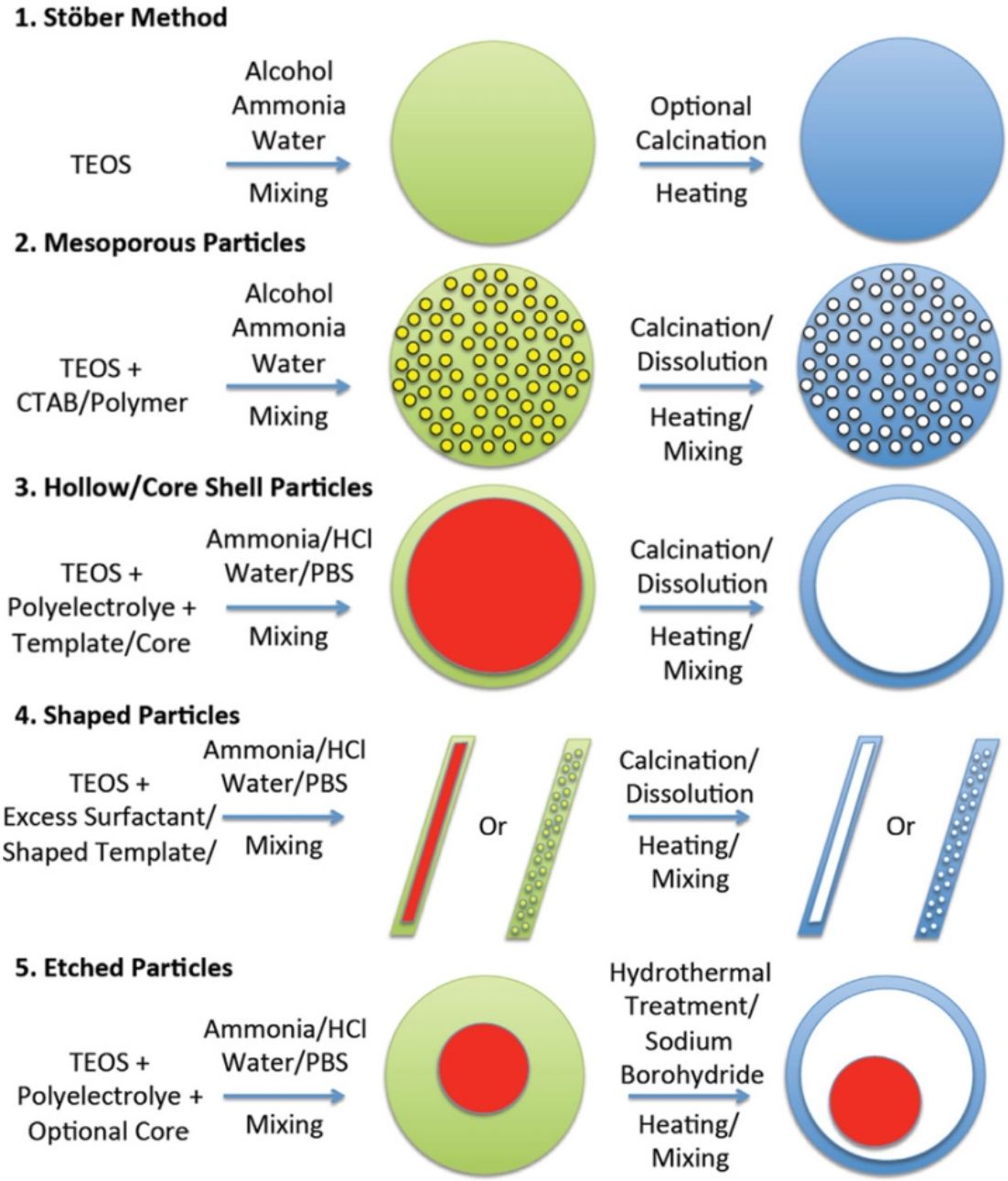

Figure 1.3: Common techniques in silica nanoparticle synthesis [31].

1.1.5 Upconversion Nanoparticles

Compare to traditional excitation/emission profile, upconversion nanoparticles (UCNP), as its name suggests, convert longer incoming wavelength photon into shorter emission wavelength [32]. UCNPs are usually composed of lanthanide- or actinide-doped transition metals. Particularly, UCNPs has a strong claim in the field of bio-imaging and

bio-sensing at the deep tissue level since visible light has very limited tissue penetration depth. Specifically, the distinctly high signal to noise ratio of UCNPs has made them great optical probes because of their utilization of long wavelength excitation in the near-infrared (NIR) range, with lower solution diffraction and environmental heating, in exchange for short wavelength visible emissions as shown in Figure 1.4 [33]. Characterized as exhibiting anti-Stokes shift effect, the charge transfer between two excited transition-metal and rare-earth metal atoms allows the upconversion to occur at a stable state.

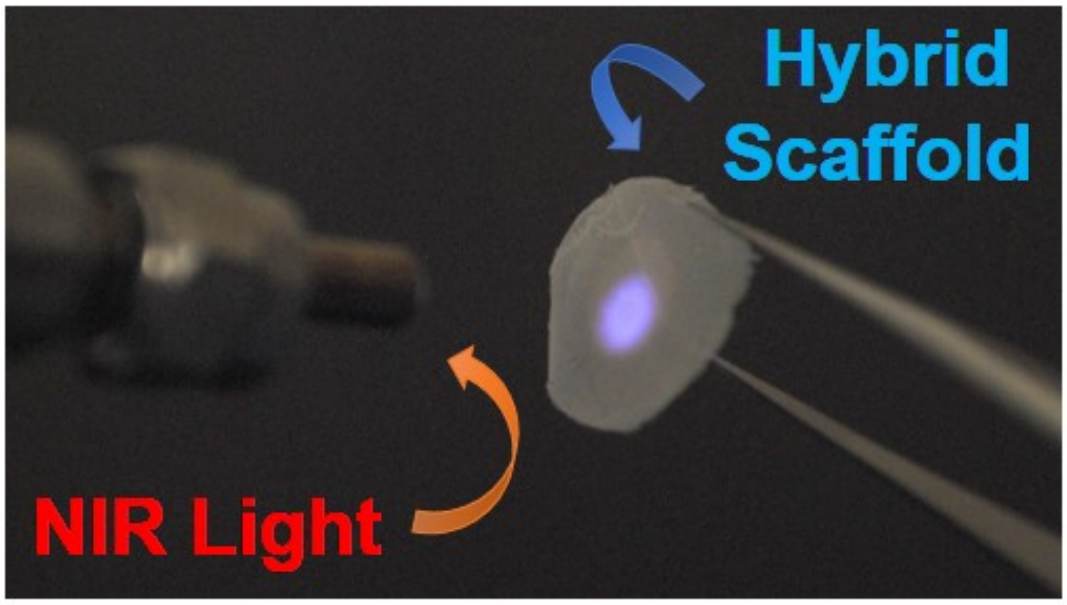

Figure 1.4: Demonstration of Upconversion Nanoparticle Optical properties. An invisible NIR laser light shines on the surface of upconversion nanoparticle embeded polyer film emitting blue, visible light. [33]

For our interest in to have high resolution in both time and space *in vitro* and *in vivo*, conventional fluorophores and their associated limitations are not well qualified. Limited by low photo-stability, auto-fluorescence, cytotoxicity, and photo-sensitivity, optical high resolution imaging remains to be challenging [34]. To this regard, the commonly used Lanthanide (Ln)-doped UCNPs exhibit their unique advantages over conventional fluorophores such as i)enhanced penetration depth into tissues upon near infrared (NIR) excitation, ii) significantly decreased auto-fluorescence from surrounding

tissues, iii)non-photobleaching and non-photoblinking, and iv) minimal photo-damage to biological specimens [34]. In general, the synthetic methods of UNCPs involve co-precipitation, thermal decomposition, sol-gel processing, and hydro/solvo thermal methods. After obtaining UCNPs, the surfaces are then modified enhanced upconversion efficiency. Typically, there exists non-radiative energy loss due to the lack of protection by the host lattice [35]. To this end, nanochemists have tried coating an inert shell onto the surface of UCNP to suppress energy loss. The luminescence intensities of these UNCPs can also be adjusted by changing the thickness of the coated shell [35]. Similar to other inorganic nanoparticles, the UCNP surface needs to be fictionalized with amphiphilic ligands for bio applications. Among various surface functionalization methods, surface silanization is the most commonly applied for two reasons: i) well established chemical approaches of silica coating and ii) silica coating is readily applicable to both hydrophilic and hydrophobic nanoparticles. The thickness of silica shells can be adjusted from 1 nm to 10 nm by varying the concentration of tetraethoxysilane (TEOS) precursor concentration [34].

The unique upconversion mechanism of UCNPs offer high sensitivey and high signal-to-noise ratio for bioimaging and biosensing. The tunable NIR excitation and UV-Vis-NIR emission further make UCNP an attractive option for biological application. The growing interdisciplinary research field should further improve this relatively new and exciting materials.

1.1.6 Nanofibers

Nanofibers are an extremely versatile class of nanomaterials for biomedical applications. Many different polymeric materials can be used to generate nanofibers. Natural materials such as collagen, cellulose, silk fibroin, keratin, gelatin, and polysaccharides have been used to generate nanofibers. Synthetic polymer such as the highly biocompatible poly(lactic acid) (PLA), polycaprolactone (PCL), polyurethane (PU), and poly(lactic-co-glycolic acid) (PLGA) have all been used for specific bioapplications. Despite the name, nanofibers can be synthesize from nanometer all the way to micrometer range depending on the parameters such as polymer concentration. As a bioscaffold material,

this type of fibrous materials have large surface area-to-volume ratio, high porosity, appreciable mechanical strength, and flexibility in functionalization [36].

The fabrication of nanfibers are also very diverse. Although there are multiple ways to make nanofibers such as drawing, self-assembly, template synthesis, and thermal-induced phase separation, the electrospinning method has been proven to be the most compatible for nanofiber fabrication for biomedical application due to its consistency and control over a long period of time [37]. Nanofibers can also be arranged in random, aligned, or woven fashion for different applications. In tissue engineering, the focus of nanofiber use is to act as an artificial extracellular matrix. However, depends on the polymer used, synthetic nanofibers typically require additional surface functionalization to help with cell adhesion.

In brief, more detailed application nanofiber design rational will be discussed further, later in the Chapter.

1.1.7 Graphene Oxide

Although graphene as been discovered the middle of the 20^{th} century, actual nanometer rage (10nm) thickness of graphene was not produced until around 2004. Since then, material scientists have heavily invested into this carbon nanomaterial [38]. Interestingly, thin layer garphene has very unique electrical optical, thermal, and mechanical properties. The theoretical descriptions of graphene structures and properties have yielded two Nobel Prize in Physics in 2010, Dr. Andre Geim and Dr. Konstantin Novoselov. Graphene is an allotrope of carbon with a single layer of cabon atoms arranged in hexagonal sp^2 hybridization. Because of its shared overlap between the valence and conduction bands, it is considered as the strongest material ever with extremely efficient heat and electricity conductance [39]. However, in the field of biomedical applications, graphene does not allow robust bioconjugation. Therefore, scientists have introduced oxide defects onto the surface of graphene to increase its biocompatibility. With the introduced surface functional groups, graphene oxide can react with many chemical groups and be modified for desired functionalities. Depends on the synthetic method, graphene oxide (GO) can then be reduced to reduced graphene oxide (rGO) to recover

some electrical properties. However, from the material science point of view, there have been many debates in the standard of graphene and its derivatives. This issue should be addressed as we become more proficient in this unique 2D nanomaterial [39].

As of the time of this writing, large-scale graphene oxide is synthesized through two major method: 1) Chemical Vapor Deposition (CVD) and 2) Hummers method [40]. Although there are alternative approaches, such as chemical and physical exfoliation, they are not practical in large-scale production. In the case of CVD, the reaction condition is typically at 1,000°C under low pressure to decompose the precursor gas into atomic radicals, which results in the dissolution of carbon atoms. After the segregation and crystallization, graphene is formed during the the cooling process. Since graphene synthesized under the CVD method undergoes negative thermal expansion during the cooling process, the formation of nanoscale ripples occur (Figure 1.5a) [40]. Furthermore, the uncontrollable nucleated graphene growth creates grain boundaries (Figure 1.5c) [40]. These defects, however, generates favorable chemical reactive sites for biological application.

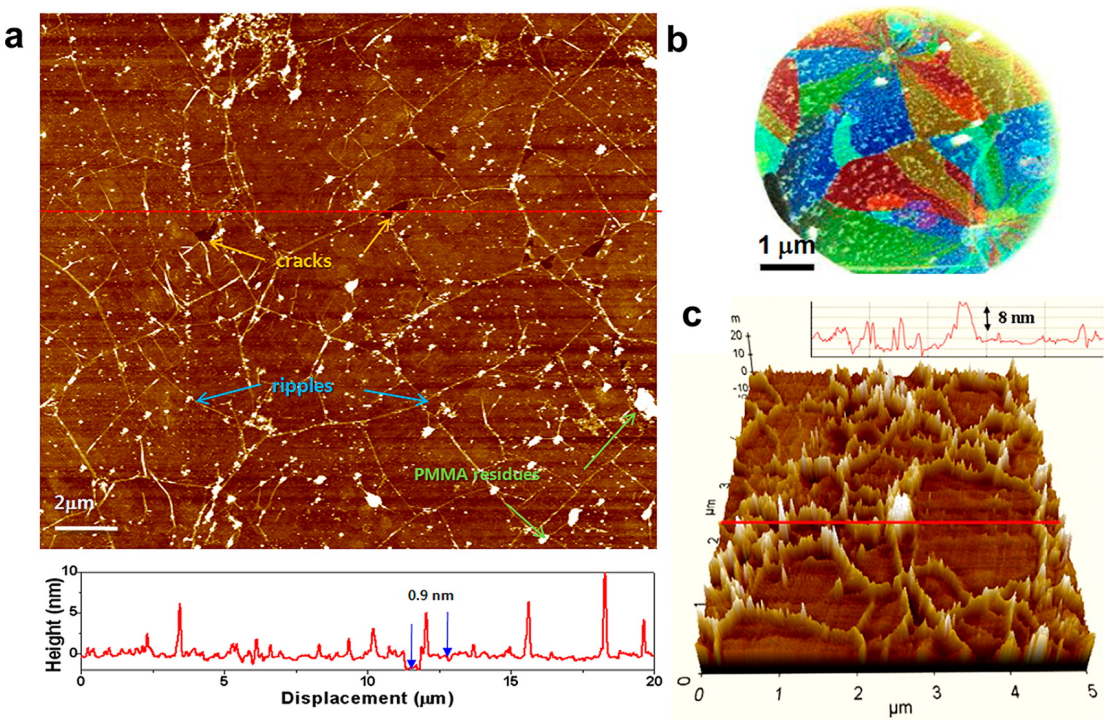

Figure 1.5: Nanoscale images showing the surface morphology of large-area graphene grown by CVD. (a) Atomic force microscope (AFM) image of a CVD graphene film transferred on a SiO2 substrate. (b) Transmission electron microscope image showing the polycrystalline domains of a CVD graphene film with false colors. (c) AMF image of electrodeposited CdSe quantum dots on CVD graphene, showing the higher electrochemical activity of grain boundaries or ripples. [40]

On the other hand, the most popular approach to GO synthesis is the Hummers method. Starting from readily available graphite, potassium permanganate ($KMnO_4$) and sulfuric acid (H_2SO_4) are used as the oxidative agents. From that point, ultrasonication in solvent is used to exfoliate the resulting graphite salts from the previous step. This method generates poor crystalline structure compared to the CVD method. However, the simple synthetic route makes it a very attractive option. Since GO created through the Hummers mehtod is easily scalabe, the unique chemical structure of GO enables various chemical modification or functionalization for biomedical applications [41].

Because of its excellent aqueous processability, amphiphilicity, surface functionalizability, surface enhanced Raman scattering (SERS), and fluorescence quenching ability, GO is considered as a perfect material for bio applications [41, 42]. Specifically, as

demonstrated, GO interacts with biomolecules very well to enhance stem cell differentiation and survival. Furthermore, there are an abundance of other demonstrations in precise biosensing through graphene-quenched fluorescence, graphene-enhanced surface Raman signal, and graphene-assisted laser desorption/ionization for mass spectrometry.

A major drawback in current stem cell therapy is the limited control over stem cell fate, which leads to low efficiency in giving rise to mature differentiated cells that can replace the original damaged cells [43, 44]. On the other hand, *ex vivo* differentiation of stem cells have been proven to be very low in efficiency and has poor cell survival upon transplantation into the body. To overcome these challenges, various multidimensional nanomaterials that are capable of precisely controlling stem cell fate in the nanometer range have been developed rapidly. Furthermore, nanomaterials are highly versatile in nature, they enable us to effectively and dynamically control the differentiation of stem cells solely through the biophysical cues of nanomaterial [45]. As demonstrated, subtle changes in the physical microenvironment such as the surface material orientation, ECM protein composition, and shape can significantly influence the therapeutic potential of stem cell [46]. This review covers novel nanomaterials used for stem cell differentiation in multidimensional approaches. Nanotechnology-based approaches to selectively guide stem-cell-based regeneration include: 1) soluble microenvironmental factors; 2) insoluble physical microenvironment; and 3) Nano-topographical features [FIGURE 1.6.

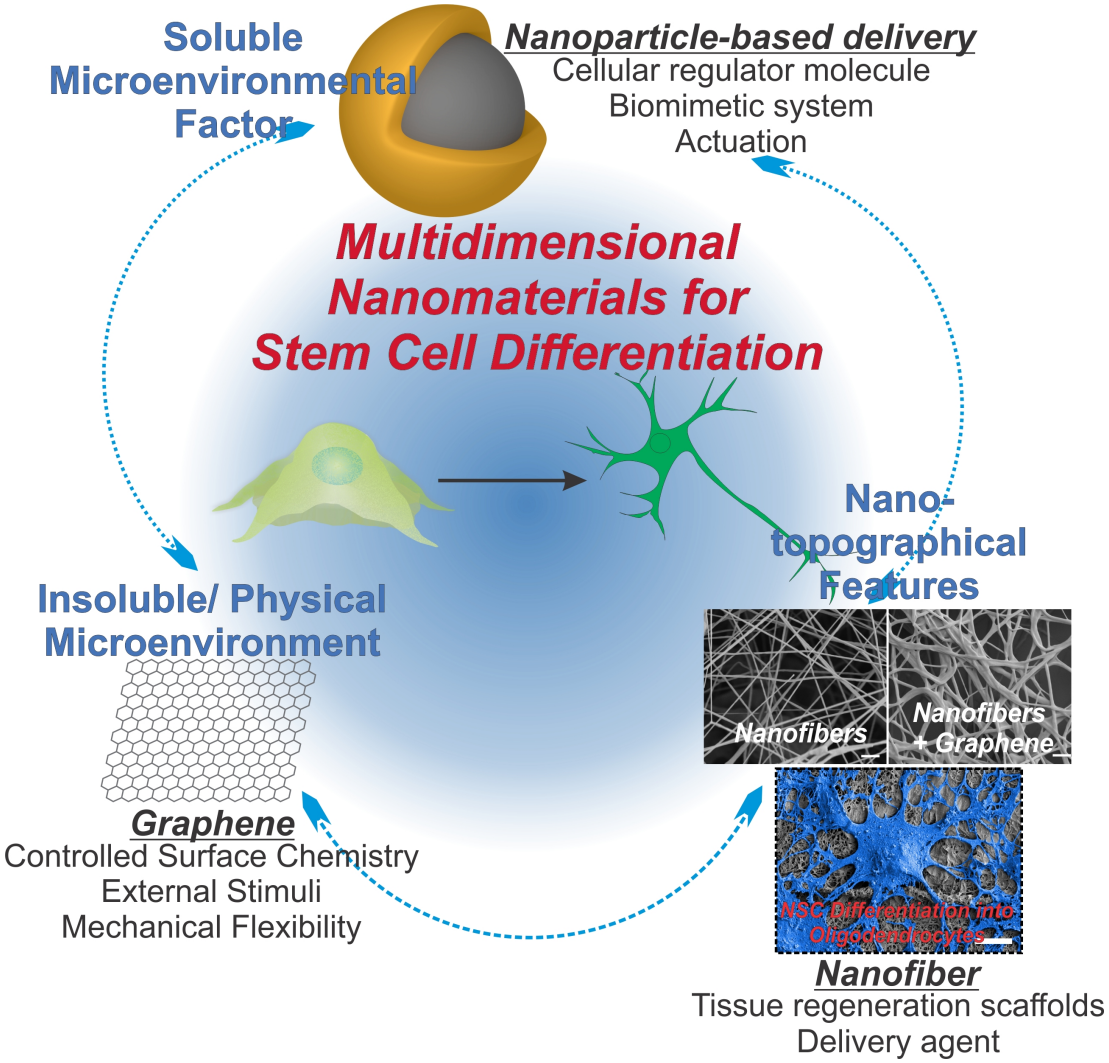

Figure 1.6: Illustrative diagram representing the multidimensional nanomaterials: soluble microenvironmental factors, insoluble physical microenvironment, and Nano-topographical features. [47]

Soluble microenvironment describes the growth factors, cytokines, and chemokines associated with nanomaterials delivered to the stem cells. Insoluble physical microenvironment describes the biochemical cues given to extra cellular matrix (ECM) protein for enhanced attachment and orientation. Lastly, nano-topographical feature describes the physical topographical cues nanaomaterial provides to the stem cell. Overall, nanotechnology-based approaches offer physicochemical control required to differentiate stem cells into cell lines of interest. With the increasing interest to develop innovative tools and technologies, we can also expect creative solutions for the complex problems

associated with stem cell biology and their applications.

1.2 Diffusive Microenvironment

With their unique sizes in the range of viruses and proteins, nanomaterials can interact with biological systems at the molecular level with high specificity [3]. Nanoparticles, different bulk materials, possess significant surface to volume ratio, composition, shape, surface, and unique optical and/or magnetic properties that are advantageous in solving biomedical challenges. Apart from numerous biomedical applications like imaging and drug/gene delivery, application of directing stem cell differentiation through nanoparticles is lacking. However, the unique properties of nanoparticles are met with strong enthusiasms from researchers for modulating stem cell behaviors and understanding stem cell signaling mechanisms [48].

1.2.1 Cellular Regulator Molecular Delivery

Regulator molecules including growth factors and signaling molecules are major factors with the key ability to regulate stem cell behaviors, However, naturally occurring regulator molecules suffer from short circulation half-life and fast degradation rate under *in vivo* circumstances. These drawbacks together with low diffusivity render the real application of stem cell therapy inefficient due to the ineffective delivery and non-specific distribution. As such, a delivery system with spatial-temporal precision is of significance for utilizing signaling molecules to guide stem cell differentiation. With tremendous surface-to-volume ratio, high loading capacity and targeting delivery modality, nanoparticles have been used frequently as signaling molecule carriers. Owning to their intrinsic properties, nanoparticle can provide prolonged growth factor releasing profile to treat stem cells effectively above concentration threshold. For example, hepatocyte growth factor (HGF) was loaded into chitosan nanoparticles (CNPs), formed by an ionotropic gelation method through strong electrostatic interactions between the CNPs and proteins, to show the successful steady release of 85% HGF for five weeks. As shown in in vitro differentiation experiments, the treated mesenchymal stem cells

(MSCs) adapted to a round-shape hepatic cell characteristic morphology with upregulated expression of albumin [49]. Further *in vivo* study was done by co-injection of MSCs with HGF-CNPs into cirrhotic mice [50]. The *in vivo* differentiation from MSCs of hepatocytes was confirmed by the expression of albumin and cytokeratin [51]. The increased level of alpha-fetoprotein and decreased expression of alpha-smooth muscle actin and type-I collagen suggested the reversal of fibrosis of hepatic extracellular matrix.

Inorganic nanoparticles, especially nanoporous/mesoporous silica nanomaterials have been used as biomolecule carrier for stem cell differentiation in bone tissue regeneration. Neumann et al. coupled Bone morphogenetic protein 2 (BMP2) on nanoporous silica nanoparticle through amino-silane linker to test the osteoinductive effect on adipose-derived human mesenchymal stem cells (ADMSCs) [52]. Apart from osteogenesis, Kolzova and colleague used nanoporous silica particles to deliver exogenous trophic mimetics Cintrofin and Gliafin, peptide mimetics for the ciliary and glial cell derived neurotrophic factors, to embryonic stem cells (ESCs). Confirmed by immunostaining, the embryonic stem cells were driven into motor neurons with the delivery of two peptide mimics. The function of the differentiated motor neuron was also characterized through electrophysiology and voltage-sensitive fluorescent protein imaging. Furthermore, the differentiated motor neurons were transplanted into mice, showing long-term survival, demonstrating the potential application in ESC differentiation for stem cell therapy [53].

By incorporating small molecules into polyelectrolyte nanoparticles consist of polyethy-leneimine (PEI) and dextran sulfate (DS), Santos et al. delivered retinoic acid into the subventricular zone (SVZ) to induce neural stem cells differentiation [54]. The differentiated neuronal function was assessed through intracellular calcium variations upon KCL depolarization and histamine stimulation. Additionally, nanoparticle-based genetic manipulation has also been shown as an alternative strategy to guide stem differentiation.

The versatility of nanoparticles also allows target delivery of genetic molecules into the cells. Lee and coworkers have firstly demonstrated that using magnetic core-shell

nanoparticles (MCNPs) to guide neural stem cells (NSCs) differentiate into different lineages (neurons and oligodendrocytes) with the delivery of genetic materials of small interfering RNA (siRNA) or plasmid DNA. The controlled differentiation of neural stem cell was succeeded in RNA interference-based approach by suppressing two key "neural switch" genes CAVEOLIN-1 and SOX9 for oligodendrocyte and neuron differentiation respectively [55]. Chen et al. also demonstrated the hepatic differentiation of induced pluripotent stem cells (iPSCs) using mesoporous silica nanoparticles (MSNs) as a non-viral gene carrier and cell imaging agent. The mesoporous silica nanoparticle based carrier showed minimal cytotoxicity and fast cellular uptake for iPSCs. Upon treatment of MSNs loaded with hepatocyte nuclear factor 3β(HNF3β) plasmid DNA, the iPSCs went into mature hepatocyte lineage differentiation with functions like low-density lipoprotein uptake and glycogen storage [56].

As shown, small molecule dosing and genetic manipulation are equally significant for directing stem cell fate in tissue engineering and regenerative medicine [57]. With this merit, Lee et al. demonstrated the co-delivery of small molecules and RNA interference agents to differentiate neural stem cells into neurons using a single vehicle delivery system based on the cyclodextrin-modified dendritic polyamine. Through the binding of small molecule retinoic acid with β-cyclodextrin and electrostatic interaction between siRNA and dendritic polyamine, the combination of small molecule and RNA interference synergistically targeted multiple cellular pathways to induce stem cell differentiation. The controlled and reliable neuronal differentiation was confirmed through immunostaining of GFAP and TuJ1 markers [58].

1.2.2 Nanomaterial Biomimetic System

Transcription factors are master regulators in orchestrating basic cellular behaviors and are responsible for critical cellular functions and cellular fate. Therefore, by modulating the expression of specific genes, the differentiation of stem cell can also be modulated through manipulating the key transcription factors [59, 60]. Contrary to traditional viral-based delivery system with drawbacks such as cytotoxicity, immunogenicity, and

undesirable for clinical applications, Lee has developed NanoScript, a nanoparticle-based synthetic transcription [FIGURE 1.7] [51]. Specifically, NanoScript consists of 1) a nanoparticle core, usually gold nanoparticle due to its biocompatibility and ease of functionalization; 2) functional peptides for nuclear localization; 3) an activation domain mimic; and 4) a Py-Im hairpin polyamide as synthetic DNA binding domain. To demonstrate stem cell differentiation, NanoScript was designed to mimic myogenic regulatory factors (MRFs), which are a group of four transcription factors, MyoD, myogenin, Myf5, and Mrf4, functioning as a crucial regulator of muscle cell differentiation. The NanoScript-MRF successfully guided ADMSCs to differentiate into mature muscle cells showing upregulated myogenin and myosin expression and myofibrils formation [61].

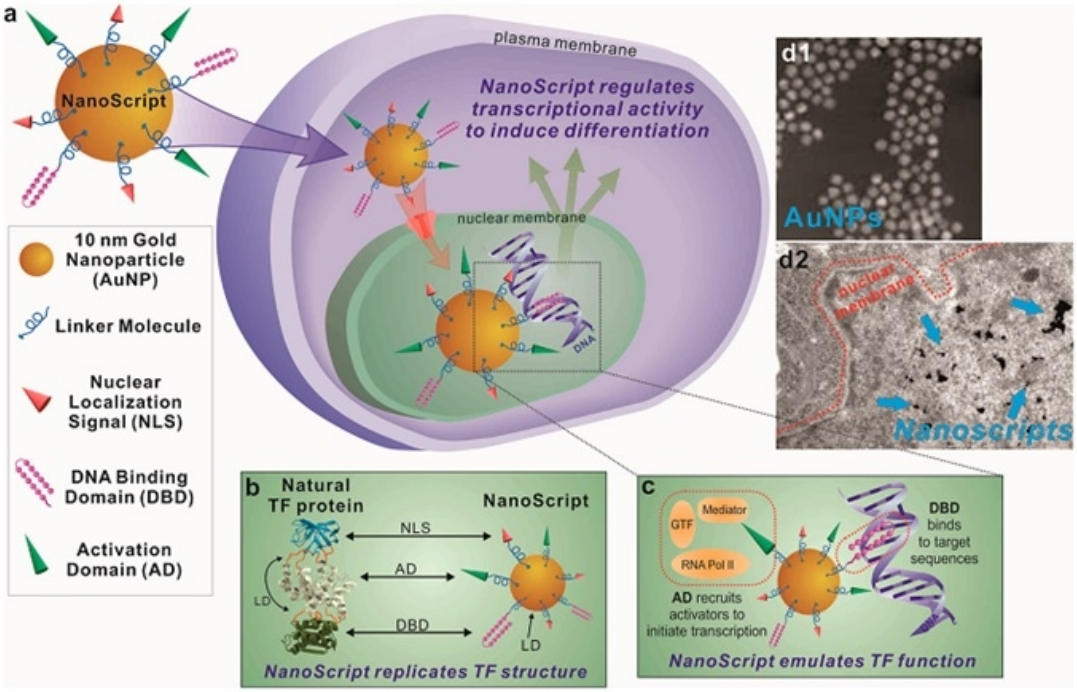

Figure 1.7: General design scheme of NanoScript. (a) NanoScript is consist of a single 10 nm gold nanoparticle, DNA binding Domain (DBD), Activation Domain (AD), and Nuclear Localization Signal (NLS), which forms assembly to mimic natural transcription factor. (b) Comparison of NanoScript with natural transcription factor. The assembly of the three essential domains of natural transcription factors is replicated by NanoScript. (c) The DBD and AD domains on NanoScript works synergistically to mimic natural transcription factors for transcriptional modulation on expression of targeted genes (d) NanoScript shows high mono-dispersity, efficient uptake and nuclear localization [51].

Furthermore, with the ability to activate endogenous gene expression activity, NanoScript was conjugated with N-(4-Chloro-3-(trifluoromethyl) phenyl)-2-ethoxybenzamide (CTB) derivative, an epigenetic modulator, to enhance chondrogenic differentiation from adipose-derived mesenchymal stem cells. Specifically, the CTB derivatives conjugated on NanoScript, triggering the p300 signaling pathway as a histone acetyltransferase (HAT) activator will induce an increase in HAT activity, transforming the chromatin structure from "tight" into "loose" form. One gene that is regulated by the p300 signaling pathway is Sox9, a key chondrogenic promoting gene. Thus, the combination of CTB derivatives and Sox9 activation, NanoScript showed enhanced chondrogenic differentiation from ADMSCs [62].

In addition to previously mentioned advantages, NanoScript can be flexibly functionalized with interchangeable components to mimic different transcription factors as well. Once natural transcription factors bind to their target genes, they can activate or repress gene transcriptions. Contrasting gene activation using the NanoScript platform, a gene repressing NanoScript was made to emulate the repression ability of natural transcription factor to downregulate gene expression at the transcription level in late 2015. By designing the repression NanoScript to downregulate Sox9 expression, neural stem cells were successfully differentiated into neurons. The mature neuron function, calcium ion flux, was observed [63].

1.2.3 Actuating Nanoparticles

Other than providing soluble cues, nanoparticles have also been shown to provide mechanical cues responsible for stem cell fate determination, tissue formation, and organ regeneration. Recently, remote magnetic actuation [FIGURE 1.8] has been demonstrated to provide mechanical stimulation to biological cells [64]. Upon mechanical stimulations, the integrin receptors at the focal adhesion of cells have been shown to correlate with cell biochemistry, morphology, and even epigenetic chromosomal activity [65, 66]. With the development of magnetic nanoparticles, cellular or even receptor level magnetic actuation can be achieved to activate different mechanosensors existing in the cell membrane [67]. Through facile surface functionalization, nano-actuators can

bind to the cell surfaces and manipulate cell function or even guide stem cell differentiation with external magnetic field. Magneto actuation technology offers a method to isolate single receptor-mediated cellular mechanotransduction process which can bring insights to related cellular-matrix interactions [68].

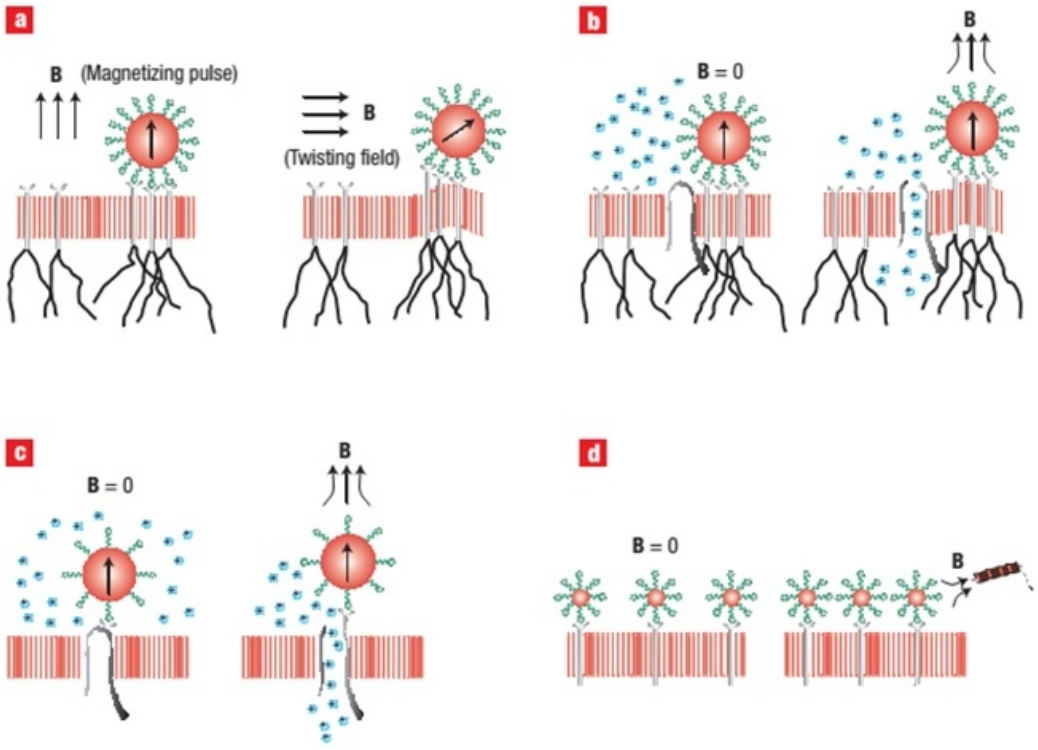

Figure 1.8: Different type of magnetic actuation. (a) magnetic twisting cytometry; (b) mechano-sensitive ion-channel activation; (c) targeted ion-channel activation; (d) receptor clustering [64].

Among the very first demonstrations of this approach, Ingber and his colleagues attached magnetic nano/microbeads to cell-surface through integrin receptors with applied tensional forces. The cellular responses were recorded with different kinds of mechanic stimuli: pulse, oscillation, static stress, and prolong stress. Through the cellular adaption to the mechanotransduction, several pathways related mechanisms like Rho signaling and mechanosensitive ion channels were identified to be responsible for the different adoption for static and dynamic mechanical changes applied to integrin [69]. Later, similar magnetic nanoparticle-based approach was applied to generate a mechanical stress to specific ion channel of interest (i.e. TREK-1). The study demonstrated the

specific activation of mechanosensitive ion channel in real time through force generated on targeting nanoparticle on the extracellular region of TREK-1 [70]. More recently, magnetic nanoparticles have been utilized to generate magneto-mechanical stimulation on cell surface receptors for stem cell differentiation. Henstock, et al. targeted the same receptor mentioned above, TREK-1, with delivery of 4pN per nanoparticle for mechanotransduction in mesenchymal stem cells, resulting in a 2.4 fold increase in the mineralization in the chick fetal femur [71]. Furthermore, due to facile functionalization on the magnetic nano-actuators, different mechano-sensitive receptors can be modulated simultaneously to study receptor interactions and pathway interplays. Hu et al. demonstrated higher mineralization ratio with the help of osteogenic culture medium and stimulating two specific cell membrane receptors: platelet-derived growth factor receptor α (PDGFRα) and integrin $\alpha\nu\beta3$ [72]. Another example of this combined receptor mechanical stimulation was demonstrated by Haj and his colleague by targeting PDGFRα and PDGFRβ. Upon cyclical magneto-mechanical stimulation, human bone marrow-derived mesenchymal stem cells (hBMSCs) differentiated into a smooth muscle cell lineage [73]. Overall, the unique size range and properties of nanoparticles enable nanoparticle-based stem cell regulatory approach with molecular level specificity, improved interaction efficiency, and spatial-temporal resolution. A nanoparticle based stem cell differentiation system with the ability to interact with cellular processes and deliver regulator molecules remotely on demand would be of significance for translating the current research to the next stage. Moreover, development of such nanomaterials with desirable degradability would be a key step for the advancement in clinical applications of nanoparticle based stem cell therapy and tissue engineering.

1.3 Insoluble Physical Microenvironment

During stem cell differentiation, cells exerts forces to and simultaneously receive forces from the surrounding extracellular matrix (ECM) proteins. Therefore, mechanical properties from the ECM play a significant role in regulating stem cell behaviors. Moreover, the physical stimulations (e.g. electrical, mechanical, and photochemical stimulation) from the substrate can provide additional dimension of control over the differentiation

process of stem cells. Furthermore, the physical microenvironments of the ECM also influence the clinical transplantation potential of stem cells. To this end, a variety of organic and inorganic scaffolds, insoluble physical microenvironments, that can mimic the ECM have been developed to have precise control over stiffness, surface topography, shear forces, degradability, and retractability. Among the various types of nanomaterials, tremendous interest has been focused on two-dimensional structured nanomaterials in the last decade since the discovery of graphene – a sp2 bonded carbon nanomaterial [74, 75]. A variety of graphene derivatives and graphene mimics have been rapidly designed, synthesized, and studied. In 2008, graphene was reported as a drug delivery vehicle for the first time, and generated intense interest in graphene-based bioapplications, ranging from biosensing, cancer therapy, drug delivery, and regenerative therapy [62,76]. For stem cell culturing and differentiation, graphene and its derivatives have been found universally to be versatile, biocompatible, and highly stable scaffolds for promoting stem cell differentiations with low inflammatory induction [77]. The broad interest generated from graphene nanosheet-based scaffolds have further inspired the development of scaffolds based on other two-dimensional nanomaterials such as ultrathin polymeric nanosheets, which is biocompatible and biodegradable. For example, the high mechanical flexibility would allow sufficient tolerance of mechanical stresses for tissue regeneration. Also, the highly absorptive and porous architecture of 2D nanomaterial constructed scaffold would be advantageous for efficient mass transport. Moreover, the high electrical conductivity of graphene based scaffold allows electrical stimulation, monitoring, and detection of differentiated neurons or cardiomyocytes. With high mechanical flexibility and versatile surface functionalities, graphene and their derivatives can be facilely engineered into scaffolds with tunable geometrical and mechanical cues to direct stem cell fate and further enhance stem cell differentiation.

1.3.1 Enhancing Stem Cell Differentiation Through Substrate Surface Chemistry

Graphene has been demonstrated as a biocompatible and promising substrate for electrical and optical interfacing devices due to their high mechanical flexibility, transparency, and conductivity. Hong et al. reported that graphene substrate fabricated by chemical vapor deposition (CVD) effectively enhanced the differentiation of human neural stem cells into neurons [FIGURE 1.9] [78]. While the mechanism remains unclear, laminin-related cellular pathways were found to be significantly enhanced and the graphene substrates were observed to act as an excellent cell-adhesion layer especially for the long-term differentiation process. Later on, also using a CVD method, Cheng et al. found that mouse hippocampal neurons cultured on graphene showed enhanced neurite sprouting and outgrowth, which could act through the GAP43 related pathways [79]. As the cell adhesion and growth factor is highly related to the surface functional groups of graphene, fluorinated graphene sheets have been developed as a scaffold to guide neural stem cell growth and differentiation as well. Loh et al. observed a further enhancement of neuronal differentiation from MSCs after they introduced neuron-inductive agent, retinoic acid, which could be attributed to an enhanced absorption and binding of retinoic acid towards the fluorinated substrate [80]. Similar to the observations in neurogenesis, enhanced cellular adhesion and proliferation on scaffolds constructed from graphene and its derivatives have also been found in the osteogenic, myogenic, chondrogenic, cardiomyogenic, and other differentiation processes in MSCs [61, 81–84].

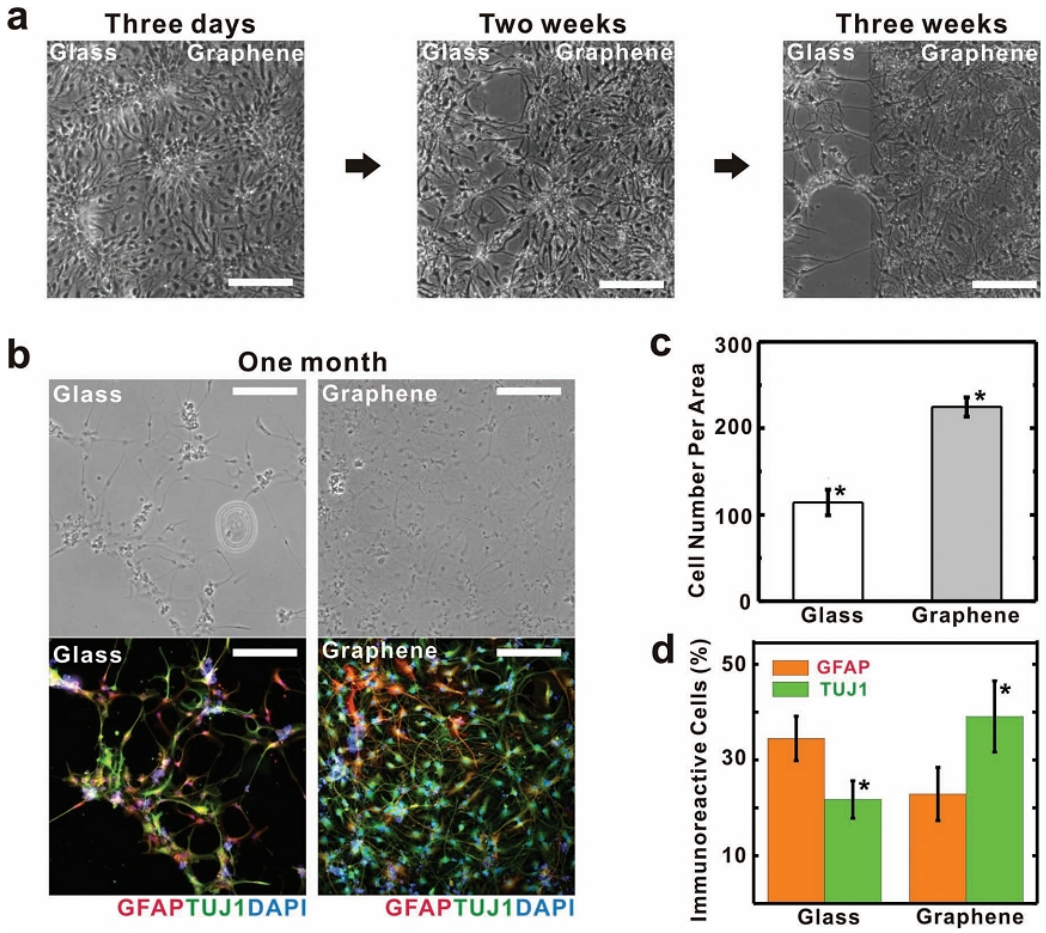

Figure 1.9: Enhanced neural differentiation of hNSCs on CVD grown graphene substrate: a) Bright-field images of the hNSCs after a differentiation process of 3 days (left), two weeks (middle) and three weeks (right). b) Bright field (top) and fluorescence (bottom) images of hNSC after differentiation on glass (left) and graphene (right) after a differentiation process of one month. Immunostaining on GFAP (red) and TUJ1 (green) for astroglial and neural cells were conducted on hNSCs. c) Cel density (per 0.64 mm^2) on graphene substrate and glass after differentiation for one month. d) Percentage of GFAP (red) and TUJ1 (green) on glass and graphene. All scale bars are 200 μ [78].

While the mechanism is still unclear, hydrophilicity, surface functionality, roughness, surface area, and nanotopographical features such as ripples were proposed to be the reasons for such enhanced adhesion. Loh et al. reported the chemical roles of graphene and graphene oxide (GO) in guiding stem cells towards specific cell lineages. They suggested that the strong noncovalent binding towards osteogenic inducers of graphene make it act as a preconcentration platform for enhanced osteogenesis [85]. They also

found that differentiation into adipocytes was suppressed on graphene-based scaffolds as insulin, a key adipogenic growth factor, was denatured through the π-π interaction on graphene scaffold. GO, on the other hand, did not interfere with the adipogenesis because they bind with insulin through electrostatic interaction. For chondrogenic differentiation, Lim et al. fabricated a cell-assembled graphene 3D biocomposite and showed enhanced chondrogenic differentiation [61]. Kim et al. later discovered that GO plays a dual role, both as an excellent cell-adhesion substrate but also as a growth factor protein preconcentration platform during the chondrogenic differentiation process [83]. In contrast to the conventional chondrogenic pellet culturing and differentiation of MSCs, the incorporation of GO preloaded with transforming growth factor-β3 (TGF-β3) can overcome the diffusion limitation of TGF-β3 that occurs inside the pellet. Chondrogenic marker, SOX-9, and Aggrecan expression were enhanced more than two-fold and three-fold respectively compared to the control group. Among the different types of stem cell differentiation, preliminary investigation on the graphene-based scaffolds for osteogenesis and neurogenesis has been conducted *in vivo*, confirming their high biocompatibility and promising applications in tissue engineering.

1.3.2 Electrical and Optical Stimulation for Enhance Stem Cell Differentiation and Detection

In addition to its surface chemistry and high aspect ratio, graphene also has unique optical and electrical properties that can stimulate stem cells and further assist differentiation. Pulse electrical stimulation has been proven to enhance the neuronal regeneration efficiently. However, it would be more practical to integrate a power supply inside body instead of inserting electrodes. Recently, to address this challenge, Wang et al. constructed a self-powered electrical stimulation system (high effective triboelectric nanogenerator, TENG) that utilized a graphene-based hybrid microfiber to enhance the differentiation of neural stem cells through electrical stimulation [FIGURE 1.10] [86].

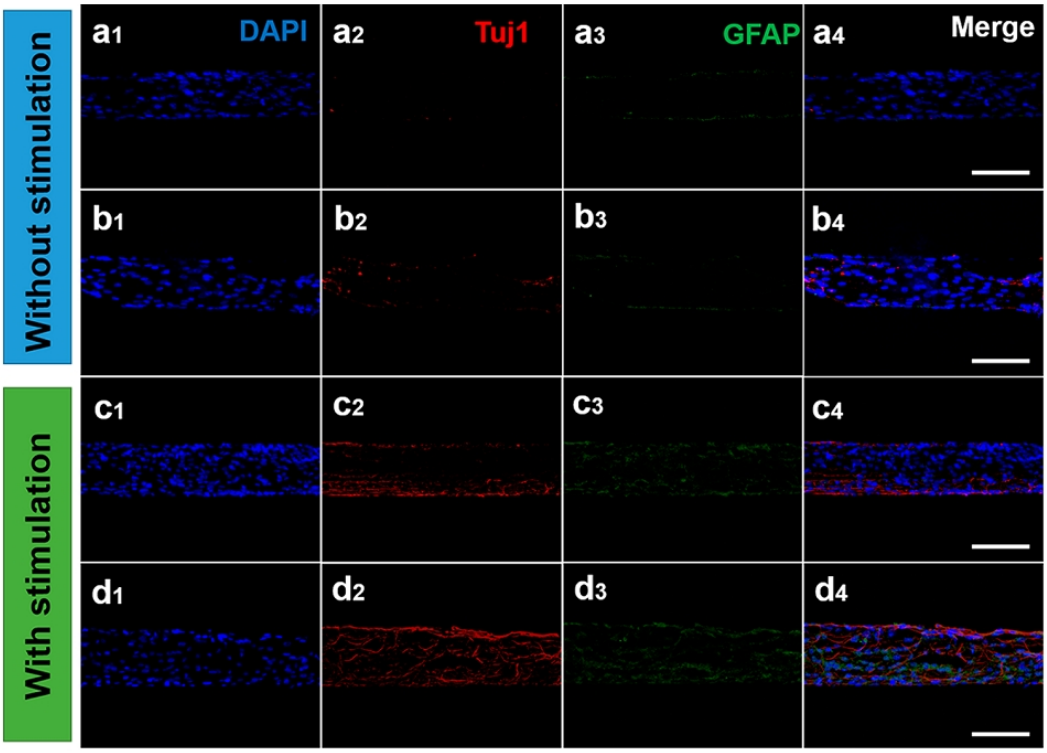

Figure 1.10: Effects of electrical stimulation of neural stem cells differentiation. a, b) After cultured under stimulation and without electrical stimulation for 21 days, cells were immunostained with DAPI (blue) for nucleus, Tuj1 (red) and GFAP (green). c, d) After cultured under TENG electrical stimulation and without TENG electrical stimulation for 21 days. All scale bars are 100 μm [78, 86].

Another study has also successfully utilized electrical field stimulation to control neural cell-cell interactions through alternating the protein synthesis related to cell mobility and cytoskeleton. More importantly, the graphene substrate also provides a good electrical coupling with the neurons for electrical stimulations. Ghaderi et al. demonstrated the differentiation of human neural stem cells (hNSCs) into neurons using reduced graphene oxide (rGO); while under pulsed laser stimulation, the photothermal effect induced radial thermal flow and resulted in the organization of the neuronal network by elongating the differentiated neurons in the radial directions [87]. In contrast, unreduced graphene oxide (GO), where there is a weaker photothermal effect, or quartz, no obvious enhanced differentiation was observed. The same group has also reported the photo-catalytical stimulation on hNSCs by utilizing an rGO/TiO_2 hybrid

scaffold [88]. They found that the flash photostimulation not only promoted proliferation (by a factor of 2.5) of the stem cells, but also guided stem cells differentiation into neuronal lineage versus glial cells. Recently, the stimulation of cardiomyocytes differentiated from ADSCs has also been demonstrated on the graphene scaffold [84].

In addition to stimulating and enhancing differentiation of stem cells, the excellent electrical and optical properties have also been utilized for detecting the behaviors of differentiated cells and for monitoring the differentiation process. For example, it is reported that the neural network can be successfully formed on graphene films and the neural signals can be effectively enhanced on graphene films [79]. Graphene can act as a conductive substrate and transfer the electrical signals to the neural cells cultured and effectively modulate neural cell behaviors. Furthermore, Choi et al. also synthesized a scaffold assembled from GO encapsulated gold nanoparticles (Au@GO NPs) that is applicable for monitoring the differentiation of NSCs based on electrochemical detection and surface-enhanced Raman Spectroscopy (SERS) [89]. It has been reported that during the stem cell differentiation, C=C bonds gradually decrease, which can be reflected from the Raman bands at 1656 cm-1. Based on this mechanism, Au@GO NPs monitored the differentiation in a non-destructive manner. By taking advantage of electrical properties of graphene, electrochemical detection of the C=C bonds was also achieved in a single platform.

1.3.3 High Flexibility for Enhanced Differentiation and Facilitated Transplantation

When acting as a coating material, the high flexibility of graphene can effectively take on the geometry, pattern, and morphology of the underlying scaffolds. Lee et al. demonstrated a silica nanoparticle-graphene oxide hybrid scaffold to promote axonal alignment of differentiated neurons [90]. Recently, Lee also developed micro-contact printing technique and fabricated combinatorial patterns of GO for the effective control over the differentiation of human adipose-derived mesenchymal stem cells (ADMSCs) [45]. The morphology of ADMSCs was effectively modulated by the GO patterns. It was found

that ADMSCs preferentially differentiate into osteoblasts and the grid pattern selectively guides the ADMSCs into neuronal lineage with highly elongated axons. Not only the aforementioned 2D scaffolds, 3D scaffolds based on graphene and its derivatives have also been fabricated by taking the advantage of their high flexibility. These 3D scaffolds could accelerate the application of graphene for tissue engineering due to the recent interest in 3D cell culture in the biological field. For example, based on layer-by-layer (LBL) assembly, Shin et al. reported a GO-embedded GelMA hybrid hydrogel scaffold that forms multiple layers of cardiomyocyte cell sheet [91]. The high flexibility of GO was proposed to facilitate cell separation and stack for the highly dense, organized 3D complex tissue architectures. Most importantly, this tissue-like cell construct demonstrated synchronous and spontaneous beating after 24-hour culture process.

Recently, scientists have fabricated a variety of 3D nanostructures based on GO and graphene using hydrothermal, electrostatic assembly, and soft templating methods. Liu et al. reported a three-dimensional hydroxyapatite – graphene hybrid forms assembled from graphene for enhanced osteogenesis [81]. Moreover, the mineralized 3D scaffold further accelerated and enhanced osteogenesis of MSCs through the increased deposition of inorganic minerals. In addition to graphene-based nanosheets, polymeric nanosheets also present high level of flexibility, which is highly advantageous for performing transplantation and adapting to local injured areas. Recently, Fujie et al. reportedly inserted a magnetic nanoparticles embedded PGA nanosheets scaffold along with in vitro cultured monolayer retinal pigment epithelial cell (RPE) for retinal recovery [92]. Due to its ultrathin nature and flexibility, the polymer nanosheet scaffold was proposed to avoid vitreous fluid leakage and minimize postsurgical infection.

Overall, the unique surface chemistry, binding toward biomolecules, fascinating electrical and optical properties of graphene-based nanosheets, and the excellent mechanical flexibilities of 2D nanomaterial have demonstrated high biocompatibility, enhanced cellular adhesion, proliferation, stem cell differentiation, detection, and transplantations. Future research would call for further investigations, especially in simulation studies on the mechanism on how graphene binds to bio-molecules and how graphene enhances

and accelerate the differentiation process. Furthermore, development of novel 2D nanomaterials assembled in 3D scaffold with biodegradable properties and studying the stem cells *in vivo* would further boost the clinical application of 2D nanomaterials in tissue engineering.

1.4 Nanotopographical Features

In addition to soluble cues, stem cells are very sensitive to the surrounding physical topographical microenvironment as well. The act of modifying the underlying substrates allows researchers to control and regulate cell adhesion, spreading, shape, elongation, and ultimately cell fate [93]. As tissue formation is heavily dependent on the recruitment of progenitor cells from the surrounding area, biomaterials introduced as implants are critical in bridging the gap when the defects are too severe to heal autogenously. Therefore, it is important for biomaterials to be able to orchestrate the biochemical and biophysical cues to facilitate cell-cell and cell-ECM interactions to facilitate stem cell therapy.

1.4.1 Nanofiber Based Stem Cell Differentiation Scaffold

Nanofiber technology has gained significant attentions and excitement in the research and development field as a potential solution to overcome some of the current challenges such as burn and wound care, tissue and organ regeneration, and various degenerative diseases in biomedical engineering. Compared to traditional bulk material, nanofiber substrates offer tremendous amount of surface area for enhanced cell adhesion, protein adhesion, and drug loading. Furthermore, nanofibers offer topographical features mimicking the macrophysical structure of natural ECM proteins in both animals and humans. Lastly, nanofibers can be fabricated through various processes and materials which have the industrial potential to be regulated and scaled up easily for mass production [94].

Typically, a nanofiber can be generated through various methods including molecular self-assembly, electrospinning, and thermally induced phase separation [95]. With

rational material design, through the use of biodegradable polymer, a nanofiber can provide time-dependent temporary support until the regenerated tissue is matured. Through the introduction of interconnected porous network, nanofibers have also been shown to promote cell-cell interaction through deep cell penetration. Additionally, a nanofiber can be fabricated by ECM protein to promote stem cell adhesion and differentiation. Moreover, a nanofiber can be controlled through fabrication to either be random or aligned to give anisotropic topographical guidance. Furthermore, bioactive compounds (growth factors, nucleic acids, and integrin-binding ligands) have also been shown to be embedded into nanofiber scaffolds. To realize the potential of nanofiber biomedical application, numerous works have been focused on the topic of tissue regeneration.

Skin Tissue Regeneration

During the early stages of nanofiber technologies in biomedical applications, many natural polymers were used. For example, in skin tissue regeneration, Park and Min et al. had demonstrated through type I collagen nanofiber [96] and surface modification of silk fibroin (SF) nanofibers with oxygen gas to increase surface hydrophilicity [97], they were able to promote the cellular activity of human dermal keratinocytes and fibroblasts. Nie group [98] and Sethuraman group [99] had used a different blend of biodegradable chitosan materials to form nanofibers that are comparable in tensile strength of normal human skin to evaluate for skin regeneration *in vitro*. By attaching bone-marrow-derived mesenchymal stem cells (BM-MSCs), Ma group demonstrated that by increasing the density of BM-MSCs, thanks to the biomimetic nanofiber scaffolds, wounds treated with BM-MSCs attached nanofibers closed more than a week earlier than untreated controls [100].

Bone Regeneration

Through a co-self-assembling peptide of phosphorylated serine peptide amphiphile and RGDS peptide amphiphile, Stupp and coworkers inserted the peptides based nanofiber

into a 5mm rat femoral critical-size defect to demonstrate bone formation and mineralization within four weeks [101]. To form the self-assembling nanofiber, the nanofiber-forming molecules contain a peptide segment with one domain that has a strong propensity to form extended β-sheets and the second domain with residues for bioactivity. The β-sheets domain is crucial for promoting assembly of fibrous aggregate instead of spherical aggregate [102]. By combining synthetic biodegradable polymers, Ramakrishna was able to increase the porosity of polycaprolactone/hyaluronic acid/gelatin to over 93% and maintain tensile strength to support osteoblast for mineralization [103]. This interconnecting porous composite nanofibrous scaffold provided large surface area for cell attachment, cell activity, and cell proliferation. Similar to the previous study [100], MSCs have also been cultured on to completely synthetic polycaprolactone nanofiber to show deep penetration of cells and the presence of abundant ECM after one week [104]. In the same report, Vaccanti group also showed that the cultured MSCs on the surface of PCL nanofibers were inclined to differentiate into osteogenic lineages as mineralization had occurred after four weeks [104].

Ligament Regeneration

Nanofibers have also been applied to ligament regeneration. Unlike other tissues, tendon and ligament have a very low propensity to regenerate due to their high ECM density and low vascularity [105]. The body typically relies on scar tissue mediated healing process which is inadequate to replace the functions of damaged or diseased tendon and ligament. As mentioned, owning to its high porosity nature, nanofiber allows for high cell infiltration rate and also allow for uniaxial alignment to mimic the anisotropic structure of native tendon and ligament. In this report [106], Ouyan and coworkers demonstrated that by seeding human tendon progenitor cells (hTSPCs) on top of aligned Poly(lactic acid) (PLLA) nanofibers higher tendon gene expression similar to native tissue was observed compare to randomly aligned fiber control which is significantly lower. The reason is that ECM production of tendon and ligament fibroblasts have specific uniaxial direction. In another approach [107], Shin stretched the nanofiber at 12 cycles/min frequency for 24h and found that human ligament fibroblast-produced

more ECM collagen on longitudinally stretch axis than the transverse axis.

Hepatocyte Regeneration

Typical nanofibers have sizes above 400 nm in diameters. However, through rational design, by functionalizing chitosan nanofiber with galactose to make galactosylated chitosan (GC) and shrinking the nanofiber to 160nm, Gu and coworkers showed the enhanced bioactivity and mechanical stability of primary hepatocytes through mimicking the ECM properties of hepatocytes [108]. Through topographical properties of nanofibers, Baharvand [109] was able to enhance the generation of hepatocyte-like cells from mesenchymal stem cells with commercially available Ultra-WebTM nanofiber with the help of inducing bio-agents. From his finding, hepatocyte markers ALB, CYP7a1, and HNF4α were consistently upregulated compared to regular tissue culture condition.

Neural Tissue Regeneration

The brain has long been considered to be more complex than the universe, and yet this spectacular piece of "organic machinery" has fascinated the scientists and clinicians endlessly. When there are subtle disturbances to the brain, complications in physical, motor, psychological, and cognitive functions can occur. Therefore, the understanding of how the central nervous system (CNS) functions and developing therapies to repair this intricate system after damages caused by diseases and injuries has been longed-for by the scientists and clinicians. In order to differentiate into specialized neural cells of interest (e.g., neurons and oligodendrocytes), researchers have been exploring the 3D microenvironment for gradient diffusion of bio-agents, cell migration, and cell-cell interaction. Zhang and coworkers [110] have developed a 3D culture system by attaching several functional motifs to self-assembling peptide RADA16. Comparing to recombinant ECM proteins, peptide-based nanofiber offers not only topographical biomimic but also the high in purity and amount of desired functional motifs. In the region with higher biological motifs, neural cells are significantly enhanced in survival. Similarly by presenting neurite-promoting IKVAV motif through 3D self-assembled peptide nanofiber, Stupp group had also shown his artificial nanofiber scaffold can rapidly

induce neuronal differentiation from neural progenitor cells [111].

For the CNS regeneration, a number of studies have been focused on the differentiation of neurons, while oligodendrocyte – a myelinating cell lineage involved in many neuronal circuits, was underappreciated. In combination with two-dimensional nanomaterial, Lee group reported a polycaprolactone (PCL) – GO hybrid scaffold for guiding stem cell differentiation into oligodendrocytes [112]. The scaffolds were fabricated from electrospinning of nanofiber scaffolds, followed by drop-casting GO solutions. The nanofiber morphology, which is a mimic of oligodendrocyte ECMs, was found to be well maintained after GO drop-casting, and the GO provides an excellent surface for cell adhesion and differentiation. From polymer chain reaction (PCR) analysis, while the PCL only and GO only (control groups) only has 1-3-fold enhancement of oligodendrocyte markers compared to the control group (glass), the PCL-GO hybrid scaffold enhanced the oligodendrocyte differentiation by over 10 folds. We have also proposed that such effective control over oligodendrocyte differentiation and development originate from integrin-mediated pathways, mainly FAK, Akt, ILK, and Fyn.

1.4.2 Nanofiber-based Delivery of Bioactive Agents

To turn nanofibers into drug carries, bioactive agents are typically immobilized into the polymer matrix for their control release. Depending on the polymer material, typical procedure consists of entrapment [113] or binding [114] as demonstrated by Stupp et al.. By entrapping the bioactive agents in an intermediate state, bioactive agents are physically encapsulated inside of the cross-linked polymers. Another method of loading bioactive agents into nanofiber is to bind the bioactive agents chemically onto the polymer structure of nanofiber through hydrogen bonds, covalent bonds, hydrophobic, and electrostatic interactions.

Drug release from nanofibers can be described through three mechanisms: desorption from fiber surface, diffusion through fibers, and *in vivo* fiber degradation [115]. When the nanofiber carrier is subjected to a physiological condition, body fluid or tissue culture media will penetrate the space in between individual nanofibers. When the nanofiber drug carrier is swollen by the aqueous phase, drugs or proteins attached to

the fiber surfaces can be released. Upon desorption from fiber surface, drugs will be disused into the aqueous phase.

1.5 Conclusion

Stem cell therapy holds the key of regenerative medicine for functional recovery from various injuries and diseases. Addressing the current challenges, nano-chemists and biologists have invested in various nanomaterials and their assembly in multidimensional domains to mimic the properties of the natural microenvironment to promote and dictate stem cell differentiation into desired lineages. In this review, the benefits of nanomaterial in the field of stem cell biology are clearly shown to be advantageous over traditional methods including bio-reagent delivery, *in vivo* imaging modality, and transplantation platform. Although much has been investigated to this point, there remains more investigation to be done in the clinical applications of multi-dimensional nanomaterials.

Chapter 2

Nanomaterial-based Insoluble/physical Microenvironment Approach for Guiding Stem Cell Differentiation

One of the critical barriers to harnessing the full therapeutic potential of stem cells is the development of an easy, effective, and non-toxic methodology to control differentiation into specific cell lineages. Stem cell differentiation can be controlled by modulating key gene expression levels or signaling pathways within the cell, which has been achieved by several conventional gene delivery methods. For the successful genetic manipulation of stem cells, the cells must typically maintain their viability for an extended period of time after single or multiple transfection procedures, without affecting the intrinsic cellular functions. This presents a considerable challenge for achieving robust and reliable control of stem cell differentiation into the desired cell lineages. To this end, in this chapter, we will explore the utilization of nanotchnolgoy and surface topography to enhance differentiation specifically in neural progenitor/stem cells (NPSCs) using insoluble cues. We will see that the nanomaterials used form a part of the extracellular matrix (ECM) and thus impact the behavior of NPSCs. By modulating the surface, we can help the elongation and alignment of differentiated neuron axons, we can also mimic the morphology of axons using nanotechnology to promote myelinating oligodendrocyte differentiation from NPSCs. Overall, we will get a taste of the emerging impact of novel nanomaterials in stem cell biology and how they can affect the behaviors of stem cells.

These works were inspired by the explosive interest of carbon based nanomaterials in the early 2000. During this time, carbon-based nanomaterials such as single or multi-walled carbon nanotubes [116, 117], pristine graphene [78, 80], or chemically derived graphene [118] have intrigued scientists due to their unique thermal, mechanical, optical, and electrical properties. Specifically for tissue engineering applications,

many scientists purposed these carbon nanomatierals for a variety of applications such as bio-scaffolds and extracellular matrices. In particular, there has been an increasing interest in using these materials to improve the growth, differentiation, and survival of stem cells6 including human neuronal stem cells (hNSCs).

In this chapter, we will dive into obtaining well-aligned hNSCs, which would be desirable for the treatment of neuroregenerative diseases. Here we report the fabrication of arrays of graphene-nanoparticle hybrid nanostructures for the differentiation and growth of adult hNSCs.In addition to enhanced neuronal differentiation, interestingly, the graphene-hybrid nanostructures resulted in highly aligned axons from the differentiating hNSCs. Specifically, this axonal alignment can be attributed exclusively to graphene and is absent in control experiments. We envision that axonal alignment of differentiated hNSCs on graphene could have significant utility in spinal cord injuries to hasten recovery. Furthermore, through the strong ECM protein and GO interaction, we further demonstrated the upregulation of stem cell adhesion and differentiation. The combination of axon mimicking surface morphology and ECM protein absorption promoted oligodendrocyte differentiation from NSCs.

2.1 Axonal Alignment and Enhanced Neuronal Differentiation of Neural Stem Cells on Graphene-Nanoparticle Hybrid Structures

2.1.1 Introduction

The ability to utilize physical cues such as nanotopographical features [119], substrate stiffness [120], geometry and the dimension of extracellular matrix (ECM) protein patterns [117,121,122] to control stem cell fate has great potential in regenerative medicine. In particular, biomaterials that are used to fabricate scaffolds and implantable substrates for stem cell-based regenerative medicine are now being investigated intensively in order to elicit specific behaviors from stem cells, including differentiation, migration and proliferation. For instance, in spinal cord and peripheral nerve injuries, the specific response of neuronal cells to nanotopographical cues is reported as one of the critical factors that must be achieved, as it is the specific guidance of axons that would lead to enhanced therapeutic effects within the injured spinal cord [123]. In particular, if the nerve gap resulting from an injury is too large, the distal and proximal sides of the damaged nerves will not be able to communicate efficiently, thus impeding the natural regeneration process [124]. As a result, a significant amount of effort has been invested in developing biomaterials that can result in axonal guidance and the growth of transplanted neurons within the injured spinal cord [124,125]. For this purpose, neural stem cells (NSCs), which can differentiate into neurons and glial cells, have been investigated for transplantation within injured spinal cords as they hold great promise for hastening functional recovery [125–127]. We and other groups have previously shown that the growth, differentiation and polarization of NSCs are strongly influenced by cell-cell and cell-extracellular matrix (ECM) interactions [117,122]. For example, ECM protein patterns and patterned nanotopographical features can be employed to control the polarity, directional growth and influence the neuronal differentiation of NSCs [122,128,129]. The challenge, however, is to provide an engineered microenvironment to the NSCs, through the development and application of novel nanomaterials, that can specifically control the axonal alignment and growth of NSC-derived neurons for the development of more effective treatments for spinal cord injuries. Here we report the fabrication of arrays

of graphene-nanoparticle hybrid nanostructures for the differentiation and growth of adult hNSCs. More importantly, these graphene-hybrid nanostructures resulted in the formation of highly aligned axons from the differentiating hNSCs.

Graphene, which consists of a monolayer of carbon atoms arranged in a 2D honeycomb lattice [74], has been shown to be a very useful nanomaterial in biomedical applications [78, 130, 131] due to its excellent flexibility, thermal properties, electrical conductivity, high strength, stiffness and biocompatibility [132]. Recently, the physicochemical properties of graphene and its biocompatibility have inspired scientists to utilize this material for stem cell-based tissue engineering [133]. For instance, graphene has been shown to support the proliferation and differentiation of adult and pluripotent stem cells [78,134]. In the case of neural tissue, it has been demonstrated that the physicochemical properties of graphene can facilitate excellent integration [78,135]. On the other hand, it has also been demonstrated that nanotopographical features that are generated using arrays of silica microbeads can lead to the acceleration of axonal growth of hippocampal neurons *in vitro* [136]. We thus hypothesized that substrates, which consist of nanoparticle-based nanotopographical features modified with graphene, could be an excellent platform to further enhance the differentiation of hNSCs into neurons and could be used to control axonal growth of the differentiating hNSCs.

2.1.2 Results and Discussion

To this end, we generated arrays of graphene-nanoparticle hybrid structures using positively charged silica nanoparticles and graphene oxide (GO), which is a chemically versatile nanomaterial containing oxygen functional groups attached to the graphene basal plane. This is particularly advantageous as the oxygen functional groups allow the GO nanosheets to attach readily to molecules or surfaces – in our case the GO nanosheets were used to coat the surface of 300 nm silica spheres (SiNPs) to form graphene-silica nanoparticle hybrids (SiNP-GO). The control and test substrates used to grow and differentiate hNSCs in this study are shown in Figure 2.1a.

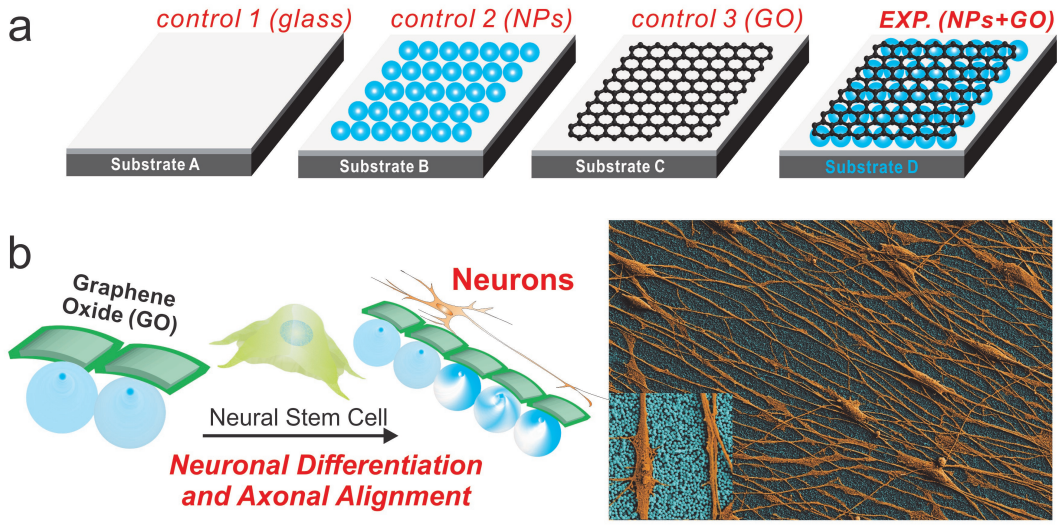

Figure 2.1: Schematic diagram depicting the influence of nanoparticle (NP) monolayers coated with graphene oxide (GO) on the alignment of the axons, extending from hNSCs, and the differentiation of hNSCs into neurons. (a) Different control and experimental conditions for differentiating hNSCs into neurons where Substrate A is a glass substrate having a positively charged surface, Substrate B is a glass substrate having a monolayer of positively charged NPs, Substrate C is a glass substrate having a positively charged surface and coated with GO, Substrate D is a glass substrate having a monolayer of positively charged NPs coated with GO. (b) hNSCs cultured and differentiated on Substrate D having a monolayers of NPs coated with GO show enhanced neuronal differentiation and axonal alignment. The differentiated hNSCs (orange) and the NPs-coated with GO (blue) in the SEM image have been pseudocolored to enhance the contrast. (Inset) Zoom-in image showing the axons aligned on a monolayer of NPs coated with GO. [90]

All of the substrates were treated with the ECM protein laminin (10 μg/mL for 4 h), which is essential for the adhesion, growth, and differentiation of hNSCs. hNSCs were then seeded onto these substrates and proliferated in culture media containing basic fibroblast growth factor (bFGF, 20 ng/mL) and epidermal growth factor (EGF, 20 ng/mL). After 24 h, differentiation was initiated by withdrawing the culture medium and replacing it with basal medium lacking growth factors. Immunocytochemistry and quantitative polymerase chain reaction (qPCR) were performed on the differentiated hNSCs after 14 days to investigate the influence of SiNP, GO and SiNP-GO on neuronal differentiation.

On Day 2 after the removal of growth factors, the hNSCs on all substrates were observed to have attached well and were growing. Typically, the axons of hNSCs grow

in random directions when cultured on most substrates, unless the substrate contains patterned proteins [117,122]. In all of our conditions, the hNSCs also grew and extended in random directions until Day 5. However, after Day 5, we observed that the extending axons began aligning only on the GO and SiNP-GO substrates and not on glass and SiNP substrates. Finally, on Day 14, the differentiated hNSCs on the GO and SiNP-GO substrates exhibited very well aligned and well-extended axons (Figure 2.2a).

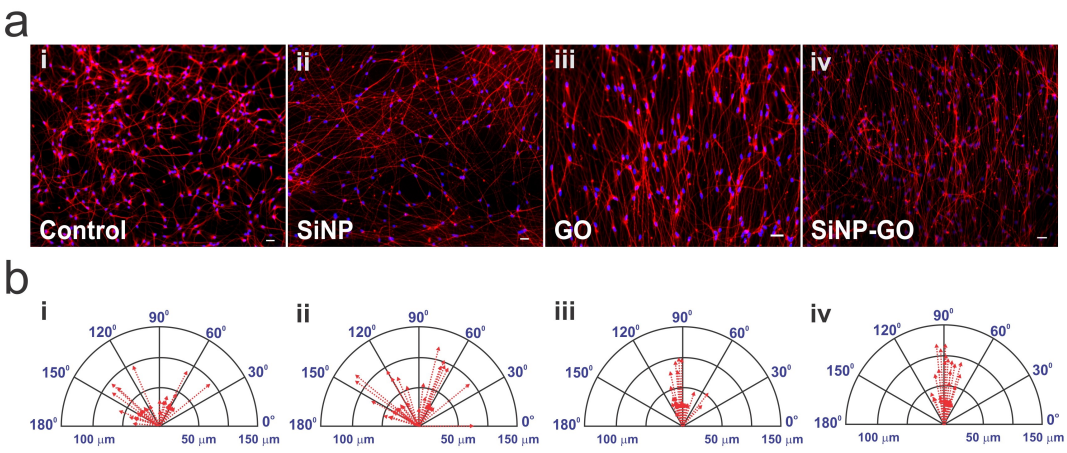

Figure 2.2: Aligned growth and extension of axons from differentiated hNSCs and compass plots showing the variation in the angle of orientation and the lengths of the axons. a) Differentiated hNSCs are immunostained with TuJ1 (red). The axons show no alignment on glass and SiNPs, whereas the axons are significantly aligned on GO and SiNP-GO. Scale bar: 10 μm. b) The compass plots show a large variation in the angle of orientation of axons on glass ($\pm 42^{\circ}$) and SiNPs ($\pm 46.11^{\circ}$) and minimal variation on GO ($\pm 17.8^{\circ}$) and SiNP-GO ($\pm 9.16^{\circ}$). The compass plot also shows that axons extending on SiNP and SiNP-GO are longer than those extending on glass and GO. [90]

On the other hand, the control hNSCs, which were differentiated on the SiNP and glass substrates, also had extended axons, but showed no alignment. To quantify this, we calculated the variation in the angle of orientation of the axons extending from differentiated hNSCs on substrates containing GO and compared it with the orientation of the axons from hNSCs differentiated on the control SiNP and glass substrates. Analysis of our data confirmed that the variation in the angle of orientation of the axons from differentiated hNSCs on the GO and SiNP-GO substrates was $\pm 17.8^{\circ}$ and $\pm 9.16^{\circ}$ respectively (Figure 2.2b), while the axons from the differentiated hNSCs on

glass and SiNP substrates extended randomly, having a much wider variation of $\pm 42^{\circ}$ and $\pm 46.11^{\circ}$, respectively, in the angle of their orientation (Figure 2.2b). The images in Figure 2.2a clearly show that the axons extending from differentiated hNSCs aligned exclusively on substrates having GO as a component of the ECM. We also investigated the influence of nanotopographical features on the length of the axons extending from hNSCs. Recently, self-assembled silica microbeads were shown to significantly accelerate the extension of axons from hippocampal neurons *in vitro* [136]. We thus analyzed the lengths of the extending axons from the hNSCs differentiated on the different substrates on Day 14. The average length of the axons extending from differentiated hNSCs cultured on SiNPs was 20.76% more than the average length of those cultured on glass, and 11.3% more than those cultured on GO (Figure 2.2b). We therefore confirmed that the alignment of axons is exclusively due to the presence of GO within the ECM while the presence of the underlying SiNP monolayer can lead to an increase in the average length of the axons from hNSCs differentiated on SiNP-GO. This hNSC behavior was also confirmed using SEM (Figure 2.3a).

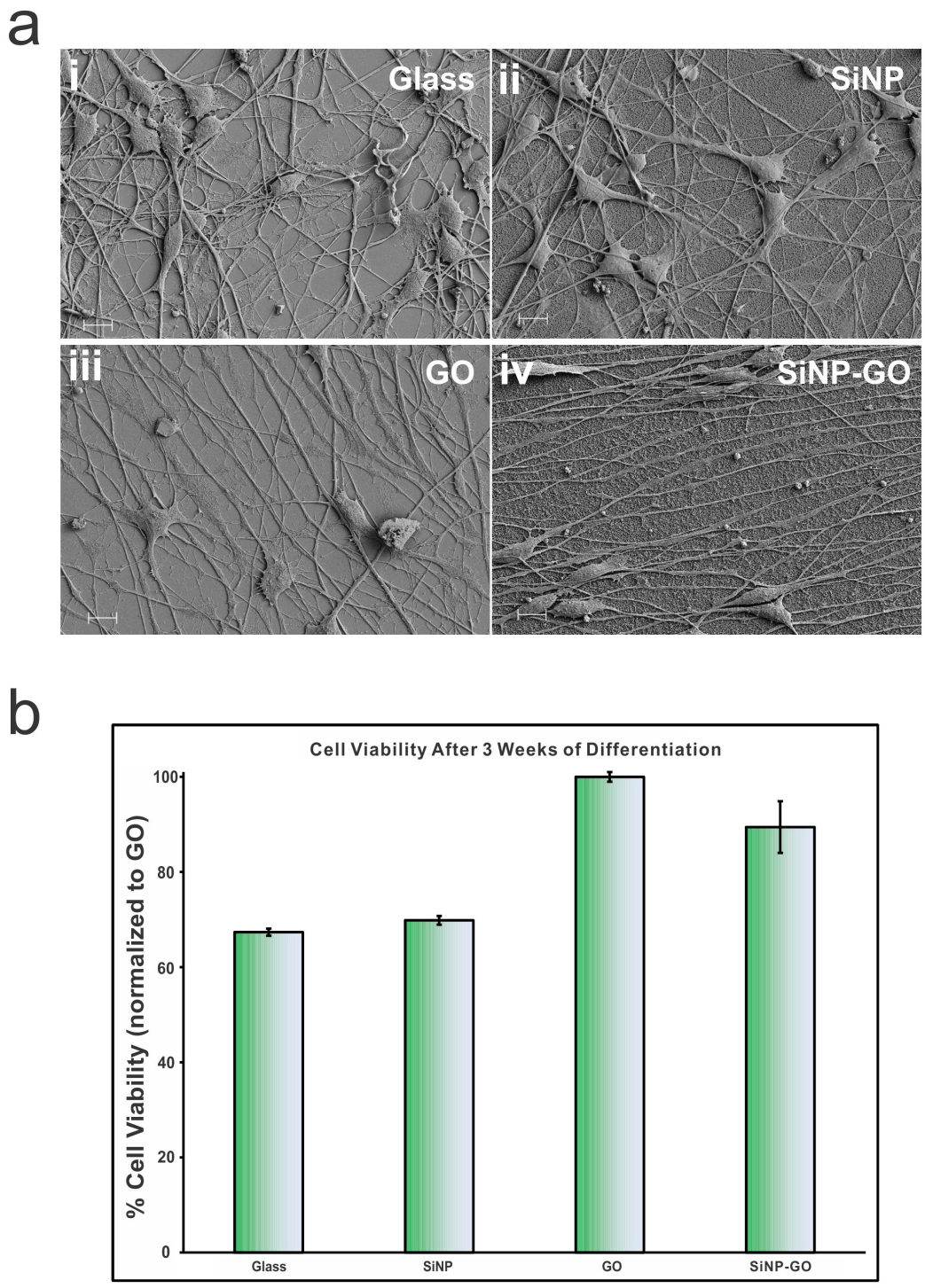

Figure 2.3: Scanning electron microscopy (SEM) showing the behavior of hNSCs and MTS assay for biocompatibility and long term survival of differentiated hNSCs on GO and SiNP-GO. a, SEM images confirm that the axons do not align on control and SiNP substrates and they align on GO and SiNP-GO substrates. Scale bar is10 µm. b, MTS assay results show that GO and SiNP-GO is biocompatible and aids in the long term survival of hNSCs as compared to glass and SiNPs. The results have been normalized to hNSC viability on GO. [90]

We then went on to investigate whether the alignment of axons from the differentiating hNSCs on GO and SiNP-GO could be due to crowding of hNSCs and thus be dependent on the seeding density as it has previously been demonstrated that differences in cell density can yield a noticeable difference in cell alignment [137]. To this end, we reduced the cell density by 50% and observed the behavior of the hNSCs over a period of two weeks. We found that the cells behaved in the same manner as described above, even at the lower cell density. This result confirmed that the axonal alignment of differentiating hNSCs on the SiNP-GO substrates is not dependent on the cellular density of the hNSCs but only on the presence of GO. This is a remarkable finding as it suggests that the only factor determining the alignment of axons from differentiating hNSCs, is the presence of GO. This result could be very useful, especially for the development of scaffolds to restore neuronal function within damaged regions of the central nervous system.

In order for our platform to be used to control cell behavior or develop scaffolds, they should be biocompatible. In the case of regenerative medicine, the materials not only have to be biocompatible but must also support stem cell differentiation and survival over long periods of time. To this end, as a potentially advantageous material for tissue engineering, graphene has already been shown to support the long-term survival and induce neuronal differentiation of hNSCs3. As such, we used a standard cell viability assay (MTS assay) which confirmed that the GO and SiNP-GO substrates significantly enhanced cells survival after 3 weeks of differentiation as compared to the control SiNP and glass substrates (Figure 2.3b). This is particularly advantageous for stem cell biology and regenerative medicine as the differentiating stem cells are required to grow, differentiate and survive to have beneficial and lasting effects.

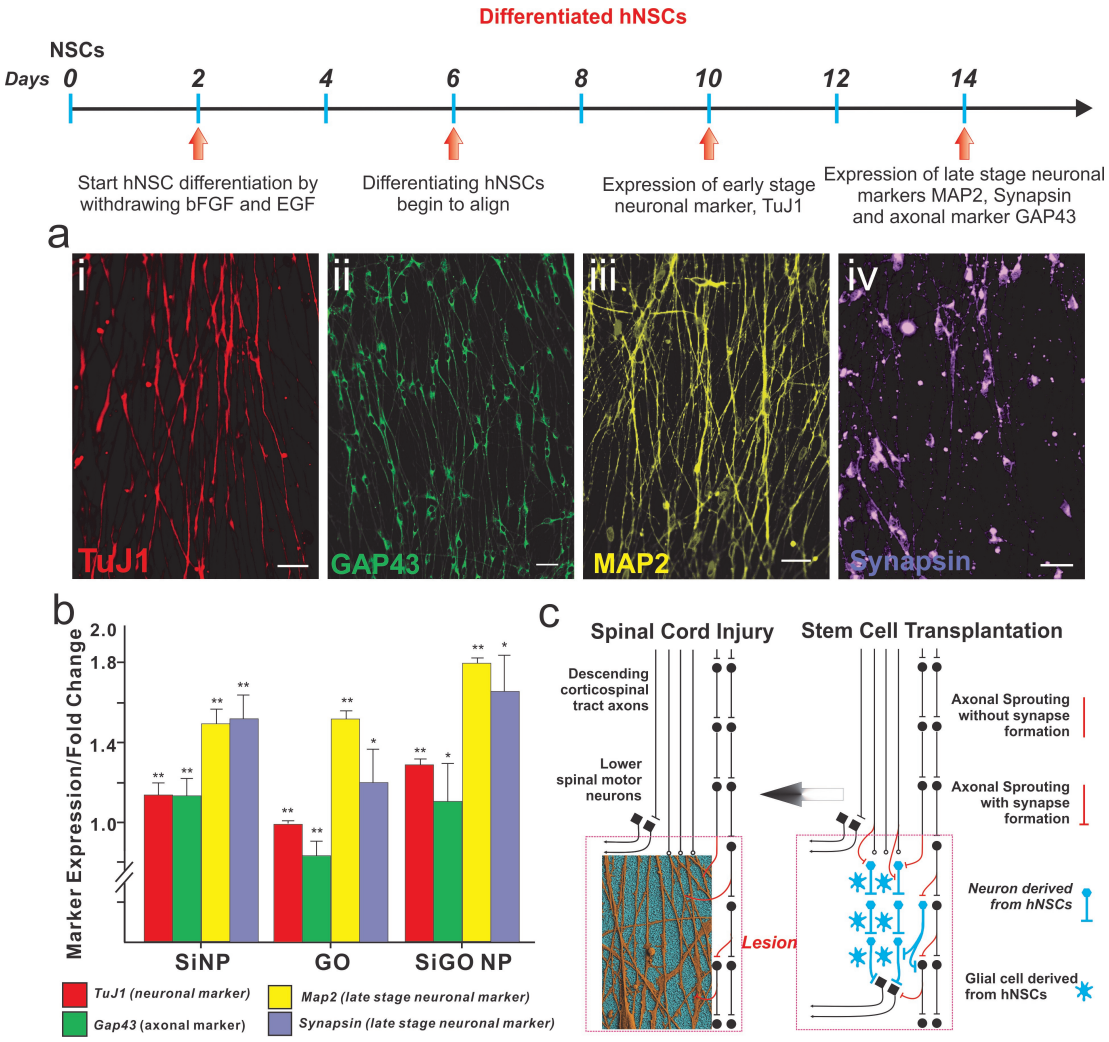

Figure 2.4: Enhanced neuronal differentiation of hNSCs on a SiNP-GO substrate. a) hNSCs spontaneously differentiated on SiNP-GO show the presence of early stage neuronal marker TuJ1(red) and late stage neuronal markers MAP2 (pseudocolored yellow) and synapsin (pseudocolored purple). They also highly express the axonal marker GAP43 (green). Scale bar: 10 μm. b) Quantitative RT-PCR (qPCR) results for early and late stage neuronal markers expressed by the hNSCs differentiated on the different substrates. The results are normalized to the expression levels of the neuronal markers in hNSCs differentiated on glass. N=4 and *P <0.05, **P<0.01 compared to hNSCs differentiated on glass using student t-test analysis. The results clearly show that hNSCs differentiated on the SiNP-GO substrate show significantly enhanced expression of early and late stage neuronal markers. The expression of axonal marker GAP43 increases due to the presence of SiNP monolayers. c) Scheme depicting the significance of alignment and growth of axons from differentiating hNSCs. The hNSCs which can be transplanted into the injured region (lesion) of a spinal cord differentiate into neurons and glial cells (image on right). The axons from the neurons (derived from hNSCs) if aligned can hasten the recovery process. Our SiNP-GO hybrid structures can provide the ideal microenvironment to align axons which could potentially improve communication leading to rapid recovery of the injured spinal cord (image on left) [90].

Having established that the SiNP-GO substrates could promote cell survival and differentiation for extended periods, we sought to explore and quantify the effects of SiNP-GO on neuronal differentiation of hNSCs. To this end, we investigated the expression of immature and mature neuronal markers in the differentiated hNSCs after two weeks. Our immunostaining data demonstrated that most of the aligned axons from differentiated hNSCs were characterized by the expression of the neuronal marker TuJ1, and also the presence of mature neuronal markers such as MAP2 and synapsin (Figure 2.4a). We also confirmed the expression of axonal marker, GAP43. Next, to quantify the expression levels of these neuronal markers, we performed qPCR analyses on mRNA collected from the hNSCs differentiated on GO and SiNP-GO substrates and compared them to hNSCs differentiated on SiNP and glass substrates. While the expression levels of neuronal and axonal markers were up-regulated on all substrates as compared to the control glass substrates, we found that the hNSCs differentiated on SiNP-GO substrates showed the highest expression levels for all neuronal markers such as TuJ1, MAP2 and synapsin (Figure 2.4b). Thus, we can conclude that the combined effect of having SiNP and GO on a single platform shows increased neuronal differentiation and remarkable alignment of differentiated hNSCs.

To determine if the axons from differentiating hNSCs align exclusively on GO, we also used pristine graphene deposited on glass, using chemical vapor deposition (CVD). Although this behavior has not been reported previously, we did observe axonal alignment on pristine graphene, similar to the axonal alignment observed on GO. However, the water solubility of GO and the presence of functional groups allows positively charged SiNP monolayers to be readily coated with GO, by simply dipping the substrate into a solution of GO. Another factor that has to be considered is the interaction of the ECM protein, laminin, with pristine graphene. Proteins have been shown to have higher and more rapid immobilization on GO, as compared to pristine graphene due to the abundant surface oxygen-containing groups such as epoxide, hydroxyl and carboxyl groups present on GO [138]. The presence of these polar functional groups on GO makes the GO-coated substrates very hydrophilic as compared to the pristine graphene-coated substrates, which significantly affects the adsorption of proteins [134].

We thus believe that laminin, which is dissolved in water, more readily assembles on GO as it is water soluble in contrast to pristine graphene, which is hydrophobic. Considering these factors, as compared to graphene, GO is more advantageous for coating SiNPs, assembling ECM proteins, and aligning the axons from differentiated hNSCs. Next, we further investigated whether the axonal alignment was due to the unique chemical structure of graphene, which is composed of carbon atoms in a hexagonal lattice. For this purpose, we chose another nanomaterial, molybdenum disulfide (MoS_2), which is from the family of two dimensional layered transition metal dichalcogenides and has a physical structure similar to that of graphene. Nanoflakes of MoS_2 were deposited on glass substrates, onto which laminin was assembled. We then grew and differentiated hNSCs on MoS2. Importantly, we observed that while the hNSCs grew well and differentiated on MoS_2, they did not showed any axonal alignment, thus confirming that the unique chemical structure of graphene causes the axons to align.

Finally, for potential future therapeutic applications in regenerative medicine, it would be crucial to demonstrate the alignment and enhanced neuronal differentiation using flexible and biocompatible polymeric substrates, which can be transplanted *in vivo*. We thus reproduced our results using flexible and biocompatible polymeric substrates made from polydimethylsiloxane (PDMS), a polymer which has been widely used for implantable neural devices such as flexible microelectrodes and three-dimensional scaffolds for tissue engineering [139, 140]. We prepared monolayers of SiNPs on thin, flexible PDMS substrates by stamping the PDMS substrates on monolayers of SiNPs generated on glass cover slips. The stamping led to clean and complete transfer of the SiNP monolayers onto the PDMS surface (Figure 2.5a, b).

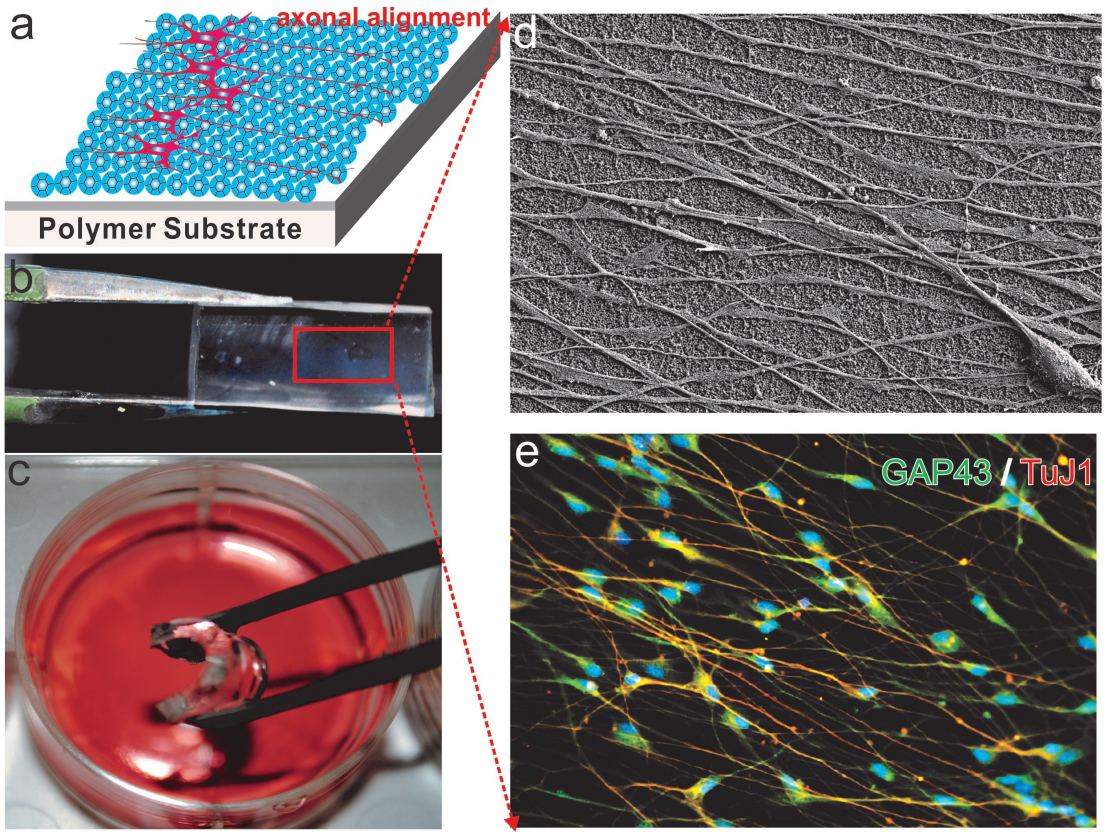

Figure 2.5: Axonal Alignment of differentiated hNSCs on SiNP-GO on flexible and biocompatible substrates made from polydimethylsiloane (PDMS). a) Schematic diagram of axonal alignment of differentiated hNSCs on SiNP-GO on polymer substrates. b) SiNP-GO monolayer on PDMS. c) Flexible PDMS substrate with SiNP-GO in media for culturing hNSCs. d) SEM image of SiNP-GO on PDMS substrate showing highly aligned axons from hNSCs on Day 14. e) Immunocytochemistry results showing the expression of neuronal marker (TuJ1) and axonal marker (GAP43) in hNSCs [90].

We then dipped the PDMS substrates having SiNPs into a solution of GO and dried the substrates using a stream of pure nitrogen gas. In this way, we achieved high-quality SiNP monolayers coated with GO using PDMS. Control substrates were similarly prepared using PDMS polymer instead of glass. We then coated these substrates with laminin and differentiated the hNSCs as before. We observed that the differentiating hNSCs showed excellent alignment of axons on the PDMS substrates containing GO and SiNP-GO. SEM image analysis confirmed that the presence of SiNP-GO on PDMS led to the alignment of axons as previously observed (Figure 2.5c). Immunostaining confirmed the presence of neuronal marker TuJ1 and axonal marker GAP43 (Figure 2.5d). We thus believe that our results using flexible implantable polymeric substrates

further demonstrates the potential of using SiNP-GO as a new hybrid material for enhancing neuronal differentiation and aligning axons, thus hastening the functional recovery of injured spinal cords.

2.1.3 Conclusion

In summary, we have demonstrated that the engineered microenvironment consisting of nanotopographical features modified with GO provides instructive physical cues that lead to enhanced neuronal differentiation of hNSCs along with significant axonal alignment. We have also demonstrated the alignment of differentiating hNSCs on implantable, flexible polymeric substrates, which has tremendous potential in regenerative medicine. We currently do not understand the mechanism governing axonal alignment. However, we are in the process of investigating the underlying principles that govern the alignment of hNSCs due to graphene-hybrid nanostructures. Nevertheless, we envision that the alignment of axons from the differentiating hNSCs using SiNP-GO can potentially be applied to developing GO-based materials for transplanting hNSCs into injured sites of the central nervous system in order to efficiently repair impaired communication. Overall, we believe our hybrid nanostructures comprised of a nanoparticle monolayers coated with GO have tremendous implications for the potential use of GO as an ECM component especially in the field of neurobiology.

2.1.4 Materials and Methods

SiNP substrate preparation

Cover glass (Number 1, 22 mm × 22 mm; VWR) was cut equally into smaller pieces (18 mm × 6 mm) and sonicated in Nanopure water (18.2 mω) for 10 mins and then cleaned in piranha solution (a 3:1 mixture of sulphuric acid and hydrogen peroxide) for 10 min (Caution: Piranha solution is extremely corrosive). The glass coverslips were then washed again in Nanopure water (18.2 Mω) and dried under a stream of pure nitrogen. To generate films of nanotopographical features, 300 nm silicon oxide nanoparticles (SiNPs, Corpuscular Inc)) were utilized. The washed cover slips were

centrifuged at 2,000 RPM for 2 min in a 2 mL eppendorf tube containing 25 mg/mL of the positively charged (amine terminated) SiNP solution. The substrates were then washed with Nanopure water and dried under a stream of pure nitrogen. The cover slips were then rinsed thoroughly with ethanol and dried under nitrogen. They were then baked at 100°C in an oven for 10 min.

Human neural stem cell (hNSC) culture and differentiation

Human neural stem cell line (ReNCell VM, Millipore) was purchased and routinely expanded according to the manufacture's protocol. The hNSCs were maintained in laminin (Sigma, 20 μg/ml) coated culture dishes precoated with poly-L-lysine (10 μg/ml) in ReNCell VM media (Millipore) supplemented with the antibiotics, geniticin (Life Technologies), in the presence of basic fibroblast growth factor (bFGF-2, 20 ng/ml, Millipore) and epidermal growth factor (EGF, 20 mg/ml, Peprotech). All of the cells were maintained at 37°C in a humidified atmosphere of 5% CO_2. For consistency, the experiments were carried out on cells between passages 2 and 5. Neural differentiation was initiated by changing the medium to basal medium (without bFGF-2 and EGF) on the different substrates (SiNP, GO, SiNP-GO and control glass) coated with laminin. The cells were allowed to differentiate for 14 days with the basal medium in each being exchanged every other day.

Image Analysis

Image analysis on images taken from scanning electron microscopy was done to determine the axonal alignment and axonal length. Alignment is recorded by tracing axons through Adobe Photoshop software and measuring linear angle from connected cell bodies. Axonal length is done using a similar method by tracing axons and calculating the pixels spanned in Adobe Photoshop. Once the number of pixels has been obtained, it is converted to µm by referencing the amount of pixels the scale bar spanned. Since there needs to be a reference angle, SEM images are rotated so that the general directions of axons are similar among all conditions. The number of cells participated in

image analysis is one hundred per condition. Data analysis was conducted after alignment angles were recorded for all four conditions. Due to the nature of sample loading of SEM, angles of axons are not a good statistical indicator of alignment. Instead, the angle of standard deviation is the better statistical representative of the effects of our platform. Figure 2.2b depicts a compass plot plotted with MathWorks Matlab software illustrating axonal angles and lengths of four conditions.

Cell Viability Assay

The percentage of viable cells on the different substrates was determined after 3 weeks of differentiation using the MTS cell viability assay following standard protocols described by the manufacturer. All experiments were conducted in triplicate and averaged. The data is represented as formazan absorbance at 490 nm, considering the differentiated hNSCs on SiNP-GO as 100% viable.

Immunocytochemistry

To investigate the extent of neuronal differentiation, at Day 14, the basal medium was removed and the cells fixed for 15 minutes in Formalin solution (Sigma) followed by two PBS washes. Cells were permeabilized with 0.1% Triton X-100 in PBS for 10 minutes and non- specific binding was blocked with 5% normal goat serum (NGS, Life Technologies) in PBS for 1 hour at room temperature. To study neuronal differentiation, antibodies against neuronal markers were used. Mouse primary antibodies were used against TuJ1 (1:500, Covance), NeuN (1:100, Millipore), and rabbit primary antibodies were used against Synapsin (1:100, Santa Cruz Biotechnology) and MAP2 (1:100, Cell Signaling). The fixed samples were incubated overnight at 4°C in solutions of primary antibodies in PBS containing 10% NGS. After washing three times with PBS, the samples were incubated for 1 h at room temperature in solution of anti-mouse secondary antibody labeled with Alexa-Fluor 647 or Alexa-Fluor 546 and anti-rabbit secondary antibody labeled with Alexa-Fluor 546 or Alexa-Fluor 488 (1:200, Life Technologies), Hoechst 33342(1:500, Life Technologies) in PBS containing 10% NGS to observe neuronal differentiation. After washing the samples thrice with PBS, the substrates were

mounted on glass slides using ProLong antifade (Life Technologies) to minimize photobleaching. The mounted samples were imaged using Nikon TE2000 Fluorescence Microscope.

PCR Analysis

Total RNA was extracted using Trizol Reagent (Life Technologies) and the mRNA expression level of TuJ1, MAP2, GAP43 and Nestin were analyzed using Reverse Transcriptase PCR (RT-PCR) and quantitative PCR (qPCR). Specifically, cDNA was generated from 1 μg of total RNA using the Superscript III First-Strand Synthesis System (Life Technologies). Analysis of mRNA was then accomplished using primers specific to each of the target mRNAs. RT-PCR reactions were performed in a Mastercycler Ep gradient S (Eppendorf) and images were captured using a Gel Logic 112 (Carestream) imaging system. qPCR reactions were performed using SYBR Green PCR Master Mix (Applied Biosystems) in a StepOnePlus Real-Time PCR System (Applied Biosystems) and the resulting Ct values were normalized to Gapdh. Standard cycling conditions were used for all reactions with a melting temperature of 60°C. Primers are listed below:

Table 2.1: Primers used for Axonal Alignment Characterization

Gene	F Primer	R Primer	Size (bp)
FAK	5'-CAATGCCTCCAAATTGTCCT-3'	5'-TCCATCCTCATCCGTTCTTC-3'	157
GAPDH	5'-ATGACTCTACCCACGGCAAG-3'	5'-GGAAGATGGTGATGGGTTTC-3'	87
Nestin	5'-GGAAGAGAACCTGGGAAAGG-3'	5'CTTGGTCCTTCTCCACCGTA-3'	122
GAP43	5'-AACCTGAGGCTGACCAAGAA-3'	5'-GGGACTTCAGAGTGGAGCTG-3'	118
MAP2	5'-GAGAATGGGATCAACGGAGA-3'	5'-CTGCTACAGCCTCAGCAGTG-3'	100
TUJ1	5'-ACTTTATCTTCGGTCAGAGTG-3'	5'-CTCACGACATCCAGGACTGA-3'	97

2.2 Guiding Stem Cell Differentiation into Oligodendrocytes Using Graphene-Nanofiber Scaffolds

2.2.1 Introduction

Damage to the central nervous system (CNS) from degenerative diseases or traumatic injuries is particularly devastating due the limited regenerative capabilities of the CNS. Among the current approaches, stem cell-based regenerative medicine has shown great promise in achieving significant functional recovery by taking advantage of the self-renewal and differentiation capabilities of stem cells, which include pluripotent stem cells (PSCs), mesenchymal stem cells (MSCs) and neural stem cells (NSCs) [141–143]. However, the low survival rate upon transplantation has been a longstanding barrier for scientists and clinicians to overcome [144]. To this end, numerous types of natural and synthetic biomaterial scaffolds have been developed, the two main classes being hydrogels and nanofibers, in an attempt to mimic the cellular microenvironment, support cellular growth and improve cellular viability [145, 146]. Yet, designing scaffolds with defined properties to selectively guide stem cell differentiation towards a specific neural cell lineage is still an ongoing challenge.

For CNS regeneration, the selective differentiation of NSCs into either neurons or oligodendrocytes (as opposed to astrocytes) is highly desirable [127, 147]. A number of approaches have been employed to guide differentiation into neurons, including genetic modifications, growth factors, cytokines, substrate topography and even nanomaterials [58, 78, 122, 148, 149]. However, oligodendrocyte differentiation has proven to be much more elusive, resulting in only a small percentage of the differentiated cell population [150]. The primary approach to guide oligodendrocyte differentiation has focused on either developing culture media containing a combination of growth factors or the forced expression of key oligodendrocyte-promoting transcription factors via viral gene transfection [151]. However, developing a biomaterials-approach to achieve efficient differentiation of NSCs into mature oligodendrocytes, which are the myelinating cells of the CNS, while eliminating the potential adverse or variable side-effects from growth factors and viral gene vectors, would be highly beneficial [143].

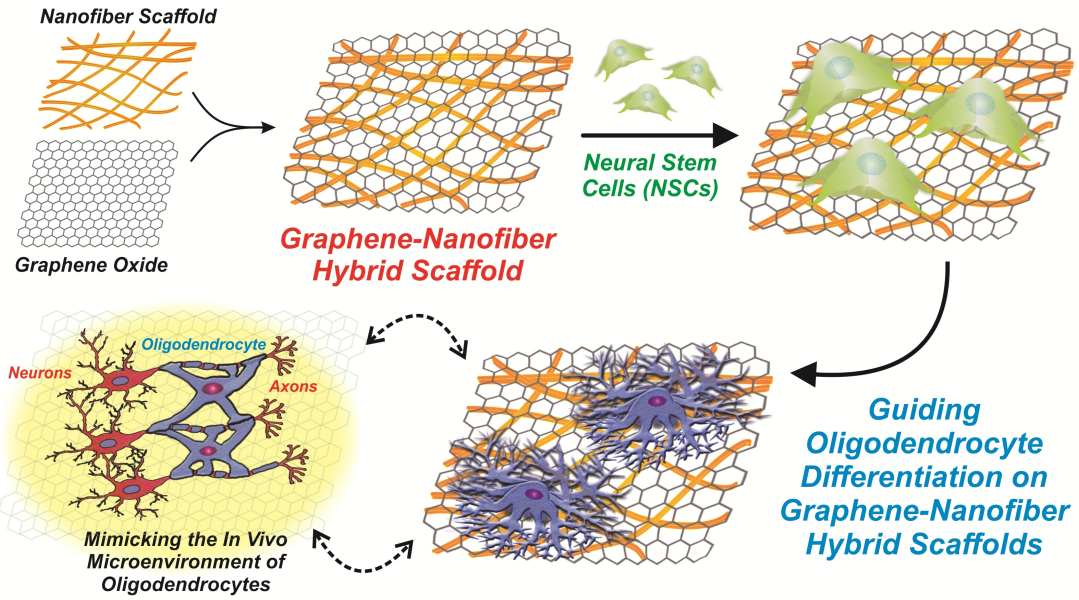

Figure 2.6: Schematic diagram depicting the fabrication and application of graphene-nanofiber hybrid scaffolds. Polymeric nanofibers (comprised of polycaprolactone) generated using electrospinning were subsequently coated with graphene oxide (GO) and seeded with neural stem cells (NSCs). NSCs cultured on the graphene-nanofiber hybrid scaffolds show enhanced differentiation into oligodendrocyte lineage cells. [112]

Herein, we report the use of a graphene-based nanomaterial for designing hybrid nanofibrous scaffolds to guide NSC differentiation into oligodendrocytes (Figure 2.6). Graphene-based nanomaterials, such as graphene oxide (GO), have recently gained considerable interest for tissue engineering applications due to their favorable chemical, electrical and mechanical properties [89, 152]. Besides serving as a highly elastic and flexible structural reinforcement, substrates coated with GO have been demonstrated to promote the growth and differentiation of various stem cell lines including induced PSCs, MSCs and NSCs [85, 134]. Based on these considerations, we demonstrate the use of GO as an effective coating material in combination with electrospun nanofibers for the selective differentiation of NSCs into oligodendrocytes. By varying the amount of GO coating on the nanofibers, we observed a GO concentration-dependent change in the expression of key neural markers, wherein coating with a higher concentration of GO was seen to promote differentiation into mature oligodendrocytes. Further investigation into the role of GO-coating on the nanofibrous scaffolds showed the overexpression of a number of key integrin-related intracellular signaling molecules that are known to

promote oligodendrocyte differentiation in normal development.

Electrospun nanofiber scaffolds exhibit several key properties that are advantageous for neural tissue engineering including a high degree of porosity, high surface-to-volume ratio, and a relatively close structural mimic of the native extracellular matrix (ECM) [153]. From the wide array of polymeric materials available, we used polycaprolactone (PCL) to generate our nanofibrous scaffolds. PCL is a biodegradable and biocompatible polyester approved by the FDA for use in the human body as a drug delivery device and suture, and is also widely used for neural tissue engineering [154].

2.2.2 Results and Discussion

In our studies, PCL was electrospun onto a metallic collector and then transferred to glass substrates for cell culture using a medical grade adhesive. Nanofibers with an average diameter of 200-300 nm were generated, which is a fiber size range that has been reported to be favorable for oligodendrocyte culture, potentially due to the close morphological resemblance to axons [155] (Figure 2.7a). Thin-layered graphene oxide (GO) was then synthesized and dispersed in deionized water. The hydrophobic PCL nanofibers were exposed to oxygen plasma to render the surface hydrophilic. The GO was then deposited on the PCL nanofiber surface, thus allowing for the efficient and uniform coating of the PCL nanofiber surface with GO, as seen with field emission scanning electron microscopy (FE-SEM; Figure 2.7b).

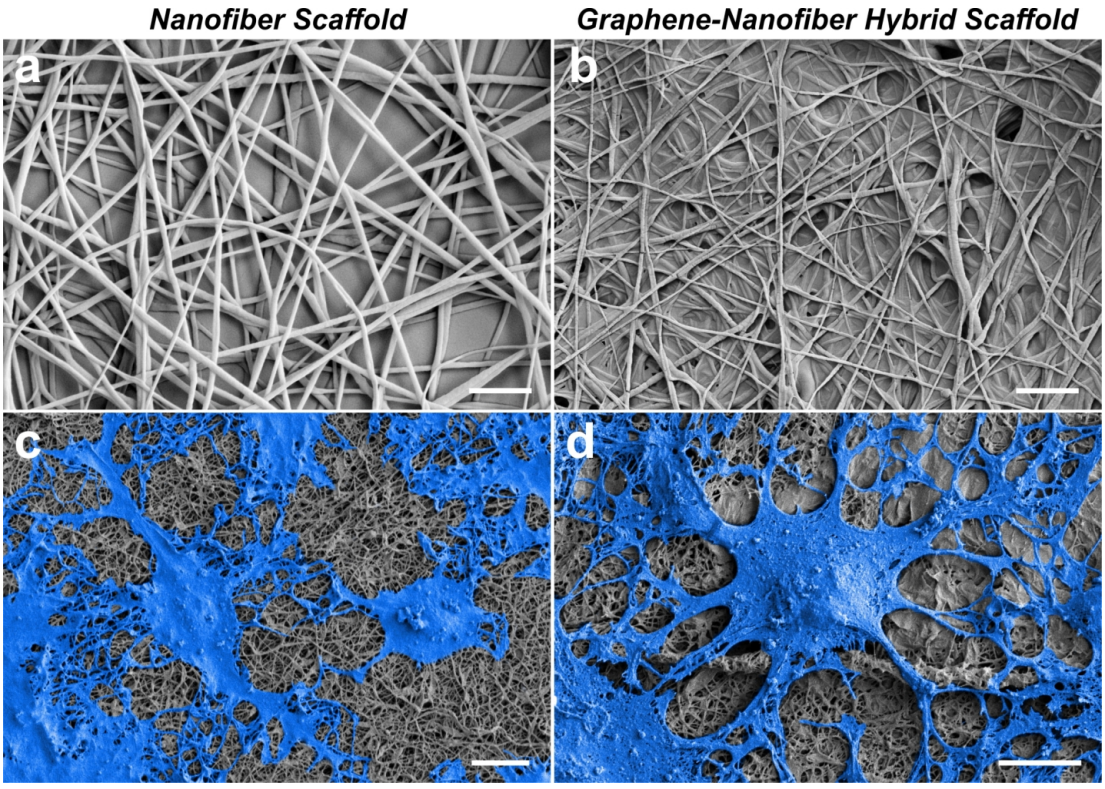

Figure 2.7: Morphology of nanofibrous scaffolds and cultured NSCs on the scaffolds. a,b) Field emission scanning electron microscopy (FE-SEM) images of a) PCL nanofibers, b) PCL nanofibers coated with GO using 1.0 mg/mL GO solution. Scale bars: 2 μm. c,d) FE-SEM of differentiated NSCs cultured on c) PCL nanofiber scaffolds and d) graphene-nanofiber hybrid scaffolds after six days of culture. Cells are pseudo-colored blue for contrast. The differentiated cells on the graphene-nanofiber hybrid scaffolds (d) show a clear morphological difference in terms of process extension compared to nanofiber scaffolds alone (c). Scale bars: 10 μm. [112]

For the culture of NSCs, the scaffolds were then coated with laminin, a well-established ECM protein which is essential for the adhesion, growth and differentiation of NSCs [156]. Green fluorescent protein-labeled rat NSCs were then seeded onto the scaffolds and the morphology was monitored using fluorescence microscopy. After six days of culture, a significant difference in the cellular morphology was evident on GO-coated nanofibers compared to the nanofibers alone. FE-SEM shows cell attachment on these surfaces in greater detail, wherein the cells on the GO-coated nanofibers display extensive branching of cell processes (Figure 2.7c-d). This type of extensive process extension is a characteristic attribute reported to distinguish oligodendrocytes from other neural cells [157]. This difference in cellular morphology provides evidence for the

potential ability of our hybrid scaffolds to enhance NSC differentiation into oligodendrocytes. To systematically investigate the effect of GO-coating on NSC differentiation, we generated hybrid scaffolds with varying amounts of GO-coating. Solutions containing three different concentrations of GO (0.1, 0.5, and 1.0 mg/mL) were deposited on oxygen plasma-treated PCL nanofibers.

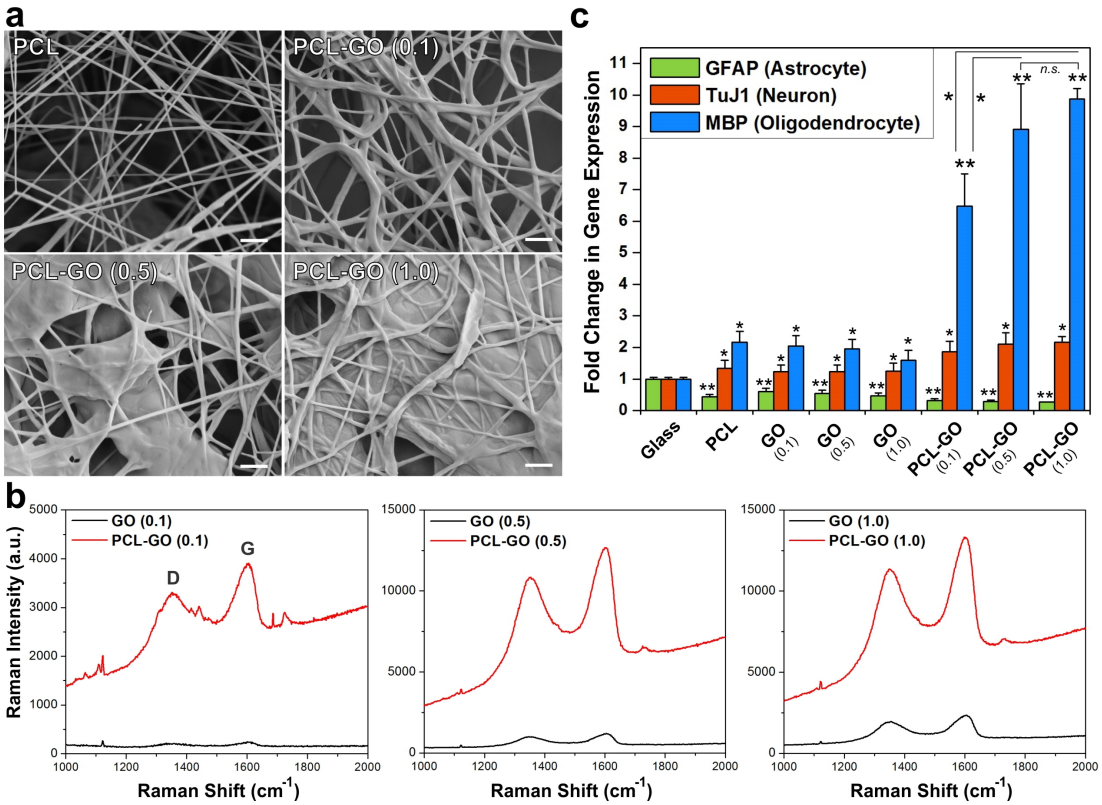

Figure 2.8: Effect of concentration-dependent GO-coating on NSC differentiation. a) FE-SEM images of PCL nanofibers coated with GO solutions of varying concentrations: 0.0 mg/mL [PCL], 0.1 mg/mL [PCL-GO (0.1)], 0.5 mg/mL [PCL-GO (0.5)], and 1.0 mg/mL [PCL-GO (1.0)]. Scale bars: 1 μm. b) Raman spectroscopy of glass and PCL nanofibers coated with varying concentrations of GO. c) Quantitative PCR (qPCR) of NSCs grown on various substrates from RNA isolated after six days of culture. The plot shows fold change in gene expression of markers indicative of neurons (TuJ1), astrocytes (GFAP) and oligodendrocytes (MBP), wherein the PCL-GO substrates show the highest expression of MBP. The gene expression is relative to GAPDH, and normalized to the conventional PLL-coated glass control. Student's unpaired t-test was used for evaluating significance (* = p <0.05, ** = p <0.01, n.s. = no significance), compared to the control glass substrates (denoted above the bar) or between different substrates. [112]

The degree of coating using the various GO concentrations was then observed using

FE-SEM (Figure 2.8a). GO-coating of PCL with 0.1 mg/mL, indicated as PCL-GO (0.1), shows the clear presence of GO compared to PCL nanofibers alone, with uniform coating on the surface of individual fibers. In contrast, PCL-GO (0.5) and PCL-GO (1.0) exhibit a much greater extent of GO attachment on the nanofibrous surface, wherein PCL-GO (1.0) shows the highest degree of GO coating and connectivity between fibers. This was confirmed quantitatively using Raman Spectroscopy, where the characteristic peaks of the D band (1,350 cm^{-1}) and G band (1,600 cm^{-1}) indicate the presence of GO. Comparison of the Raman intensity of these peaks further supports the trend described above in terms of concentration-dependent GO coating on the PCL nanofiber surfaces (Figure 2.8b). Moreover, the nanofibrous scaffolds at all three concentrations show significantly higher GO content compared to control glass surfaces coated with the same respective amounts of GO (Figure 2.8b). The higher surface area-to-volume of the nanofibers available for GO attachment, in conjunction with the 3D structure of these scaffolds, may attribute to this difference in coating.

These various PCL-GO substrates were then used to examine the influence of GO-coating on modulating NSC differentiation. For comparison, the following control substrates were used: 1) PLL-coated glass (standard substrate for *in vitro* neural cultures), 2) PCL nanofibers alone, and 3) GO-coated glass (at the abovementioned three GO concentrations). All of the substrates were coated with laminin to facilitate NSC attachment, and the cells were harvested after six days of culture to compare the gene expression of key neural markers. Quantitative PCR (qPCR) was utilized to compare gene expression of three key markers that are indicative of differentiated NSCs: glial fibrillary acidic protein (GFAP; astrocytes), β-III tubulin (TuJ1; neurons) and myelin basic protein (MBP; mature oligodendrocytes). First, it is important to note that both the PCL nanofibers alone and GO-coated glass (at all three concentrations) individually show enhanced oligodendrocyte gene expression, with about a 2-fold increase in MBP expression (Figure 2.8c). At the same time, TuJ1 shows only about a 1.3-fold increase and GFAP shows about a 0.5-fold decrease in expression, which indicates a stronger preference for differentiation towards oligodendrocytes rather than neurons and astrocytes (Figure 2.8c). While no reports exist for the effect of graphene-based

nanomaterials on oligodendrocyte differentiation, previous studies have reported that electrospun nanofibers can act as permissive culture platforms for oligodendrocyte culture [158, 159].

Since each individual component (nanofibers and GO) displayed a favorable trend in NSC differentiation towards oligodendrocytes, we hypothesized that the combination of GO and nanofibers in a single scaffold may have a synergistic effect. In the PCL-GO samples, we observed a remarkable trend in gene expression of these neural markers. The nanofibers coated at the lowest GO concentration (0.1 mg/mL) showed a 6.5-fold increase in MBP, which is much higher than the expression on PCL nanofibers alone and GO-coated glass controls (Figure 2.8c). Interestingly, this enhancement in MBP expression was even more pronounced when the concentration of GO was further increased, wherein the cells on PCL-GO (0.5) showed an 8.9-fold increase and PCL-GO (1.0) showed a 9.9-fold increase in MBP expression (Figure 2.8c). Based on the data, there is no statistically significant difference in MBP expression on the PCL-GO (0.5) and PCL-GO (1.0), indicating the saturation of GO on the PCL nanofiber surface. The overall increase in MBP expression of the cells grown on the PCL-GO substrates points to the role of GO in the observed result, in which the 3D PCL nanotopography serves to increase the amount of GO coating and the consequent surface interface in contact with the NSCs compared to the traditional 2D surfaces. In addition, the simultaneous decrease in GFAP expression and relatively small increase in TuJ1 expression provides further evidence that the hybrid scaffold promotes selective NSC differentiation, with a strong preference towards oligodendrocyte lineage cells (Figure 2.8c). To explore the potential of these hybrid scaffolds as a culture platform for oligodendrocyte differentiation, we elected to use PCL-GO (1.0) for all subsequent experiments (termed PCL-GO hereafter). In regard to biocompatibility, NSCs grown on these scaffolds show excellent survival, as found with cell viability assays.

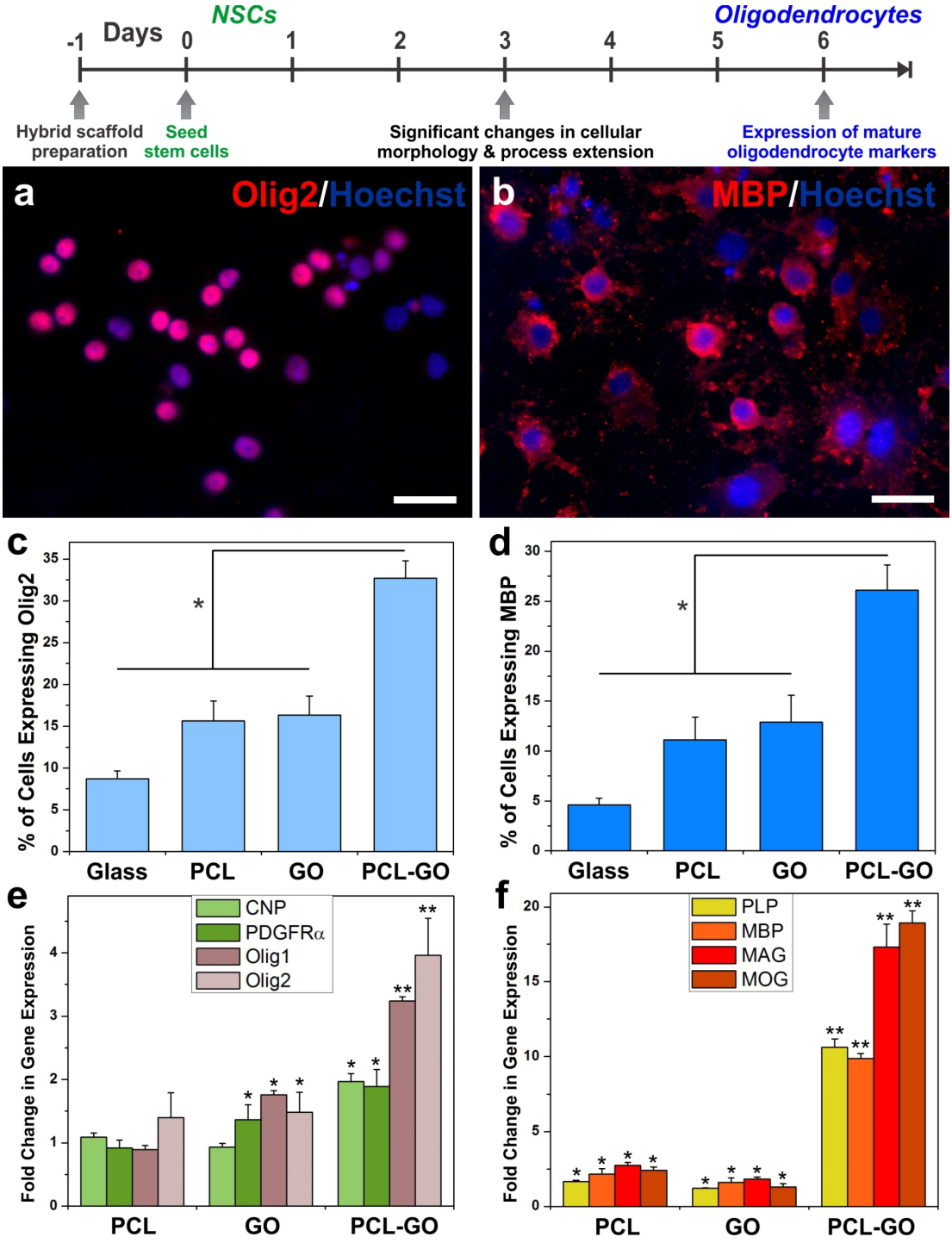

Figure 2.9: Enhancement in oligodendrocyte differentiation on PCL-GO. a,b) Fluorescence image of NSCs grown on PCL-GO after six days of culture, stained for the a) early oligodendrocyte marker Olig2 and b) the mature oligodendrocyte marker MBP. Scale bars: 20 μm. c,d) Quantitative comparison on various substrates of the percentage of cells expressing c) Olig2 and d)MBP. Graphs show mean $\pm$ s.e.m, n=3, comparison by ANOVA * = p <0.01. e,f) Quantitative PCR analysis was used to assess the gene expression of e) early oligodendrocyte markers including CNP, PDGFR, Olig1, and Olig2; f) mature oligodendrocyte markers including PLP, MBP, MAG, and MOG. The gene expression is relative to GAPDH, and normalized to the conventional PLL-coated glass control. Student's unpaired t-test was used for evaluating significance (* = p <0.05, ** = p <0.01), compared to the control glass substrate. [112]

We next sought to further characterize the degree of differentiation into oligodendrocytes by examining the expression of well-established oligodendrocyte markers at the genetic- and cellular-level. After six days of culture, the cells grown on PCL-GO were immunostained for the early marker Olig2 and the mature marker MBP (Figure 2.9a-b). The immunostained cells show extensive expression of both the nuclear-localized Olig2 and the cytosolic MBP. A similar expression was also observed for the oligodendrocyte-specific surface markers O4 (early) and GalC (mature). Expression of these early and mature protein markers confirms the successful NSC differentiation into oligodendrocytes. The degree of differentiation was further quantified by determining the percentage of cells expressing Olig2 and MBP on the various substrates (Figure 2.9c-d). While the conventional PLL-coated glass substrates showed only about 9% of the cells expressing Olig2, both the PCL only and GO-coated glass substrates showed about 16% Olig2-expressing cells (Figure 2.9c). On the other hand, the PCL-GO substrate displayed about 33% of the cells expressing Olig2, which is significantly higher than all other conditions (Figure 2.9c). A similar trend was also observed for MBP expression, wherein 26% of the cells on PCL-GO were positive for MBP, which corroborates the gene expression results shown earlier (Figure 2.8c). Comparison of the percentage of cells stained for TuJ1 (neurons) and GFAP (astrocytes) further supports the selective differentiation into oligodendrocytes, with PCL-GO displaying a significant decrease in GFAP-positive cells and a minor increase in the number of TuJ1-positive cells.Given the difficulty in achieving the spontaneous differentiation of stem cells into oligodendrocytes, our unique graphene-nanofiber hybrid scaffolds exhibit a significant enhancement in oligodendrocyte formation.

To further confirm that the hybrid scaffolds promote oligodendrocyte differentiation, we evaluated changes in gene expression for a variety of well-known early and mature oligodendrocyte-specific markers. qPCR was carried out for detecting the gene expression of: 1) early markers including 2',3'-cyclic-nucleotide 3'-phosphodiesterase (CNP), platelet-derived growth factor receptor alpha (PDGFRα), Olig1, and Olig2, and 2) mature markers including proteolipid protein (PLP), MBP, myelin-associated

glycoprotein (MAG), myelin oligodendrocyte glycoprotein (MOG), adenomatous polyposis coli (APC), glutathione S-transferase-pi (GST-π), and galactocerebroside (GalC). For all genes of interest, NSCs on PCL-GO exhibited the strongest level of expression compared with all other control substrates (Figure 2.9e-f). Interestingly, several of the known genes indicative of myelinating oligodendrocytes also showed a substantial increase in gene expression. For instance, MAG and MOG, which are glycoproteins reported to be crucial during the myelination process in the CNS [157], were seen to have a 17-fold and 19-fold increase in gene expression, respectively (Figure 2.9f). Taken together, these results confirm that NSCs cultured on PCL-GO substrates exhibit a strong preference towards oligodendrocyte differentiation.

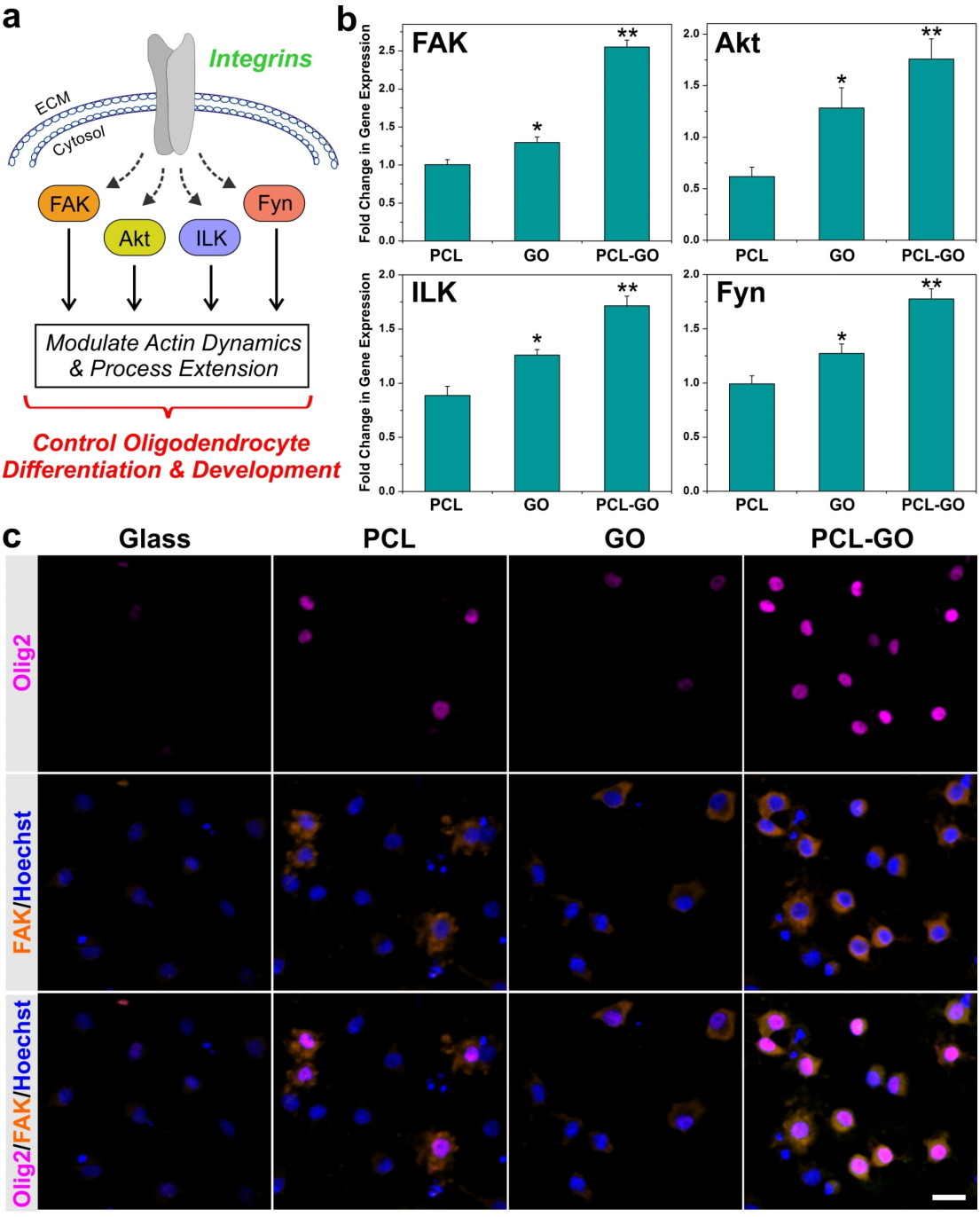

Figure 2.10: Expression of integrin-related signaling proteins on nanofibrous scaffolds. a) Schematic diagram depicting the integrin signaling proteins involved in oligodendrocyte differentiation and development. b) Quantitative PCR analysis was used to assess the gene expression of the integrin signaling proteins FAK, Akt, ILK and Fyn. The gene expression is relative to GAPDH, and normalized to the conventional PLL-coated glass control. Student's unpaired t-test was used for evaluating significance (* = $p < 0.05$, ** = $p < 0.01$), compared to the control glass substrate. c) Confocal image of NSCs grown on various substrates (PLL-coated glass, PCL only, GO-coated glass, and PCL-GO) after six days of culture, co-stained for Olig2 (purple) and FAK (orange). Scale bar: 20 μm. [112]

These hybrid scaffolds provide a unique microenvironment that was found to be permissive to oligodendrocyte formation. Yet, how the extracellular cues from these hybrid scaffolds modulate intracellular signaling pathways to control this selective differentiation remains to be explored. Numerous studies report the importance of stem cell-extracellular matrix interactions in directing oligodendrocyte differentiation [160]. These interactions have been observed to modulate intracellular signaling pathways, primarily through the activation of integrin receptors found on the cellular membrane. Integrin-mediated signaling has been found to be especially important for facilitating fundamental oligodendrocyte processes including survival, differentiation and myelination [161]. Culminating evidence from previous reports suggests the role of several key signaling proteins downstream of integrins in regulating oligodendrocyte differentiation and development, including focal adhesion kinase (FAK), Akt, integrin-linked kinase (ILK) and Fyn kinase (Fyn) [161] (Figure 2.10a). Therefore, we investigated whether oligodendrocyte differentiation-related signal transduction is promoted in NSCs cultured on PCL-GO.

Among the various cell signaling proteins, we examined the expression of FAK, Akt, ILK and Fyn, which have been found to mediate cytoskeletal remodeling and process extension during oligodendrocyte development. Moreover, disruption of each of these proteins has been reported to cause a variety of developmental defects including reduced process extension, aberrant myelin formation and attenuated expression of myelin proteins [162–165]. We found that NSCs cultured on the GO-coated surfaces enhanced the gene expression of all of these factors (Figure 2.10b). These signaling molecules exhibited the same trend in expression, wherein the GO-coated glass showed higher expression than PCL, and PCL-GO showed the strongest level of expression with a 2.6-fold increase in FAK and about a 1.7-fold increase in Akt, ILK and Fyn (Figure 2.10b). Additionally, treating the cells grown on PCL-GO scaffolds with cell signaling inhibitors showed a significant decrease in gene expression of mature oligodendrocyte markers, which provides further evidence for the potential role of such cellular signaling in the observed oligodendrocyte differentiation. Collectively, this data supports the role of GO-coating in the upregulation of these downstream molecules in the integrin

signaling pathway and may explain, at least in part, the enhanced oligodendrocyte differentiation of NSCs on our hybrid scaffolds.

In order to further elucidate this correlation, we sought to observe cellular co-localization of markers indicative of both integrin signaling and oligodendrocyte differentiation using confocal microscopy. Dual staining was carried out for: 1) Olig2, an oligodendrocyte marker, and 2) FAK, one of the main regulators of integrin-ECM signaling[19d] and found in our study to show the highest expression in cells cultured on PCL-GO. The immunostaining for Olig2 (purple) and FAK (orange) was compared for NSCs cultured on PCL-GO with the other control substrates (Figure 2.10c). As observed earlier, cells grown on PCL-GO showed the strongest intensity and highest number of cells expressing Olig2, with minimal expression on the glass control and moderate expression on PCL and GO. A similar trend was also observed in FAK staining, which corresponds to the gene expression levels shown in Figure 2.10b. Since the localization of FAK is in the cytoplasm and Olig2 is in the nucleus, the co-localization of the two markers within the same cell can be easily visualized. Interestingly, the cells expressing FAK also expressed Olig2, a phenomenon that was observed on all substrates (Figure 2.10c). Moreover, PCL-GO showed the strongest expression of both markers and the highest number of cells co-expressing FAK and Olig2. Together, our data suggests that the GO-coating on the nanofiber scaffolds may promote oligodendrocyte differentiation through specific microenvironmental interactions which activate integrin-related intracellular signaling.

2.2.3 Conclusion

Overall, we have demonstrated the capability of a unique graphene-nanofiber hybrid scaffold to provide instructive physical cues that lead to the selective differentiation of neural stem cells into mature oligodendrocytes, without introducing differentiation inducers in the culture media. The ability to selectively guide stem cell differentiation by merely changing the properties of an underlying biomaterial scaffold is a valuable approach for tissue engineering, which can help complement or potentially eliminate the use of exogenous differentiation inducers such as viral gene vectors, growth factors

and small molecule drugs. Moreover, our hybrid scaffold is exceptional in that it combines the well-established properties of nanofibers and graphene-based nanomaterials. For instance, nanofibers have been shown to provide ideal topography for fabricating nerve guidance conduits, directing neurite outgrowth and promoting axonal regeneration [145, 153]. On the other hand, graphene-based nanomaterials provide permissive surfaces for protein and cell adhesion, as well as high conductivity to mediate electrical stimulation for supporting neuronal electrophysiology [166]. In turn, a hybrid scaffold which combines the morphological features of nanofibers and the unique surface properties of graphene in a single culture platform can be highly beneficial. We envision that such a platform can serve as a powerful tool for developing future therapies for CNS-related diseases and injuries.

2.2.4 Materials and Methods

Electrospinning PCL Nanofibers

Polycaprolactone (PCL, 80 kDa, Sigma, cat. #440744) was dissolved in a 3:1 (v/v) mixture of chloroform-methanol to prepare a 5% (w/v) polymer solution. The solution was placed into a syringe with a 22-guage needle and electrospun onto an aluminum surface, which was positioned horizontally, at a flow rate of 0.8 mL/hr. A 20-kV voltage was applied with a high voltage power supply and a 15-cm working distance was utilized. The scaffolds were then dried under vacuum for two days, and then transferred to cover glass (No. 1, VWR) using a medical grade adhesive (Factor2, cat. #B400).

Synthesis of Graphene Oxide

Thin-layered GO was synthesized by first making graphite oxide using a modified Hummer's method [1]. Briefly, graphite (1 g; Sigma Aldrich, 100 mesh) was mixed with 98% H_2SO_4 (12 mL), $K_2S_2O_8$ (2.5 g) and P_2O_5 (2.5 g) at 80°C on a hotplate for six hrs. Then, de-ionized water (500 mL) was added into the mixture and the solution was stirred overnight. The preoxidized graphite was filtered out by using filter paper with

200-nm pores. After dried under ambient conditions overnight, graphite with pre-treatment was stirred with concentrated H_2SO_4 (98%). After 10 mins, $KMnO_4$ (15 g) was slowly added into the mixture in a 30 min time period with stirring under the ice bath condition (temperature was kept below 15°C). After the addition of $KMnO_4$, the temperature of the mixture was gradually raised to 35°C and was stirred for three hours. Successively, de-ionized water (250 ml) was slowly dropped into the mixture (temperature below 50°C) with vigorous stirring, followed by stirring for four hours. Finally, the reaction was quenched by the addition of de-ionized water (700-ml) followed by the addition of 30% H_2O_2 (20 ml). The graphite oxide was centrifuged down under 10,000 rpm for 10 minutes and washed with 10% HCl solution (three times) and de-ionized water (five times) to get the graphite oxide. A two hour ultrasonication process (40 kHz, 40 W, 1 second ultrasonication and 1 second resting period) was used to exfoliate the graphite oxide aqueous solution into graphene oxide (GO). Finally, the GO solution was centrifuged under 13,300 rpm for 30 minutes to get rid of multi-layered GO.

Generating GO-coated PCL Hybrid Scaffolds

GO was dispersed in deionized water at varying concentrations (0.1, 0.5 and 1.0 mg/mL). The substrates (cover glass or PCL nanofibers) were treated with oxygen plasma for one min, followed by deposition of the GO solution directly on top of the substrate for five mins. Substrates were then vacuum dried for at least six hr. The Renishaw inVia Raman microscope was used to quantify the amount of GO-coating. After gold sputtering, the Zeiss Sigma field emission scanning electron microscope (FE-SEM) and the ORION helium ion microscope was used to visualize the scaffolds.

Rat NSC Culture and Differentiation

GFP-labeled rat neural stem cells (Millipore) were purchased and expanded according to the manufacture's protocol. The NSCs were maintained in laminin (Sigma, 10 μg/ml) coated culture dishes precoated with poly-L-lysine (PLL, 10 μg/ml) in Millitrace basal media (Millipore) supplemented with the penicillin and streptomycin (Life

Technologies), in the presence of basic fibroblast growth factor (bFGF-2, 20 ng/ml, Millipore). All of the cells were maintained at 37^circC in a humidified atmosphere of 5% CO_2. For consistency, the experiments were carried out on cells between passages 2 and 5. In preparation for NSC culture, the substrates treated with oxygen plasma for 1 min and then coated with laminin (10 μg/mL) overnight in the culture hood. While oxygen plasma treatment was observed to be sufficient for sterilization, substrates were alternatively sterilized under UV for 30 mins prior to laminin coating. Control glass substrates were coated with PLL (10 μg/ml) overnight followed by laminin (10 μg/mL) overnight. NSCs were cultured on the substrates at 0.8 $\times$ 105 NSCs/mL in basal medium (without bFGF) to initiate differentiation. The cells were allowed to differentiate for six days, with the basal medium exchanged every other day.

Immunocytochemistry

Cell cultures were fixed with 4% formaldehyde (ThermoScientific) for 15 min, blocked for 1 hr with 5% normal goat serum (NGS, Life Technologies), and permeabilized with 0.3% Triton X-100 when staining for intracellular markers (MBP, Olig2, TuJ1, GFAP, and FAK). The combinations of the following primary antibodies were incubated overnight at 4°C: mouse antibody to Olig2 (1:300, Millipore, MABN50), mouse antibody to MBP (1:300, Abcam, ab62631), mouse antibody to O4 (1:50, StemCell Technologies, 01416), mouse antibody to GalC (1:200, Millipore, MAB342), mouse antibody to TuJ1 (1:500, Covance, MMS-435P), rabbit antibody to GFAP (1:300, Dako, Z033429-2) and rabbit antibody to FAK (1:75, Santa Cruz Biotech, sc-557). Appropriate Alexa Fluor 546- and Alexa Fluor 647-conjugated secondary antibodies were used to detect the primary antibodies (1:200, Molecular Probes) and Hoechst 33342 (1:100, Life Technologies) as a nuclear counterstain. The substrates were mounted on glass slides using ProLong Gold antifade (Life Technologies) and imaged using either the Nikon TE2000 Fluorescence Microscope or Zeiss LSM 710 Confocal Microscope.

Cell Viability

Cell viability of the cells on the various substrates (PLL-coated glass, GO-coated glass, PCL and PCL-GO) was determined after six days of culture using MTS Assay (Promega). All experiments were conducted in triplicates and the percentage of viable cells was determined following standard protocols described by the manufacturer. The data is represented as formazan absorbance at 490 nm, and normalized to the conventional PLL-coated glass control.

PCR Analysis

Total RNA was extracted using Trizol Reagent (Life Technologies) and the mRNA expression levels were analyzed using quantitative PCR (qPCR). Specifically, cDNA was generated from 1 μg of total RNA using the Superscript III First-Strand Synthesis System (Life Technologies). Analysis of mRNA was then accomplished using primers specific to each of the target mRNAs. qPCR reactions were performed using SYBR Green PCR Master Mix (Applied Biosystems) in a StepOnePlus Real-Time PCR System (Applied Biosystems) and the resulting Ct values were normalized to GAPDH. Standard cycling conditions were used for all reactions with a melting temperature of 60°C. The primer sequence for the genes which were analyzed is provided below (Table 2.2):

Table 2.2: Primers used for NSCs Differentiation on Hybrid Nanoscaffold Characterization

Gene	F Primer	R Primer	Size (bp)
GAPDH	ATGACTCTACCCACGGCAAG	GGAAGATGGTGATGGGTTTC	87
TUJ1	ACTTTATCTTCGGTCAGAGTG	CTCACGACATCCAGGACTGA	97
GFAP	GAGAGAGATTCGCACTCAGTA	TGAGGTCTGCAAACTTGGAC	89
GALC	GAAGGTCTCCAGCGAGTGAG	TCAAGCAGCACAGAAGAGGA	74
MBP	CACAAGAACTACCCACTACGG	GGGTGTACGAGGTGTCACAA	103
CNP	AGGGGCTTATCTCTCACCGT	AACCAGAGATGTGGCTTCCG	117
PDGFRα	TGGAAATGGACGGACAAGGG	TGGGAATCTCACCAATGCCC	76
OLIG1	GTTAACCACAGCAAGGCAGC	TCGGCTACTGTCAACAACCC	178
OLIG2	GAACCCCGAAAGGTGTGGAT	TTCGATTTGAGGTGCTCGCT	93
PLP	GCCACACTAGTTTCCCTGCT	ATCAGAACTTGGTGCCTCGG	91
MAG	CACACAAGTGGTCCACGAGA	GCTCCGAGAAGGTGTACTGG	164
MOG	TGTGTGGAGCCTTTCTCTGC	CCCAGGAGATATACGGCACG	160
APC	TACTTCATCGTCCACGCAGC	ACAATGGTGTACGGTGGCAT	72
GST-π	GTCCACACCTCTGTCTACGC	GGACTTGAGCGAGCCTTGAA	165
FAK	CAATGCCTCCAAATTGTCCT	TCCATCCTCATCCGTTCTTC	157
AKT	GCCACGGATACCATGAACGA	AGCTGACATTGTGCCACTGA	197
ILK	GGGCTCTTGTGAGCATCTGT	TGTTCAGGGTCCCATTTCGG	183
FYN	GGTGGGGAACGGACTCATTT	CCAAAGGACCACACGTCAGA	168

Chapter 3

Nanoparticle-based Synthetic Transcription Factor as Soluble Microenvironment Factor for Neural Stem Cell Differentiation and Central Nervous System Treatment

Using the ectopic expression of key transcription factor (TF) proteins not only has high impact in the field of neuro-regenerative medicine but can also provide new insight into the fundamental mechanisms of cellular reprogramming [60, 167, 168]. Transcription factors (TFs), recently demonstrated by Yamanaka and other scientists, have shown to be extremely potent in regulating gene expressions during cellular reprogramming [169]. While TFs plays a critical role in gene expression and are often considered the master regulators of cellular processes, introducing TFs into neurons to induce neuronal behaviors including axonal guidance and regeneration is quite challenging, thereby it requires efficient, robust, innovative, and non-toxic delivery systems. Numerous approaches including electroporation [170], nanocapsules [171], lipid micelles [172], polymer-based carriers [173], and nanoparticle-based delivery [174, 175] have been developed for this purpose [176]. However, these methods have low delivery efficiency and are extremely vulnerable to degradation by intracellular proteases [177]. On the other hand, viral-based delivery of TFs has also been widely used by biologists and clinicians owing to its high transfection efficiency [178]. However, it has inherent drawbacks such as cytotoxicity and immunogenicity of the virus itself, which are especially undesirable for human clinical use. Furthermore, conventional methods to activate genes mainly depend on the use of viral vectors or the delivery of plasmid DNA, which poses significant safety issues due to integration with the patient's genome and potential cancer formation [179, 180]. Therefore, there is a clear need to develop an alternative platform for regulating the

TF-mediated gene expression and inducing cellular reprogramming in an efficient, selective non-viral manner, which is safe for translation into the clinic for treatment of devastating diseases.

While current viral vector-based gene therapies appear promising, a number of barriers hinder their practical use in the clinic; mainly the significant safety concern of tumor causing integration within the human genome [179, 180]. As a result, the FDA has not approved using viral-based gene therapy against SCI and other stem cell research [181]. On the other hand, alternative methods to manipulate gene expression are available, such as small interfering RNA (siRNA) delivery [182, 183]. However, the use of siRNA in the clinic is stalled by the inability to effectively deliver it *in vivo* into the cells, its poor stability [184], and inhibitory costs [185]. Furthermore, most previously reported methods to regrow damaged neurons/axons involve either viral-vectors [186] (e.g., DNA plasmids and retroviruses) or small molecules [187, 188] (e.g., RNAi and synthetic molecules) that regulate translation or target a specific signaling pathway, or nanomaterial-based delivery soluble cues (e.g., drugs and genetic materials).

Addressing the current challenges in viral-vector based gene therapeutics as well as advancing the research of neuronal/axonal regrowth and the clinical potential of gene therapies [189, 190], we have focused on developing a nanoparticle-based, biomimetic transcription factor called NanoScript platform, which can non-virally and specifically regulate targeted genes (up- or down-regulate) in a spatiotemporal and transient manner [191]. Our bio-inspired platform seeks to mimic naturally-occurring transcription factor (TF) proteins, which are known to be the master regulators of gene expression and cellular processes. NanoScript is comprised of a highly biocompatible and FDA approved gold/magnetic nanoparticle core-shell nanoparticle [192] that can be further functionalized with interchangeable small molecule domains including i) a DNA binding domain that specifically binds to the gene of interest, ii) a regulatory domain that is designed to either activate or repress the targeted gene by recruiting endogenous transcriptional machinery, and iii) a targeting sequence that facilitates cell and nuclear uptake. NanoScript can be modified to mimic the structure and function of almost any TF protein for various applications that require gene manipulation. Specifically,

integrating magnetic core-shell nanoparticle (MCNPs) with STFs has numerous advantages over conventional methods (e.g., viruses and plasmids). The development of the NanoScript platform is a collaborative research effort with synergy form the fields of nanomedicine, stem cell-based regenerative medicine, and clinical applications. The NanoScript platform integrates three fields of research, nanotechnology, chemical biology, and neuroscience, to develop a novel nanomaterial-based therapeutic that recapitulates key TF activity. Our primary innovation was the discovery that transcription factor functional domains could be mimicked using short peptides, arranged on the surface of a nanoparticle, essentially creating a "synthetic" transcription factor. This discovery alleviates the need to use native transcription factors and is expected to simplify the delivery to the target cell. We also found that we can target entry into specific cell types by functionalizing the surface of the nanoparticle with cell targeting moieties. By using a nanoparticle, we have found that we can transiently force transcription mediated cell maturation. This transient over-expression of TF activity is critical to force cell maturation while avoiding the deleterious effects of constituitive overexpression (as can occur in gene therapy), or gene damage, that can lead to dysfuntion, or even cancer in some cases [193]. Combing these elements into a single therapeutic provides a novel approach to improve regenerative medicine.

3.1 Induction of Stem Cell-derived Functional Neurons via NanoScript-based Gene Repression

3.1.1 Introduction

Gene repression is a powerful approach to exogenously regulate cellular behavior. However, the development of a platform to effectively repress targeted genes, especially for stem cell applications, remains elusive. Herein, we introduce a nanomaterial-based platform that is capable of mimicking the function of transcription repressor proteins to downregulate gene expression at the transcriptional level for enhancing stem cell differentiation. We developed the NanoScript platform by integrating multiple gene repression molecules with a nanoparticle. First, we show a proof-of-concept demonstration using a GFP-specific NanoScript to knockdown GFP expression in neural stem cells (NSCs-GFP). Then, we show that a Sox9-specific NanoScript can repress Sox9 expression to initiate enhanced differentiation of NSCs into functional neurons. Overall, the tunable properties and gene knockdown capabilities of NanoScript enables its utilization for gene-repression applications in stem cell biology.

Gene regulation is an inherent cellular mechanism through which gene expression is either increased or decreased, and this has a direct impact on cellular behavior such as proliferation, migration, and differentiation [194]. The complex process of gene regulation is intrinsically regulated by transcription factors (TFs), which function by binding to specific gene sequences, thereby controlling the initiation of transcription of genetic information [60]. Once TFs bind to their target gene, the gene can either be activated or repressed, depending on which domains are present on the TFs. A typical TF contains three fundamental domains: 1) a DNA-Binding Domain (DBD) which is sequence-specific and binds to target sequences, 2) a nuclear localization domain to enable the TF proteins entry inside the nucleus, and 3) either an activation domain or a repression domain (RD). If an activation domain is present on the TF, then the targeted gene will be transcribed and gene expression will be upregulated [195,196]; and if a RD is present on the TF, then the target gene will be repressed and gene expression will be downregulated [197].

The nanomaterial-based platform, NanoScript, developed in Prof. KiBum Lee's laboratory, mimics the fundamental structure and function of TF activator proteins [62, 198]. NanoScript was designed by attaching specific small molecules on a nanoparticle. These small molecules emulate the function of individual domains on TF proteins, and when multiple small molecules are assembled together on a single nanoparticle, the resulting NanoScript platform can mimic the function and structure of natural TF proteins. NanoScript is a platform with interchangeable components that can be modified depending on the desired application.

3.1.2 Results and Discussion

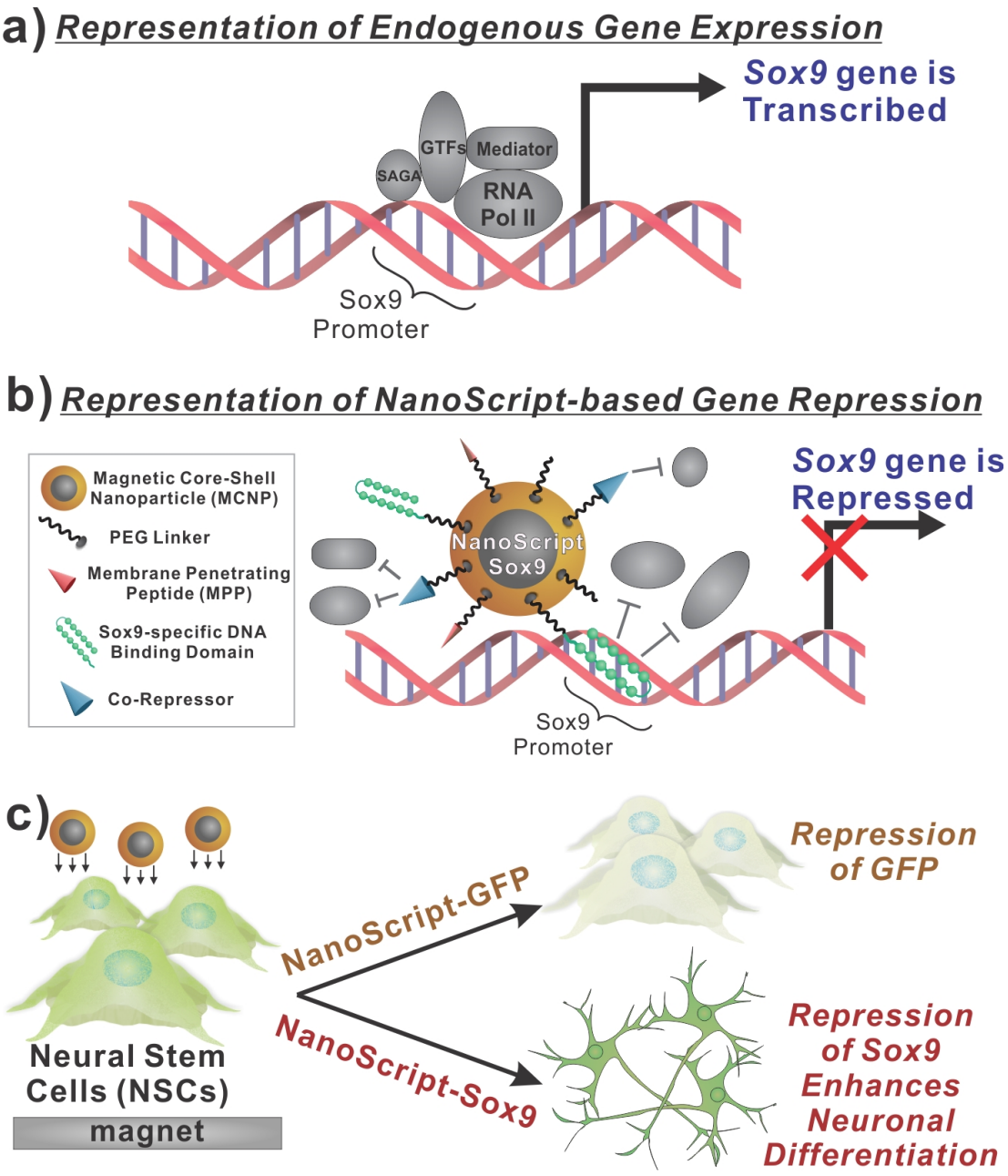

Figure 3.1: Schematic Representation of NanoScript-based Gene Repression. (a) When components of the transcriptional basal complex assemble on a target DNA sequence, such as the Sox9 promoter sequence, the corresponding gene is transcribed. (b) NanoScript-based gene expression is based on the synergistic effect of the DNA Binding Domain molecule for steric hindrance and the co-repressor molecule to disrupt the formation of the transcriptional basal complex on the target DNA sequence. (c) To demonstrate NanoScript-based repression in neural stem cells (NSCs), a GFP-specific NanoScript silences expression of GFP and a Sox9-specific NanoScript represses Sox9 to induce neuronal differentiation. [63]

Herein, we developed the NanoScript platform to effectively mimic the fundamental structure and gene-silencing function of TF repressor proteins. In order to emulate the function of each domain on natural TF repressor proteins, NanoScript was constructed by assembling multiple gene repression molecules, which function to inhibit and block the recruitment of factors to the DNA binding site to prevent gene expression, together on a multifunctional nanoparticle [Figure 3.1a, b]. We performed a proof-of-concept experiment by successfully repressing endogenous expression of green fluorescence protein (GFP) in neural stem cells. Moreover, NanoScript was utilized to repress the neuro-specific gene Sox9 in neural stem cells which induced their differentiation into neurons (Figure 3.1c). The primary advantage of our multifunctional NanoScript platform over conventional approaches is its ability to tether multiple repressor molecules, which function through different mechanisms, on a single nanoparticle to synergistically repress gene expression.

The NanoScript platform was functionalized with multiple molecules in order to emulate the function and structure TF repressor proteins. The first component of NanoScript is the hairpin polyamide molecule, specific for the GFP and Sox9 genes. The hairpin polyamide is a small molecule comprised of the pyrrole (Py) and imidazole (Im) groups which binds to A-T and G-C base pairs on the DNA respectively with nanomolar affinity [199, 200]. The binding of the hairpin polyamide to the DNA sterically hinder the attachment of enzymes like RNA Polymerase II to the binding site, which in turn, prevents the gene from being transcribed [201]. The GFP promoter sequence was obtained from the company from which GFP-labeled rat neural stem cells (rNSCs) were purchased.

A hairpin polyamide with a sequence of PyPyPy-β-PyPyIm-γ-PyPyPy-β-PyImPy-β-Dp-NH2 (γ is γ-aminobutyric acid, β is β-alanine, and Dp is dimethylaminopropylamide) that targets the GFP promoter was synthesized using a previously established solid-phase synthesis protocol [51]. An *in vitro* binding assay study was performed using surface plasmon resonance (SPR) and revealed a high nanomolar binding affinity. Moreover, we synthesized a Sox9-specific hairpin polyamide with a sequence of PyPyPy-β-PyImPy-γ-PyPyPy-β-PyImIm-β-Dp-NH2 that also showed nanomolar binding affinity

to its target sequence [202].

The second molecule is the corepressor peptide with a sequence of WRPW. The WRPW peptide was specifically chosen because: 1) it has been demonstrated to induce gene repression by preventing the formation of the basal transcriptional machinery at the binding site, 2) it induces repression of genes via the Groucho family proteins, which have been demonstrated to play a role in neurogenesis, and 3) it is a short tetrapeptide with only 4 amino acids, and hence it is readily soluble in physiological environments [203–205]. The third molecule is the membrane penetrating peptide (MPP) which has been previously demonstrated to effectively shuttle nanoparticles across the plasma and nuclear membrane [206].

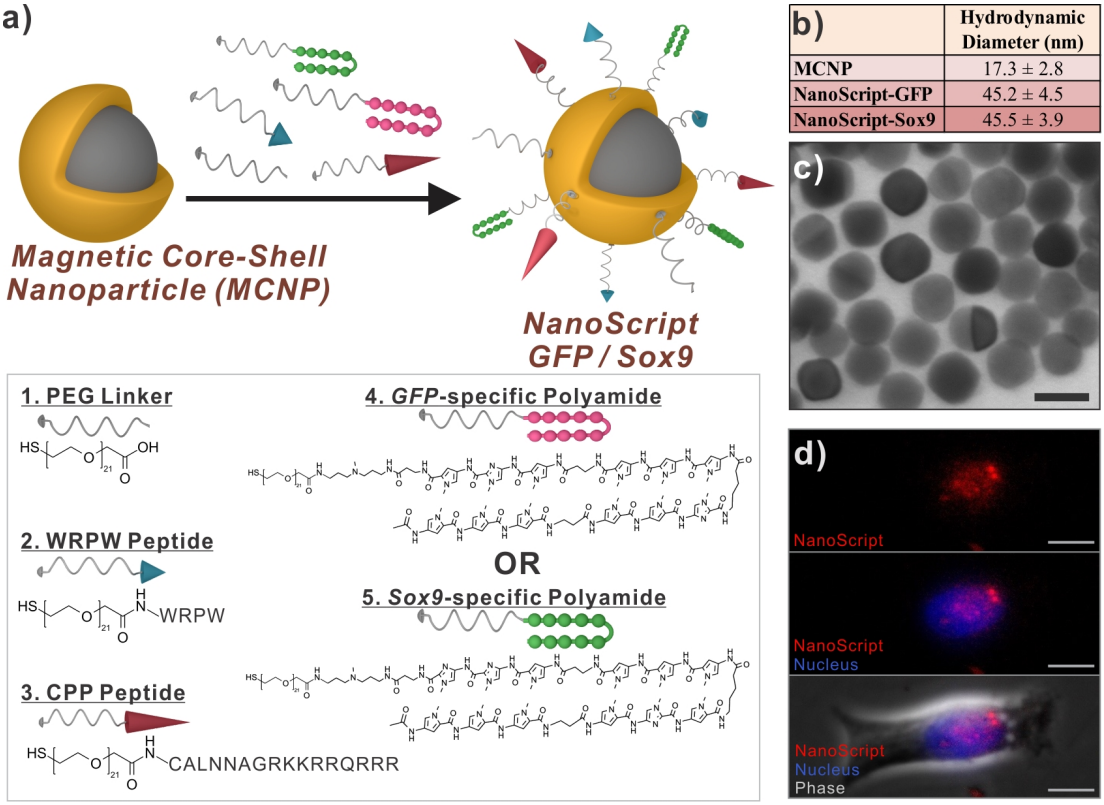

Figure 3.2: Construction and Characterization of NanoScript. (a) The magnetic core-shell nanoparticle (MCNP) was functionalized with PEG-terminated biomolecules, through thiol-gold interactions, to develop the NanoScript platform specific for either GFP or Sox9. (b) The hydrodynamic diameter and (c) transmission electron micrographs of NanoScript (scale bar = 20 nm). (d) A dye-labeled NanoScript (red) was transfected into rat NSCs and NanoScript was detected within the nucleus (blue) (scale bar = 20 μm). [63]

These small molecules (hairpin polyamide, WRPW peptide, and MPP) were conjugated to PEG-based linker molecules to enhance their solubility, with the PEG linker having with a thiol terminus to enable functionalization onto the magnetic core-shell nanoparticles (MCNPs) [207]. MCNPs were chosen because of their high biocompatibility, inert properties, ability to induce magnetofection by placing a magnet underneath the culture plate to attract MCNP onto the cell surface, and multifunctional gold surface which enable attachment of multiple molecules on a single nanoparticle [55, 208, 209]. After the nanoparticles were functionalized with the PEG-terminated small molecules, the resulting platform was termed NanoScript [Figure 3.2a]. Using a combination of dynamic light scattering and transmission electron microscopy, we found the size of the MCNP to be 17.3 nm, and after functionalization, the size of both NanoScript-GFP and NanoScript-Sox9 was found to be about 45 nm [Figure 3.2b]. Through UV-vis absorption spectroscopy, we observed a shift in the plasmon resonance which is indicative of surface functionalization. Based on previously demonstrated studies which show that there are approximately 4.3 ligands/nm^2, we predict that there are approximately 3,902 ligands on the nanoparticle [210]. Moreover, the monodispersity of NanoScript was confirmed through transmission electron microscopy, wherein we visualized well-rounded and monodispersed sizes [Figure 3.2c]. Furthermore, we tested if NanoScript can localize within the nucleus by labeling NanoScript with an Alexa Flour 568 dye and transfecting them into rat neural stem cells (rNSCs). After 24 hours, we performed fluorescence imaging and NanoScript was detected within the nucleus [Figure 3.2d]. We also performed transmission electron microscopy on cellular cross-sections and found that NanoScript was distributed in the nucleus and cytoplasm. Moreover, we performed inductively coupled plasma optical emission spectrometry (ICP-OES) and observed that NanoScript was uptaken inside the cells.

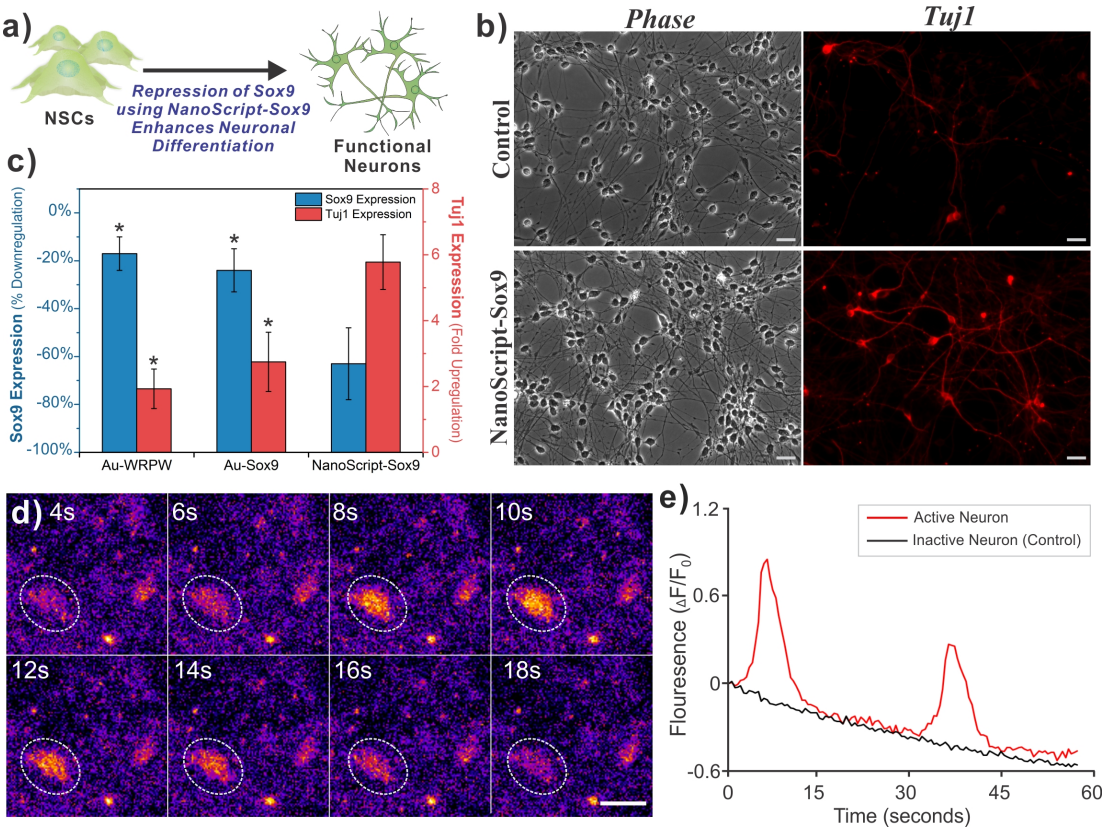

Figure 3.3: NanoScript-Sox9 Represses Sox9 to Induce Functional Neuronal Differentiation. (a) Schematic representation of Sox9 repression in human NSCs by NanoScript-Sox9 induces enhanced neuronal differentiation. (b) Fluorescence images of hNSC stained with Tuj1 5 days post-transfection shows greater Tuj1 expression (red) when NanoScript-Sox9 is transfected. (Scale bar = 20 μm). (c) Gene expression analysis using qPCR in hNSCs reveals that repression of Sox9 correlates with an upregualtion of Tuj1. (Percent down-regulation of Sox9 and fold up-regulation of Tuj1 was calculated by normalizing to the housekeep gene, GAPDH, from the control) Standard error is from three independent trials (* = P<0.05). (d) Spontaneous calcium fluctuations via Fluo4 fluorescence (orange/yellow color) for an active neuron (white circle) during 18 seconds of imaging (scale bar = 20 μm). (e) Traces for the normalized fluorescence change ($\delta F/F_0$) representing spontaneous calcium ion influx for an active neuron (red line) and an inactive neuron (black line). Decreasing trend of the fluorescence is due to mild photobleaching. [63]

Though a proof-of-concept demonstration, we have successfully demonstrated that NanoScript can repress gene expression, we then translated the NanoScript-based gene repression approach for stem cell differentiation applications. To this end, the Sox9 gene has been identified as a critical gene to regulate neuronal differentiation in stem cells. Studies have shown that repression of Sox9 in neural stem cells initiates a pathway to

guide their differentiation into neurons [148, 211]. Hence, we developed a Sox9-specific NanoScript (termed NanoScript-Sox9), and we predict that if NanoScript-Sox9 can effectively repress Sox9 in human neural stem cells (hNSCs), enhanced differentiation into neurons can be observed [Figure 3.3a].

To test this, we transfected NanoScript-Sox9 into hNSCs, and then we evaluated the expression of neuronal markers through qPCR and immunocytochemistry. Specifically, the expression of Tuj1 was evaluated because it is a prominent marker for neurons [212]. We predict that the suppression of Sox9 by NanoScript-Sox9 should lead to enhanced neuronal differentiation, and hence, an increase in Tuj1 expression. We fixed and stained for Tuj1 on Day 5, and the resulting fluorescence images indicated a greater expression of Tuj1 as compared to the control [Figure 3.3b]. This was further confirmed by testing gene expression through qPCR, wherein the expression levels induced by NanoScript-Sox9 showed a decrease of Sox9 expression by 63% and a 5.7-fold increase in Tuj1 expression as compared to the control [Figure 3.3c]. The expression levels of other control conditions (nanoparticle with WPRW and nanoparticle with Sox9 polyamide) were also able to induce Sox9 repression and Tuj1 expression, but not as strongly as compared to the NanoScript-Sox9 conditions [Figure 3.3c]. The expression levels of additional control experiments including unconjugated Sox9 polyamide and WRPW showed minimal changes as compared to the control. Expression of Sox9 protein levels was further evaluated using immunostaining which revealed a similar decreasing trend in the NanoScript-Sox9 condition. Moreover, by performing scanning electron microscopy (SEM), we were able to visualize neurons in high resolution. High cell survival was confirmed with a cell viability assay.

To evaluate if the induced neurons have spontaneous neuronal activity, we monitored changes in intracellular calcium levels. Functionally active neurons are known to spontaneously fire action potentials that allow influx of cations including calcium [213]. Using a commercially available calcium indicator dye, Fluo4, changes in intracellular calcium concentrations were visualized and its fluorescence intensity was quantified. After 7 days post-transfection, we performed calcium imaging using Fluo4 and observed changes in fluorescence levels in the induced neurons [Figure 3.3d]. Furthermore, we

quantified the fluorescence changes and observed spontaneous fluctuations of calcium ions in the active neuron over a 60 second period while the control inactive neuron did not show any changes in fluorescence [Figure 3.3e]. These results suggest that the induced neurons show functional activity.

3.1.3 Conclusion

In summary, the overall goal of introducing a tunable and efficient platform that can mimic TF repressor proteins for effectively repressing genes to induce stem cell differentiation was achieved. As a result, this is the first-ever demonstration of utilizing a nanomaterial-based platform for emulating the function of TF repressor proteins to downregulate gene expression at the transcriptional level for inducing stem cell differentiation. We developed the NanoScript platform by functionalizing a nanoparticle with multiple gene repression molecules such as gene-specific polyamides and the WRPW peptide. We first show a proof-of-concept demonstration that utilizes a GFP-specific NanoScript to knockdown GFP expression in GFP-labeled rNSCs. Then we show that a Sox9-specific NanoScript can repress Sox9 expression in hNSCs to initiate enhanced differentiation into functional neurons. The only difference between these two demonstrations is the gene-specific polyamide, thus highlighting the versatility and tunability of the NanoScript platform.

Furthermore, the results from both demonstrations (GFP knockdown and Sox9 repression) suggested that the synergistic effect of the polyamide and WRPW peptide on the NanoScript is needed for enhanced gene repression. One hypothesis for this result is that the two molecules contribute to gene repression through two different mechanisms. Previously reported mechanistic studies have shown that the binding of the polyamide to the target DNA sequence sterically occlude factors like RNA polymerase II for assembling on the DNA [201]; and the WRPW peptide is known to initiate the Groucho family proteins which are well-established corepressor factors that prevents the formation of the transcriptional basal complex [204]. By assembling both molecules on the NanoScript, we not only synergistically enhance gene repression, but enable NanoScript to more closely mimic the structure of TF repressor proteins.

While NanoScript does not completely knockdown GFP, its knockdown level is comparable to other nanomaterial-based methods that regulate GFP knockdown at the translational level [148]. Other methods for inducing neuronal differentiation such as viral vectors, small molecules, and nanomaterial-based platforms have been developed [58, 148, 214], but because of NanoScript unique features including its non-viral gene regulation and interchangeable components, we are further investigating to optimize and evaluate NanoScript against current methods. Furthermore, previous studies have shown that the extra cellular matrix plays a role in inducing neuronal differentiation [215], and so, the effect of ECM on assisting in NanoScript-based differentiation may require further investigation. Thus far, the current NanoScript platform is primarily applicable for gene regulation in adherent cells, but when NanoScript was evaluated for gene regulation in hNSCs cultured in suspension, we observed knockdown of the Sox9 gene; however, we are further optimizing and investigating the potential of applying NanoScript for other cell types, such as those in suspension.

In conclusion, the introduction of NanoScript platform as an approach to repress gene expression will significant impact the field of stem cell biology. First, because NanoScript regulates gene repression in a non-viral manner, it can be a candidate for stem cell-based research and potential therapies. Second, the high cell viability of NanoScript-transfected rat and human NSCs ensures the potential applicability of NanoScript for other stem cells lines. Third, by simply redesigning the polyamide sequence to complement a targeted gene, it is possibly to modify NanoScript to target and repress almost any gene of interest. We are confident that the versatility, effectiveness, and tunable properties of NanoScript will give scientists a new tool for gene-regulating applications such as stem cell biology and cellular reprogramming.

3.1.4 Materials and Methods

Synthesis of Peptides

The corepressor peptide, with a sequence of NH2-GWRPW-OH, was purchased from GenScript. The membrane penetrating peptide (MPP), with a sequence of NH2-CALNNAGRKKRRQRRR-OH, was purchased from GenScript.

Synthesis of GFP and Sox9 Hairpin Polyamides

All hairpin polyamides were synthesized by adopting our previously published protocol. The Py-Im (pyrrole [Py], imidazole [Im]) polyamide synthesis was machine assisted using a PSSM-8 peptide synthesizer (Shimadzu, Kyoto) with a computer-assisted operation system at 40 mg of Fmoc-β-Ala-Wang resin (ca. 0.55 mmol/g, 100-200 mesh, Novabiochem) by using Fmoc chemistry. The following synthetic procedure was performed: i) deblocking steps for 4 min (2 times), 20% piperidine in DMF; ii) coupling step for 60 min, using corresponding carboxylic acids, 1H-Benzotriazolium, 1-[bis(dimethylamino)methylene]-5chloro-hexafluorophosphate (1-),3-oxide (HCTU) (88 mg), diisopropylethylamine (DIEA) (36 μL); iii) washing steps for 1 min (5 times) in DMF. In the coupling step, each of the corresponding carboxylic acids were prepared in a 1-methyl-2-pyrrolidone solution of Fmoc-Py-COOH (77 mg), Fmoc-Im-COOH (77 mg), Fmoc-PyIm-COOH (100 mg), and Fmoc-γ-COOH (69 mg), with stirring by N2 gas bubbling. Typically, resin (40 mg) was swollen in 1 mL of NMP in a 2.5-mL plastic reaction vessel for 30 min. 2-mL plastic centrifuge tubes with loading Fmoc-monomers with HCTU in NMP 1 mL were placed in programmed position. After each solution transfer, all lines were washed with DMF. After the completion of the synthesis by the last acetyl capping on the peptide synthesizer, the resin was washed with DMF (1 mL, 2 times) and methanol (1 mL, 2 times), and dried in a desiccator at room temperature in vacuo.

To synthesize the GFP polyamide with sequence PyPyPy-β-PyPyIm-γ-PyPyPy-β-PyImPy-β-Dp (γ is γ-aminobutyric acid, β is β-alanine, and Dp is dimethylaminopropylamide), a dried resin was cleaved with 0.4 ml of 3,3'-diamino-N-methyldipropylamine

for 3 h at 45 °C. Then the reaction mixture was filtered, triturated from CH_2C_{12}-Et_2O. This yielded a crude yellow powder. Purification of the crude was performed by flash column chromatography (elution with 0.1% trifluoroacetic acid in water and a 0-35% acetonitrile linear gradient (0-35 min) at a flow rate of 1.8 mL/min under 254 nm).

To synthesize the Sox9 polyamide with sequence, AcPyPyPy-β-PyImPy-γ-PyPyPy-β-PyImIm-β-NH2, a dried sample resin was cleaved with 0.4 ml of 3,3'-diamino-N-methyldipropylamine for 3 h at 45 °C. The reaction mixture was filtered, triturated from CH_2C_{12}-Et_2O, to yield Py-Im polyamide as a white-yellow crude powder. The crude was purified by HPLC (elution with trifluoroacetic acid and a 20-50% acetonitrile linear gradient (0-30 min) at a flow rate of 3.0 mL/min under 254 nm).

Synthesis of Magnetic Core-Shell Nanoparticles

Both the magnetic cores and core-shell particles were synthesized according to a previously reported protocol with slight modifications.[2] The 10 nm zinc doped iron oxide magnetic cores were synthesized by thermal decomposition. In a 100 mL 3-neck round bottom flask, 1.5174 mmol $Fe(Acac)_3$, 0.4825 mmol $FeCl_2$, 0.3338 mmol ZnCl2, 10 mmol 1,2-hexadecandiol, 6 mmol oleic acid, 6 mmol oleylamine and 20 mL tri-n-octylamine were mixed at 150°C under vacuum for 45 min. The vacuum was then removed and the temperature was increased to 200°C at a rate of 4°C per min under dry air for 2 hr, and then further increased to 300°C for 30 min at rate of 4°C per min also under dry air. The reaction mixture was cooled to room temperature and the particles were purified by dispersing the reaction mixture in ethanol and centrifuging at 10,000 rpm several times to produce a dry pallet. The particles were then dispersed and stored in chloroform. The particles were characterized by dynamic light scattering (DLS) using a Malvern Instruments Zetasizer Nano ZS-90 and a Philips CM12 transition electron microscope (TEM).

The gold-coated magnetic nanoparticles (MNP@Au) were synthesized by reducing $AuCl_3$ on the 10 nm zinc-doped iron oxide magnetic cores. In a 50 mL 3-neck round bottom flask, 5 mgs of the 10 nm magnetic cores were mixed in 20 mL of tri-n-octylamaine

and heated to 60°C under vacuum for 10 min to evaporate the chloroform. Upon cooling the reaction mixture to room temperature, 0.3mmol (100 μL) of oleylamine and 60 μl of a 5 mg/300 $\mu\mu$L stock solution of $AuCl_3$ were added and heated to 70°C under vacuum to evaporate the solvents, after which the temperature was increase to 150°C at a rate of 10°C per min under atmosphere for 4 hr. The reaction mixture was then cooled to room temperature and centrifuged at 10,000 rpm to collect the particles. The particles were purified with chloroform and magnetically decanted several times. The purified particles were dispersed and stored in minimal amount of chloroform.

The chloroform dispersed MNP@Au were rendered water soluble by carrying out a ligand exchange in TMAOH and citrate buffer. A TMAOH solution was prepared by dissolving 0.09 g of trisodium citrate in 15 mL of 1 M TMAOH. The previously prepared MNP@Au particles were added to the TMAOH solution and sonicated using a probe sonicator for 30 min. The solution was magnetically decanted and the particles were purified several times using DI water and magnetic decantation and finally dispersed in DI water. The citrate-capped core-shell particles were verified using a Cary US UV-Vis spectrometer and a Philips CM12 TEM.

Construction of NanoScript

We developed the NanoScript platform using a two-step method. First, the three amine terminated biomolecules (WRPW peptide, MPP peptide, and GFP/Sox9 polyamides) were conjugated to a linker molecule, SH-PEG-COOH (Thiol-PEG-Carboxy 1KDa [Creative PEGWorks, PBL-8073]). 50 mM of 1-ethyl-3-(3-dimethylaminopropyl) carbodiimide) (EDC) (Sigma) and 50 mM of N-hydroxysuccinimide (NHS) (Acros Organics) was added to a solution of PEG (50 mM in EtOH), and placed on a shaker for 1 hr. A solution containing 10 molar excess of PEG-WRPW, PEG-MPP, and PEG-GFP/Sox9 polyamide (5 mM) with a mole ratio of 2:1:2 respectively was added drop-wise to the nanoparticle solution and allowed to stir for 2 hr. The functionalized nanoparticles (termed NanoScript) were filtered three times using a 10,000 MCFWO filter (Millipore) to remove unreacted molecules and to adjust the concentration.

The dye-labeled NanoScript, used for tracking intracellular localization of NanoScript, was constructed by conjugating the Alexa Flour 568 (Invitrogen) fluorescent dye to the PEG molecules. Specifically, the free carboxy group on PEG was conjugated to the Alexa Flour 568 Hydrazide dye via EDC/NHS coupling as described above. Characterization of NanoScript was performed using multiple methods. The nanoparticle concentration and confirmation of functionalized was obtained using UV-visible absorption spectra (Varian Cary 5000 UV Vis-NIR Spectrophotometer). Using Dynamic Light Scattering (Malvern Zetasizer Nano-ZS90), we determined the hydrodynamic size of NanoScript. The shape and monodisperse properties of the nanoparticles was confirmed using transmission electron microscopy (TEM). The nanoparticles were drop-cast on the Holey-carbon grids (Electron Microscopy Sciences), allowed to dry overnight under vacuum, and subsequently imaged using a JEOL JEM-2010F high-resolution TEM operated at an accelerating voltage of 200 kV.

SPR Binding Affinity

The SPR assays were performed using a BIACORE X instrument. The biotinylated hairpin DNAs that is complementary for each of the polyamides were purchased from JBioS (Tokyo, Japan) (See table 3.1 below for the biotinylated hairpin DNA sequences).

Table 3.1: GFP and Sox9 polyamides for NanoScript Hairpin SPR Binding Affinity

For GFP Polyamide	3'-CCGA**GGTATACAA**CGGTTTTCCG**TTGTATACC**TCCG-Biotin-5'
For Sox9 Polyamide	3'-GCGT**GGTAACA**AGCTTTTGCT**TGTTACC**ACGC-Biotin-5'

The hairpin biotinylated DNA was immobilized to streptavidin-coated sensor chip SA to obtain the desired immobilization level (approximately 900 RU rise). SPR assays were performed using HBS-EP buffer (10 mM HEPES pH 7.4, 150 mM NaCl, 3 mM EDTA, and 0.005% Surfactant P20) with 0.1% DMSO at 25°C. A series of sample solutions with various concentrations were prepared in the buffer with 0.1% DMSO and injected at a flow rate of 20 μl/min. To measure the rates of association (ka), dissociation (kd) and dissociation constant (KD), data processing was performed with

a fitting model using the BIAevaluation 4.1 program. The 1:1 binding with mass transfer was used for fitting the sensorgrams.

Rat Neural Stem Cell (rNSC) Culture and GFP Knockdown

The GFP-labeled rat neural stem cells (rNSCs) were purchased from Millipore and cultured according to the manufacturers' protocol. The culture media specific for rNSCs was purchased from Millipore. All cells were maintained at 37°C in a humidified incubator with 5% CO2. All experiments were carried on cells between passage 3 and 5.

For GFP knockdown studies, the cultured rNSCs (75,000/well, 12-well plate) were transfected with the NanoScript-GFP constructs (1 nM) in growth medium, and the cell culture plates were placed on the Nd-Fe-B magnetic plates (OZ Biosciences, France) for 15 mins. After 4 hr, the cells were washed twice with PBS and fresh rNSC media (now without bFGF to stop proliferation) was added. The rNSCs were transfected on Day 0 and Day 2, and the GFP knockdown levels was imaged and analyzed on Day 2 and Day 4. Fresh media was exchanged every other day.

Human Neural Stem Cell (hNSC) Culture and Neuronal Differentiation: The human neural stem cell (hNSC) line was purchased from Millipore and cultured according to the manufacturer's protocol. All cells were maintained at 37°C in a humidified incubator with 5% CO2. All experiments were carried on cells between passage 3 and 5. The hNSCs were seeded in plates (125,000/well, 12-well plate; and 62,500/well, 24-well plate) in hNSC specific media (from Millipore) supplemented with basic fibroblast growth factor (bFGF, 20 ng/mL) and epidermal growth factor (EGF, 20 ng/mL), 24 hr prior to experimentation.

To induce neuronal differentiation, the NanoScript-Sox9 constructs (1 nM) were added to the hNSCs with the culture plates placed a magnetic plate as described above, and after 4 hr, the cells were washed twice with PBS and fresh hNSC media (without growth factors to stop proliferation) was added. The hNSCs were transfected on Day 0 and Day 2, and the gene expression were analyzed on Day 3 (for the Sox9 gene) and Day 5 (for the Tuj1 gene) through qPCR. To quantify cell viability, a MTS assay (Promega)

was performed on Day 5. For the study involving patch-clamp, the cells were seeded on cover slips with media exchanges occurring every other day.

Immunocytochemistry

All fluorescence images were obtained using a Nikon T2500 inverted fluorescence microscope. To investigate the nuclear localization of the dye-labeled NanoScript in hNSCs, the media was removed and the cells were fixed for 15 minutes in formalin (Sigma) followed by two washes with PBS. The nucleus was stained with DAPI (Life Technologies) for 30 minutes and then washed with PBS three times.

To investigate the extent of neuronal differentiation on Day 5, the hNSCs were fixed with formalin for 15 minutes and then washed twice with PBS. Cells were then permeabilized with 0.1% Triton X-100 in PBS for 10 minutes and non-specific binding was blocked with 5% normal goat serum (NGS, Life Technologies) in PBS for 1 hr at room temperature. To study the extent of neuronal differentiation, the mouse monoclonal antibody against Tuj1 (1:200 dilution, Covance MMS-435P) and a rabbit polyclonal antibody against Sox9 (1:200 dilution, Abcam ab26414) was used. Following the manufacturer's protocol, the fixed samples were incubated overnight at 4°C in a solution of these antibodies in PBS containing 10% NGS. After washing three times with PBS, the samples were incubated for 1 hr at room temperature in a solution of anti-mouse secondary antibody labeled with Alexa Flour 568 (1:100, Life Technologies) and DAPI (1:100, Life Technologies), in PBS containing 10% NGS, and washed three times thereafter.

PCR Analysis

Total RNA was extracted with TRIzol reagent (Invitrogen) and was reverse transcribed to cDNA with Superscript III Reverse Transcriptase (Invitrogen). Conventional quantitative RT-PCR was performed using a SYBR Green PCR Master Mix (Applied Biosystems) on a StepOnePlus Real-time PCR System (Applied Biosystems) following the manufacturers protocol. Primers sequences for the genes can be found in Table 3.2.

Table 3.2: Tuj1, Sox9, GFP, and GAPDH Primer Sequences

Target	Forward Primer (5' – 3')	Reverse Primer (5' – 3')
Tuj1	GGCCGCAACCAAAATTCAGG	CAGCTCCGACAGATCCAGT
Sox9	ATCACCCGCTCACAGTACGA	GTGGCTGTAGTAGGAGCTGG
GFP	CCACATGAAGCAGCAGGACTT	GGTGCGCTCCTGGACGTA
GAPDH	CATGTTCCAATATGATTCCACC	GATGGGATTTCCATTGATGAC

SEM Imaging Preparation

To investigate the morphology of neuronal differentiation, the basal medium of mature neurons was removed and the neurons were fixed for 15 minutes in Formalin solution (Sigma) followed by two PBS washes. The biological samples were then dehydrated in ethanol. The dehydration process entailed replacing PBS with 50% ethanol/water, 70% ethanol/water, 85% ethanol/water, 95% ethanol/water, and absolute ethanol for 10 minutes each in succession. The biological samples were then stored in absolute ethanol before transferring to critical point dryer to eliminate traces of ethanol. Then 20 nm of platinum was sputter coated onto the surface of biological samples after drying. Zeiss Sigma Field Emission-Scanning Electron Microscope (FE-SEM) was used to acquire the micrographs.

Calcium Imaging

Fluorescent calcium indicator dye Fluo4 AM (Life Technologies) was used for calcium imaging experiments. The dye was dissolved in DMSO and added to the cell culture to achieve a final concentration of 2 μM. Cells were incubated for 20 min with Fluo4 AM dye. Free dye was washed out with pre-warmed HBSS (Life Technologies). Cells then were incubated for 30 min in DMEM media (Life Technologies) for de-esterification of the Fluo4 AM dye. The media was replaced with pre-warmed HBSS during the imaging session. Images were acquired using a Zyla sCMOS camera (Andor) mounted on an Olympus IX71 using a 20×, 0.75 NA objective. Images were taken at 0.5 sec intervals for 1 min. Calcium imaging movies were displayed at 20 Hz. Images for calcium imaging were processed and intensity was quantified using the NIH ImageJ software.

ICP-OES Measurement

After hNSCs were seeded in a 12-well plate (125,000 cells/well), 1 nM of NanoScript was added. After 6 hours, the cells were washed with PBS and detached using Accutase (Gibco). After centrifugation, the supernatant was removed and 25 μL of lysis buffer was added. Then 180 μL of aqua regia (caution: extremely reactive) was added and allowed to sit overnight in an eppendorf tube (Note: Immediately after closing the cap of the eppendorf tube, puncture a small hole in the cap to prevent pressure buildup within the tube). The next day, the solution was transferred to 5.8 mL of distilled water (6 mL total volume with 3 % aqua regia). Cellular uptake experiments were performed three times and each replicate was measured for gold, iron, and zinc content three times by Inductively coupled plasma optical emission spectroscopy (Perkin Elmer Optima 7300 DV), operating under normal conditions.

Cell Transmission Electron Microscopy (TEM)

hNSCs cells were cultured with NanoScripts using the same method as above. 24 hr post-transfection, the cells were trypsinized and fixed with Trump's Fixative (Electron Microscopy Sciences) for 1 hr, washed with sodium cacodylate buffer (Electron Microscopy Sciences), suspended in a 1% osmium tetroxide solution for 1 hr, washed with water, and then progressively dehydrated with ethanol (50, 70, 80, 95, and 100%). Then the cells were embedded in epoxy resin using the Low Viscosity Embedding Media Spurr's Kit (Electron Microscopy Sciences) following the manufacturer's protocol. The images were obtained with the JEOL 100CX TEM.

3.2 NanoScript-based Non-Viral Transient Repression of PTEN for Axonal Regeneration in the CNS

Spinal cord injury (SCI) results in devastating cellular dysfunctions that cause severe and permanent neurological deficits1. Given the intrinsically limited regenerative potential of the central nervous system (CNS) and the complex inhibitory SCI environment, there is a critical need for effective strategies to stimulate robust axon regeneration and neurite outgrowth to re-establish the damaged neural circuitry. To this end, we have developed a nanoparticle-based artificial transcription factor (NanoScript) capable of efficiently and selectively regulating the well reported PTEN/mTOR pathway in a non-viral transient manner to promote axon growth and regeneration. Specifically, we successfully delivered PTEN repressing NanoScript to the motor cortex of spinal cord injured rats, and we observed the regeneration of axon at the cortical spinal tract. Collectively, we anticipate that our NanoScript platform provides an innovatively, highly effective and selective method for SCI treatment and other neural injury therapy as well.

3.2.1 Introduction

Developing an effective and reliable therapeutic approach to treat spinal cord injury (SCI) is a difficult challenge for several reasons [216]. First, the acute primary insult [217] and secondary injury to the spinal cord [218] cause central hemorrhagic necrosis [219] and disruption of ascending and descending spinal tracts which communicate sensory and motor information to and from the brain [220, 221]. Second, subsequent gliosis [222] at the injury site repairs the blood-brain barrier (BBB) can obstruct axon growth/regeneration and release inhibitory factors preventing axon regeneration [216, 223]. Third, adult neurons lose the capacity for continued axonal growth, through a genetic switch after the development has stopped [224]. Altogether, these issues represent significant obstacles towards regeneration in the damaged CNS (central nervous system) [193]. These problems are further compounded by the disruption of normal tissue cellular adhesion and other guidance molecules at the injury site,

accumulation of pro-inflammatory cytokines, and deposition of neurite outgrowth inhibitory biomolecules [225]. Addressing the aforementioned issues, deletion or silencing of phosphatase and tensin homolog (PTEN), a widely expressed tumor repressor which prevents cells from growing and dividing, has been shown to enhance motor axon regeneration at the injury sites [226–228]. However, an effective, safe, and transient method to silence PTEN gene expression without viral transfection is an urgent and critical need to be addressed for this PTEN-based therapeutics against CNS injuries to have more extensive clinical relevance and impact.

While current viral vector-based gene therapies targeting the axon-regrowth gene (PTEN) appear promising, a number of barriers hinder their practical use in the clinic; mainly the significant safety concern of tumor causing integration within the human genome [179, 180]. As a result, the FDA has not approved using viral-based gene therapy against SCI and other stem cell research [181]. On the other hand, alternative methods to repress PTEN and other genes are available, such as small interfering RNA (siRNA) delivery [182, 183]. However, the use of siRNA in the clinic is stalled by the inability to effectively deliver it *in vivo* into the cells, its poor stability [184], and inhibitory costs [185]. To this end, we elected to target ectopic expression of key transcription factor (TF) proteins as they play a critical role in gene expression and are often considered the master regulators of cellular processes.

Addressing the aforementioned challenges in gene therapeutics for treatment of SCI as well as advancing the research of neuronal/axonal regrowth and the clinical potential of gene therapies [189, 190], we have focused on developing a nanoparticle-based, biomimetic transcription factor called NanoScript platform, which can non-virally and specifically regulate targeted genes (up- or down-regulate) in a spatiotemporal and transient manner [191] [Figure 3.4]. Our bio-inspired platform seeks to mimic naturally-occurring transcription factor (TF) proteins, which are known to be the master regulators of gene expression and cellular processes. NanoScript is comprised of a highly biocompatible and FDA approved gold/magnetic nanoparticle core-shell nanoparticle [192]

that can be further functionalized with interchangeable small molecule domains including i) a DNA binding domain that specifically binds to the gene of interest, ii) a regulatory domain that is designed to either activate or repress the targeted gene by recruiting endogenous transcriptional machinery, and iii) a targeting sequence that facilitates cell and nuclear uptake [Figure 3.4a].

We hypothesized that the delivery of PTEN repressing NanoScripts into the motor cortex where the cell bodies of injured neurons are will repress PTEN expression efficiently, which will lead to upregulation of mTOR and therefore promote regeneration of axons at the spinal injury site. The NanoScript platform replicates the multi-domain structure of natural TF proteins and emulates the gene-regulating function of TFs. Most importantly, we believe NanoScript can provide a safe and efficient gene manipulation method that will accelerate efforts for axonal regeneration and ultimately functional recovery of spinal cord injury [Figure 3.4].

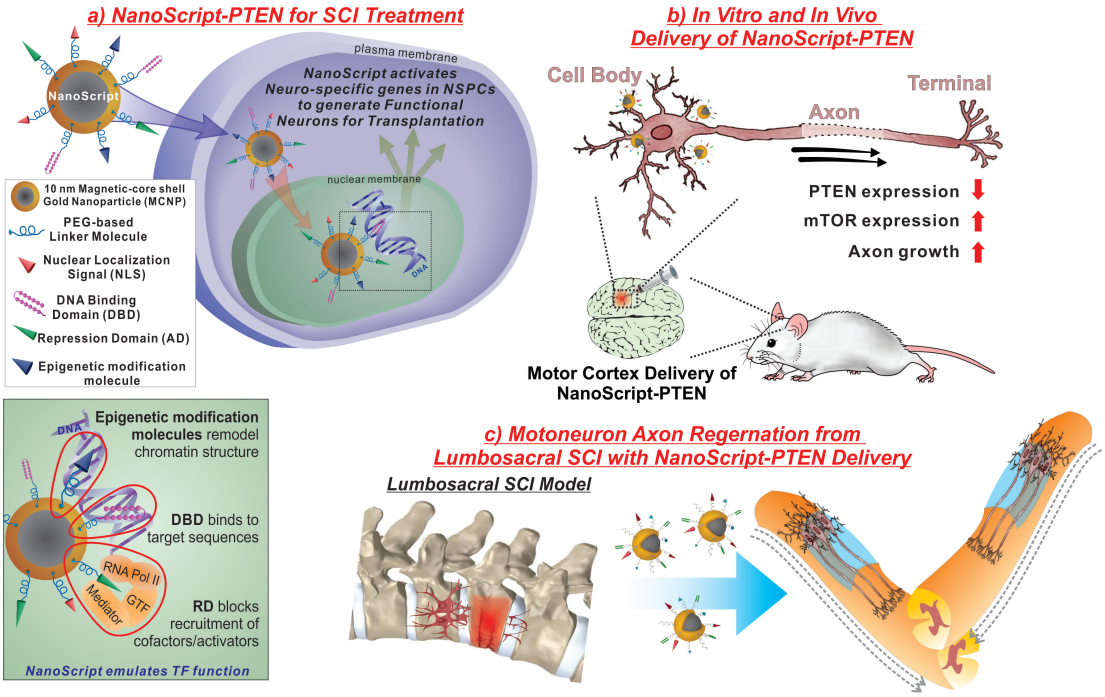

Figure 3.4: Schematic of synthetic transcription factor (TF) protein NanoScript-PTEN to repress PTEN expression for axon regeneration. a) Small molecules and peptides are assembled onto magnetic-core shell gold nanoparticle (MCNP) to develop the NanoScript-PTEN. b) NanoScript-PTEN delivery to tissue cultured neurons and motocortex of rats. c)Regeneration of damaged axons from lumbosacral SCI with NanoScript-PTEN treatment. (Unpublished)

3.2.2 Results and Discussion

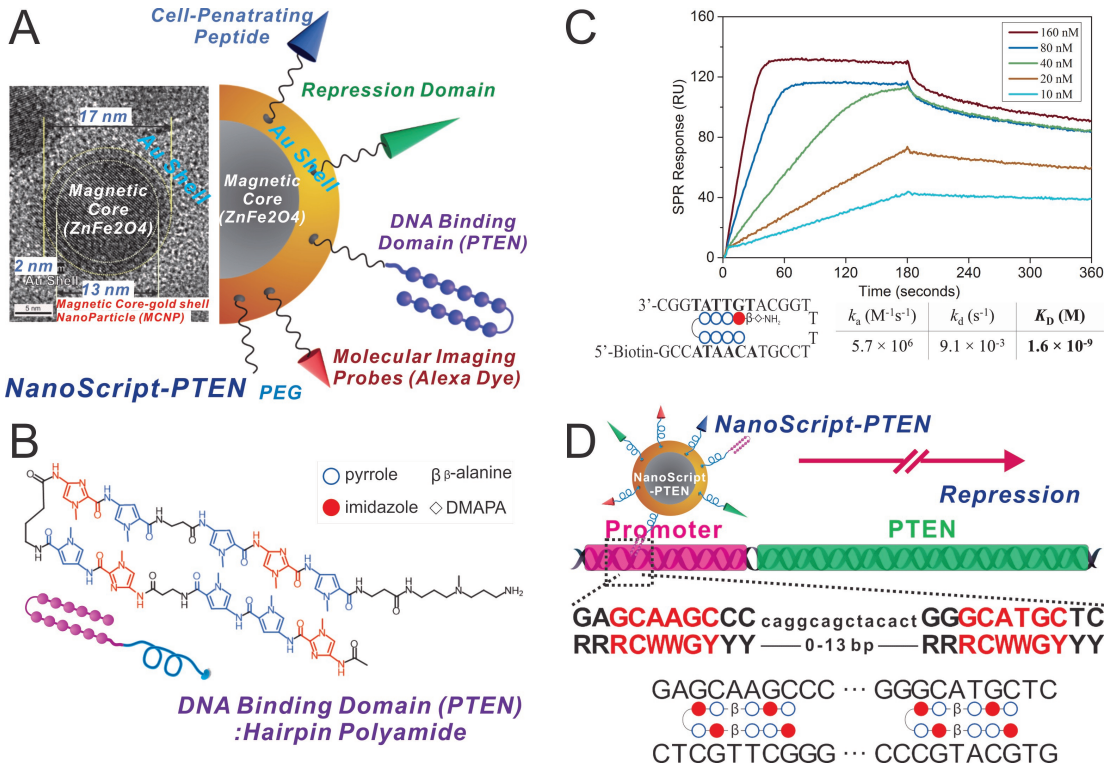

Figure 3.5: Schematic diagram of NanoScript-PTEN design and functions. (A): Synthesis of MCNPs and NanoScript-PTEN using individual domain molecules. (B): The hairpin polyamide structures of the DBD containing pyrrole (Py) and imidazole(Im) motifs, which bind to A-T and G-C base pairs, respectively, are arranged to target DNA sequences in the PTEN promoter region. (C): SPR sensorgrams show the interaction of varying polyamide DBD concentrations with complementary hairpin DNAs. (D): Hairpin Polyamides Specific for PTEN repression: Structures of hairpin polyamide DBDs with pyrrole (blue) and imidazole (red) motifs arranged in specific sequences to complement the promoter regions of PTEN gene for axonal regeneration. (Unpublished)

As shown in Figure 3.5, we first designed hairpin polyamides to act as DNA-binding domains for PTEN NanoScript. We tested for their binding affinities and specificities. We conjugated the activation domain and TAT peptides [cell-penetrating peptides (CPPs)] onto magnetic core nanoparticles to improve on the current NanoScript constructs. We hypothesized that NanoScript will bind to the DNA sequences with a high affinity and selectivity *in vitro*. Studies have established that axonal growth and regeneration is possible by TF-mediated deactivation of endogenous genes.

However, to tune the NanoScript system for SCI therapy by promoting axon regeneration, the priority was to fabricate NanoScript containing 1) DNA binding domain of PTEN, 2) cell membrane penetrating peptide, and 3) other corepressors. In particular, we utilized a magnetic core-gold shell nanoparticle (MCNP) as the core, which we have substantial expertise in synthesizing [229]. By utilizing an MCNP platform, we could image and track the resultant PTEN-targeting NanoScript localization via MRI and dark field imaging as demonstrated in previous publications.

The synthesized MCNPs, consisting of a highly magnetic core ($ZnFe_2O_3$) and a functional outer shell (Au) [Figure 3.5A] provided several advantages over established MNPs including i) enhanced stability in aqueous solutions, ii) facile surface chemistry, iii) non-invasive imaging (Raman), and iv) the combination of different physical and chemical properties in a single nanocomposite. Nanoparticles, such as MCNPs, have desirable physiochemical properties, biological inertness, high stability in physiological conditions, and excellent magnetic properties that allow for non-invasive imaging and enhanced cellular uptake, thus establishing MCNPs as excellent carriers of small molecules and biomolecules [208, 229].

We have synthesized different nanoparticle sizes (5, 10, 20, and 30 nm) to optimize cellular uptake. We had also optimized their size and doping composition to achieve higher MRI contrast. Through dynamic light scattering (DLS) characterization and transition electron microscope (TEM), we confirmed their size and monodispersity.

NanoScript-PTEN was assembled with STFs, small molecules, and peptides onto the MCNP linker domain. With strong literature support, we used a reputable PTEN promoter sequences (NH_2-RRRCWWGYYY-0-13bp-RRRCWWGYYY-OH) [230] to repress PTEN activity [Figure 3.5B] via p53 binding site. The DNA-binding domain (DBD) was synthesized through previously established solid-state synthesis procedure [231,232] comprised of pyrrole (Py) and imidazole (Im) groups [Figure 3.5B]. After MCNPs have been functionalized with the polyethylene glycol (PEG)-terminated hairpin polyamides targeting sequences, NH_2-WRPW-OH repression domain (RD) [203], and cell penetrating peptide (CPP) with the sequence of NH_2-CALNNAGRKKRRQRRR-OH [233, 234] the NanoScript-PTEN complex was formed.

Through surface plasmon resonance (SPR), as shown in Figure 3.5C, we can confirm the binding specificity and affinity of our NanoScript-PTEN to the DNA. We can also confirm surface functionalization through UV/Vis absorption spectroscopy, and use DLS and TEM to confirm the monodispersity of particles. Furthermore, nuclear magnetic resonance (NMR) spectroscopy, matrix-assisted laser desorption/ionization (MALDI) and high-performance liquid chromatography (HPLC) can also be utilized to confirm the final ratio of the individual components on the MCNP.

To confirm PTEN repression through NanoScript-PTEN via *in vitro* tissue culture assay, we tested the potency of the proposed NanoScript platform for PTEN repression using HEK293 cells [235] to check for gene expression levels of PTEN/mTOR pathway closely related to axon regeneration [186] (Figure 3.6).

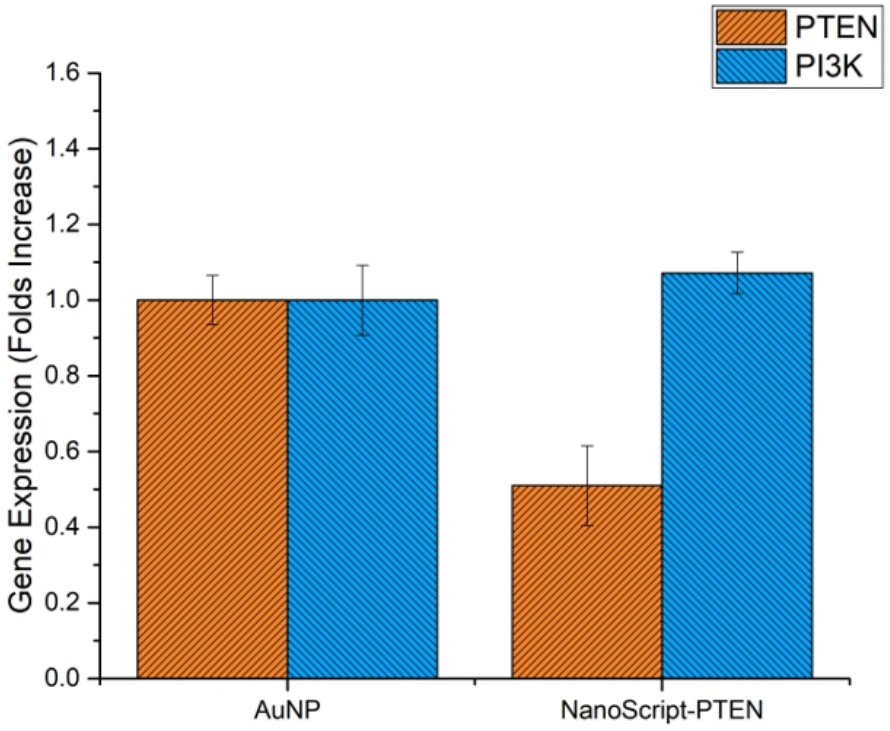

Figure 3.6: PCR Analysis of PTEN/mTOR pathway for NanoScript-PTEN delivered to HEK 293. NanoScript-PTEN was delivered to HEK293 cells to check for its effects on the PTEN/mTOR pathway. (Unpublished)

After confirming the positive results of PTEN repression and mTOR upregulation

(Figure 3.6), we then delivered NanoScript-PTEN to neural progenitor cells, ReNCell (EMD Millipore). We first cultured the cells on tissue culture flask based on the manufacturer's recommendation. Seven days after differentiation, neurons were successfully generated. Upon introduction of NanoScript-PTEN, we observed 1.8 × stronger neuronal (Tuj1) expression compared to untreated control. This indicates that the repression of PTEN gene through non-viral nanoparticle based approach promoted cellular growth (Figure 3.7).

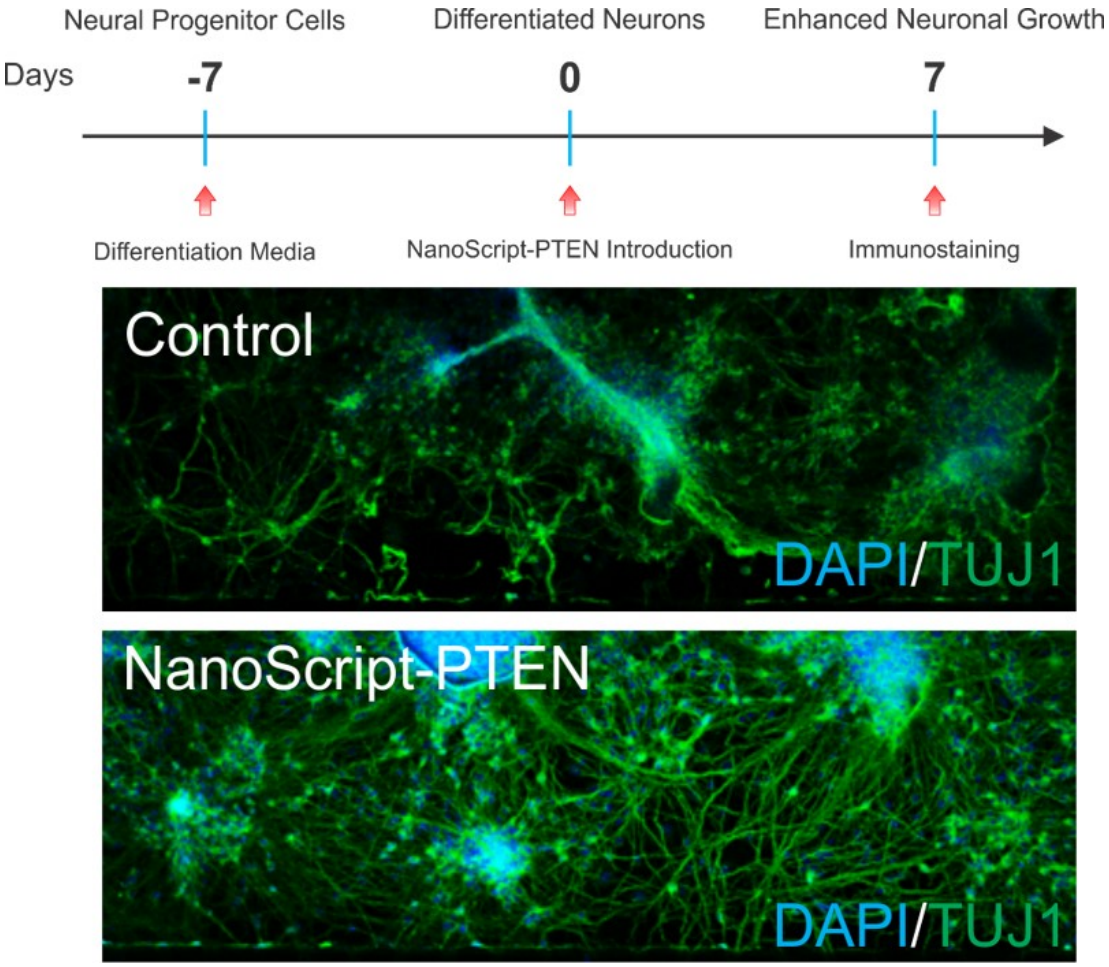

Figure 3.7: NanoScript-PTEN treated hNPC (ReNCell) derived neurons showed 1.8× stronger neuronal (TuJ1) expression. (Unpublished)

After confirming the potency of NanoScript-PTEN *in vitro*, we focused on the delivery of a transient, non-viral method to induce axonal regeneration *in vivo*. We expanded our ability to deliver NanoScript *in vitro* to *in vivo* via a collaborative effort with Prof.

Wise Young (Rutgers-WM Keck Center for Collaborative Neuroscience). The first order of task was to identify and optimize motor cortex injection location of NanoScript for *in vivo* delivery to the neurons. In order to show the axonal regeneration after a spinal cord injury, we used the corticospinal tract as the model. It has been shown that the corticospinal projection neurons are distributed in motor cortices and somatosensory cortices. To demonstrate that NanoScript-PTEN is capable of localizing to motor neurons, we performed direct motor cortex injection of NanoScript using Sprague-Dawley rats (10 weeks) supplied by the W.M. Keck Center for Collaborative Neuroscience. We clipped the rats' hair on the top of their heads. Skins were cleaned with 3 alternating preps of Betadine scrub and alcohol. We used isoflurane anesthesia (5% + 95% O_2 by inhalation for up to 2 hrs.) for all the surgeries. Following a craniotomy, a 10-microliter micro-syringe was used to inject NanoScript-PTEN (different concentrations [1-10 mg/kg], using the optimized component ratio) stereotactically at a depth of 0.5 mm below the dura into the motor cortex, and the particles were diffused for 1 minute before needle withdrawal (Figure 3.8A). Then, NanoScript-PTEN was injected into the motor cortex in both hemispheres with 5 injections per hemisphere following a previously established procedure of functional mapping of the cortex to locate the proper injection sites.

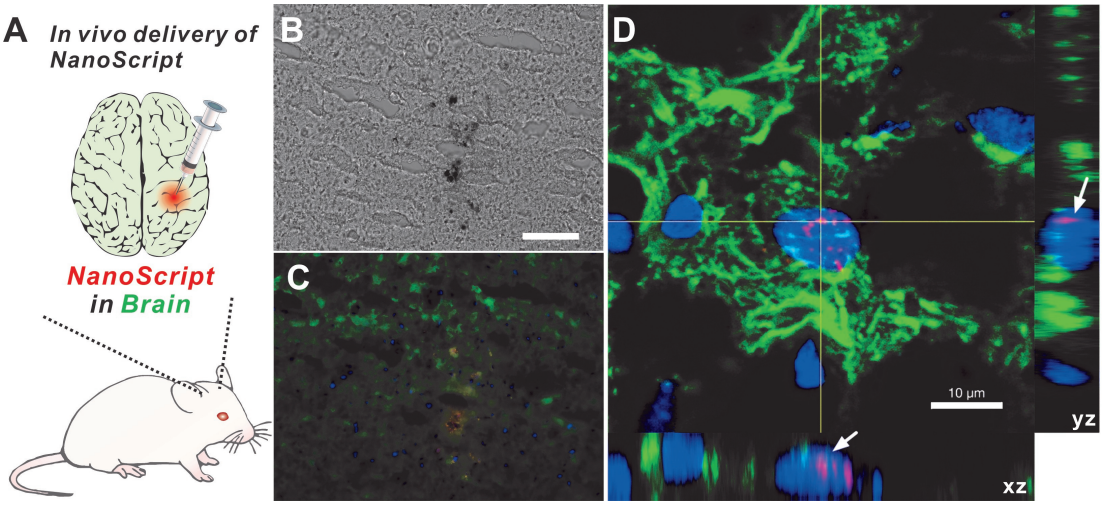

Figure 3.8: *In vivo* delivery of NanoScripts into the targeted neural cells and their nucleus localization. (A) Schematic diagram of cranial injection of NanoScript in Rat. (B-D) Cross-sectional brain slice of three days after a rat received in vivo intracranial NanoScript delivery. The tissue was immunostained with Hoechst (blue), neurofilament antibody (green), and Alexa-dye labeled NanoScript (red), and imaged with a confocal microscope showing the nucleus localization of NanoScripts (white arrow) in the targeted neural cells (cortical spinal neurons). Scale bar: 100 μm (B, C), 10 μm (D) (Unpublished)

The injection of NanoScript-PTEN through syringe needle was proven to not enlist significant inflammatory response as shown in Figure 3.8B, C with cross-sectional brain slices. The images was taken from the brain slices three-day after injection. The successful intracranial direct injection of NanoScript-PTEN proved this method is feasible for studying the non-viral based method for axonal regeneration. Furthermore, as demonstrated in Figure 3.8D, through confocal microscopy, dye-labbed NanoScript-PTEN particle localized in the nucleus of the neurons after motorcortex injection. Furthermore, we have found that NanoScript-PTEN could enter the neuron after injection and could stay inside of the nuclei of the neurons for up to 6 weeks.

Interestingly, we have found that our NanoScript-PTEN localizes favorably in the neucli of neurons. In our observation, through immunostaining results, 60.75% of the neurons stained have NanoScript-PTEN in them whereas glial cells (GFAP positive) did not uptake any particles. We did however found the non-uptaken nanoparticles in the intercellular space.

Owing to the design as a completely modular system, we designed our NanoScript

platform to be transient in modulating gene expressions. This is advantageous as it can avoid the major limitations associated with traditional approaches. Moving forward, a long-term study will help us determine the therapeutic feasibility of NanoScript-PTEN. For example, over the course of up to 12 weeks, rats will be euthanized at different time points (1 week, 4 weeks, 8 weeks, and 12 weeks), and their brains will be sectioned to identify the location of NanoScript-PTEN. Through immunohistological study, the presence and location of fluorescent labeled NanoScript-PTEN in the brain will be determined by fluorescence microscopy. The location of NanoScript-PTEN is critical since the migration of NanoScript-PTEN can lead to potentially undesired effect in the surrounding cells.

After confirming the localization of our NanoScript-PTEN, we then studied the cellular response of injured neurons. Since PTEN and mTOR are inversely correlated, we elected to use a reputable downstream marker of mTOR, phosphorylated S6 ribosomal protein (p-S6), as the indicator for axonal regeneration. P-S6 has been shown to have predictive clinical response [236–238] [Figure 3.9B].

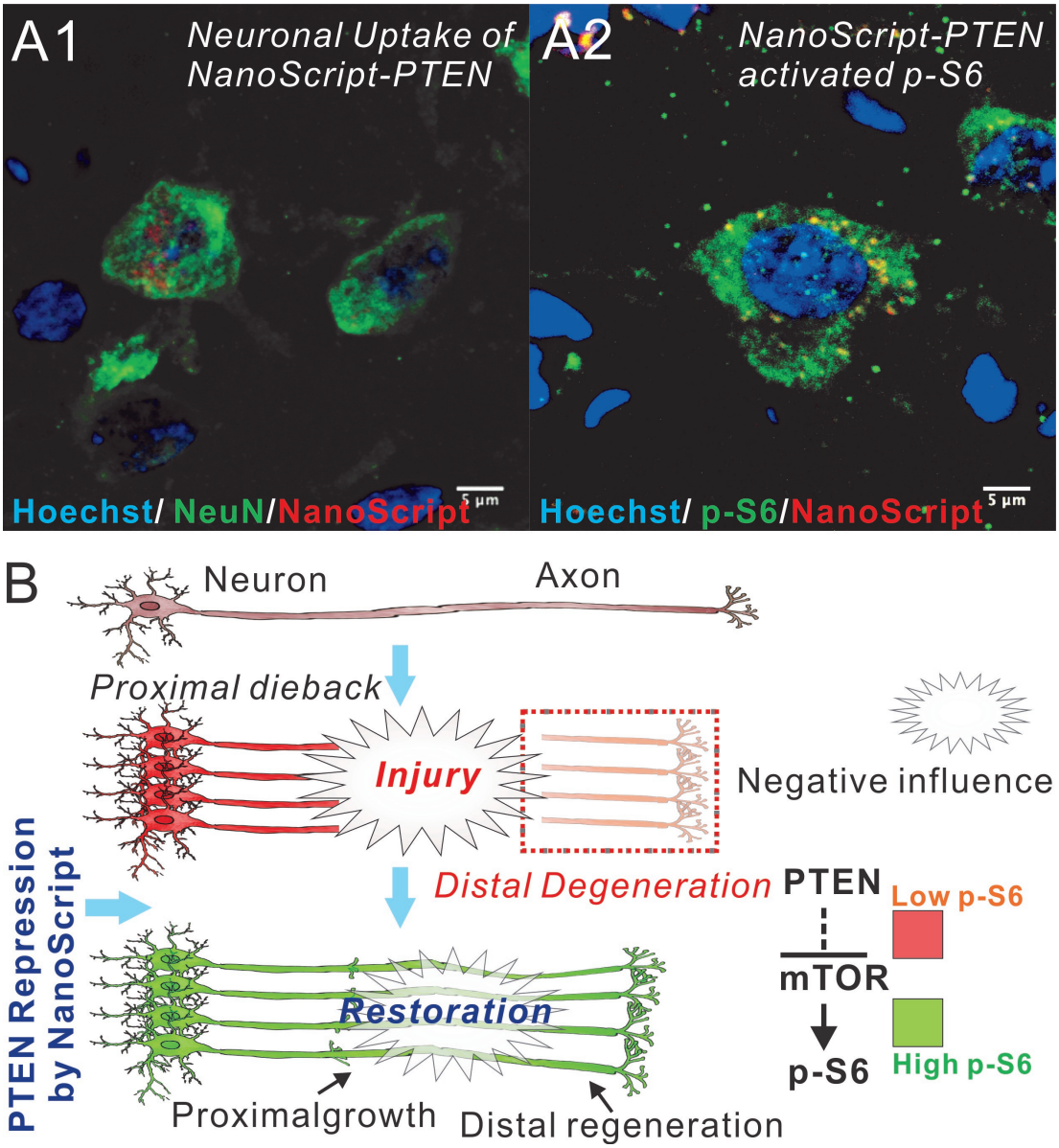

Figure 3.9: (A) Immunostaining of long-term NanoScript-PTEN localization to neurons *In vivo*. (A1) The brain was sectioned and the horizontal sections were stained with neuronal marker NeuN (green), Hoechst nuclear marker (blue), and fluorescent tag labeled NanoScript-PTEN (red). (A2) PTEN gene suppressed by NanoScript-PTEN is demonstrated through mTOR pathway with the activation of p-S6 expression in neurons. We demonstrated exceptionally high level of p-S6 expression (green) after NanoScript-PTEN (red) injection to the cortex and localized to the nuclei (blue). (B) Illustration of the repression of PTEN pathway in the neuron promotes proximal growth and distal regeneration of axon through the mTOR upregulated p-S6 expression. (Unpublished)

From our immunostaining data [Figure 3.9A1, A2], we found that the expression of p-S6 is only present when the neurons have uptaken NanoScript-PTEN. Since mature

neurons do not grow under normal condition, the growth of NanoScript-PTEN delivered neurons supported the proliferated effect of our technology. Through the upregulation of p-S6, we demonstrated 1) NanoScript-PTEN delivery to the targeted neurons and ii) the upregulation of mTOR pathway following NanoScript-PTEN delivery which is correlated to the regneration process. From our time series study, we found high level of p-S6 expression even 6 weeks after intracranial injection. However, after 12 weeks, the neurons were no longer growing from brain slice collection. This indicated the transient effect of NanoScript-PTEN. From this time course study, all animals were injected with NanoScript-PTEN only once.

To confirm that NanoScript-PTEN can promote axonal regeneration, we then inject NanoScript-PTEN into the motor cortex after a standard lumbosacral spinal cord injury. We elected to use the lumbosacral model since it is a reproducible, consistent SCI model. Rats were randomly divided into three groups: untreated control, STFs treated control, and NanoScript-PTEN treatments. Contusion of rat spinal cord at T13-L1 vertebral junction were induced with a 10-gram weight dropped from a height of 25 mm onto the dural surface of the spinal cord, causing a moderately severe injury. NanoScript-PTEN were then injected into the motor cortex as previously described. For the treatment, the optimal concentration and component ratio of NanoScript-PTEN were used according to the result of the time course study.

Rats were perfused and sacrificed at different time points (3d, 7d, 2w, 4w, 6w, and 8w), and brains were sectioned coronally to access the axonal regeneration upon NanoScript-PTEN delivery. We also sectioned the spinal cord transversely to monitor axon regeneration [Figure 3.10A]. Additionally, we conducted corticospinal tract (CST) labeling through biotinylated dextran amine (BDA) [Figure 3.10B] by anterograde tacking. The CST were labeled two weeks before sacrifice [239, 240]. Because the contusion injury destroyed the corticospinal tract, any growth and termination patterns of the labeled axons at and below the injury site represented axon regeneration. To quantify the BDA labeled CST axon, we counted the CST fibers at the level of medulla oblongata 1 mm proximal to the pyramidal decussation [226]. We also quantified the number of sprouting axons by examining axons extending from the central canal to

the lateral rim. The quantification of sprouting fibers were monitored through digital images taken from a fluorescence microscope.

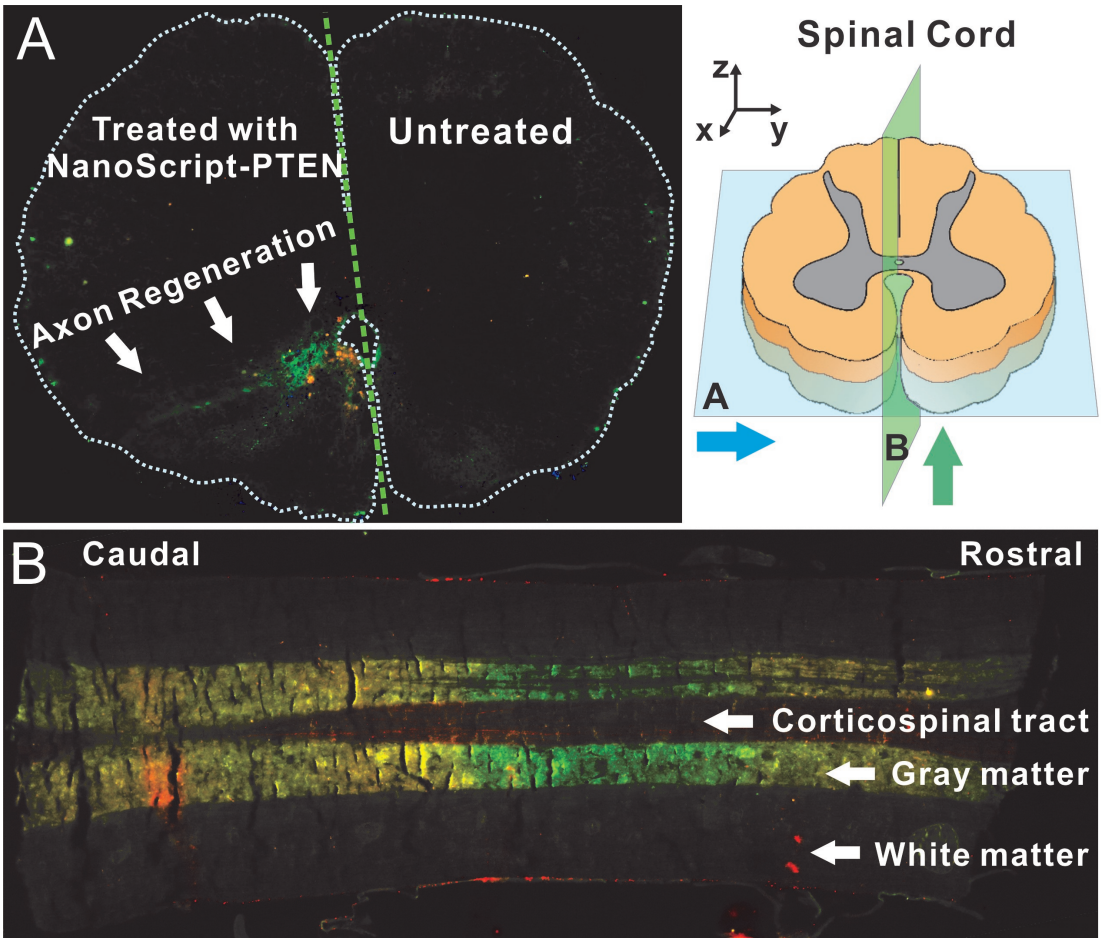

Figure 3.10: (A) Transverse cross section of rat spinal cord 3 mm above injury site. The NanoScript-PTEN treated hemisphere shows clear axonal regeneration at the spinal cord. Neuron specific isotype Protein Kinase C gamma (PKC-γ, green), nucleus (Hoechst, blue). (B) Longitudinal section of rat spinal cord showing biotinylated dextran amine (BDA) labeling of corticospinal track (red). (Unpublished)

Furthermore, we conducted another round of axonal regeneration study over a course of a twelve week. Although we did not observe functional recovery of the animal through the Basso, Beattie, and Bresnahan (BBB) scoring system, we observed a great difference between the two conditions. Through fourteen animals (7 animals with particles treated control without DNA-binding domain, 7 animals with complete NanoScript-PTEN construct), we found, through BDA labeling of the CST, significant extension of axons into the injury site. Without NanoScript-PTEN treatment, we found the injured

axons retracted from the injury site (Figure 3.11a). We found that in the NanoScript-PTEN treated condition, the axons extended into the injury site 500 μm on average whereas the retraction of untreated control was 600 μm on average (Figure 3.11b).

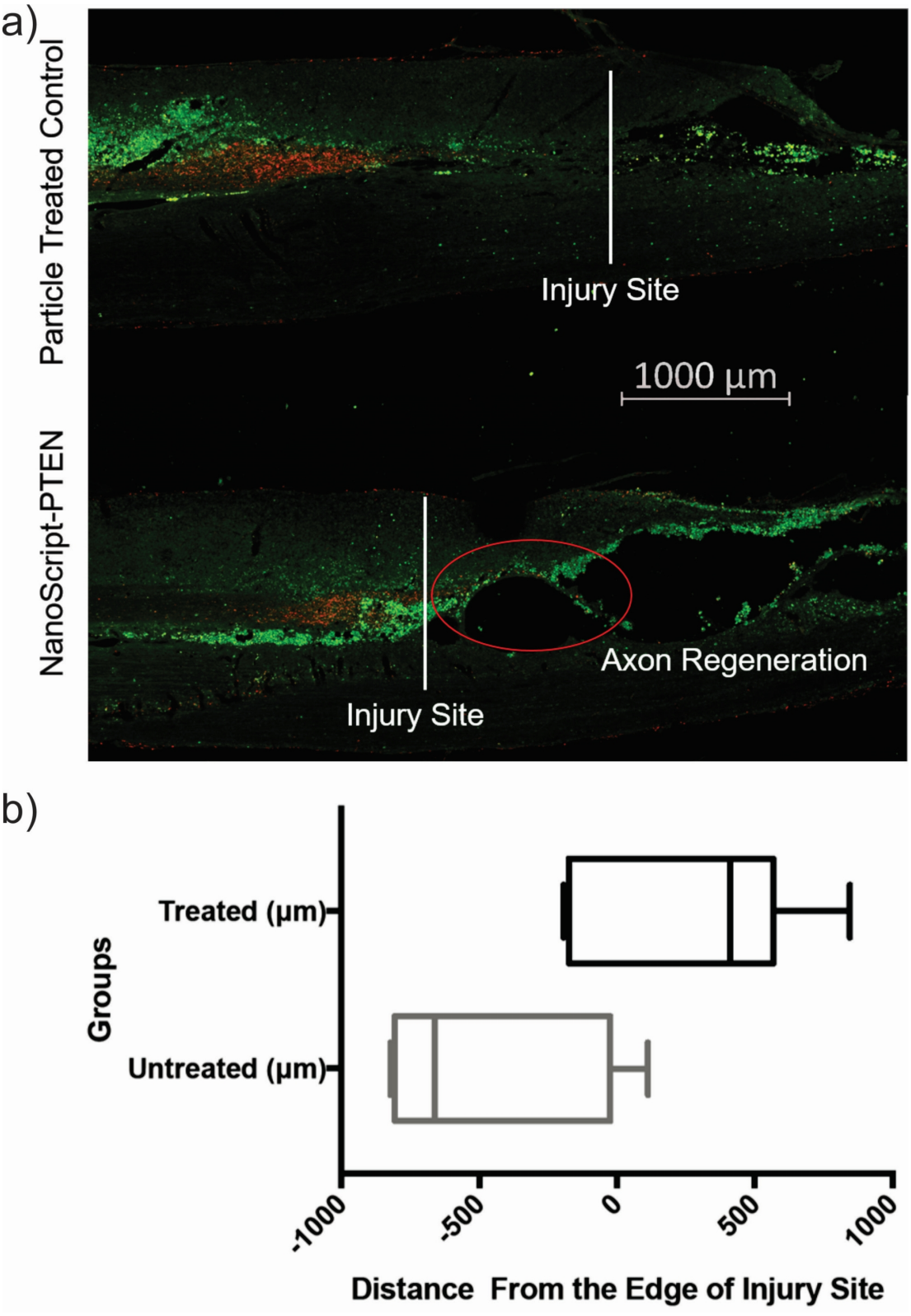

Figure 3.11: a) Biotinylated dextran amine (BDA) labeling of spinal cord injury site. Compared to particle treated control, NanoScript-PTEN treated neurons condition showed axonal extension well into the injury site. b) Statistical analysis of 14 spinal cords showing extension of axons in NanoScript-PTEN treated condition, and axonal retraction in untreated condition. (Unpublished)

3.2.3 Conclusion

In conclusion, we demonstrated the feasibility of the NanoScript platform *in vivo*. Particularly, we successfully delivered a non-viral, transient PTEN repressing NanoScript for axonal regeneration after spinal cord injury. Given the intrinsically limited regenerative potential of the central nervous system (CNS) and the complex inhibitory SCI environment, there is a critical first step for effective strategies to simulate robust axon regeneration and neurite outgrowth to re-establish the damaged neural circuitry. Collectively, we anticipate that our proposed studies will provide an innovative, highly effective and selective method for SCI treatment and other neural injury therapy as well. Since our NanoScripts is suitable for non-invasive imaging such as magnetic resonance imaging (MRI and dark-field imaging), the neuron-targeted NanoScript becomes a novel class of double agents for both diagnostic and therapeutic applications.

Our long-term goal is to effectively and selectively induce axonal regeneration of injured neurons in the CNS through a non-viral gene regulation method. The rationale that underlies the investigation is that the NanoScript platform replicates the multi-domain structure of natural TF proteins and emulates the gene-regulating function of TFs. Most importantly, we believe NanoScript can provide a safe and efficient gene manipulation method that will accelerate efforts for axonal regeneration and ultimately functional recovery of spinal cord injury. Taken together, NanoScript has enormous potential in the field of neuro-regenerative medicine and can extend to any therapy or discipline where modulating gene expression is desired compared to traditional approaches.NanoScript is the first bio-inspired nanomaterial-based platform that mimics natural TFs by binding to endogenous DNA and regulating gene expression. The design of NanoScript constructs are highly flexible and can be altered by simply swapping different small molecules to mimic TF activity. This unique feature makes NanoScript a flexible platform to efficiently regulate cellular functions.

3.2.4 Materials and Methods

Power Anslysis

We have performed a power analysis to determine the minimum sample size with two-tailed α= 0.05. For *in vitro* NanoScript optimization where we analyzed gene expression, we used n=4 per condition was adequate as the variance was expected to be low [241]. For the animal *in vivo* model, we will use n=8 per condition to allow for accommodating the probability of accepting the null hypothesis (a power of 80%, β=0.20)100.

Data interpretation and statistical analysis

Before conducting experiments, we selected a sample size based on the conducted power analysis above. Data were presented as the means and standard deviation in presentation and publications. Outliers were defined based on thorough consideration with vigor study integrity in mind [242]. For NanoScript optimization, we evaluated normality and variance of our data before comparing the means and variance using one-way analysis of variance (ANOVA) with $p<0.05$ for statistical significance [243]. To quantify *in vivo* gene expression, we utilized ANOVA followed by Bonferroni's post-hoc test to compare between the two hemispheres where one hemisphere was treated with NanoScript-PTEN while the other was treated with saline control across all of the animals [244].

Synthesis of Peptides

The corepressor peptide, with a sequence of NH2-GWRPW-OH, was purchased from GenScript. The membrane penetrating peptide (MPP), with a sequence of NH_2-CALNNAGRKKRRQRRR-OH, was purchased from GenScript.

Synthesis of PTEN Hairpin Polyamides

All hairpin polyamides were synthesized by adopting our previously published protocol. The Py-Im (pyrrole [Py], imidazole [Im]) polyamide synthesis was machine assisted

using a PSSM-8 peptide synthesizer (Shimadzu, Kyoto) with a computer-assisted operation system at 40 mg of Fmoc-β-Ala-Wang resin (ca. 0.55 mmol/g, 100-200 mesh, Novabiochem) by using Fmoc chemistry. The following synthetic procedure was performed: i) deblocking steps for 4 min (2 times), 20% piperidine in DMF; ii) coupling step for 60 min, using corresponding carboxylic acids, 1H-Benzotriazolium, 1-[bis(dimethylamino)methylene]-5chloro-hexafluorophosphate (1-),3-oxide (HCTU) (88 mg), diisopropylethylamine (DIEA) (36 μL); iii) washing steps for 1 min (5 times) in DMF. In the coupling step, each of the corresponding carboxylic acids were prepared in a 1-methyl-2-pyrrolidone solution of Fmoc-Py-COOH (77 mg), Fmoc-Im-COOH (77 mg), Fmoc-PyIm-COOH (100 mg), and Fmoc-γ-COOH (69 mg), with stirring by N_2 gas bubbling. Typically, resin (40 mg) was swollen in 1 mL of NMP in a 2.5-mL plastic reaction vessel for 30 min. 2-mL plastic centrifuge tubes with loading Fmoc-monomers with HCTU in NMP 1 mL were placed in programmed position. After each solution transfer, all lines were washed with DMF. After the completion of the synthesis by the last acetyl capping on the peptide synthesizer, the resin was washed with DMF (1 mL, 2 times) and methanol (1 mL, 2 times), and dried in a desiccator at room temperature *in vacuo*.

Construction of NanoScript

We developed the NanoScript platform using a two-step method. First, the three amine terminated biomolecules (WRPW peptide, MPP peptide, and PTEN polyamides) were conjugated to a linker molecule, SH-PEG-COOH (Thiol-PEG-Carboxy 1KDa [Creative PEGWorks, PBL-8073]). 50 mM of 1-ethyl-3-(3-dimethylaminopropyl) carbodiimide) (EDC) (Sigma) and 50 mM of N-hydroxysuccinimide (NHS) (Acros Organics) was added to a solution of PEG (50 mM in EtOH), and placed on a shaker for 1 hr. A solution containing 10 molar excess of PEG-WRPW, PEG-MPP, and PEG-PTEN polyamide (5 mM) with a mole ratio of 2:1:2 respectively was added drop-wise to the nanoparticle solution and allowed to stir for 2 hr. The functionalized nanoparticles (termed NanoScript) were filtered three times using a 10,000 MCFWO filter (Millipore) to remove unreacted molecules and to adjust the concentration.

The dye-labeled NanoScript, used for tracking intracellular localization of NanoScript, was constructed by conjugating the Alexa Flour 568 (Invitrogen) fluorescent dye to the PEG molecules. Specifically, the free carboxy group on PEG was conjugated to the Alexa Flour 568 Hydrazide dye via EDC/NHS coupling as described above. Characterization of NanoScript was performed using multiple methods. The nanoparticle concentration and confirmation of functionalized was obtained using UV-visible absorption spectra (Varian Cary 5000 UV Vis-NIR Spectrophotometer). Using Dynamic Light Scattering (Malvern Zetasizer Nano-ZS90), we determined the hydrodynamic size of NanoScript. The shape and monodisperse properties of the nanoparticles was confirmed using transmission electron microscopy (TEM). The nanoparticles were drop-cast on the Holey-carbon grids (Electron Microscopy Sciences), allowed to dry overnight under vacuum, and subsequently imaged using a JEOL JEM-2010F high-resolution TEM operated at an accelerating voltage of 200 kV.

Human neural stem cell (hNSC) culture and differentiation

Human neural stem cell line (ReNCell VM, Millipore) was purchased and routinely expanded according to the manufacture's protocol. The hNSCs were maintained in laminin (Sigma, 20 μg/ml) coated culture dishes precoated with poly-L-lysine (10 μg/ml) in ReNCell VM media (Millipore) supplemented with the antibiotics, geniticin (Life Technologies), in the presence of basic fibroblast growth factor (bFGF-2, 20 ng/ml, Millipore) and epidermal growth factor (EGF, 20 mg/ml, Peprotech). All of the cells were maintained at 37°C in a humidified atmosphere of 5% CO_2. For consistency, the experiments were carried out on cells between passages 2 and 5. Neural differentiation was initiated by changing the medium to basal medium (without bFGF-2 and EGF) on the different substrates (SiNP, GO, SiNP-GO and control glass) coated with laminin. The cells were allowed to differentiate for 14 days with the basal medium in each being exchanged every other day.

Lumbosacral spinal cord contusion

Sprague-Dawley female rats were anesthetized with isoflurane (5% initially and 2% maintenance), shaved, and the skin on the back cleaned with betadine and alcohol wipes. Contusion of rat spinal cord at T13-L1 vertebral junction were induced with a 10-gram weight dropped from a height of 25 or 50 mm onto the dural surface of the spinal cord, causing a moderately severe injury from which 90% of the rats did recover weight-supported stepping from previous literature data. Subcutaneous fat was placed on the dural surface to retard adhesion of dura to surrounding tissues. The skin was closed with stainless steel clips.

Histology

All the animals were fixed by intracardiac perfusion of 4% paraformaldehyde. The spinal cords were then post-fixed at 4°C for another 24 hours immersed in 4% paraformaldehyde. A 2-cm spinal cord with the injury site (±5 mm of the epicenter) were cut with razor blades, and then cryosectioned horizontally for the following antibody staining: Neurofilament, MBP, Caspr, GFAP, and TuJ1. For corticospinal tract (CST) and rubrospinal tract (RST) tracing, the rats were anesthetized a week before euthanasia and injected with dye. CST were traced by injecting biotinylated dextran amine (BDA) into the motor cortex. The rats were perfused through the heart with 300ml of 4% formaldehyde, after 1% lidocaine and saline perfusion to wash the blood from the vasculature. The brains and spinal cords were removed and post-fixed overnight at 24 hours, sent out for paraffin embedding and sectioning. The CST were visualized on sagittal sections of the spinal cord. The number of fluorescent red nucleus neurons in midbrain sections were counted.

Care of spinal-injured rats

The rats received seven days of prophylactic antibiotics (cefazolin 50 mg/kg) and daily bladder expression after spinal cord injury. If urine becomes cloudy or hemorrhagic after a week, the rats were quarantined and started on a fluoroquinolone antibiotic

(enrofloxacin 2.5 mg/kg/day) for 10 days. The rats were examined daily for autophagia. At the first sign of skin irritation in dermatomes below the injury site, the rat were started on daily acetaminophen (oral 65 mg/kg/day "Baby's Tylenol); if the autophagia progresses, the rat would be euthanized. The rats were euthanized at scheduled times by pentobarbital (65 mg/kg IP) and decapitation or fixative perfusion.

Euthanasia

Rats were anesthetized through pentobarbital and euthanized by perfusion to preserve both brains and spinal cord tissues. This technique was used because ketamine has rapid anesthetic effects and the perfusion method ensures death within seconds. This procedure or method of euthanasia was consistent with recommendations from the Panel on Euthanasia of the American Veterinary Medical Association (AVMA) Guidelines for the Euthanasia of Animals. Animal facility technician performed all procedures.

Consistent, Quantifiable, and Graded Rat Lumbosacral Spinal Cord Injury Model

The Young lab has established a standardized rat lumbosacral spinal cord injury model that causes consistent motoneuronal loss and behavior deficits [245]. Contusion of the rat spinal cord at the T13-L1 vertebral junction with a 10-gram weight dropped 25 or 50 mm resulted in graded lumbosacral SCI accompanied by reproducible graded tibial and peroneal motoneuronal losses, white matter losses, peripheral nerve axonal diameter decrease, reduced myelinated axonal thickness, and atrophy of the tibialis anterior and gastrocnemius muscles, as well as easily quantifiable measurement in both the static and walking footprints of the rats. This model shows reproducible anatomical, histological and functional outcomes that mimic human lumbosacral injuries and can be used to assess regenerative therapies of lumbosacral SCI.

Immunocytochemistry

Two instruments were used in this project. Epi-fluorescence images were obtained using a Nikon T2500 inverted fluorescence microscope. Confocal fluorescence images were

taken using Zeiss LSM510 Meta confocal laser scanning microscope. To investigate the nuclear localization of the dye-labeled NanoScript in hNSCs, the media was removed and the cells were fixed for 15 minutes in formalin (Sigma) followed by two washes with PBS. The nucleus was stained with DAPI (Life Technologies) for 30 minutes and then washed with PBS three times.

General cell fixation procedure were used. *In vitro* cultured cells were fixed with formalin for 15 minutes and then washed twice with PBS. Cells were then permeabilized with 0.1% Triton X-100 in PBS for 10 minutes and non-specific binding was blocked with 5% normal goat serum (NGS, Life Technologies) in PBS for 1 hr at room temperature. To label the brain tissues, the mouse monoclonal antibody against Tuj1, NeuN, NF, p-S6, and GFAP (1:200 dilution, ThermoFisher) were used. Following the manufacturer's protocol, the fixed samples were incubated overnight at 4°C in a solution of these antibodies in PBS containing 10% NGS. After washing three times with PBS, the samples were incubated for 1 hr at room temperature in a solution of anti-mouse secondary antibody labeled with Alexa Flour 568 (1:100, Life Technologies) and DAPI (1:100, Life Technologies), in PBS containing 10% NGS, and washed three times thereafter.

PCR Analysis

Total RNA was extracted using Trizol Reagent (Life Technologies) and the mRNA expression level of PTEN, mTOR, PI3K, and TuJ1 were analyzed using Reverse Transcriptase PCR (RT-PCR) and quantitative PCR (qPCR). Specifically, cDNA was generated from 1 μg of total RNA using the Superscript III First-Strand Synthesis System (Life Technologies). Analysis of mRNA was then accomplished using primers specific to each of the target mRNAs. RT-PCR reactions were performed in a Mastercycler Ep gradient S (Eppendorf) and images were captured using a Gel Logic 112 (Carestream) imaging system. qPCR reactions were performed using SYBR Green PCR Master Mix (Applied Biosystems) in a StepOnePlus Real-Time PCR System (Applied Biosystems) and the resulting Ct values were normalized to Gapdh. Standard cycling conditions were used for all reactions with a melting temperature of 60°C.

Biotinylated Dextran Amine (BDA) for Visualization of Anatomical Morphology of Corticospinal Tract

Biotinylated dextran amine (BDA) was injected into the posterior funiculus of the spinal cord in the cervical (C5-T2) and lumbar (L3-6) segments of adult rats. The spinal cord was cut into serial frozen sections. The BDA labeling was clearly delineated from the surrounding structure. The labeling traversed the cervical, thoracic, and lumbar segments, and was located on the ventral portion of the posterior funiculus on the injected side, proximal to the intermediate zone of the dorsal gray matter.

Chapter 4

Hybrid Nanomaterial Approaches for Therapeutic and Diagnostic Applications

Biosensing in general has been a highly invested field for its clinical use for diagnosis and potential to identify diseases at the very early stage. One of a critical analytes is Neurotransmitters. Neurotransmitters are responsible for signal transduction between neurons, thereby controlling many essential body functions, including physical (motor control and arousal) and mental activities (cognition and motivation) [246–250]. For example, dopamine (DA) has been identified as a key biological molecule whose dysfunction can result in severe diseases. As such, its detection is imperative for the diagnosis of neurological diseases like Parkinson's (PD), schizophrenia, and Huntington's disease. Also, there has been a recent interest in using stem cell-based therapies to create DA-neurons that can be implanted as a treatment for PD [251–255]. To create DA-neurons, differentiation of stem cells into DA-neurons is essential. However, the functionality of differentiated DA-neurons must be confirmed by detection of DA at the single cell level before transplantation. To this end, there is a clear need to improve DA detection in a real-time, non-invasive manner. Biosensors for high selectivity and sensitivity utilizing electrical, electrochemical, and optical methods have been reported [256–259]. Of these, label-free electrochemical biosensors are thought to be the most relevant because of their distinct redox (reduction and oxidation) properties governed by the $2e^-/2H^+$ redox reactions51-59. However, the presence of other molecules such as ascorbic acid (AA), uric acid (UA), and epinephrine (EP) can actively interfere with electrochemical detection of DA because they can also be oxidized or reduced at similar potentials, resulting in an overlap of the voltammetric responses. Other biosensing concepts utilizing field effect transistors (FETs) [258,259] fluorescence [256,260,261],

and Raman/ SERS [262–264] also face significant challenges such as fabrication (FET), low sustainability (fluorescence), and huge signal variations (SERS) that need to be addressed. Hence, it remains challenging to develop biosensors for neurotransmitters with high selectivity, sensitivity, and stability that can operate in realistic biological conditions. To address the aforementioned scientific and technological challenges, this chapter discusses the development of novel *in situ* nano-biosensors as a platform to detect neurotransmitters monitor mature neuronal differentiation of neural stem cell via detection of the secreted neurotransmitters and miRNAs in a noninvasive manner.

Collectively, these novel hybrid biosensing systems will facilitate the fundamental study of biological phenomena such as the role of neurotransmitters during stem cell differentiation and the mechanism for neuro-differentiation. Moreover, we will develop biosensors suitable for *in situ*/real-time measurements in complex biological matrices that represent real cellular environment, something that has eluded the community thus far.

4.1 Large-scale nanoelectrode arrays to monitor the dopaminergic differentiation of human neural stem cells

4.1.1 Introduction

A novel cell-based biosensing platform (Large-scale Homogeneous Nanoelectrode Arryas, LHONA) is developed using a combination of sequential laser interference lithography and electrochemical deposition methods. This enables the sensitive discrimination of dopaminergic cells from other types of neural cells in a completely non-destructive manner owing to its enhanced biocompatibility and excellent electrochemical properties. As such, this platform/detection strategy holds great potential as an effective non-invasive *in situ* monitoring tool that can be used to determine stem cell fate for various regenerative applications.

Over the last decade, stem cell-based therapy has emerged as a promising therapeutic strategy with significant implications for regenerative medicine due to the intrinsic ability of stem cells to differentiate into practically any given cell type [45, 265–271]. For instance, human neural stem cells (hNSCs) are multipotent and have the ability to differentiate into both neurons and glial cells (e.g., oligodendrocytes, astrocytes and microglia) [112, 272–274]. As such, they hold immense potential for the treatment of neurological diseases/disorders such as Alzheimer's disease (AD), Parkinson's disease (PD), Huntington's disease and spinal cord injury [275]. In the case of PD, stem cell-based research has typically focused on the transplantation of stem cell-derived dopaminergic neurons as PD is primarily caused by the loss of dopaminergic neurons in the substantia nigra (SN) of the mid brain [276–278]. To identify and characterize these differentiated cells, which is critical to achieve prior to transplantation, fluorescence-based methods (e.g., immunostaining and FACS) and biomolecular analysis of the expression of biomarkers (DNAs/RNAs/proteins) are currently widely used. These techniques are highly sensitive and, as a result, can be used to precisely determine the biological characteristics of differentiated cells; however, they tend to be laborious, time-consuming and most importantly, involve destructive steps such as cell fixation or cell lysis, which prevents the subsequent use of these characterized cells for clinical applications. As

such, to realize the full potential of stem cell-based therapies, there is an urgent need for techniques that can not only effectively identify stem cell fate but also do so in non-destructive and quantitative manner.

4.1.2 Results and Discussion

Addressing these challenges, we report a novel cell-based sensing platform (Large-scale Homogeneous Nanocup-electrode Arrays, LHONA) that is capable of achieving real-time and highly sensitive electrochemical detection of neurotransmitters that are produced from dopaminergic cells. As such, it can discriminate dopaminergic neurons from other types of cells in a completely non-invasive and label-free manner (Figure 4.1).

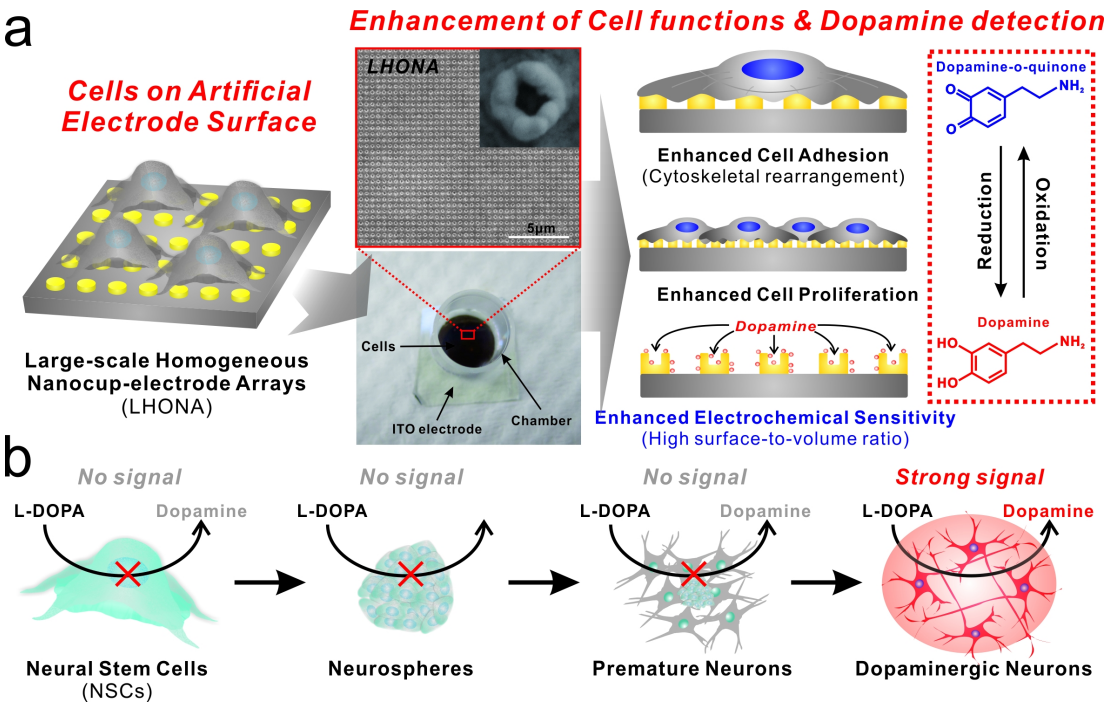

Figure 4.1: (a) Schematic diagram representing superiority of large-scale homogeneous nanocup electrode arrays (LHONA) as a conductive cell culture platform which enhances major cell functions, as well as electrochemical sensitivity toward dopamine detection, both are extremely important for cell-based sensors. Picture is cell-based chip used for the detection of dopamine released from dopaminergic cells that is composed of ITO electrode, LHONA and the chamber for cell culture. Image above is the structural of LHONA characterized by scanning electron microscopy. (b) Detection strategy for the discrimination of dopaminergic neurons from other types of their progenitor cells using L-DOPA pretreatment and LHONA as the cell culture platform (working electrode) based on electrochemical method. Only cells capable of converting L-DOPA to dopamine can give distinct redox peaks which could be used as an indicator of the presence of dopaminergic neurons. [279]

In particular, LHONA is composed of distinct periodic cup-like nanostructures that were generated on an indium tin oxide electrode (ITO, 1.5cm X 1.5cm) via sequential laser interference lithography (LIL) and electrochemical deposition (ECD) methods. Owing to its unique nano-scale structure, LHONA has a number of advantages over other cell-based biosensors. First, recent studies have reported that nanostructured arrays can enhance cell functions via the spatiotemporal and dynamic rearrangement of focal adhesions and the cellular cytoskeleton [65, 128, 280–284]. As such, LHONA overcomes one of the major challenges faced by current cell-based biosensors- specifically, their dependence on cell adhesive molecules to promote cell anchoring to the electrode,

which can adversely decrease the achievable sensitivity [285, 286]. On the other hand, the three-dimensional nanostructures of LHONA are also highly preferred for detecting electrochemical signals owing to their capability to improve the selectivity, sensitivity and spatial resolution. Hence, by combining these aforementioned advantages, we demonstrated that LHONA can serve as an outstanding platform for the sensitive detection of both dopamine (DA) exocytosed from a model dopaminergic cell line (PC12) and dopaminergic neurons derived from hNSCs via the direct attachment/culturing of cells on the surface of LHONA in a biocompatible and non-destructive manner (Figure 4.1a). This enabled the sensitive discrimination of dopamine-producing neurons from other cell types including progenitor cells (hNSCs, neurospheres and premature neurons), non-dopaminergic neurons and other cell types (astrocytes and human dermal fibroblasts) (Figure 4.1b).

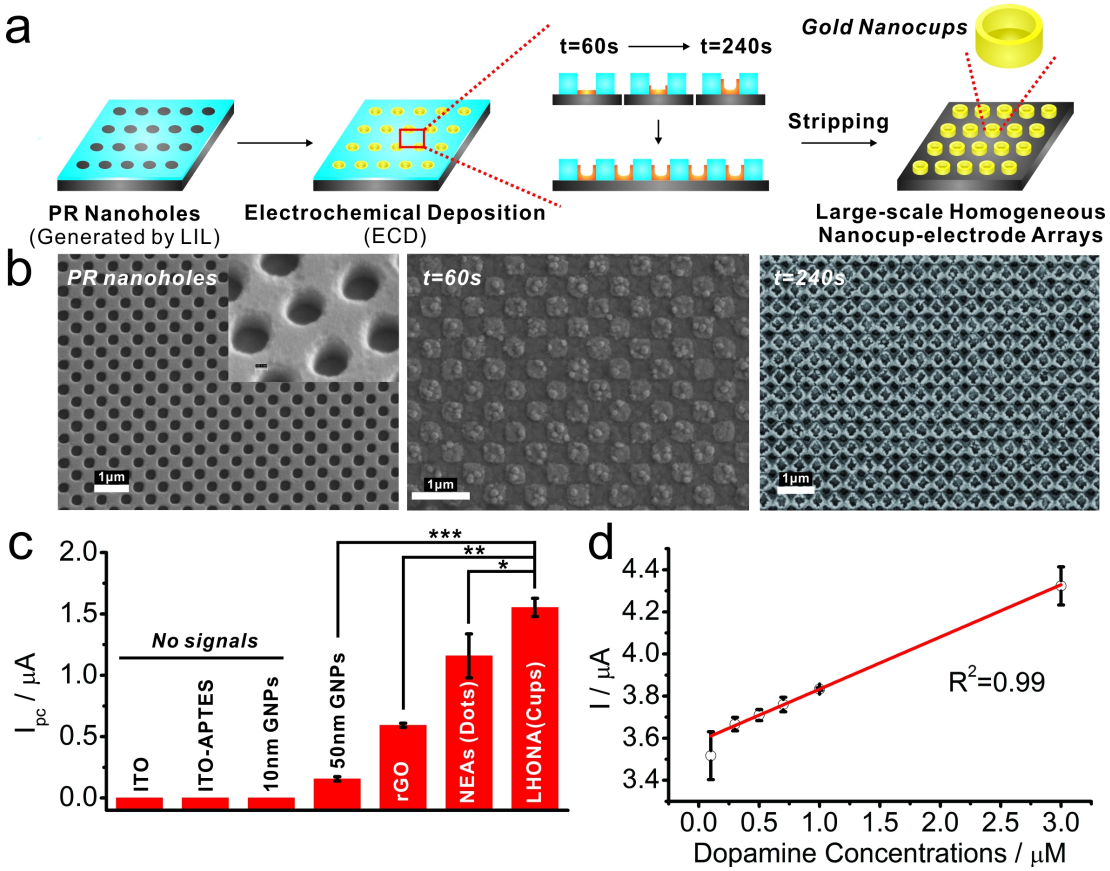

Figure 4.2: (a) Schematic diagram showing sequential steps to generate LHONA on ITO electrode via laser interference lithography (LIL) and electrochemical deposition method. (b) SEM images of (i) polymer nanohole template generated by LIL and electrochemically deposited gold nanostructures with different deposition time. (c) Intensities of cathodic peaks of dopamine obtained from cyclic voltammetry using different types of substrates and (Student's t-test, N=3, *p<0.05, *p<0.01, *p<0.001). (d) The linear correlations between concentrations of dopamine and signal intensities at reduction potential of cyclic voltammetry. [279]

Figure 4.2a illustrates the experimental steps that were used to obtain the periodic metal nanostructures. Briefly, homogenous photoresist (PR) grid nanopatterns were first fabricated on the surface of ITO using LIL with different sizes and shapes (Figure 4.2b). Thereafter, the PR nanoholes were utilized as a template to deposit gold using the electrochemical deposition (ECD) method. By carefully adjusting the solution composition (e.g., concentration of gold chloride and type of surfactant) and the electrochemical parameters (e.g. voltage applied and time), which are related to the growth rate parallel or perpendicular to the direction of the current [287], distinct cup-like or

dot-like nanostructures were successfully generated on the entire ITO electrode (Figure 4.2b). Besides the concentration of gold ions, deposition time was also a key parameter in controlling the geometry of the nanotopographic features. Patterns were formed as a thin film-like structure within a short period of time (t = 60s, Figure 4.2b) and finally, cup-like structures were generated when deposition time reached 240s, which was the best platform in terms of both its topographical characteristic (Figure 4.2b) and its electrochemical sensitivity toward DA detection.

Next, we compared the electrochemical performance of LHONA with other types of electrodes that use ITO as a supporting substrate in terms of sensitivity toward DA detection. As an initial proof-of-concept, we used a cell-free configuration where DA was detected in situ. At a concentration of 10 μM DA, the cathodic peak current (I_{pc}) were not detectable on bare ITO electrodes and ITO modified with 10 nm AuNPs (gold nanoparticles), while ITO-50nm AuNPs showed a very weak reduction peak (I_{pc} = 0.155 μA). On the other hand, ITO modified with reduced graphene oxide (rGO), which has previously been reported as an outstanding material for the detection of DA [288,289], showed better performance ($I_{pc} = 0.592\mu$A). However, interestingly, LHONA substrates exhibited the most distinct redox peaks (I_{pc} = 2.25μA), which was 13.5 and 2.8 times higher than ITO-50nm Au NPs and ITO-rGO substrates (Figure 4.2c). Remarkably, the reduction current of LHONA (nanocups) was even higher (59.6%) than homogeneous nanoelectrode arrays [NEAs (dot-like structure)] generated using the same ECD method (I_{pc} = 1.41 μA), which is speculated to be due in part to the increased surface area, proving its excellent sensitivity for the electrochemical detection of DA. The redox peaks were constant and increased with increasing scan rates (20, 40, 60, 80 and 100 mV/s), proving that the cathodic peaks originated from DA and not from noise or other contaminants. Moreover, LHONA showed good linearity at both low (0.3-3μM, R2=0.99) and high concentrations (0-50μM, R2=0.986) of DA, with a limit of detection (LOD) of 100 nM (Figure 4.2d). Since the fabricated substrate (LHONA) showed excellent performance in terms of DA detection, which is superior to other transparent electrodes (GNP- and rGO-modified ITOs, homogeneous gold nanodot arrays), it is highly likely that LHONA will be the suitable material for effective

in situ electrochemical detection of DA synthesized from dopaminergic cells in sensitive and non-invasive manner, which is at the ultimate goal of this study.

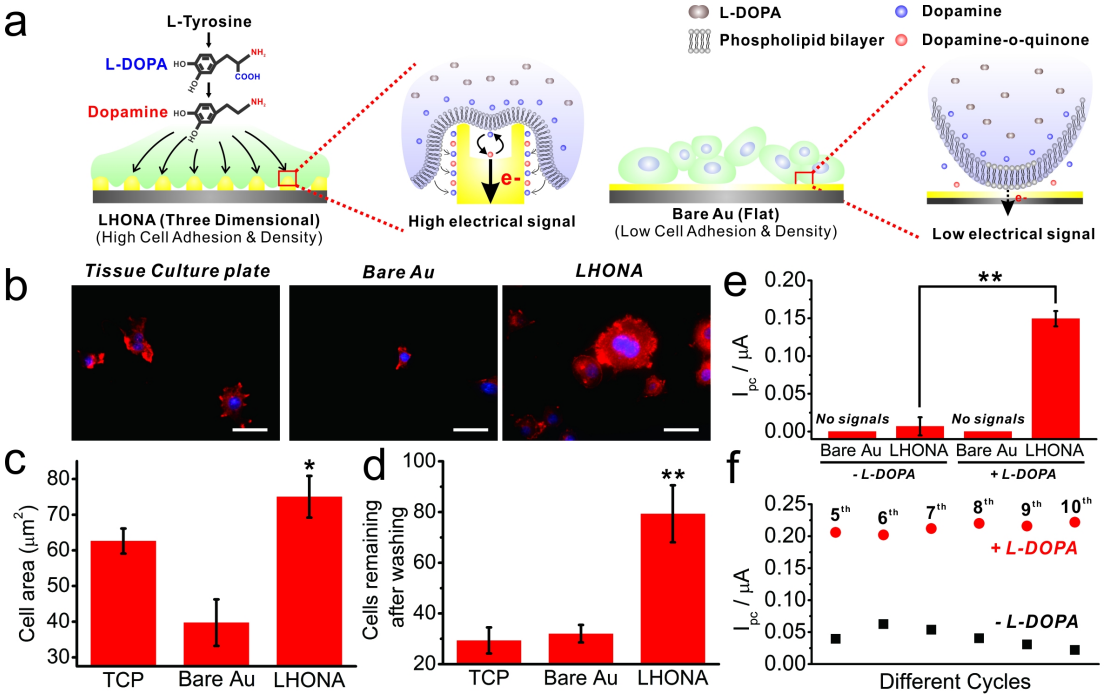

Figure 4.3: (a) Schematic diagram showing the interaction between cell membrane and the surface of electrodes that result in the increase of electrical signals of model dopaminergic cells on LHONA due to the enhanced cell spreading, adhesion and proliferation compared to flat (two dimensional) surface. (b) F-actin-stained fluorescence images of PC12 cells (Scale bar = 40μm), (c) analysis of cell surface area (cell spreading) and (d) cells remaining on the surface after washing for cell fixation which were calculated from F-actin-stained images of PC12 cells on three different substrates (Student's t-test, N=3, *p<0.05, **p<0.01). (e) I_{pc} values of cyclic voltammogram achieved from PC12 cells on Bare Au and LHONA substrates. PC12 cells treated with L-DOPA prior to the electrochemical analysis indicated as "+ L-DOPA" while cells without L-DOPA indicated as "-L-DOPA". (f) I_{pc} values calculated from cyclic voltammetric curves with different cycle numbers, which were obtained from PC12 cells on LHONA-M. [279]

It is important to note that unlike typical biosensors, the electrode of cell-based biosensors must be highly biocompatible in order to promote cell attachment, growth, and subsequent secretion of the biomolecule of interest, which in this case is DA [285,290]. As such, we next investigated whether LHONA could act as an effective substrate for culturing neural cells. In particular, it was our hypothesis that the nanoscale topographic characteristics of LHONA (periodic and homogeneous) would contribute to the enhancement of cell adhesion, spreading and growth of the model dopaminergic

cells (PC12) (Figure 4.3a) [280, 281, 291]. Since PC12 cells are highly sensitive to the adhesion materials, as expected, cell spreading on bare gold and normal tissue culture plates (TCPs) was found to be highly restricted (Figure 4.3b). In contrast, interestingly, PC12 cells spread well on bare LHONA [without extracellular matrix (ECM) materials], where they exhibited a well-spread morphology throughout the entire surface that was similar to the cells on Matrigel-coated TCPs (Figure 4.3b). Remarkably, the total surface area of the cells spread on the LHONA was found to be 12.4% and 88.9% higher than that on TCPs and bare gold substrates (Figure 4.3c), respectively, and the number of cells remaining on the LHONA after washing was 270% higher than both TCP and bare gold substrates due to the enhanced cell adhesion (Figure 4.3d). Moreover, cell proliferation was found to be increased on LHONA substrate compared to bare gold substrates, proving that LHONA is an excellent platform for culturing and enhancing major functions of model dopaminergic neurons which will be suitable for electrochemical study over other types of substrates. These effects of nanostructured arrays on the cell functions became completely negligible after the modification of thick Matrigel layer on LHONA, proving that the enhancement of cell functions solely originated from the distinct nanotopographical features of LHONA.

After confirming the superior characteristics of the LHONA in terms of biocompatibility, cyclic voltammetry (CV) was applied to detect DA released from PC12 cells attached to electrode. For this purpose, L-DOPA, a precursor which can be converted to DA by dopa decarboxylase (DDC), was added prior to the detection of DA to increase the amount of DA synthesized by the dopaminergic PC12 cells [285, 290]. As expected, bare gold electrodes showed no redox signals regardless of treatment with L-DOPA (Figure 4.3e). This was hypothesized to be mainly due to the limited number of cells attached to the bare gold substrate, cell aggregation (less spreading), and limited growth, all of which indicated that the major functions of the PC12 cells were highly compromised (Figure 4.3b-d). After modification with Matrigel, the morphology of the cells and their growth were significantly improved; however, no reduction and oxidation peaks appeared on the voltammogram owing to Matrigel blocking electron transfer to the surface of the electrode. We next attempted to use a reduced amount

of Matrigel (4 times more diluted than normal concentration) to enhance the electron transfer from cells to the electrode; however, the diluted Matrigel modified on the gold substrate was found to be insufficient to improve cell spreading and proliferation. In contrast, interestingly, cells on LHONA showed clear reduction and oxidation peaks at -33 mV and 125 mV, respectively, proving its outstanding potential to be applied for in situ monitoring of DA released from dopaminergic cells (Figure 4.3e). Remarkably, PC12 cells on diluted Matrigel-modified LHONA (LHONA-M) also showed strong redox signals of DA slightly higher than LHONA, which was clearly different from bare gold substrate. The peak-to-peak separation (Epa – Epc) was 158 mV, which was slightly higher than that of chemical DA (58mV), probably due to the cell membrane binding to the electrode that resulted in the increase of resistance. Next, to confirm the stability of electrochemical signals of DA released from PC12 cells, the signals from PC12 cells with or without L-DOPA pretreatment were compared based on the I_{pc} values of cyclic voltammogram with different cycle numbers. As shown in Figure 3e, the cathodic peaks from both groups were continuously appeared at around 0.21 μA and 0.04 μA for L-DOPA pretreated and non-treated PC12 cells, respectively, with increasing cycle numbers up to 10. The cathodic peak from L-DOPA pretreated PC12 cells (I_{pc}=0.222 μA) was 10 times higher than L-DOPA non-treated PC12 cells (I_{pc}=0.022 μA) at 10th cycle due to the increased amount of DA produced from cells via conversion of L-DOPA to DA, proving that the signals are highly stable and reliable which could be important for the determination of DA production capability of dopaminergic neurons. The electrochemical signals achieved from PC12 cells were also found to increase as the increase of cell numbers, indicating that LHONA is reliable platform capable of detecting dopamine produced from cells in quantitative manner. Finally, the DC amperometric method, a conventional tool that is useful for the simultaneous monitoring of changes in currents when applying a specific voltage [290], was further utilized to validate electrochemical DA signals of dopaminergic cells that were measured using CV. As expected, a clear spike-like currents appeared on the i-t graph following addition of KCl (120mM) to trigger DA release while applying a cathodic voltage on PC12 cells, proving the presence of DA in PC12 cells which can be sensitively detected

by LHONA substrate. Hence, it can be concluded that the fabricated large-scale homogeneous nanocup electrode arrays (LHONA) is a suitable material for the in situ monitoring of cellular signals, especially for the detection of DA from cells, mainly due to its outstanding electrochemical properties as well as its excellent biocompatibility.

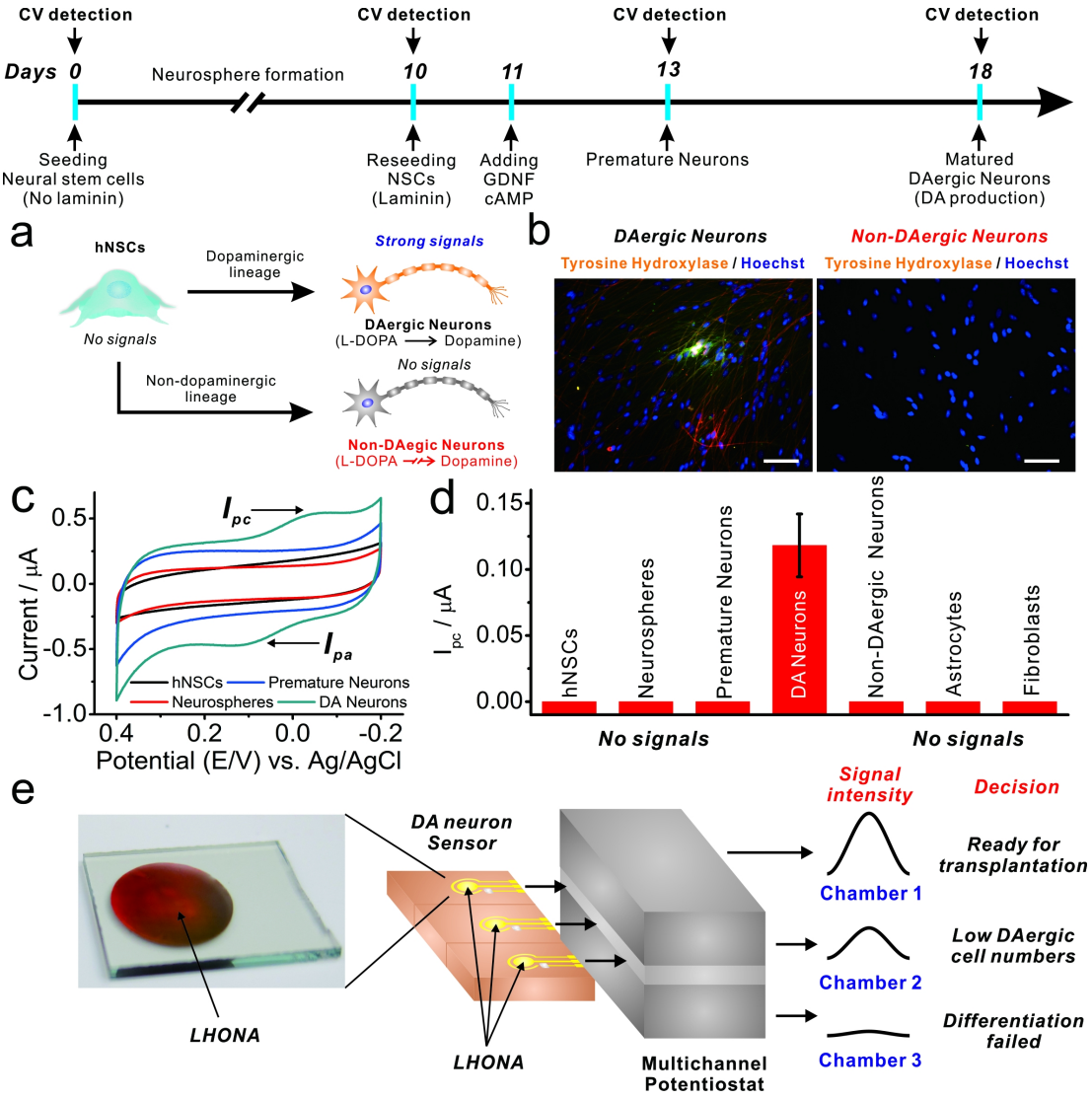

Figure 4.4: (a) Schematic diagram showing the conversion of hNSCs into dopaminergic (DAergic) and non-DAergic neurons. (b) Fluorescence images of cells stained with tyrosine hydroxylase to identify DAergic and non-DAergic neurons derived from hNSCs. Scale bar = 100 μm. (c) Cyclic voltammogram achieved from cells undergoing differentiation into DAergic neurons (DA Neurons). Only completely matured DAergic neurons are showing distinct redox peaks as opposed to their progenitor cells (hNSCs, neurospheres and premature neurons). (d) I_{pc} values calculated from (c) and other types of cells (astrocytes and fibroblasts). 'No signals' means that I_{pc} values cannot be calculated due to the absence of cathodic peaks. (e) Possible strategy to use LHONA platform to confirm successful differentiation of NSCs into DAergic neurons and their DA production ability which could be critical for making decision on the transplantation of DAergic neurons generated *ex vivo*. [279]

Next, we attempted to detect DA signals from hNSC-derived dopaminergic neurons since the hNSC-derived dopaminergic neurons are the actual source of transplantation which could be utilized for the treatment of DA-related psychiatric diseases/disorders [277, 292]. The hNSCs can be converted into dopamine-producing neurons through neurosphere generation, which are clusters of NSCs that still retain multipotency capable of differentiating into different types of neural cells. Since the dopaminergic neurons are only specific cell lines which express DOPA decarboxylase (DDC) that enables conversion of L-DOPA to DA, by detecting electrochemical signals of DA synthesized from L-DOPA, we can obtain some clues that prove the presence of DA-producing neurons derived from NSCs simply, easily and precisely in completely non-invasive/non-destructive way.

To this end, hNSCs were differentiated into two different neurons- dopaminergic neuron and non-dopaminergic neuron and their electrochemical signals were compared with that of undifferentiated hNSCs, neurospheres and premature neurons (Figure 4.4a). ReNcell VM cell lines was chosen as a model stem cell line since it has been proven to be highly effective for the generation of dopaminergic neurons [293–295]. Similar to the PC12 cells, dopaminergic neurons derived from hNSCs spread well on the surface of LHONA. To confirm the dopaminergic and non-dopaminergic differentiation of hNSCs, respectively, cells were stained with tyrosine hydroxylase (TH), which is a representative marker of dopaminergic neurons [296]. As shown in Figure 4.4b, only cells that have undergone dopaminergic differentiation showed TH expression while non-dopaminergic cells failed to show any significant TH expression. A transcriptional activator for TH, Nurr 1, was also found to be highly expressed in the differentiated dopaminergic neurons when analyzed by real-time reverse transcription-PCR. After the validation of dopaminergic differentiation of hNSCs, cells were detached and re-seeded on the LHONA to confirm the difference between dopaminergic cells with other types of cells when analyzed by cyclic voltammetry. Remarkably, as hypothesized, only hNSC-derived dopaminergic neurons showed distinct redox peaks in voltammogram while its progenitor cells including hNSCs, neurospheres and even premature neurons failed to show any reduction/oxidation peaks (Figure 4.4c). I_{pc} values could only be calculated

from dopaminergic neurons and was found to be approximately 0.13 μA, indicating that only dopaminergic neurons produced DA from externally added DA precursor (L-DOPA) via DDC (Figure 4.4d). To support these electrochemical results showing the ability of LHONA to detect dopamine and to distinguish dopaminergic neurons from other types of progenitor cells, the high-performance liquid chromatography (HPLC) was performed to confirm the dopamine release from L-DOPA pretreated dopaminergic neurons. We tested several different conditions: i) dopamine dissolved in medium, ii) medium collected from L-DOPA pretreated hNSCs, iii) L-DOPA non-treated dopaminergic neurons derived from hNSCs, and iv) L-DOPA pretreated dopaminergic neurons. Only dopaminergic neurons pretreated with L-DOPA showed a clear dopamine peak (iv) while other groups failed to show the same peak, which were consistent with the electrochemical results.

Thereafter, to confirm that only functional dopaminergic neurons can produce DA from L-DOPA, cells were intentionally damaged by incubation with DPBS for different periods of time (30 min, 60 min, and 3 days) prior to the electrochemical detection. The electrochemical signals were clearly detectable from the slightly-damaged or non-damaged cells (30 min) while cells incubated with DPBS for longer period of time (60 min) showed decreased reduction peaks that were 28.6% lower than that of 30 minutes at same reduction potential (Epc = -33mV). Finally, the voltammetric signals became completely negligible from the damaged dopaminergic neurons (cultured in DPBS for 3 days), proving that redox signals are only detectable from the viable/functional dopaminergic neurons, which will be highly useful to determine DA production ability of differentiated neurons prior to the clinical transplantation of them for replacing damaged/abnormal dopaminergic neurons that are responsible for many different types of neuronal diseases/disorders. Additionally, we also successfully confirmed that this distinct stable redox signals are not achievable from other type of similar neurons (non-dopaminergic neurons), glial cells (astrocytes) and completely different cells (human dermal fibroblasts) with same conditions (L-DOPA pretreatment), indicating that redox peaks are only specific to functional dopaminergic neurons (Figure 4.4d).

4.1.3 Conclusion

In conclusion, we have developed large-scale homogeneous nanocup electrode arrays (LHONA) for the effective detection of dopamine production from dopaminergic cell lines, as well as the monitoring of differentiation of hNSCs into dopaminergic neurons. LHONA bearing distinct cup-like nanostructures were successfully generated on transparent ITO electrode via two-step sequential process- laser interference lithography (LIL) and electrochemical deposition (ECD) method. The LHONA platform showed excellent performance in the detection of chemical DA at both low range of concentrations (0.3-3μM, R2=0.99) and high concentrations (0-50μM, R2=0.986), with the limit of detection (LOD) of 100nM, which was even higher than and other types of ITO-gold nanoparticle substrates, as well as the ITO modified with reduced graphene oxide (rGO). DA produced by model dopaminergic cells was found to be sensitively monitored on the LHONA due in part to its nanoscale pattern sizes and nanotopographical characteristics, which are large-scale periodic and homogeneous, that resulted in the enhancement of major functions of dopaminergic cells such as cell spreading, adhesion and proliferations, as well as the enhanced sensitivity toward DA detection. Furthermore, due to the excellent biocompatibility and electrochemical performance of LHONA, the differentiation of hNSCs into dopaminergic neurons was successfully monitored, which showed distinct redox peaks that were clearly distinguished from its progenitor cells (e.g., hNSCs, neurospheres and pre-mature neurons), as well as the other cell types (e.g. non-dopaminergic neurons, astrocytes and fibroblasts). Since the destructive process such as cell lysis and fixation are totally excluded for detecting DA production and monitoring dopaminergic differentiation of hNSCs, the developed periodic nanostructured platform (LHONA) and the electrochemical detection strategy introduced here can hold huge potential for pre-clinical testing of newly-achieved dopaminergic neurons. Specifically, the LHONA platform can be useful for the assessment of the DA secretion from dopaminergic neurons derived from ESCs/iPSCs/NSCs/MSCs prior to the clinical usage, as well as for the optimization of protocols to generate more dopaminergic neurons from pluripotent/multipotent stem cells in easy, simple but precise way (Figure 4.4e). Hence, it can be concluded that this work advances cell-based biosensors as an

effective non-destructive *in situ* monitoring tool for stem cell differentiation which can lead to more effective stem cell-based therapies for incurable diseases/disorders.

4.1.4 Materials and Methods

Materials and Cells

ITO electrode was purchased from U.I.D., South Korea. In case of gold electrode, chromium (adhesion layer) and gold were deposited on the cover glass with thickness of 2nm and 50nm, respectively using E-beam evaporator. All the chemicals used in this study including gold(III) chloride hydrate, ammonium sulfate, potassium citrate tribasic monohydrate, dopamine hydrochloride, 3,4-Dihydroxy-L-phenylalanine and Formalin solution (neutral buffered, 10%) were purchased from Sigma-Aldrich, USA. All the materials used for photolithographic process including photoresist (AZ2020), solvent (AZ EBR Solvent), developer (AZ MIF3000) and stripper (AZ 400T) were obtained from AZ Electronic Materials, USA. SYLGARD 184 silicon elastomer kit was purchase from Dow Corning, USA.

All materials used for cell culture and differentiation including Dulbecco's modified eagle's medium (DMEM), Dulbecco's phosphate buffered saline (DPBS), 0.05% trypsin, fetal bovine serum (FBS), Penicillin/Streptomycin, Neurobasal medium, B-27 supplements, basic fibroblast growth factor (bFGF-2), fibroblast growth factor (FGF), epidermal growth factor (EGF), Glutamax supplement, heparin sodium salt (1000U/ml), gentamicin, laminin and Matrigel were purchase from Life technologies, USA.

For the cells, PC12 (p=15) cells, which were derived from a pheochromocytoma of the rat adrenal medulla, were purchased from ATCC, USA and were utilized as a model dopaminergic cell line in this study. To obtain dopaminergic neurons from hNSCs, ReNcell VM, a neural cell line that was derived from the ventral mesencephalon region of the brain, was obtained from EMD Millipore, USA.

Generation of Homogeneous Polymer Nanohole Arrays

Lloyd's mirror interferometer was utilized to generate interference between the light coming from the light source (He-Cd laser, KIMMON KOHA Laser Systems, Japan) and the light reflected from the mirror, as previously reported. First, ITO-coated glass (10 ω/cm2, 0.5mm thickness) was sonicated in 1% Triton X-100, deionized water, ethanol (95%), followed by drying using N_2 gas. Hexamethyldisilazane (HMDS) was first coated using spin coater (Laurell Technologies, USA) and then, a photoresist diluted with its solvent with ratio of 1:0.8 was further spin-coated on HMDS-coated ITO electrode substrates, followed by baking it on hot plate at 125°C for 60s (soft baking). The substrate was exposed to UV (λ=325nm, 0.78mW) using Lloyd's mirror interferometer. The angle of sample holder incorporating Lloyd's mirror was adjusted to generate PR nanopatterns with different sizes according to the equation given by

$$\Lambda = \lambda UV / 2Sin\Theta$$

Where Λ, λ UV, and θ are size of the pitch (nm), a wavelength of the UV laser (325nm) and the incident angle (°). The incident angles adjusted to generate the pitch sizes of 300nm, 400nm, 500nm, 600nm and 900nm were 32.8°, 24.0°, 19.0°, 15.7°, and 10.4°, respectively. For the generation of PR nanohole patterns, samples were double-exposed to UV with degree of sample rotation (0°, 90°) for 14s each. Samples were baked at 125°C for 60s again (post exposure baking) and the unexposed photoresist was removed by developer, followed by washing with DI water. Samples were subjected to oxygen plasma treatment to remove PR residual on the surface ITO (140W, 50sccm of O_2) for 2min and further baked at 135°C for a minute prior to the electrochemical deposition.

Fabrication of Gold Nanostructure Arrays on ITO Substrate

Small plastic chamber was first attached on the surface of PR-nanopatterned ITO substrate using polydimethylsiloxane (PDMS) with ratio of 10:1 between PDMS and thermal curing agent. Solution containing 5mM $HAuCl_4$, 0.5mM ammonium sulfate

and 2mM potassium chloride tribasic monohydrate was prepared for the electrochemical deposition of gold on ITO substrate. Gold was deposited on the surface of ITO through PR nanoholes using DC amperometry (Epsilon potentiostat, BASi, USA) with potential of -1.2V for 60s, 120s, 180s, 240s and 300s to confirm their nanotopographical characteristics and the sensitivity toward DA detection. 300s deposition time was found to be inappropriate since it resulted overgrowth of gold, making it impossible to strip PR, which is essential step to fabricate gold nanostructured arrays. After the deposition of gold, plastic chamber was detached and the substrates were immersed in PR stripper at 65 $^{\circ}$C for 70min, followed by washing it with acetone, DI water and ethanol three times each. To remove residual stripper, two step cleaning methods were applied. First, samples were immersed in a solution containing 50mM KOH and 25% H_2O_2 for 15min and washed with DI water 3 times. After chemical cleaning, samples were immersed in 50mM KOH and subjected to CV whose potential was swept from -200 to -1200mV (vs. Ag/AgCl) two times with scan rate of 50mV/s. Substrates were thoroughly washed with DI water to remove KOH.

In the case of the GNP-modified ITO electrodes, the ITO electrode was first exposed to oxygen plasma to make the surface hydrophobic and was further immersed in a solution containing 5% aminopropyltriethoxysilane (APTES) for 10 minutes, followed by washing three times with 95% ethanol. After annealing APTES at 135 $^{\circ}$C for 15 minutes in the oven, APTES-coated ITO electrodes were reacted with the GNP-containing solutions for 24 hours at 4 $^{\circ}$C. The GNP-modified ITO electrodes were finally washed three times with ethanol and deionized water prior to using them for electrochemical studies.

Electrochemical Detection

Cells were seeded on the prepared electrode (approximately 50,000 cells/chip), and incubated 1 day for stable attachment on the surface. 100μM of L-Dopa dissolved in media was treated for 2 hours prior to the electrochemical detection. Electrochemical detection was carried out with EC Epsilon Potentiostat (Basi, IN, USA), and buffer was changed to DPBS (0.01M, PH 7.4) containing 5mM KCl to trigger dopamine release

from dopaminergic cells. A fabricated electrode served as the working electrode and an Ag/AgCl (1M KCl) and a Pt wire served as the reference and counter electrode, respectively. Cyclic volatammetry (CV) was performed with the potential range (vs. Ag/AgCl) of 0.4 V and -0.2 V at 50 mV/s in PBS, and DC potential amperometry (DCPA) was performed at -50mV (vs. Ag/AgCl) for 1000 seconds. Applied potential was settled to reduction peak potential of dopamine. 20μl of 100mM KCl was injected to buffer while DCPA was running.

Cell Culture and Differentiation

ReNcell VM Cells were used to achieve dopaminergic neurons as previously described. Specifically, on day 1, 1.5 million ReNcell VM Cells were placed in a 10 cm diameter TCP and treated with the medium (mixture of neurobasal medium and DMEM/F12 medium with ratio of 1:1) containing 20 ng/ml of EGF and 20 ng/ml of bFGF to generate neurospheres. After 7 days of incubation in normal culture condition (37°C, 5% CO2), neurospheres were spun down at 1.0 k rev/min for 60 sec and transferred to a laminin-coated TCP, followed by further incubation for 3days with the medium supplemented with 20 ng/ml of EGF and bFGF. On day 10, cells were detached using Accutase detaching agent and re-plated at density of 10 million on laminin-coated TCP. 2ng/ml of GDNF and 1mM of dibutyrl-cAMP were also introduced to cell culture media on day 10 for dopaminergic differentiation. On day 17, differentiation process was completed and after that, cell culture medium was replaced every 3 days without addition of growth factors and small molecules.

Fluorescence Imaging

For actin staining of PC12, cells were washed with DPBS (pH 7.4) and fixed with 4% formaldehyde solution for 10 minutes at RT, followed by three times of washing with DPBS. Cells were then treated with 0.1% Triton X-100 in PBS for 10 min, washed with DPBS two times and stained with Alexa Fluor 546 Phalloidin-containing solution for 20 minutes at RT. After washing cells with DPBS for two times, actin-stained PC12 cells were placed on the slide glass using ProLong Gold Antifade Mountant as mounting

solution. For immunofluorescence staining, differentiated neurons were fixed same as actin staining described as above. After cell fixation, cells were treated with 0.1% Triton X-100 solution containing 5% normal goat serum for 1 hour at RT. Solution containing primary antibody specifically binds to TH was applied kept for 1 hour, followed by washing with DPBS. Secondary antibody (Anti-Mouse IgG) labeled with Alexa-Fluor 647 was further applied to tag primary antibody, kept for 1 hour at RT, followed by washing three times with DPBS. Finally, Hoechst (3μg/mL) was used to stain nucleus for immunofluorescence imaging (Eclipse Ti-U, Nikon, Japan).

HPLC Analysis

To verify the secretion of dopamine from L-DOPA pretreated dopaminergic neurons, the media collected from the cells cultured was analyzed by using an Agilent 1260 infinity series HPLC with a UV detector. Prior to the HPLC analysis, hNSCs and dopaminergic neurons were pretreated with L-DOPA-containing (100 μM) neurobasal medium for 2 hours and then, KCl (100mM) was added to each cell to trigger dopamine release for the detection. Dopamine and L-dopa were separated using a mobile phase with a composition of 97% phosphate buffer (PBS) and 3% methanol on a Phenomenex Luna 5μ C18 reverse-phase column at a flow rate of 1ml/min. The dopamine and L-dopa peaks were verified using a 0.653mM and 0.507mM standards, respectively, and the detection limit was verified as a 3:1 signal to noise ratio and was below 3nM. The volume of injection was 5μL for both the standards and the samples.

Substrate Characterization

Photoresist nanopatterns and LHONA substrates were imaged by scanning electron microscopy (SEM, GENESIS-1000, Emcrafts, South Korea) or field emission SEM (FE-SEM, SIGMA, Zeiss, Germany). Briefly, gold was deposited on the surface of samples with thickness of 10nm or 20nm by using ion coater (KIC-1A, COXEM, South Korea). The acceleration voltages used for imaging gold-coated samples were 20kV and 5kV for SEM and FESEM, respectively.

4.2 Non-destructive Real-Time Monitoring of Enhanced Stem Cell Differentiation using a Graphene-Au Hybrid Nanoelectrode Array

4.2.1 Introduction

Stem cells have attracted increasing research interest in the field of regenerative medicine because of their unique ability to differentiate into multiple cell lineages. However, controlling stem cell differentiation efficiently and improving the current destructive characterization methods for monitoring stem cell differentiation are the critical issues. To this end, we developed multifunctional graphene-gold (Au) hybrid nanoelectrode arrays (NEAs) to i) investigate the effects of combinatorial physicochemical cues on stem cell differentiation, ii) enhance stem cell differentiation efficiency through biophysical cues, and iii) characterize stem cell differentiation in a non-destructive real-time manner. Through the synergistic effects of physiochemical properties of graphene and biophysical cues from nanoarrays, our graphene-Au hybrid NEAs facilitated highly enhanced cell adhesion and spreading behaviors. In addition, by varying the dimensions of the graphene-Au hybrid NEAs, we showed improved stem cell differentiation efficiency, resulting from the increased focal adhesion signal. Furthermore, we utilized our graphene-Au hybrid NEAs to monitor osteogenic differentiation of stem cells electrochemically in a non-destructive real-time manner. Collectively, we believe our unique multifunctional graphene-Au hybrid NEAs can significantly advance stem cell-based biomedical applications.

Stem cell-based regenerative medicine has attracted increasing attention in the area of biomaterial science and tissue engineering. For example, stem cell-based approaches hold great potential in treating many musculoskeletal diseases and injuries [297–300]. However, the ability to differentiate stem cells into specific cell types of interest (e.g., bones, cartilages, and muscles) in a highly selective and efficient manner, and the development of non-destructive, real-time characterization methods to assay stem cell differentiation are crucial in harnessing the full potential of stem cell-based biomaterial applications [301–304].

Conventional methods to control stem cell differentiation using soluble cues such

as growth factors, cytokines, and small organic molecules have shown limited success in achieving high differentiation specificity and efficiency. Recent findings show that biophysical (or insoluble) cues also play a critical role in guiding stem cell differentiation [85, 305–311]. Encompassing nanotopographical and mechanical properties of microenvironment, biophysical cues are known to be effective regulators of cytoskeletal dynamics and downstream gene expression [e.g., extracellular matrix (ECM)-integrin-cytoskeleton signaling transduction], thereby modulating stem cell behaviors such as proliferation, migration, and differentiation [65]. Therefore, there is a clear need to develop a novel method to identify the optimal biophysical cues in a combinatorial way for guiding stem cell differentiation into specific cell lineages. These identified biophysical cues can be further combined with defined soluble factors to bring synergistic differentiation conditions, which will facilitate the advancement of stem cell-based applications such as the regeneration of certain types of damaged tissues/organs of patients.

Another critical challenge is to avoid the possible tumorigenicity associated with stem cell therapy [303, 304]. To this end, the precise characterization of stem cell differentiation at each stage using biomarkers in a non-destructive manner while maintaining high cell viability is essential. Conventional methods for analyzing the biological characteristics of differentiated cells such as fluorescence-based methods [e.g., immunostaining and fluorescence-activated cell sorting (FACS)] and analysis of the expression of biomarkers (DNAs/RNAs/proteins) [e.g., polymerase chain reaction (PCR) and western blot] are commonly used; however, these methods typically require destructive steps such as cell fixation or cell lysis, which prevent the subsequent applications of the characterized cells [279, 312]. Therefore, the development of novel methods that can effectively monitor stem cell differentiation dynamics in a non-destructive manner is urgent.

4.2.2 Results and Discussion

Addressing the challenges above, herein we demonstrate the versatility of our novel graphene-Au hybrid nanoelectrode combinatorial arrays (graphene-Au hybrid NEAs)

to: i) investigate the combinatorial effects of physicochemical cues on stem cell differentiation [Figure 4.5a], ii) identify the optimal biophysical cues to enhance stem cell osteogenic differentiation [Figure 4.5b], and iii) non-destructively monitor the dynamic status of stem cell differentiation in a real-time manner [Figure 4.5b]. The osteogenesis of human mesenchymal stem cell (hMSC) was selected as a proof-of-concept model for this study [313–315].

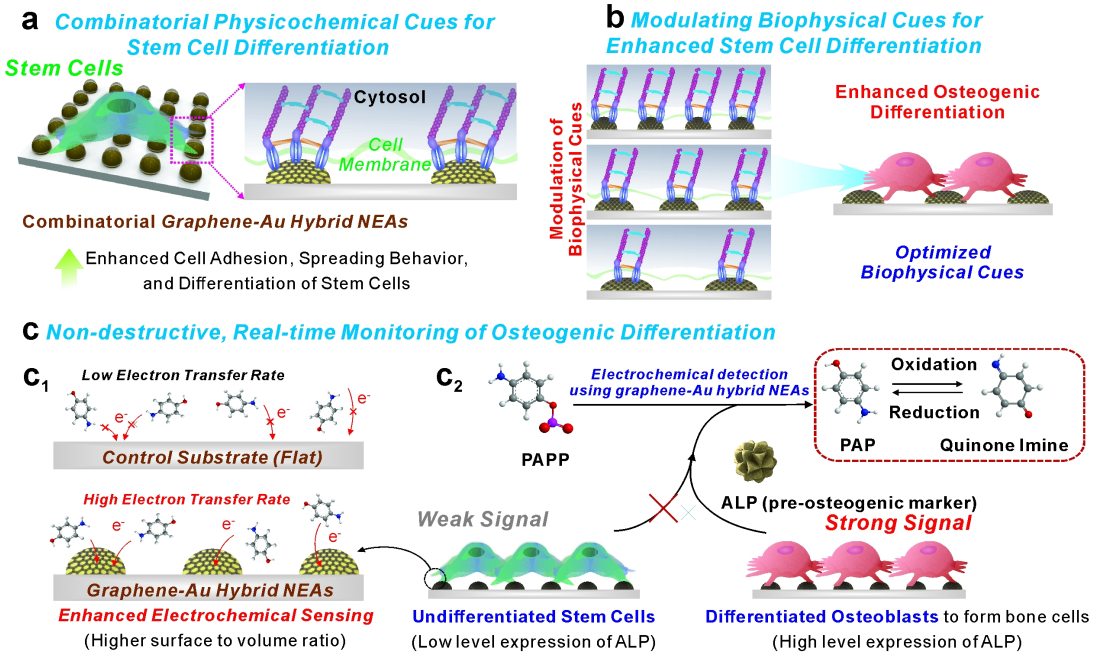

Figure 4.5: Schematic illustration of multifunction of graphene-Au hybrid nanoelectrode arrays (NEAs). a) Investigation of the combinatorial effects of physicochemical cues on stem cell. b) Identification of optimal biophysical cues for stem cell differentiation. c) Enhanced electrochemical signal for monitoring osteogenic differentiation. [316]

Typically, our multifunctional graphene-Au hybrid NEAs are fabricated via laser interference lithography (LIL) and physical vapor deposition (PVD) methods. We tested different variables of the graphene-Au hybrid NEAs such as pitch and pattern sizes to identify the optimal biophysical cues for osteogenic differentiation of stem cells. Reduced graphene oxide (rGO) was chemically attached and modified to the surface of Au NEAs to enhance the adhesion and spreading behaviors of the stem cells. Since the focal adhesion and the rearrangement of the cytoskeleton is critical in determining cell behaviors, we hypothesized that our developed multifunctional graphene-Au

hybrid NEAs could regulate stem cell fate through physicochemical and biophysical cues [Figure 4.5b] [65,66,317–319]. Also, the unique physicochemical properties of rGO can promote cell adhesion and spreading behaviors on the NEAs without comprising its electrochemical property [Figure 4.5a] [85, 320–322]. Taking advantage of the high electron transfer rate based from 3D nanostructures [Figure 4.5c_1], our graphene-Au hybrid NEAs has the potential to be utilized as an excellent electrochemical sensing platform, enabling scientists to characterize the subtle changes of biomarker expression [alkaline phosphatase (ALP, a pre-osteogenic marker)] [Figure 4.5 c_2]. Collectively, our graphene-Au hybrid NEAs, as designed, could have the ability to enhance and monitor osteogenic differentiation of stem cell, hMSCs, in a non-destructive real-time manner.

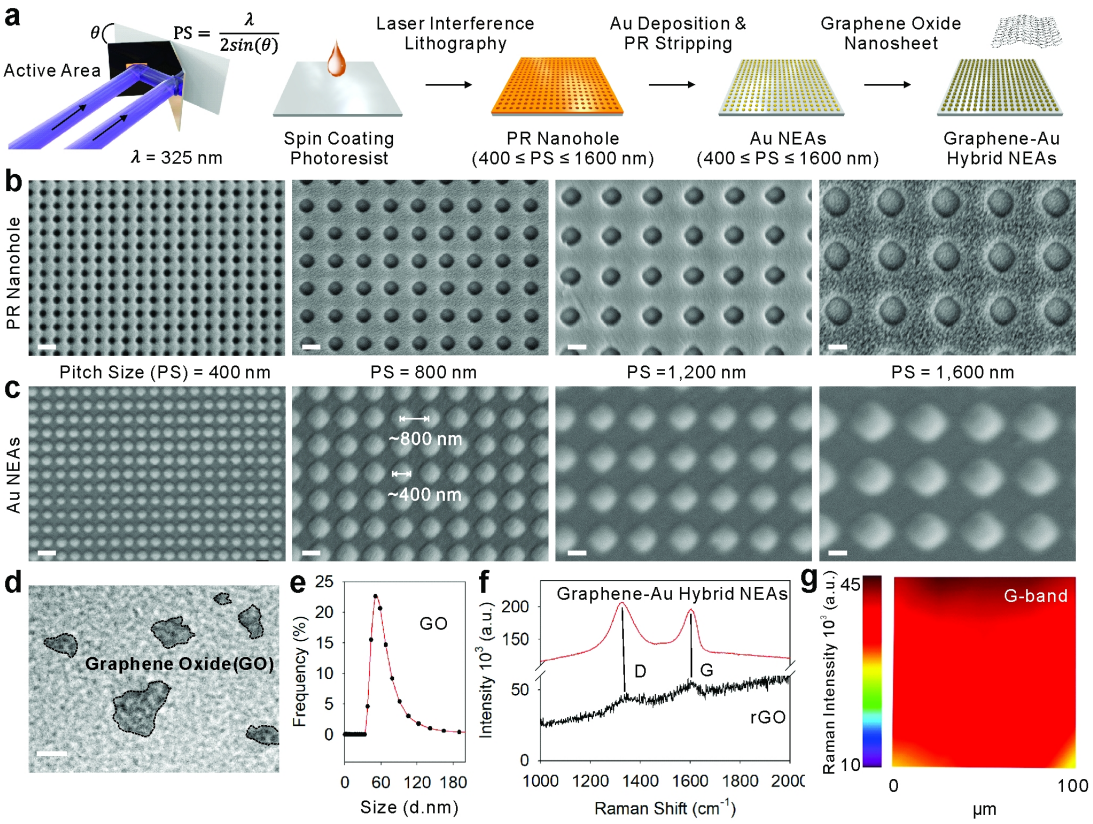

Figure 4.6: Generation of graphene-Au hybrid nanoelectrode arrays (NEAs). a) Schematic illustration of sequential steps to generate graphene-Au hybrid NEAs on ITO electrode via laser interference lithography (LIL) and metal deposition method. (b-c) Representative scanning electron microscope (SEM) images (Magnification of 40K X) of b) photoresist nanohole after the LIL process and c) resulting Au NEAs after metal deposition process according to pitch size (400, 800, 1200, and 1600 nm, respectively). d) Representative transmission electron microscope (TEM) image, e) size distributions, and f) Raman spectra of synthesized graphene oxide nanosheet and after formation of graphene-Au hybrid NEAs. g) Homogeneity analysis by Raman map obtained from graphene-Au hybrid NEAs with notable Raman transitions band (G-band of graphene at around 1600 cm^{-1}. Scale bars are 500 nm (b,c) and 50 nm (d). [316]

As biophysical cues (e.g. nanotopography, elastic module, pattern dimension, and geometry) have been shown to enhance stem cell differentiation by regulating cell adhesion and spreading behaviors [65, 66, 269, 317–319], we generated a combinatorial graphene-Au hybrid NEA as illustrated in Figure 4.6a. To identify the optimized biophysical cues for stem cell osteogenesis, four different pitch sizes (400, 800, 1,200, and 1,600 nm) of large-scale (1×1 cm^2) homogeneous photoresist (PR) nano-hole pattern

arrays were generated through the LIL technique on an indium tin oxide (ITO) substrate [Figure 4.6b] [323]. We then deposited 15 nm of chromium (Cr) as an adhesion layer and 90 nm of gold (Au) as a conducting layer via PVD onto the PR nano-hole array. The PR was sequentially removed to obtain the four different sized homogenous Au NEAs with controlled width (200, 400, 600, and 800 nm), gap (200, 400, 600, and 800 nm), and height (105 nm) parameters [Figure 4.6c]. The pitch size and height of Au NEAs were carefully designed not only to isolate cells from the underlying flat substrate by disrupting integrin-substratum interactions but also to reconstitute integrin clustering on NEAs by controlling the width and gap of physical dimensions to the submicron range [[65, 324]. In parallel, graphene oxide (GO) sheets were synthesized through a modified Hummers' method with a pre-oxidation step. For the sufficient coating of GO onto the Au NEAs surface, the size of GO sheet was adjusted to below 200 nm by an additional filtration process to obtain smaller GO nanosheets. To characterize the as-prepared GO sheets, transmission electron microscopy (TEM) measurement was performed [Figure 4.6d]. We also analyzed the size distribution of GO by both dynamic light scattering (DLS) measurement and TEM images. The size distribution of the GO sheets ranged from 37.84 nm to 190.10 nm with an average size of 63.75 $\pm$ 24.63 nm in DLS analysis, [Figure 4.6e] and 100.4 $\pm$ 39.4 nm in TEM images. Both results clearly demonstrates the selected size distribution of GO less than 200 nm after filtration process. Further, as-prepared GO sheets were functionalized onto the surface of Au NEAs through electrostatic interactions by utilizing a chemical linker (cysteamine hydrochloride: $C_2H_7NS\cdot$ HCl). Finally, GO sheets are chemically reduced by hydrazine monohydrate ($NH_2NH_2 \cdot H_2O$) solution to obtain the graphene-Au hybrid NEAs. Due to the unique physicochemical structure of atomic thin layered rGO, we conducted Raman spectroscopy to properly validate the rGO coating on the Au NEAs. As expected, Raman transition band at the location of the distinct D (1,350 cm^{-1}) and G (1,600 cm^{-1}) band of reduced GO (rGO) were observed from both rGO (functionalized on bare Au substrate) and graphene-Au hybrid NEAs, which meets previously reported literature [45, 325, 326]. The reduction of GO to rGO on graphene-Au hybrid NEAs was also validated by the comparison of Raman intensity ratio between D and G band

(I_D/I_G) before and after the reduction process. The I_D/I_G ratio increases from 0.90 to 1.22 as GO reduces to rGO, respectively [327,328]. Moreover, a remarkably strong Raman transition band of rGO [Figure 4.6f] as well as intense, homogenously distributed Raman transition (distinct G band, 1,600 cm^{-1}, of rGO) signals over a large scan area (100×100 spots per 100×100 μm^2) [Figure 4.6g] were observed from the graphene-Au hybrid NEAs owing to the surface-enhanced Raman scattering effect caused by the Au nanodots.

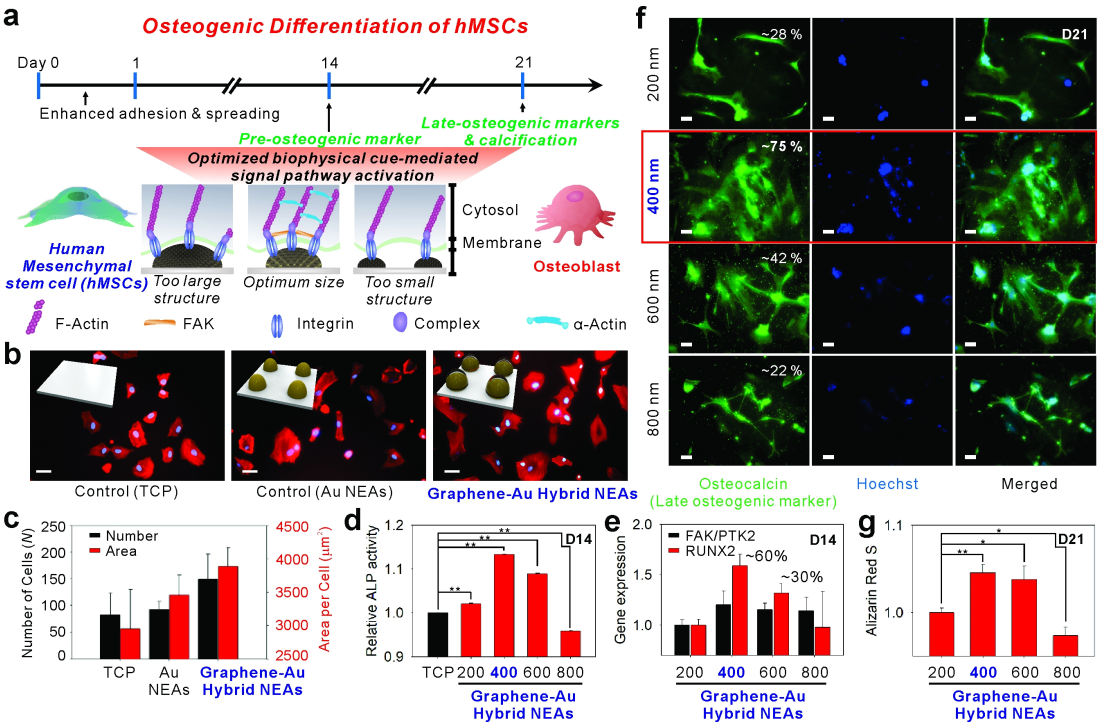

Figure 4.7: Enhanced osteogenic differentiation of hMSCs by graphene-Au hybrid NEAs. a) Schematic illustration of graphene-Au hybrid NEAs effect on the osteogenic differentiation of hMSCs. (b-c) Analysis of cell adhesion and spreading behavior. b) Representative Hoechst and F-actin-stained fluorescence images of hMSCs labeled with Alexa Fluor 633 (scale bar = 50 μm) and c) the calculated number of cells after washing (adhesion) and cell surface area (spreading) from F-actin-stained images of hMSCs on TCP, Au NEAs, and graphene-Au hybrid NEAs (width = 400 nm), respectively. (d-g) Effect of graphene-Au hybrid NEAs on osteogenic differentiation of hMSCs based on different width size range from 200 to 800 nm. d) Alkaline phosphatase (ALP) assay to confirm the expression of the pre-osteogenic marker based on different pitch size. e) PCR analysis of osteogenic markers including runt-related transcription factor 2 (RUNX2) and focal adhesion kinase (FAK) for verifying nano-topographic effect. f) Fluorescence images of hMSCs differentiated into osteoblasts stained for osteocalcin with Alexa 594 (red, left column), a nucleus with Hoechst (blue, middle column) and merged (right column) (scale bar = 50 μm). g) Quantitative analysis of calcium expression by extracting Alizarin red S based on different width size. Results are average of absorbance signals (405 and 562 nm for ALP and Alizarin red S, respectively obtained from three independent experiments) (Error bars represent mean $\pm$s.d.; n=3, *p<0.05, **p<0.001 by one-way ANOVA with Tukey post-hoc test.) [316]

Knowing cell adhesion/spreading behaviors and the elongated cell morphology can promote stem cell osteogenesis [65,329], we hypothesized that our graphene-Au hybrid NEAs could enhance osteogenic differentiation of hMSCs through the unique physiochemical cues from our graphene-Au hybrid NEAs [Figure 4.7a]. To test this hypothesis,

hMSCs, cultured on tissue culture plate (TCP), Au NEAs, and graphene-Au hybrid NEAs for 4 hrs, were fixed for 10 mins and characterized using Hoechst to stain their nucleus and fluorescent dye (Alexa Fluor 633) to stain their cytoskeleton (F-actin). No notable difference was observed for the number of cells adhered on the TCP and Au NEAs; however, the presence of nanotopographical cues in Au NEAs allowed the cells to spread more extensively and homogeneously, compared to the experimental condition of TCP. Moreover, due to the unique physiochemical property of graphene (e.g., amphiphilic and nanoscopic properties), both the number and the size of adhered cells significantly increased on the graphene-Au hybrid NEAs, compared to that of TCP and Au NEA conditions [Figure 4.7b]. We quantitatively analyzed the number and the size of adhered cells using five 1,320 $\times$ 1,320 μm$^(2)$ area-fluorescent images, randomly selected from each condition. The average number of cells were 83.0 $\pm$ 40.3, 92.6 $\pm$ 15.2, and 149.4 $\pm$ 46.7, and the average size of the cells were 2,955.9 $\pm$ 584.9, 3,457.9 $\pm$ 298.9, and 3,890.8 $\pm$ 272.6 μm$^(2)$, corresponding to the TCP, Au NEA, and graphene-Au hybrid NEA conditions respectively [Figure 4.7c].

To examine further, hMSCs that were grown on graphene-Au hybrid NEAs for a day were treated with differentiation induction medium (osteogenic medium: OM) to study the optimal biophysical cues on osteogenesis. All the cells treated with OM showed the expression of ALP (pre-osteogenic marker) regardless of substrate types used; however, hMSCs on the graphene-Au hybrid NEAs with 400 nm sized (in diameter) nanodots among the 4 different conditions (pattern sizes; 200, 400, 600, and 800 nm) [Figure 4.7d] showed the highest ALP activity on day 14 (D14), supporting the synergistic effect of the biophysical cues combined with the soluble cues [Figure 4.7d] [330]. We also conducted real-time quantitative PCR on D14 to detect biomarkers of osteoblast lineage such as runt-related transcription factor 2 (RUNX2) and focal adhesion kinase/protein tyrosine kinase 2 (FAK/PTK2) genes to investigate the effects of each nanopattern on osteogenic differentiation [311]. It is known that appropriate biophysical cues, such as nanotopography and pattern dimension, can enhance the formation of integrin-mediated small clustering adhesion sites termed focal adhesions (FAs) [65], which affect cell spreading behavior and facilitate lamellipodial protrusions [331]. Moreover, the formation of

FA complexes stimulates multiple intracellular signaling cascades such as the mitogen-activated protein kinase-extracellular signal-regulated kinase (MAPK-ERK) 1/2 pathway that activates RUNX2, resulting in increased osteogenic differentiation [332, 333]. We also confirmed the clear co-related upregulation between the FAK/PTK2 gene and the RUNX2 gene in our tested graphene-Au hybrid NEAs. In particular, as predicted from the ALP activity assay, the level of molecular markers for both osteoblast lineage (RUNX2) and the focal adhesion kinase (FAK/PTK2) gene also showed the highest expression from the 400 nm sized graphene-Au hybrid NEA condition [Figure 4.7e]. This indicates that early osteogenic differentiation can be synergistically enhanced through the proper choice of biophysical cues. Immunostaining also showed the highest coverage and expression of osteocalcin from the 400 nm diameter graphene-Au hybrid NEA condition [Figure 4.7f]. From the Alizarin red S assay, which checks the level of calcification, one of the most significant indicators for bone regeneration, we also observed cells grown on the 400 nm sized graphene-Au hybrid NEAs showed the highest level of calcification [Figure 4.7g] [310]. Collectively, the above results support our hypothesis that appropriate biophysical cues of our graphene-Au hybrid NEAs can enhance the formation of mature osteoblasts, which is highly desirable for further *in vivo* applications such as treating bone defects.

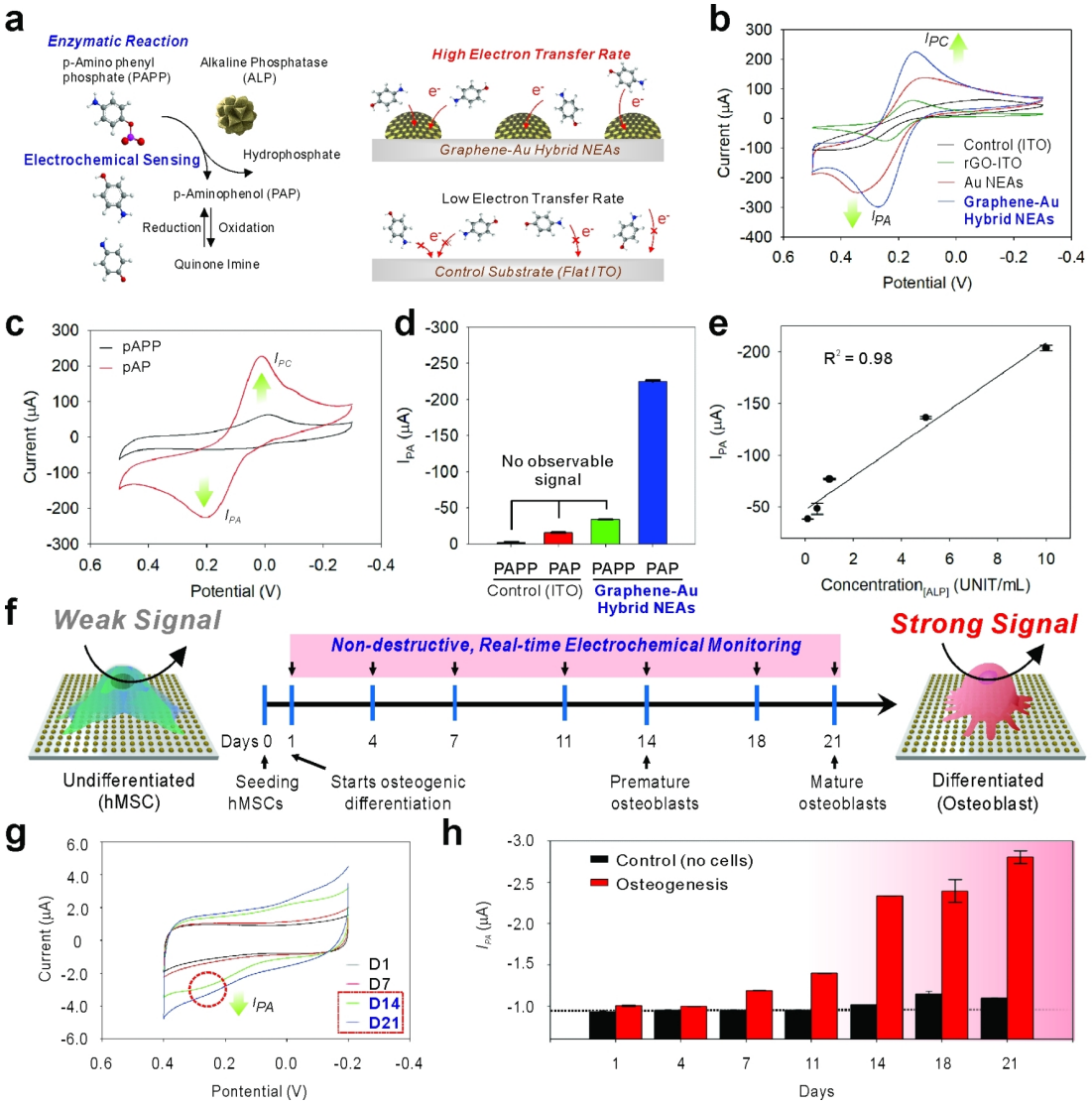

Figure 4.8: Utilization of graphene-Au hybrid NEAs as an electrochemical sensing platform for *in-situ* monitoring of osteogenic differentiation of hMSCs. a) Schematic illustration of an enzymatic reaction and electrochemical sensing mechanism of alkaline phosphatase (ALP) and improved electron transfer kinetic based on the 3D surface in graphene-Au hybrid NEAs compared to 2D flat ITO surface. b) Cyclic voltammogram of 1 mM of $[Fe(CN)_6]_4$-dissolved in DPBS obtained at a 50 mVs^{-1} scan rate using a bare ITO substrate, rGO coated ITO substrate, Au NEAs, and graphene-Au NEAs, respectively. c) Cyclic voltammogram of P-aminophenyl phosphate (PAPP) on graphene-Au NEAs before and after enzyme reaction with alkaline phosphatase (ALP). d) Anodic peak (oxidation potential: I_{PA}) value change achieved from of cyclic voltammogram of PAPP, before and after enzyme reaction (ALP), on bare ITO substrate and graphene-Au hybrid NEAs. e) The linear correlations between concentrations of ALP and the current signal at oxidation potential (I_{PA}) of cyclic voltammetry. f) Schematic illustration of electrochemical signal change between undifferentiated and differentiated (osteocyte) hMSCs based on ALP generation. g) Cyclic voltammetry, and h) calculated I_{pc} values from time-dependent monitoring (range from D1 to D21) of hMSCs during osteogenic differentiation. 8.0 × 103 cells are seeded on 0.4 cm^2 area and treated with osteogenic differentiation medium (OM). The medium was changed after each electrochemical measurement.) [316]

Furthermore, we developed our graphene-Au hybrid NEAs (400 nm sized graphene-Au hybrid NEAs, hereafter termed graphene-Au hybrid NEAs) as a non-destructive real-time electrochemical sensing platform to monitor stem cell differentiation [Figure 4.8]. Since most of the electrochemical reaction happens in proximity to the electrode surface, the surface dimension and its modification are crucial for the performance of electrochemical sensing. For this purpose, nanomaterial (Au and carbon)-based electrochemical sensors have been developed owing to their unique physicochemical properties including high conductivity, inertness, and biocompatibility [334,335]. Additionally, the higher surface-to-volume ratio of the nanostructures can also increase the electrochemical sensing performance [336,337]. We conducted cyclic voltammograms (CV) by using 1mM of ferrocyanide $[Fe(CN)_6]^{4-}$ as a well-defined electroactive (reduction and oxidation: redox) chemical in phosphate buffered saline (PBS, pH 7.4) at a scan rate of 50 mV/s to measure the electrochemical signal from each electrode (bare ITO, Au NEAs, and graphene-Au hybrid NEAs) [Figure 4.8b]. As expected, there was no observable faradaic current on the bare ITO substrate. However, a large current, intense oxidation and reduction peak (IPA and IPC) were observed on the both rGO-ITO and Au NEAs. In particular, graphene-Au hybrid NEAs displayed a narrower and higher I_{PA} and I_{PC} due to the better electron transfer rate and faster diffusion of oxidant/reductant obtained through the additive effect obtained by both rGO and Au NEAs [320–322]. We also validated the electrochemical performance based on the reduction degree of rGO. No observable faradaic current on the GO coated ITO substrate, which could be due to the impeded electron transfer. However, an intense IPA and IPC were observed after reduction process. The signal was kept increased and saturated after 9 hr reduction [338].

We then utilized our graphene-Au hybrid NEAs to examine an ALP-based enzymatic reaction in a cell-free configuration as an initial proof-of-concept before monitoring the osteogenic differentiation process of hMSCs. The expression of ALP, a major biomarker for osteogenesis [339,340], arose sequentially during the osteogenic differentiation. As shown in Figure 4.8a, ALP catalytically hydrolyzed the P-aminophenyl phosphate (PAPP) to produce electroactive p-aminophenol (PAP), and the redox reaction

between PAP and Quinone imine (QI) was monitored through cyclic voltammogram by utilizing graphene-Au hybrid NEAs as a sensing platform [Figure 4.8a]. Before the addition of ALP, no observable redox peak was monitored for the PAPP (1mM) dissolved PBS solution. However, observable redox peaks were obtained 30 minutes after the addition of ALP into the solution, at approximately 0.2 V for the oxidation (I_{PA}) potential and 0.01 V for the reduction (I_{PC}) potential [Figure 4.8c]. Comparably, no observable oxidation signal (I_{PA}) was obtained on the bare ITO substrate for neither condition: absence or presence of ALP. Particularly, a remarkable oxidation peak was observed only at the graphene-Au hybrid NEAs when ALP was presented, which proved its excellent sensitivity for the electrochemical detection of PAP resulted from ALP catalytic reaction [Figure 4.8d]. To support these results, we also calculated the HOMO and LUMO of PAP molecule and compare it to the band edge positions of rGO, Au and ITO that are reported in literature [341, 342]. When no voltage bias is applied, rGO has less barrier to receive electron from PAP molecules, which leads to the oxidation of PAP into QI. In addition, Graphene-Au hybrid NEAs with increased electrode surface area could also increase electron transfer rate by facilitating the electron and mass diffusion. Such improvements can be directly supported by the increased IPA shown in Figure 4.8c and narrowed voltage difference between I_{PA} and I_{PC} shown in Figure 4.8b. Moreover, graphene-Au hybrid NEAs showed good linearity (R2 = 0.98) at different concentrations (range from 0.1 to 10 units/mL) of ALP with a limit of detection (LOD) of 0.03 UNIT/ml [Figure. 4.8e] which well agreed with previously reported quantitative ALP assays [343]. Additionally, the clear oxidation peak was observed within 10 minutes after addition of ALP, and the overall enzyme reaction was starting to saturate at approximately 40 minutes.

After verifying the electrochemical property of graphene-Au hybrid NEAs in cell-free condition, hMSCs (2.0×104 cells/cm^2) that were grown on graphene-Au hybrid NEAs for a day were treated with OM. The cyclic voltammetry was conducted for differentiation period (3 weeks) with the addition of PAPP molecule for real-time monitoring of the osteogenic differentiation of hMSCs in a nondestructive manner [Figure 4.8f]. We observed no obvious redox peaks on the voltammogram up to D7 even though the

background signal is slightly increased. In contrast, clear, distinct redox peaks were observed in the period of the premature (D14) and mature (D21) osteoblast formation. The calculated IPA values from time-dependent monitoring (range from D1 to D21) of hMSCs during osteogenic differentiation demonstrated the sequential increment of ALP activity as expected. In particular, the remarkable signal increment was observed from D14, where premature osteoblast starts to form [Figure 4.8g]. Additionally, graphene-Au hybrid NEAs also showed excellent stability by maintaining the I_{PA} value for 3 weeks under the cell-free condition [Figure 4.8h]. We also analyzed for myogenic differentiation electrochemically at D21 to show that our graphene-Au hybrid NEAs could discriminate osteogenic differentiation from other types of differentiation. Compared to hMSCs, myoblast cell also demonstrated higher ALP activity [344, 345]; however, osteoblasts expressed approximately 2 times higher signals (ΔI_{PA}: -1.80 μA) relative to myoblasts (ΔI_{PA}: -0.82 μA) which showed the ability of graphene-Au hybrid NEAs to discriminate osteogenic differentiation from other differentiation. Supportably, cell destructive a PNPP based optical ALP assay also demonstrated similar trends on ALP activity of each cell line (undifferentiated hMSC, osteoblast, and myoblast) observed by graphene-Au hybrid NEAs. Thus, we believe that our graphene-Au hybrid NEAs will be particularly valuable for enhancing and monitoring stem cell behaviors through unique biophysical and electrochemical properties. The non-destructive, real-time monitoring of stem cell differentiation would be valuable for the clinical application of stem cell therapies to repair the damaged tissue\organs of patients.

4.2.3 Conclusion

In summary, we have successfully developed multifunctional graphene-gold (Au) hybrid nanoelectrode arrays (NEAs) for modulating the extent of osteogenic differentiation of stem cells. Potentially, our developed approach can be beneficial for deconvoluting biophysical cues from the complex microenvironmental cues and identify the combinatorial cues to enhance stem cell differentiation. More detailed mechanistic studies on how the combination of physicochemical and biophysical cues modulate the signaling cascades involved in stem cell osteogenesis are currently under investigation. Furthermore, due to

the excellent biocompatibility and electrochemical performance of our hybrid NEAs, the osteogenic differentiation of hMSCs was successfully monitored in both non-destructive and real-time manner. Since the destructive analysis process such as cell lysis and cell fixation are not necessary for assaying the osteogenic differentiation of hMSCs for transplantation, our developed combinatorial arrays and novel electrochemical detection method can bring a breakthrough in the preclinical investigation of differentiated osteoblasts. Collectively, this work will not only advance stem cell differentiation assays by providing a practical, non-destructive, real-time monitoring tool but also help scientists understand the fundamental interactions between nanostructures and stem cells better.

4.2.4 Materials and Methods

Generation of homogeneous polymer nanohole arrays

ITO-coated glass (10 Ω/cm^2, 0.5mm thickness, active patterning area 1 $\times$ 1 cm^2) substrate was sonicated with 1 % Triton X-100 (4-$(C_8H_{17})C_6H4_4OCH_2CH_2)_nOH$, n 10), deionized water and ethanol (95%) in a sequential manner for cleaning. After drying under N_2 gas, the substrate was functionalized with hexamethyldisilazane (HMDS) ($(CH_3)_3$ SiNHSi $(CH_3)_3$) through vapor phase deposition and then, a UV-cross-linkable photoresist (PR) (AZ2020) diluted with solvent (AZ EBR Solvent) with ratio of 1:0.8 was spin-coated (Laurell Technologies, USA) on to the substrate. PR coated substrate was soft baked on a hot plate at 100 $^\circ$C for 60s and then exposed to UV (λ=325nm, 0.81mW) using Lloyd's mirror interferometer. Lloyd's mirror interferometer was utilized to generate periodic intensity profiles through constructive/destructive interference which occurred between the light coming from the light source (He-Cd laser, KIMMON KOHA Laser Systems, Japan) and the light reflected from the mirror. The angle of sample holder incorporating Lloyd's mirror was adjusted to generate PR nanopatterns with different sizes according to the equation given by $\Lambda = \lambda/2\mathrm{Sin}\theta$ Where Λ, λ, and θ are the size of the pitch (nm), a wavelength of the UV laser (325nm) and the incident angle ($^\circ$), respectively. The incident angles were adjusted to generate the pitch

sizes of 400 nm, 800 nm, 1200 nm, and 1600 nm, which were 24.0°, 11.7°, 7.8°, and 5.8°, respectively. For the generation of PR nanohole patterns, the substrate was double-exposed to UV with a degree of sample rotation (0°, 90°) for 10s each. The substrate was baked at 115°C for 120s (post-exposure baking), and the unexposed photoresist was removed by the developer, followed by washing with DI water. The substrate was subjected to oxygen plasma treatment to remove PR residues on the surface (140W, 50sccm of O_2) for 2 min and further baked at 135°C for a minute prior to the metal deposition.

Generation of homogeneous graphene-Au hybrid nanoelectrode arrays

On the nanohole array, 5 nm of chromium (Cr) and 100 nm of gold (Au) were deposited by physical vapor deposition (PVD) and PR is sequentially removed by stripper (AZ 400) to obtain homogeneous Au nanoelectrode arrays (NEAs) with controlled size (pitch: 400, 800, 1200 and 1600 nm, respectively). Graphene oxide was synthesized by a modified Hummers method with a pre-oxidation step: 1.0 g of graphite, 2.5 g of potassium persulfate ($K_2S_2O_8$) and 2.5 g of phosphorus pentoxide (P_2O_5) were carefully added into 12 mL of sulfuric acid (H_2SO_4) solution at 80 °C and stirred for 7 h to achieve pre-oxidized graphite. The pre-oxidized graphite was vigorously washed, filtered and dried to obtain a purified powder. The powder was then slowly added to 12.0 mL of sulfuric acid (H_2SO_4) together with 15 g of potassium permanganate (KMnO4) while stirring at 35 °C for 3 h. After 250 mL of distilled water (DIW) was added to the solution and stirred for additional 2 h and 700 mL of DIW and 20 mL 30% hydrogen peroxide (H_2O_2) was added to finalize the reactions, resulting in a bright yellow color. To remove multi-layered graphene oxide (GO), the solution containing GO flakes was filtered with 0.2 μm filter, ultrasonicated (Brandson, Inc) for 2h, then centrifuged at 10000 rpm for 45 minutes and the supernatant was collected as the final product. GO was further encapsulated on the surface of Au NEAs through electrostatic interaction between the positively charged amine surface of Au nanodot and the negative charged GO. 10 mM cysteamine hydrochloride ($HSCH_2CH_2NH_2 \cdot HCl$) was then incubated for 24 h at 25 °C to obtain positively charged surface, followed by 3 washes with DIW. GO

was ultrasonicated for 1 h and centrifuged for 20 min at 13,200 rpm to achieve single-layered GO with small size prior to use. 0.3 mg/ml of GO solution was then applied to Au NEAs and incubated for 6 h, followed by another 3 washes with DIW. Finally, diluted hydrazine monohydrate ($NH_2NH_2 \cdot H_2O$) solution (dilution factor 1:1000) was applied to the GO coated Au NEAs and kept for 12 h at 80 $^{\circ}$C to obtain the chemically reduced graphene-Au hybrid NEAs.

Substrate Characterization

The PR nanohole pattern, Au NEAs, and Graphene-Au hybrid NEAs were imaged by scanning electron microscopy (SEM, GENESIS-1000, Emcrafts, South Korea) or field emission SEM (FE-SEM, SIGMA, Zeiss, Germany). Briefly, for the PR nanohole pattern, gold was sputtered with a thickness of approximately 15 nm by using ion coater (KIC-1A, COXEM, South Korea). The acceleration voltages used for imaging were 20kV for SEM and 5kV for FE-SEM, respectively. Additionally, Raman spectra and mapping image were obtained to confirm the rGO coating on the Au NEAs using a Renishaw inVia Raman microscope (1200gr/mm @633nm) by averaging signals which were collected for three times to achieve statically relevant data. A blank spectrum was acquired prior to each step, which allowed the absorbance to be subsequently measured. (Error bars represent mean ±s.d.; n=3)

Cell Culture and Differentiation

Human mesenchymal stem cells (hMSCs) (American CryoStem) were maintained in Alpha MEM (L-Glutamine) supplemented with 10% SCM141 (PLTMax Human Platelet Lysate), 30mg of Heparin Sodium Salt and 1% penicillin/streptomycin (P/S) (Gibco). Cell cultures were incubated at 37°C and equilibrated in 5% CO2 and air. To differentiate cells, cell culture dish was coated with fibronectin (0.65 μg/cm^2) dissolved in Hank's buffered salt solution (HBSS) in the incubator for 1 h. Approximately, 4.0 × 104 of hMSCs were seeded in the 24 well cell culture dish containing the pre-sterilized 1 × 1 cm^2 graphene-Au hybrid NEAs (2.0 × 104 cells/cm^2). After 1 day of cultivation to promote cell attachment and spreading, the growth medium was changed to

osteogenic medium (OM), DMEM containing 10% FBS, 100 nM dexamethasone, 200 μM ascorbic acid and 10 mM β-glycerolphosphate to induce osteogenic differentiation of hMSCs. After, the medium was changed every 3 4 days during the differentiation. For consistency, all experiments were carried out on cells between passages 2 to 8.

Immunocytochemistry

For actin staining of hMSCs, cells were washed with DPBS (pH 7.4) and fixed with 4% formaldehyde solution for 10 min at room temperature (RT), followed by washing three times with DPBS. Then, cells were permeabilized with 0.1% Triton X-100 in PBS for 10 minutes, and non-specific binding was blocked with 5% normal goat serum (NGS, Life Technologies) in PBS for 1 hour at room temperature. The nucleus was stained with Hoechst (3 μg/mL, Life Technologies) and actin was stained with Alexa Fluor 633-Phalloidin (1:100 dilution, Sigma-Aldrich) containing the solution for 20 min at RT and then washed with PBS three times. To study the extent of osteogenic differentiation, the cells were fixed as described above, and the primary rabbit antibody against osteocalcin (1:100 dilution, Sigma-Aldrich) was used. Following the manufacturer's protocol, the fixed samples were incubated overnight at 4°C in a solution of this antibody in PBS containing 10% NGS. After washing three times with PBS, the samples were incubated for 1 hr at room temperature in a solution of anti-rabbit secondary antibody labeled with Alexa Flour 546 (1:100, Life Technologies) and Hoechst (3 μg/mL, Life Technologies) in PBS containing 10% NGS. After washing three times, all the samples were imaged using the Nikon T2500 inverted fluorescence microscope with 10X objectives (imaging area: 1,320 $\times$ 1,320 μm^2).

Alkaline Phosphatase Assay

Alkaline phosphatase (ALP), an enzyme expressed by cells, is a marker of osteogenic differentiation. Cells were assayed for ALP at the approximated midpoint in differentiation (D7). Briefly, media was removed, and 100 μL of cell lysis buffer (Sigma) was added to each chamber. Plates were incubated with shaking for 40 min, followed by addition of 100 μL of p-nitrophenyl phosphate (PNPP) to each chamber. After 30 min

of incubation in the dark at room temperature, 50 μL of 3 M NaOH was added to stop the reaction. Absorbance was measured at 405 nm using Infinite 200 PRO microplate reader (Tecan, Switzerland). In addition, to confirm that whether the expression level of ALP can be utilized as monitoring agent, cell destructive alkaline phosphatase assay based on PNPP was conducted with cell lysates sample collected through 3 weeks during the osteogenic differentiation and verified the sequential increment in its activity (expression). (Error bars represent mean $\pm$s.d.; n=3, *p <0.05, **p<0.001 by one-way ANOVA with Tukey post-hoc test.)

qPCR Real-time quantitative RT-PCR

Total RNA was extracted with TRIzol reagent (Invitrogen) and was reverse transcribed to cDNA with Superscript III Reverse Transcriptase (Invitrogen). Conventional quantitative RT-PCR was performed using an SYBR Green PCR Master Mix (Applied Biosystems) on a StepOnePlus Real-time PCR System (Applied Biosystems), and the resulting Ct values were normalized to GAPDH. Standard cycling conditions were used for all reactions with a melting temperature of 60°C. The primer sequence for the genes which were analyzed are included in the Supplemental Information. (Error bars represent mean $\pm$s.d.; n=3)

Alizarin Red S Assays

For Alizarin Red S assay, cells were washed with DPBS (pH 7.4) and fixed with 4% formaldehyde solution for 10 min at RT, followed by washing three times with DPBS. After cell fixation, the Alizarin Red solution (40 mM, pH 4.2) was added to each well and kept for 30 min with gentle shaking. Note that since pH is critical for calcium staining, the pH of Alizarin Red solution was carefully adjusted using pH meter (Accumet Basic, AB15, Fisher Scientific). The solution was removed, and cells are washed with DI water 3 times. To achieve quantitative results, cells were destained using 10% cetylpyridinium chloride (CPC) in 10 mM sodium phosphate (pH 7.0) solution for 30 min at RT. Finally, Alizarin Red S concentration was determined by absorbance measurement at 562 nm using Infinite 200 PRO microplate reader (Tecan, Switzerland). (Error bars represent

mean ±s.d.; n=3, *p <0.05, **p<0.001 by one-way ANOVA with Tukey post-hoc test.)

Cell Viability Test

Prior to induction of osteogenic differentiation, hMSCs were incubated with different concentrations of PAPP solutions (ranging from 1 μM to 10 mM) for 40 minutes, and the cell viability was determined by PrestoBlue assay. More than 95% of cells were viable even at a 200 μM concentration of PAPP, and only a slight decrement (ca. 90 %) showed from 400 μM of PAPP, showing that the effect of PAPP on cell viability was negligible. However, to avoid any adverse responses on cells, 200 μM of PAPP was used for the further experiments. (Error bars represent mean ±s.d.; n=3)

Electrochemical Measurement

On the Graphene-Au hybrid NEAs 400 cultured with hMSCs, 1 mM of P-aminophenyl phosphate (PAPP) dissolved in DPBS was treated for 30 min prior to the electrochemical detection. Electrochemical detection was carried out with an EC Epsilon Potentiostat (Basi, IN, USA). A fabricated electrode served as the working electrode, and an Ag/AgCl and a Pt wire served as the reference and counter electrode, respectively. Cyclic voltammetry (CV) is performed with the potential range (vs. Ag/AgCl) of 0.5 V and -0.3 V at 50 mV/s. Applied potential was settled to oxidation peak potential of electroactive p-aminophenol (PAP) resulted from enzymatic reaction resulting from the PAPP and ALP. (Error bars represent mean ±s.d.; n=3)

Density Functional Theory (DFT) Simulation

Density Functional Theory (DFT) method (B3LYP) using 6-31+G (d,p) was performed to obtain energy levels of PAP molecule. The molecule was first optimized (predicted energy change = -3.5036 E^{-07} Ha) before calculating its highest occupied molecular orbital (HOMO) and lowest unoccupied molecular orbital (LUMO). HOMO and LUMO were estimated to be -0.17702 and 0.00753 Ha, which correspond to -4.8169 eV and 0.2049 eV, respectively. The molecular coordination for the optimized PAP molecule is attached, Table 4.1.

Table 4.1: Molecular Coordination for the Optimized PAP Molecule

Center Number	Atomic Number	Atomic Type	Coordinates (Angstroms)		
			x	y	z
1	8	0	-2.408946	-1.458736	0.000000
2	7	0	2.435815	1.376561	0.000000
3	6	0	1.225497	0.693087	0.000000
4	6	0	0.000000	1.387038	0.000000
5	6	0	1.191636	-0.717993	0.000000
6	6	0	-1.228957	-0.702350	0.000000
7	6	0	-1.214902	0.695091	0.000000
8	6	0	-0.020265	-1.405931	0.000000
9	1	0	-0.002948	2.473417	0.000000
10	1	0	2.124026	-1.275714	0.000000
11	1	0	-2.147569	1.254230	0.000000
12	1	0	-0.046505	-2.489447	0.000000
13	1	0	3.309332	0.880790	0.000000
14	1	0	2.463880	2.380525	0.000000
15	1	0	-3.197411	-0.883492	0.000000

4.3 Real-time Indirect Monitoring of Stem Cell Differentiation through Exosomal miRNA detection

4.3.1 Introduction

Overcoming the current destructive characterization methods for monitoring stem cell differentiation into a specific lineage is critical for the full realization of efficient stem cell treatment. Recently, exosome has emerged as a promising biomarker owing to the molecular constituents, which represents their cells of origin, thereby offering a non-destructive avenue for molecular analyses. Here, we report a multifunctional nanorod (NR) platform consists of: i) immuno-magnetic extraction and concentration of exosome through the selectively functionalized nickel component and ii) metal-enhanced fluorescence-based sensitive exosomal microRNA (miRNA) analysis through rationally designed gold component. Our multifunctional NR successfully monitored the neuronal differentiation of human-induced pluripotent stem cell-derived neuro-progenitor cells (hiPSC-NPC) by tracking the expression level of exosomal miRNA-124 (miR-124) in a non-destructive, real-time efficient manner. Furthermore, our system offers a full range of versatility with interchangeable target specific molecular beacons and antibodies as demonstrated using brain tissue explants. We believe that our multifunctional magnetic-gold NRs based exosome monitoring platform is particularly valuable to advance stem cell-based therapies.

Stem cell therapy has emerged as a promising method in the field of biomedicine owing to their unique ability to differentiate into multiple cell lineages [346–348]. For instance, stem cell-based approaches hold great potential in treating neurodegenerative diseases and injuries which can not only lead to functional deficits such as sensation loss, memory failure but also threaten the patient's life [1,349–351]. Although cell transplantation therapies have shown promising functional recovery in animal models [352–354], the lack of precise characterization method to monitor stem cell differentiation in a non-destructive manner while maintaining high cell viability has limited the feasibility of these therapies [303,346,355,356]. Mainly, conventional methods such as polymerase chain reaction (PCR), immunostaining, fluorescence assisted cell sorting (FACS) or

western blot, commonly used for characterizing nucleotide (DNA and RNAs) and protein expression levels, require destructive steps such as cell fixation of cell lysis. Despite their highly sensitive and effect nature, conventional characterization methods prevent the subsequent therapeutic applications of the differentiated stem cells [312,316]. Thus the urgency to develop a non-destructive tool that can distinguish differentiated cells from undifferentiated population to advance stem cell therapy is clear [299, 301–303].

Exosomes, actively secreted by mammalian cells, have emerged as a promising biomarker [357–360] for clinical application such as cancer diagnostics. These membrane-bound phospholipid nanovesicles (approximately, 50-100 nm in diameter) are stable and comprised of unique molecules (including proteins and nucleic acids) reflecting their cells of origin. Furthermore, exosome also carries different forms of nucleic acids (e.g., RNA and DNA). Notably, recent evidence suggested the importance of the small non-coding RNAs, microRNAs (miRNAs) (approximately, 76% of total oligonucleotides) as a posttranscriptional gene regulator, which are involved in the determination of cell identities and subtype specification [361,362]. Therefore, analyzing exosomal molecules is an excellent approach for monitoring cellular behaviors and characteristics in a non-destructive, real-time manner [357]. However, despite such clinical potential, current exosome collection process requires large sample volume and specialized tools (ultrahigh centrifuge with 100K and specific filtration membrane) to compensate for weak signals and poor isolation efficiency. These various drawbacks have severely hampered the full realization of a comprehensive exosome-based biomolecular diagnostic system [363–365].

4.3.2 Results and Discussion

Addressing the challenges above, we developed a novel real-time nondestructive platform to characterize exosomes and monitor stem cell differentiation by incorporating multifunctional magnetic-gold NRs [Figure 4.9].

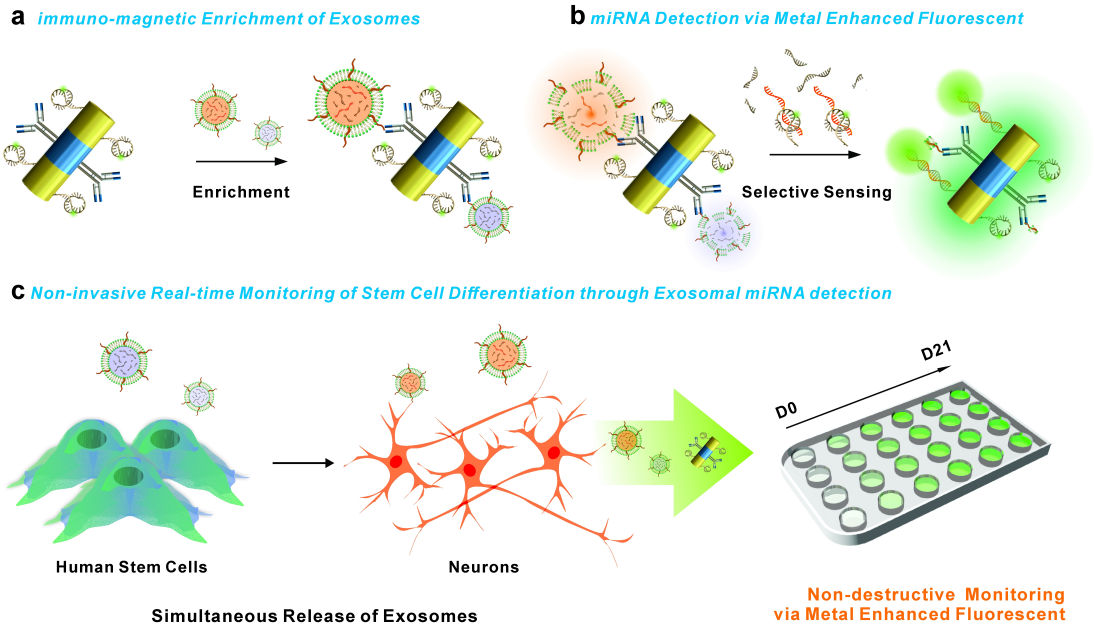

Figure 4.9: Schematic diagram illustrating the non-invasive real-time monitoring of stem cell differentiation through exosomal miRNA detection. Multifunctional magnetic-gold nanorods are utilized to a) extract and concentrate exosomes immuno-magnetically, b) analyze exosomal miRNA sensitively via metal enhanced fluorescence effect, and c) monitor stem cell differentiation non-destructively. (Unpublished)

We synthesized homogeneous magnetic-gold NRs with a high throughput fabrication method utilizing anodized aluminum oxide (AAO) as a template. With rational design, the magnetic (nickel, Ni) component in the middle of the NR selectively captures and extracts exosomes through attached antibody [Figure 4.9a] while the plasmonic (gold, Au) components at both ends of the NR recognize target miRNA through molecular beacon (MB, oligonucleotides) and amplify fluorescence signal through metal-enhanced fluorescence effect (MEF) [Figure 4.9b]. Taking advantage of the unique physical and optical property of each component, the non-destructive real-time monitoring of stem cell differentiation is possible [Figure 4.9c]. During the stem cell differentiation process, exomes can be immuno-magnetically collected from the host allowing a significant increase in the concentration of analytes. Sequentially, at the surface of the multifunctional NRs, the captured exosomes would be lysed to give rise to target miRNA and MB hybridization which results in the strong fluorescence signal from tagged fluorophore via metal enhanced fluorescent effect. In our proof-of-concept demonstration,

we characterize neuronal differentiation of Human induced pluripotent stem cell-derived neuro-progenitor cells (hiPSC-NPC) using our novel multicomponent NR platform to monitor miRNA-124 (miR-124) signal for potential neurodegenerative diseases and injuries treatment.

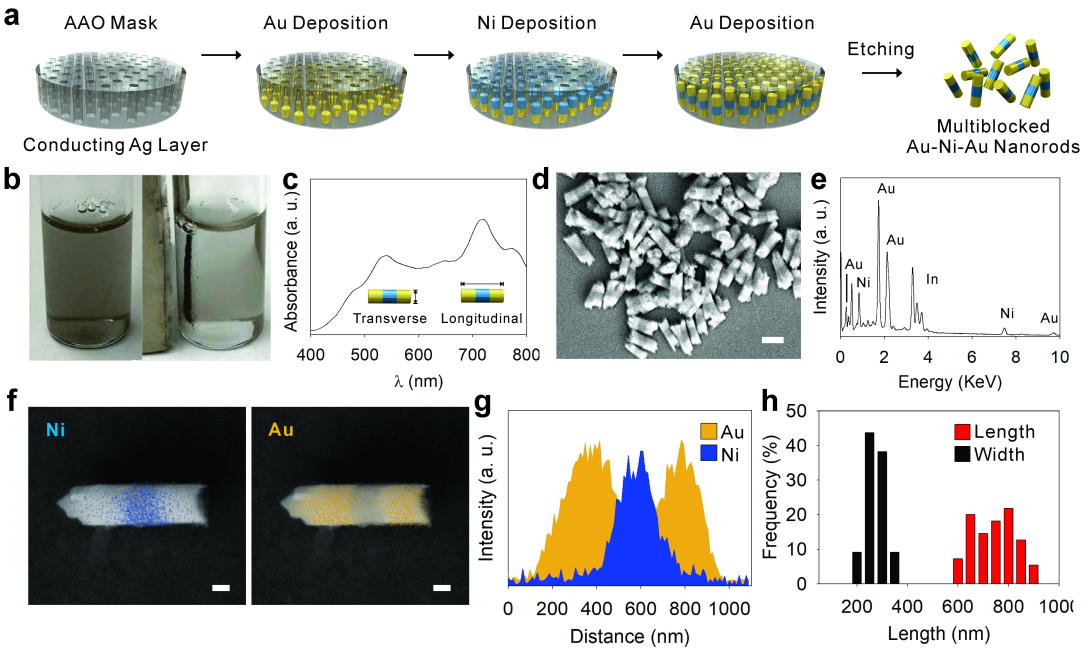

Figure 4.10: Generation and characterization of multicomponent magnetic-gold nanorods. a) Schematic illustration of sequential steps to generate multicomponent magnetic-gold NRs using electrochemical deposition method on an anodized aluminum oxide (AAO) template. b) Optical image of magnetophoretic separation property of multicomponent magnetic-gold NRs. c) Corresponding UV-Vis-NIR absorption spectrum of multicomponent magnetic-gold NRs. d) Representative SEM image of multicomponent magnetic-gold NRs. (scale bar: 200 nm) e) Energy-dispersive X-ray spectroscopy spectrum (EDS) and relative atomic percentages of as-prepared multicomponent magnetic-gold NRs. f) Representative SEM images of single multicomponent magnetic-gold NR and corresponding EDS element mappings. (Scale bar: 100 nm) g) EDS elemental line profiles of multicomponent magnetic-gold NRs. h) Size distributions of multicomponent magnetic-gold NRs. (Unpublished)

As presented in Figure 4.10a, the homogeneous multicomponent magnetic-gold NRs were synthesized by potentiostatic electrochemical deposition through the utilization of anodized aluminum oxide (AnodiscTM 13, pore size 0.2 μm, Whatman) as a template. The template pore size determined the diameter of the multicomponent magnetic-gold

NRs. We also tailored the length of each component (Au and Ni) blocks by adjusting the total charge applied to the electrochemical cell during the deposition process. We rationally designed the Au-Ni-Au triblock structure by placing Au components on both ends of the Ni component to protect the Ni component from degradation due to the etching process. By dissolving the AAO template, homogeneous multicomponent magnetic-gold NRs were obtained in the solution, and both physical and optical properties of these magnetic-gold NRs were characterized. By applying an external magnetic field, synthesized colloidal multicomponent magnetic-gold NRs were able to be isolated in the solution due to the ferromagnetic property of Ni components [Figure 4.10b]. Additionally, owing to the unique optical property of Au, we were able to observe two absorption bands from visible to near-infrared (NIR) region reflecting both transversally (approximately, 540 nm) and longitudinally (approximately, 720 nm) localized surface plasmon resonances of rod-shaped multicomponent NRs [Figure 4.10c]. As demonstrated, the multicomponent magnetic-gold NRs are a unique hybrid nanomaterial having independent magnetic and optical properties.

To further examine as-prepared multicomponent magnetic-gold NRs, field emission scanning electron microscopy (FE-SEM) measurement was carried out. Representative SEM images show the combined structural morphology of NRs with two different components clearly [Figure 4.10d]. Peaks corresponding to Au and Ni atoms were also presented in the energy dispersive X-ray spectrum (EDS) of the multicomponent magnetic-gold NRs [Figure 4.10e], proving that the resulting NRs is bimetallic (Au and Ni) multicomponent structure. Furthermore, an SEM image of single multicomponent magnetic-gold NRs and the corresponding elemental maps of Au and Ni indicates the apparent distribution of two different Au and Ni elements as separate blocks in a single NR [Figure 4.10f]. Supportably, the compositional line profile was also consistent with elemental maps in a distribution [Figure 4.10g]. We further characterized 55 randomly selected multicomponent magnetic-gold NRs in the SEM images to analyze their size and homogeneity statistically. The average sizes of the resulting multicomponent magnetic-gold NRs are found to be ca. 267.35 $\pm$ 23.78 nm in diameter and ca. 745.31 $\pm$ 89.09 nm in length with aspect (ratio of length/width) ratios ca. 3 divided by ca.

250 nm for Au on both edges and ca. 250 nm for Ni on the center, respectively [Figure 4.10h]. Note that the size of magnetic-gold NRs was carefully designed to be larger than exosome (30 100 nm) for exosome extraction and concentration. Furthermore, the aspect ratio of Ni block was also designed to be less than 1 to prove the possibility of SPR coupling between two gold side blocks for selective excitation [366].

On the surface of ferromagnetic Ni block of the prepared magnetic-gold NRs, we functionalized antibody against CD63, a type III lysosomal membrane protein enriched in exosomes, using the carboxyl group to target and magnetically extract and concentrate extracellular vesicles including exosomes [359, 360]. On the other hand, specially designed oligonucleotide strand, molecular beacon (MB), was separately functionalized onto the Au blocks through gold-thiol interaction to analyze miRNA expression [367]. In this study, MB was designed to target miR-124 as a proof-of-concept to monitor neuronal differentiation of stem cell in a non-destructive real-time manner. miR-124 has been well documented to expressed at low levels in the stem cells (including progenitor cells) and highly upregulated during neuronal differentiation and mature neurons [368], which demonstrates the potential as a marker to distinguish the neuronal differentiation of stem cells. Taking full advantage of the plasmonic gold nanostructure has on fluorophores such as quenching the fluorescence signal (<5 nm metal-fluorophore separation) and enhancing the fluorescence signal (between 5 nm to 15 nm metal-fluorophore separation) through metal-enhanced fluorescence (MEF) [369, 370], we carefully designed MB (length of complementary strands approximately between 5 to 15 nm) to control the leading phenomena between quenching and enhancement of fluorescence signal. The designed neuron-detecting, miR-124-specific MB had a hairpin structure with a 6-carboxyfluorescein (FAM) at 5'-end terminus and a thiol group at the 3'-end terminus. This design promoted the covalent bonding of miR-128 MB to the surface of Au regions of the multicomponent NRs via gold-thiol interaction. Without the presence of a complementary sequence, the fluorescence signal of FAM would be quenched by the gold surface due to the hairpin conformation of miR-124 (<5nm). However, with the presence of a targeted commentary sequence, miR-124 hairpin structure would unfold

and open. As a result, FAM extends away from the Au blocks with optimal distance (approximately between 5 to 15 nm) to enhance fluorescence signal through the existence of plasmonic Au block [Figure 4.11a]. Owing to the broad absorption band (transverse and longitude) from our multicomponent NRs, wide range of fluorophores in different wavelength from visible to NIR region can be incorportated to achieve metal enhance fluorescence effect; however, FAM was carefully selected as fluorophore to match the emission band of the fluorophore (approximately, 520 nm) with the transverse plasmon absorption of magnetic-gold NRs (approximately, 540 nm) for our demonstration [371].

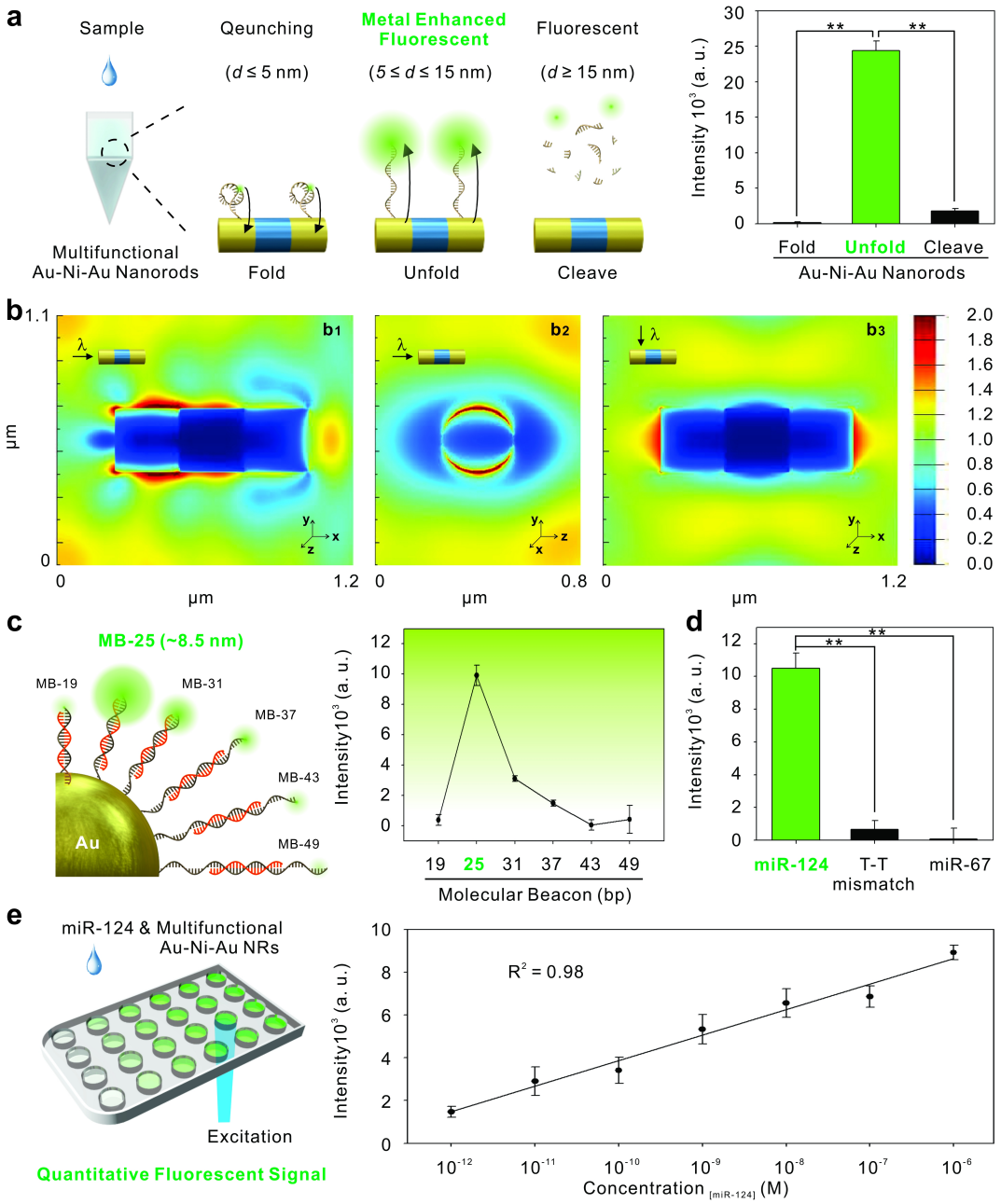

Figure 4.11: Surface functionalization of multicomponent magnetic-gold nanorods for miRNA detection. a) Schematic illustration of fluorescence intensities from quenched, metal enhanced fluorescence, and free fluorescence respective to the folded, unfolded, and cleaved MB from the Au surface of nanorods. b) Side (b2) and top view (b1, and b3) of EM field intensity ($<|E|^2>$) of multicomponent magnetic-gold nanorods under three-dimensional finite-difference-time-domain simulation using 490 nm wavelength light. c) Schematic illustration and calculated fluorescence signal intensities based on different lengths (bps) of molecular beacons. d) Fluorescence signal value obtained from positive complementary miR-124 DNA sequence, T-T single mismatched synthetic DNA sequence, and mature miRNA67 DNA sequence (negative target) using a solution assay. e) The linear correlations between concentrations (range from 1 pM to 1μM) of miRNA-124 and observed fluorescence signals. (The error bars represent mean $\pm$ s.d.; n = 3, **p<0.001 by one-way ANOVA with Tukey post hoc test.) (Unpublished)

We quantified the readings from 3 different conditions (folded MB, unfolded MB, and cleaved MB) to verify the ability of our MB functionalized magnetic-gold NRs to both quench and enhance fluorescence signal [Figure 4.11a]. As expected, we obtained no observable fluorescence signal from the folded MB on the magnetic-gold NR sample at room temperature due fluorescence quenching. Contrarily, clear and strong fluorescence signal at 520 nm was observed when MB strand was unfolded at 65 $^{\circ}$C for 30 min; however, relatively weak fluorescence signal (approximately, 1/15 fold less) was observed when MB was cleaved by the addition of exonuclease I (ExoI). Note that the melting temperature of a hairpin structure of molecular beacon was calculated to be 56.7 $^{\circ}$C based on the stem-loop of six pairs of G-C and two pairs of A-T. These results clearly demonstrated the MEF effect could be obtained by our miRNA sensing system based on magnetic-gold NRs. To help us optimize the fluorescence signal amplifications through multicomponent magnetic-gold NRs, we also conducted electromagnetic (EM) simulation [Figure 4.11b]. In the EM simulation, we defined the dimensions of our multicomponent magnetic-gold NRs from the measurements obtained through SEM analysis [Figure 4.10h]. Furthermore, the local electric field enhancement ($|E|/|E_0|$) from the ratio of near-field ($|E|$) and the incident field ($|E_0|$) was calculated. The EM field distribution images indicated that when multicomponent magnetic-gold NRs were exposed with incident light (□: 490 nm) in either direction, longitude [Figure 4.11b1 and 4.11b2] or transverse [Figure 4.11b3], the local electric field enhancement significantly increased around the Au blocks. We also tested different lengths of MBs to optimize the fluorescence signal enhancement by modulating the number of base pairs (bps) (range from 19 to 49 bps, which corresponds to approximately, 6.5 to 16.7 nm in length). As shown in Figure 4.11c, MB-25 (approximately, 8.5 nm in a length) showed the strongest fluorescence signal due to metal enhancement. As expected, the fluorescence signal was quenched for the shorter MBs. On the other hand, the fluorescence signals were also significantly reduced with the increase of MB length as the metal enhancement effect diminished. Moreover, we also examined the specificity of synthesized miR-124-targeting MB by quantifying fluorescence signals while treating with positive complementary miR-124 DNA sequence, T-T single mismatched synthetic DNA sequence, and mature

miRNA-67 (miR-67) DNA sequence (a negative target) using a solution assay. Our multicomponent magnetic-Au NR system demonstrated high selectivity as strong fluorescence signal was observed when positive complementary miR-124 DNA sequence was treated; no significant signals were obtained for both T-T single mismatched and mature miR-67 DNA sequences conditions [Figure 4.11d]. In addition, our multifunctional magnetic-gold NRs based miRNA sensing system showed good linearity (R2 = 0.98) at different concentrations (range from 1 pM to 1 μM) of complementary miR-124 DNA sequence [Figure 4.11e] agreeing with previously reported highly sensitive and quantitative miRNA assays [372–374].

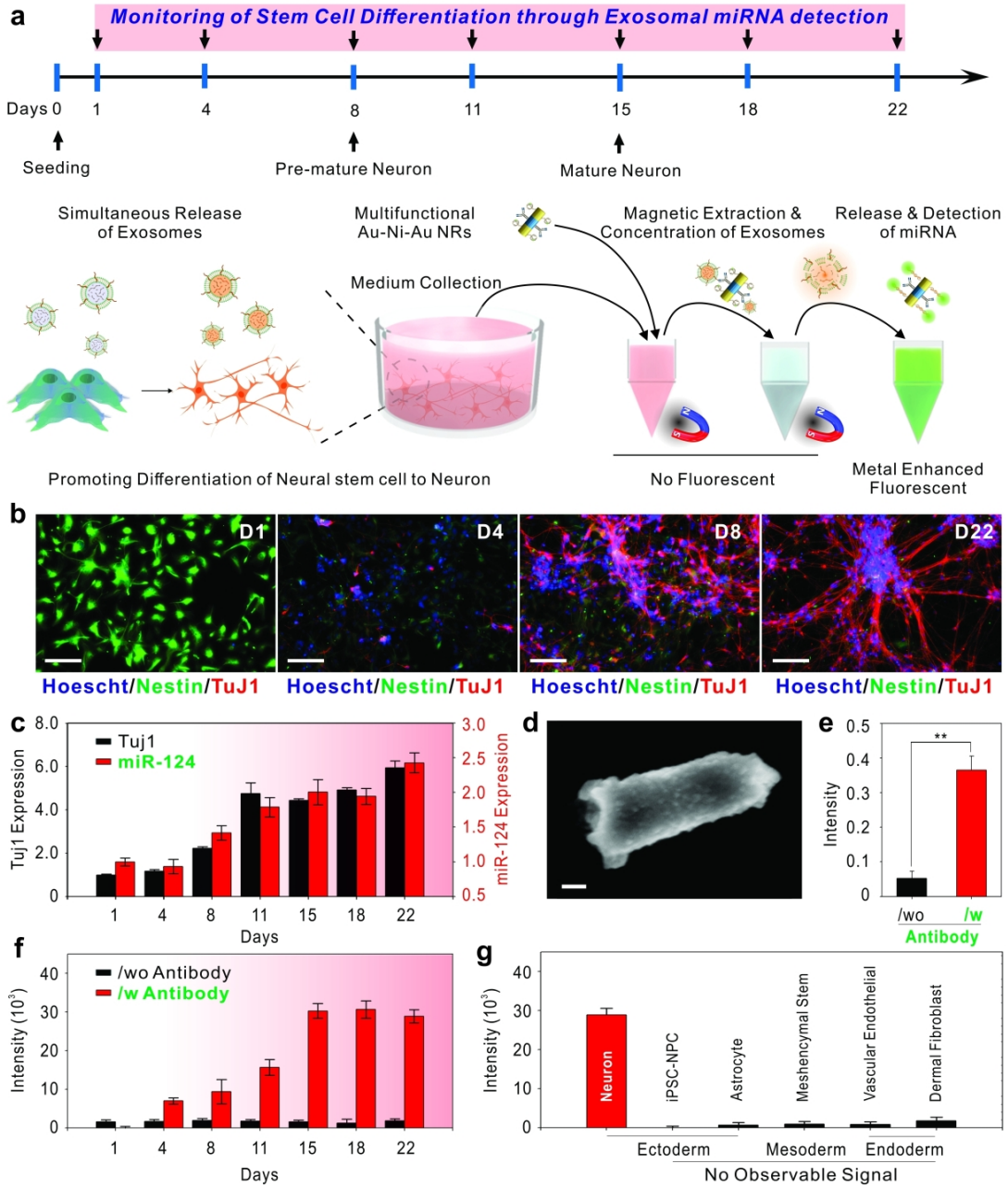

Figure 4.12: a) Schematic illustration of monitoring of stem cell differentiation through multifunctional magnetic-gold NRs. b) Representative immunocytochemistry images of hiPSC-NPCs differentiation into neurons. Nucleus (Hoechst, blue), Nestin (Alexa 488, green), and TuJ1 (647, red) (scale bar = 100 μm). c) PCR analyses of cell lysate for neuronal markers, TuJ1, and miRNA-124 expression during the neuronal differentiation period (from D1 to D22). d) Scanning electron microscope (SEM) images of captured exosomes on the multifunctional magnetic-gold NRs surface (scale bar = 100 μm). e) Absorbance intensities obtained from HRP-TMB reaction (630 nm) in the absence and presence of anti-CD63 antibody on the magnetic-gold NRs surface. f) Time-dependent fluorescence signal monitoring (from D1 to D22) of hiPSC-NPC neuronal differentiation. g) Fluorescence signals from cells of different lineages. (The error bars represent mean $\pm$ s.d.; n = 3, **p<0.001 by one-way ANOVA with Tukey post hoc test.) (Unpublished)

After verifying the miRNA sensing properties of multicomponent magnetic-gold NRs in the cell-free condition, we induced neuronal differentiation of human induced pluripotent stem cell-derived neuro-stem cells (hiPSC-NPC) (3.0×104 cells/cm^2) by withdrawing growth factors from the proliferation media [Figure 4.12a]. To verify the feasibility of using miR-124 expression as neuronal differentiation, we first confirmed the neuronal differentiation of hiPSC-NPCs through immunocytochemistry staining of Nestin and neuron-specific class III β-tubulin (TuJ1), representative markers of neuro-progenitor cells (NPCs) and differentiated neurons respectively [375, 376]. As shown in Figure 4.12b, only cells that have undergone neuronal differentiation showed clear TuJ1 expression (D8 and D22) while undifferentiated hiPSC-NPCs cells (D1 and D4) showed Nestin expression only and failed to show any significant TuJ1 expression. Additionally, we conducted reverse transcription polymerase chain reaction (RT-PCR) for differentiation period (3 weeks) and found that the expression trend of miR-124 was similar with Tuj1 mRNA expression. From time-dependent monitoring (range from D1 to D22) of hiPSC-NPC during neuronal differentiation, the expression level of miR-124 showed sequential increment and saturation as neuronal differentiation proceeded [Figure 4.12c]. Based on these results, we hypothesized that the monitoring of miR-124 expression could characterize the neuronal differentiation of hiPSC-NPC as the expression of miR-124 correlated well with neuronal marker TuJ1 expression.

Moreover, cell culture medium was collected throughout the neuronal differentiation period (22 days) of hiPSC-NSCs and mixed with functionalized magnetic-gold NRs to not only immuno-magnetically extract and concentrate exosome but also analyze miR-124 expression in a non-invasive, real-time manner [Figure 4.12a]. The capturing and concentration of exosomes by multifunctional magnetic-gold NRs were verified through two factor analysis of SEM analysis and 3, 3', 5, 5'-tetramethylbenzidine (TMB) reaction assay [359]. When functionalized magnetic-gold NRs were incubated with cell culture medium, the surface of anti-CD63 antibody labeled nickel region of magnetic-gold NRs was densely covered with cell-derived exosomes [Figure 4.12d]. In addition, TMB reaction also showed clear absorbance signal, while no observable signal was obtained from magnetic-gold NRs without functionalization of anti-CD63 antibody [Figure

4.12e]. These results supported the capturing and concentrating property of exosomes through functionalized magnetic-gold NRs. After immunomagnetic extraction of exosomes, concentrated exosomes were lysed by PBS-T buffer to release the encapsulated components including miRNAs. As shown in Figure 4.12f, no observable fluorescence signal was registered by undifferentiated hiPSC-NPCs (D1). In contrast, the clear distinct fluorescence signal begun to be prominent starting from the premature (D4) and saturated at the mature (D15) neuron formation [Figure 4.12f]. Furthermore, the result collected by our multicomponent magnetic-Au NRs agreed with the results collected by RT-PCR on the cell lysis for characterizing neuronal differentiation [Figure 4.12c]. However, without the extraction and concentration of exosomes, we did not see any observable fluorescence signal even after 3 weeks of differentiation period (from D1 to D22) representing the importance of extraction and concentration for sensitive monitoring. In addition, owing to the specificity of MB, our multifunctional magnetic-gold NRs showed the ability to discriminate neurons from other types of ectoderm cells including hiPSC-NPC and astrocyte, as well as endoderm and mesoderm cells [Figure 4.12g].

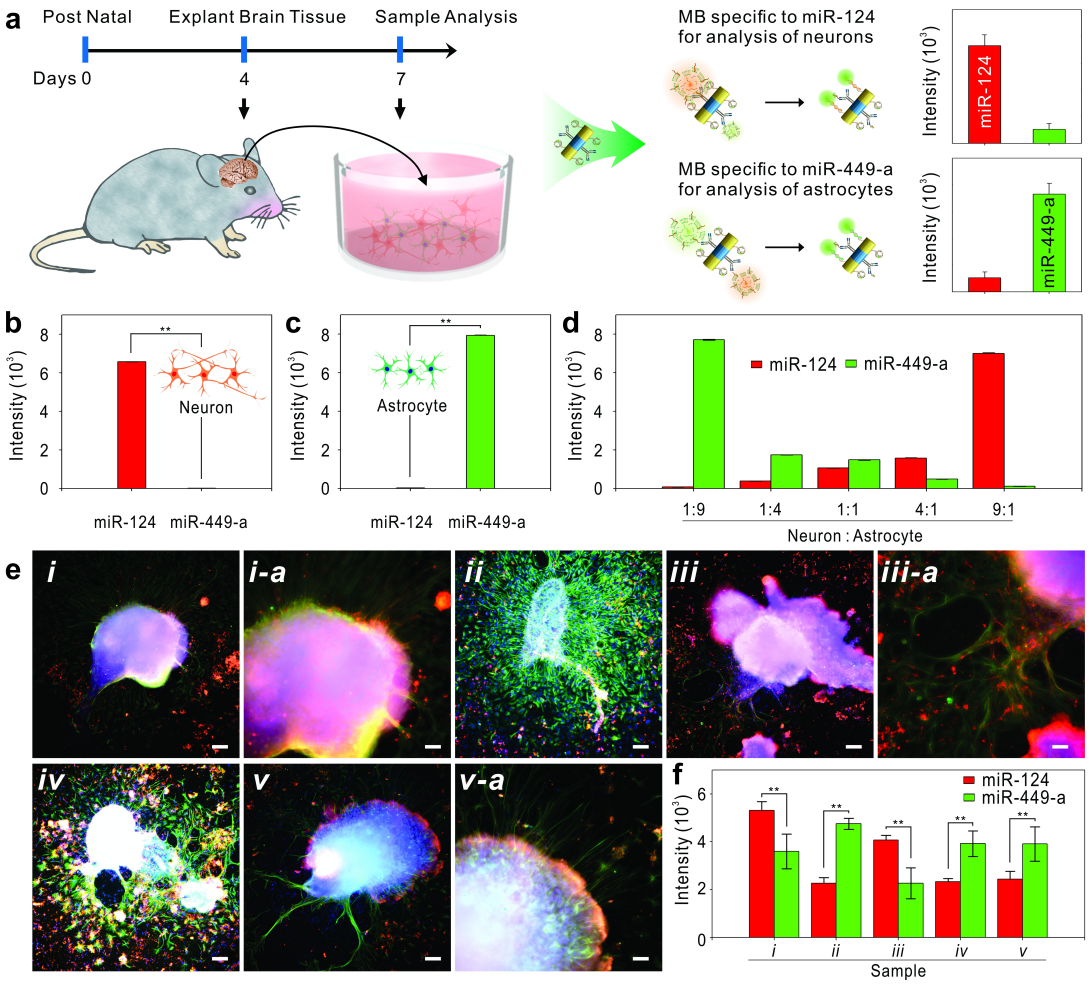

Figure 4.13: Non-destructive characterization of cell distribution in the explanted brain tissues. a) Schematic illustration of non-destructive real-time characterization of dissected brain tissues explant using multifunctional magnetic-gold NRs. (b-d) Relative fluorescence signal values from b) neuron population, c) astrocytes population, and d) neuron/astrocyte co-cultured conditions with different ratios. e) Representative immunocytochemistry staining images of brain tissue explants. Nucleus (Hoechst, blue), GFAP (Alexa 488, green), and TuJ1 (647, red) (scale bar = 100 μm) (i-v). f) Relative fluorescence signals obtained from multifunctional magnetic-gold NRs for each miRNA expression from different cross-section of brain tissue explants in e (i-v). (The error bars represent mean $\pm$ s.d.; n = 3, **p<0.001 by one-way ANOVA with Tukey post hoc test.) (Unpublished)

Owing to the modular, interchangeable targeting moieties (e.g., target specific MB and antibody) of our magnetic-gold NRs, we further demonstrated the non-destructive characterization of heterogeneous cell population through mouse brain tissue explants [Figure 4.13a]. To characterize astrocyte, miRNA-449-a (miR-449-a), which is known

to be specifically enriched in the astrocyte but diminished in neuron and oligodendrocyte, was carefully selected to recognize astrocytes [377, 378]. To characterize the cell distribution in the brain tissue, we first verified the correlation between exosomal miRNA expressions specific to neuron and astrocyte separately by using miR-124 and miR-449-a specific MB functionalized magnetic-gold NRs [Figure 4.13b and c]. As expected, neurons (2.0 × 106 cells) only showed fluorescent signal from miR-124 specific magnetic-gold NRs, and astrocytes only showed fluorescent signal with miR-449-a specific magnetic-gold NRs. In addition, we also collected ratiometric fluorescence signals among co-cultured neurons and astrocytes at various ratios [Figure 4.13d]. As shown, our magnetic-gold NRs were able to distinguish and characterize the heterogeneous populations of neurons and astrocytes by targeting miR-124 and miR-449-a.

Brain tissues were dissected from mouse (post-natal day 4), and cultured on the matrigel coated 24-well plate. After three days of cultivation, the cell culture medium was collected for analysis, and tissues were fixed with formaldehyde solution. The distribution of neurons and astrocytes were characterized through immunocytochemistry staining of neuron-specific class III β-tubulin (TuJ1) and glial fibrillary acidic protein (GFAP), representative markers of neurons and astrocytes, respectively [Figure 4.13e]. The populations of neuron and astrocyte varied from each brain tissue sample, which agreed with the glia to neuron ratio reported for rodent based on the section of the brain (such as cerebral cortex, cerebellum, and rest of brain) [379]. Our magnetic-gold NR based assay system also showed similar fluorescent signal ratio on each brain tissue samples compared to immunostaining results [Figure 4.13f]. These results demonstrate the exceptional ability of our magnetic-gold NRs to verify the distribution ratio of each cell type in real tissues in a non-destructive manner. Although these results were obtained from brain tissue explants, we believe it could be extended to real clinical settings for patients with neurodegenerative diseases and injuries as well.

4.3.3 Conclusion

In conclusion, we have successfully developed a non-invasive, real-time monitoring system for stem cell differentiation based on multifunctional magnetic-gold NRs which

integrated two functional compartments 1) targeted magnetic-extraction and concentration of extracellular vesicles through antibody labeled nickel components and 2) highly sensitive detection of miRNA expression via MEF effect through molecular beacon labeled gold components. Due to the excellent selectivity and sensitivity, the neuronal differentiation of hiPSC-NPC was successfully monitored in both non-destructive and real-time manner. We further demonstrated a potential application of our magnetic-gold NRs system by characterizing heterogeneous populations of brain tissue explants. To be even more clinically-relevant, we will further explore the versatility of multifunctional magnetic-gold NR-based miRNA analysis system such as specific neuron (i.e., dopaminergic, motor neuron, etc) detections. Moreover, by avoiding the destructive analysis process such as cell lysis and cell fixation, our multifunctional magnetic-gold NRs based detection method can bring a breakthrough in the preclinical investigation such as the transplantation of differentiated stem cells. Collectively, we believe that our multifunctional magnetic-gold NRs system will not only advance stem cell differentiation assays by providing a practical, non-destructive, real-time monitoring tool but also help to pursue the full potential of stem-cell based therapies.

4.3.4 Materials and Methods

Generation of magnetic-gold nanorod via electrodeposition

The generation method for magnetic-gold nanorods was adopted from previous reports. Briefly, a thin layer of silver (approximately, 300 nm) was evaporated on one side of the anodized aluminum oxide (AAO) template (Anodisk 13, Whatman) by physical vapor deposition as a conducting layer. By providing electrical contact with aluminum foil in the Teflon cell with Ag layer on one side of the AAO template, AAO template was served as a working electrode in an electrochemical setup. In addition, an Ag/AgCl and a Pt wire served as the reference and counter electrode to form a three-electrode configuration. To block the irregular branch part of AAO nanopores, Ag was pre-deposited into AAO by commercial plating solution at -0.95 V (vs Ag/AgCl). In order to fabricate the magnetic-gold nanorods, approximately 250 nm of both Au, Ni and Au

are sequentially deposited by a commercial plating solution at -0.95 V (vs Ag/AgCl). The desired configuration and length of each block of nanorod were controlled by the type of plating solution selected and the depositing coulomb value applied. Specifically, ca. 0.07 coulombs was needed for the growth of 250 nm block of Au and ca. 0.20 coulombs was needed for the growth of 250 nm block of Ni. The Ag layer were etched out with 4:1:1 ratio mixture of methanol (CH_3OH), hydrogen peroxide (H_2O_2) (30% vol/vol) and ammonium hydroxide (NH_4OH) (28% in H_2O), respectively[3]. The AAO template was then completely removed by 3 M NaOH for 50 min. The resulting samples were rinsed with distilled water and visualized with a field emission scanning electron microscope (FE-SEM, SIGMA, Zeiss, Germany).

Preparation of Multifunctional magnetic-gold Nanorods

Each component of magnetic-gold NRs was functionalized with a molecular beacon (MB) against miR-124 and antibody against CD63, respectively. First, pre-synthesized magnetic-gold NRs were washed with phosphate buffered saline (PBS) three times using centrifugation (centrifuge 5415R; Eppendorf, Germany). To specifically functionalize Au side only, magnetic-gold NRs were incubated with thiol group functionalized MB (final concentration 10 μM) and 1,4-dithiothreitol ($C_4H_{10}O_2S_2$, DTT) (final concentration 100 μM) for 8 h at 4°C to promote covalent bonding between Au and thiol. After functionalizing Au block, magnetic-gold NRs were washed with PBS for three times and incubated with the anti-CD63 antibody (final concentration range from 10 μg/mL) to function Ni block as well. After an 8 h incubation period at 4°C, 3 % bovine serum albumin (BSA) was added to the mixed solution to stabilize the multifunctional magnetic-gold NRs.

Fluorescence measurements and experimental setup

Anti-CD63 antibody and FAM tagged miR-124 targeting MB modified magnetic-gold NRs (20 mg/ml) were mixed with cell culture medium (1 mL) which are obtained during neuronal differentiation of hiPSC-NPC. After 30 min, magnetic-gold NRs were isolated under magnetic field (BioMag , Polyscience Inc) and re-suspend in a transparent 96

well plate with phosphate buffered saline with 0.1% Tween 20 (PBS-T) (100 μL). The fluorescence spectra were recorded for the excitation 490 nm and emission 520 nm at 25 $^{\circ}$C using a 96 well plate reader (Infinite M200pro, TECAN Group, Ltd., Switzerland).

Density Functional Theory (DFT) simulation

To study the metal-enhanced fluorescence surrounding the magnetic-gold NRs, electromagnetic field enhancement surrounding the magnetic-gold NRs were simulated and calculated using a Finite Difference Time Domain (FDTD) package provided by Lumerical . To match the fluorescence excitation wavelength, a plane wave light source model with a single wavelength of 490 nm were introduced. Magnetic-gold NRs with a diameter of 278 nm and heights of 248 nm, 250 nm and 248 nm for each section was used to be consistent with the nanorods we synthesized. Re (index) and Im (index) were used from the materials library without further modifications. To simulate light from different directions, two models were calculated: one model with light source vertical to the longitudinal axis of NR; and the other model with light source horizontal to the longitudinal axis of the NR. In the vertical model, the light source was placed at 400 nm on top of the NR while the horizontal model the distance is kept at a distance of 500 nm. Mesh size of 4 nm was utilized for all simulations and the media surrounding the nanorods were set as a vacuum. Monitors were set at different locations of NR with fixed wavelengths of 490 nm. The electromagnetic field were calculated and plotted in the heat map of log (E/E_0) and summarized in Figure 4.11b.

Cell Culture and Differentiation

The Human induced pluripotent stem cell-derived neuro-progenitor cells (hiPSC-NPC) (UCSD) were maintained in mixture of neural basal medium (Gibco) and DMEM/F12 (Gibco) (50:50 ratio) supplemented with 0.5 % N2 (Gibco), 0.5 % B27, and 20 ng/mL FGF basic (Fibroblast growth factor-basic, PeproTech) respectively. All cells were maintained at 37°C in a humidified incubator with 5% CO_2. To differentiate cells, hiPSC-NPCs were seeded on matrigel (Life Technologies) pre-coated plates (300,000 cells/well for 6-well plate) 24 hr prior to experimentation. After 1 days of cultivation

to promote cell attachment and spreading, the fresh hiPSC-NPC media without FGF basic (differentiation media) was treated to stop proliferation and induce neuronal differentiation. The medium was changed with fresh differentiation media every 3 4 days during the differentiation. For consistency, all experiments were carried out on cells between 3 passage differences. Human mesenchymal stem cells (hMSCs) (American CryoStem) were maintained in Alpha MEM (L-Glutamine) supplemented with 10% SCM141 (PLTMax Human Platelet Lysate), 30mg of Heparin Sodium Salt and 1% penicillin/streptomycin (P/S) (Gibco). The human cerebral microvascular endothelial cell (hCMEC) were cultured in the human endothelial cell culture medium (Cell Applications, Inc.) supplemented with 5% FBS, penicillin (100 units/ml), and streptomycin (100 μg/ml), 1.4 μM of hydrocortisone, 5 μg/ml of ascorbic acid, 10 mM of HEPES, and 1 ng/ml of Basic fibroblast growth factor (bFGF). The Astrocyte were maintained in the astrocyte culture medium (Sciencell) with 10% FBS and penicillin (100 units/ml), and streptomycin (100 μg/ml). The human dermal fibroblast were cultivated in the fibroblast growth medium (Cell Applications, Inc.). For the collection of exosome from each of the cell lines, 3×10^6 cells were seeded in 6-well plate and each media were collected after 3 days from the seeding. ReNCells (human neural progenitor cell line) were obtained from Merck and maintained in DMEM/F12 (Gibco) supplemented with 1% L-glutamine (200 nM, Invitrogen), 2% B27, and 20 ng/ml heparin (Sigma-Aldrich), gentamycin (10 μg/ml), 0.1 % bFGF (basic fibroblast growth factor, Sigma-Aldrich), and 0.1 % EGF (epidermal growth factor, Sigma-Aldrich) respectively. In case of the ReNCell differentiation, similar protocol was used with hiPSC-NPC. ReNCells were seeded on matrigel pre-coated plates (2,000,000 cells/well for 6-well plate) 24 hr prior to experimentation. After 1 day of cultivation to promote cell attachment and spreading, the fresh ReNCell media without bFGF basic (differentiation media) was treated to stop proliferation and induce neuronal differentiation. ReNCells and astrocyte were co-cultured in one dish and induced neural differentiation. Both were maintained in mixture of DMEM/F12 (Gibco) and astrocyte culture medium (1:1 ratio) with all supplements. Total seeding numbers of cells were 2.0×10^6 corresponding to 1:9 / 1:4 / 1:1 / 4:1 / 9:1 ratio for ReNCells and astrocytes, respectively. ReNCells and astrocytes

were seeded on matrigel pre-coated plates 24 hr prior to experimentation. After 1 days of cultivation to promote cell attachment and spreading, the fresh mixture cell media without bFGF basic was treated to stop proliferation and induce neuronal differentiation. The medium was changed with fresh differentiation media every 3 ~ 4 days during the differentiation. The culture media was collected after 10 days of the induction of neural differentiation. Then, the media were centrifuged at 2,000 rpm for 5 min to separate the cell debris. For consistency, all experiments were carried out on cells between passages 3 to 5.

Immunocytochemistry

To study the extent of neuronal differentiation, cells and explanted brain tissue were washed with DPBS (pH 7.4) and fixed with 4% formaldehyde solution for 10 min at room temperature (RT), followed by three times of washing with DPBS. Then, cells are permeabilized with 0.1% Triton X-100 in PBS for 10 minutes and non-specific binding is blocked with 5% normal goat serum (NGS) (eLife Technologies) in PBS for 1 hour at room temperature. The primary rabbit antibody against Nestin (1:200 dilution, Invitrogen) and primary mouse antibody against TuJ1 (1: 200 dilution, Biolegend) are used for the cells. And the primary rabbit antibody against GFAP (1:200 dilution, Invitrogen) and primary mouse antibody against TuJ1 (1: 200 dilution, Biolegend) are used for the explanted brain tissues. Following the manufacturer's protocol, the fixed samples are incubated overnight at 4°C in a solution of this antibody in PBS containing 1% BSA and 0.3% Triton X-100. After washing three times with PBS, the samples are incubated for 1 hr at room temperature in a solution of anti-rabbit secondary antibody labeled Alexa Flour 488 (1:100, Life Technologies), anti-mouse secondary antibody labeled with Alexa Flour 647 (1:100, Life Technologies) and Hoechst (3 μg/mL, Life Technologies) to stain nucleus in PBS containing 1% NGS and 0.3% Triton X-100. After washing three times, all the samples are imaged using the Nikon T2500 inverted fluorescence microscope.

Gene Expression Analysis

Gene expression level was analyzed by quantitative reverse transcription PCR (RT-qPCR) from total RNA extracted from cells by a TRIzol reagent (Invitrogen, MA). The total RNA (1μg) was reverse transcribed to cDNA using the SuperScript III First-Strand Synthesis System (Invitrogen, MA) following the manufacturer's protocol. Subsequently, quantitative PCR was performed on a StepOnePlus Real-time PCR System (Applied Biosystems, MA) using an SYBR Green PCR Master Mix (Applied Biosystems, MA) with the gene-specific primers. The Standard cycling conditions were used for all PCR reactions with a melting temperature of 60°C. All the measurements were run in triplicate. The gene expression level was reported relative to the endogenous control gene, GAPDH.

Quantification of Intracellular miRNA Expression

The intracellular miRNA expression was quantified over the course of differentiation (21 days). At each time point, the total RNA, including miRNA, was extracted from cultured cells using the miRNeasy Micro Kit (Qiagen, MD) following the manufacturer's protocol. The first-strand cDNA was synthesized from total RNA (50ng) using a universal reverse transcription reaction system offered in a miRCURY LNA RT Kit (Qiagen, MD). The as-synthesized cDNA template was diluted 60 times prior to real-time PCR amplification on a StepOnePlus Real-time PCR System (Applied Biosystems, MA). Each real-time PCR was carried out in a miRCURY LNA miRNA PCR system (Qiagen, MD) in a 10 mL-reaction with 3 mL of cDNA, 5 mL of 2 $\times$ SYBR Green Master Mix, and the miRNA-specific PCR assays (primers): hsa-miR-124-5p as miR-124-specific primers and hsa-miR-103a-3p as the endogenous control. The 2-step cycling conditions were performed as follows: Initiation activation at 95°C for 2 min, 40 cycles of denaturation at 95°C for 10s and combined annealing/extension at 56°C for the 60s. The resulting CT values were normalized and reported in fold changes relative to endogenous control (miR-103a-3p). All the measurement was repeated for 3 times.

Confirmation of extraction and concentration of exosome via magnetic-gold nanorods via HRP-TMB reaction

Anti-CD63 and miR-124 targeting MB functionalized magnetic-gold NRs (20 mg/ml) were mixed with cell culture medium (1 mL), which were attained during neuronal differentiation of hiPSC-NPC. After 30 min, NRs were isolated under magnetic field and re-suspended with the anti-CD9-HRP antibody (Santa Cruz Biotechnology, Inc.) in PBS (final concentration 10 μg/mL). After 30 min, multifunctional magnetic-gold NRs were repeatedly isolated under magnetic field and re-suspend with PBS three times for separation of unbound anti-CD9-HRP. Finishing the washing step, 3,3',5,5'-tetramethylbenzidine (TMB) (MP Biomedicals, Inc.) was added to the multifunctional magnetic-gold NRs solution for 30 min. The UV/vis absorbance value was obtained at 650 nm using a 96 well plate reader (Infinite M200pro, TECAN Group, Ltd., Switzerland)

Non-destructive characterization of cell distribution in the explanted brain tissues

CD1 Post-natal day 4 (P4) mice brain tissue were dissected and maintained in mixture of neural basal medium (Gibco) and DMEM/F12 (Gibco) (50:50 ratio) supplemented with 0.5 % N2 (Gibco), 0.5 % B27, respectively. Brain tissue were maintained at 37°C in a humidified incubator with 5% CO_2. After 1 days of cultivation, non-adhered tissue were removed and the fresh medium was treated. The medium was changed with fresh differentiation media every 3 ~ 4 days during the differentiation. For the collection of exosome, media were collected after 3 days from the explant. The cultured media were then centrifuged at 2,000 rpm for 5 min to separate the cell debris.

Chapter 5

Conclusion and Prospective

Stem cell therapy holds the key of regenerative medicine for functional recovery from various injuries and diseases. Addressing the current challenges, nano-chemists and biologists have invested in various nanomaterials and their assembly in multidimensional domains to mimic the properties of the natural microenvironment to promote and dictate stem cell differentiation into desired lineages. In this review, the benefits of nanomaterial in the field of stem cell biology are clearly shown to be advantageous over traditional methods including bio-reagent delivery, in vivo imaging modality, and transplantation platform. Although much has been investigated to this point, there remains more investigation to be done in the clinical applications of multi-dimensional nanomaterials. This dissertation is the embodiment of the application of nanotechnology in the field of regenerative medicine. The microenvironment nanomaterials can provide gives us the insight into controlling stem cell fate. Through rational design of nanomaterials, the scientists have set very high expectation for advancement in clinical applications. Although there has been ethical concerns regarding stem cells, we should have faith in the humanities for making the right decision. This thesis merely scratched the surface in providing a few examples of methods, based on nanotechnology, to control and enhance the neuronal differentiation of NSCs, to monitor stem cell differentiation, and to regenerate axons in a spinal cord injury model for potential translational application.

In the introduction chapter, we explored and familiarized with the different tools in the nanomaterial tool box that are part of this dissertation and their common applications in the literature. On their own, each nanomaterial posses unique functions; however, when combined together, these nanomaterials can give rise to innovative hybrid biomaterials to advance therapeutics and diagnostics in biomedical application.

Together, the zero-dimensional nanoparticles, one-dimensional nanofibers, and two-dimensional graphene materials assemble to form 3D nanomaterials with rationally designed features. As an overview, we also demonstrated a few examples of nanomaterials used in the diffusive microenvironment where they are introduced into the cells to regulate cellular activities and pathways from within the cell. This type of application generally involves in cargo delivery and is most demonstrated in the literature with the most effort from the pharmaceutical industry. At the diffusive microenvironment, nanomaterials can also be used to bring organelles close or apart by remote actuation. This type of studies will unlock the mechanistic nature of our cellular organelles and is much of interest to fundamental biologists. At the diffusive microenvironment, we can also pursuit the biomimetic route to re-engineer each cellular components for both scientific curiosity reason and therapeutic application. As demonstrated with the NanoScript platform, this is a tremendous approach to a current therapeutic limitation. We then dived into the insoluble physical microenvironment to show the control nanomaterials have on cell fate through cell-microenvironment interactions. These approaches are especially valuable to the design of the features for translated devices. For example, by modifying the surface chemistry of the substrate which cells grow on, we can enhance stem cell survival, proliferation, migration, and differentiation. These type of studies bring values to the surface chemical properties of a biomaterial design. Furthermore, we also introduced the electrical and optical functions we can add to biomatreials to guide and direct stem cell fate. From the enhancement of cell behavior on rationally designed nanomaterial, we can then have the confidence in the future of transplantation to the currently incurable diseases and injures. One of the most versatile transplantable biomaterial in tissue engineering is through the use of nanofibers. Nanofiber, at the macroscale, provides the advantageous three dimensional microenvironment for enhanced cell behaviors. As shown, the biomedical field has a wide range of applications of tissue regeneration. Combining with other nanomaterials such as embedding and decorating nanoparticles and nanosheets inside and on the surface of nanofiber, multi-modalities can be introduced to the nanofiber. Additionally, currently established therapeutic agents can also be introduce in a similar manner to further

advance the current therapeutic standard. Overall, the introduction initiated our views on how we should utilize these nanomaterials, and the limitation of nanomaterials really is the imagination of the users.

In the second chapter, Nanomaterial-based Insoluble/physical microenvironment approach for guiding stem cell differentiation, we discussed the efficient physical microenvironment cues that can be used to efficiently differentiate stem cells to replace the original damaged or diseased cells for regenerative medicine. As demonstrated, nanomaterials provide unique physical size, surface chemistry, conductivity, and topographical cues that cannot be replicated by traditional small molecule based stem cell differentiation method. Furthermore, by not introducing extrinsic agents, the differentiated cells can be readily used for clinical application as minimal manipulation has been done. The rational nanomaterial design for biomedical application was the intersection of nanomaterial science, surface chemistry, stem cell biology, and biomedical engineering. The collaboration overcame the critical barrier of the development of effective non-toxic methodology to control stem cell differentiation into desired lineages. As demonstrated through the regulation of stem cell differentiation, we showed that the optimal size of nanoparticle monolayers can extend differentiated axonal length. The inclusion of graphene-oxide (GO) coating on both glass and nanoparticle surface had guidance toward axonal alignment. Although we still do not understand the underlying mechanism of this engineered microenvironment had on neurons, we also demonstrated the clinical translational potential on implantable, flexible polymeric substrates. Nevertheless, we envision that the alignment of axons from the differentiating hNSCs using SiNP-GO can potentially be applied to developing GO-based materials for transplanting hNSCs into injured sites of the central nervous system in order to efficiently repair impaired communication. To further expand upon our scope in the underlying nanotopography, we substituted the SiNP with electrospun polycaprolactone (PCL) nanofibers. The instructive physical cues provided by this graphene-nanofiber hybrid scaffold guided the differentiation of neural stem cells into myelinating oligodendrocytes. Remarkably, as mentioned before, the differentiation guidance was from the insoluble cues alone without any differentiation inducing molecules in the cell culture

media. These two demonstration suggested that hybrid nanoscaffold is extremely useful in supplying ideal nerve guidance conduits and providing the re-establishment of neural circuitry. A hybrid scaffold combines the morphological features of nanotopography and the unique surface properties of 2D nanomaterials a single platform. Going forward, scientists can explore and construct hybrid nanomatierals that encompass all the desirable properties for future therapies.

In the third chapter, Nanoparticle-based synthetic transcription factor as soluble microenvironment factor for neural stem cell differentiation and central nervous system treatment, we discussed an innovative gene modulating platform mimicking natural transcription factors for stem cell differentiation applications and spinal cord injury treatment. Transcription factors (TFs) have been well-studied by biologists. However, since the invention of induced pluripotent stem cells by Yamanaka, the field of cellular reprogramming has really expanded. TFs are extremely potent in regulating gene expression and in turns cellular response. Seeing the opportunity, we, nanochemist, saw our expertise can be integrated into stem cell biology and regenerative medicine. Current approach of gene modulation requires the use of viral-vector which has very limited clinical potential such as cytotoxicity and immunogenicity of the virus itself. Furthermore, undefined non-transient approach regulate genes poorly and may lead to potential integration with the host genome to give undesired effect such as tumor formation. Our approach, nanoparticle-base synthetic transcription factor, NanoScript, not only has bioinert core, it also regulate genes in a transient manner. Furthermore, due to the modular design, NanoScript can fine tune each domains (DBD, NLS, AD/RD) to increase efficiency which cannot be done by nature. Therefore, NanoScript represents an clear alternative for regulating the TF-mediated gene expression and inducing cellular reprogramming in an efficient, selective non-viral manner, which is safe for translation into the clinic for treatment of devastating diseases. We designed NanoScript with the following consideration: i) a DNA binding domain that specifically binds to the gene of interest, ii) a regulatory domain that is designed to either activate or repress the targeted gene by recruiting endogenous transcriptional machinery, and iii) a targeting sequence that facilitates cell and nuclear uptake. In the two demonstration, we

focused on the gene-repression approach for i) neural stem cell to functional neuron differentiation and ii) *in vivo* delivery of NanoScript for axonal regeneration in a spinal cord injury model. Specifically, we showed a proof-of-concept demonstration of the repression of Sox9 gene in neural stem cells by the synergistic effect of the polyamide and WRPW peptide on the NanoScript. By assembling both the repression peptide and PIP molecules on the NanoScript, we not only synergistically enhance gene repression, but enable NanoScript to more closely mimic the structure of TF repressor proteins. With the confidence from this project, we then demonstrated the feasibility of the NanoScript platform *in vivo*. The delivery of our non-viral, transient PTEN repressing NanoScript for axonal regeneration represented hope for the regeneration of the intrinsically limited regenerative potential of the central nervous system (CNS) and the complex inhibitory SCI environment. Going forward, there is a critical need for robust and effective method to re-establish the damanged neural circuitry. The future long-term goal is to effectively and selectively regulate genes related to therapeutic purpose through our novel NanoScript platform. We believe that the introduction of this versatile, effective, and tunable NanoScript platform will significant impact the field of stem cell biology and medicine. .

In the fourth chapter, Hybrid nanomaterial approaches for therapeutic and diagnostic applications, we investigate need for both sensitive and selective platforms for real-time, non-destructive cellular sensing application. The field of cellular characterization in general is well developed, and many commercially available products have appeared. However, in the clinical use of stem cell, there reminds a need for non-destructive yet both quantitative and qualitative method for characterizing stem cell before transplantation. For example, the transplantation of dopaminergic neurons have been identified as a potential treatment for devastating Parkinson's (PD). However, currently, besides a viable transplantation method, we still do not have a standard for ensuring the differentiated cells are mature for transplantation. In this chapter, we presented three different method to achieve such non-destructive, real-time cellular characterization. In the first demonstration of this chapter, we fabricated through light interference lithography the

large-scale homogeneous nanocup electrode arrays (LHONA) for the effective detection of dopamine production from dopaminergic cell lines. In addition, the LHONA platform allowed us to monitor the differnetiation of hNSCs into dopaminergic neurons in real-time. The LHONA platform showed excellent performance with selective and sensitive properties due the nanoscale pattern sizes and nanotopographical characteristics. Echoing the topic disccused in the second chapter, the nanotopography enhanced major functions such as such as cell spreading, adhesion, and proliferations. The LHONA platform is an advanced effective non-destructive biosensor for monitoring stem cell differentiation for more effective stem cell-based therapies. The second demonstration of this chapter, the multifunctional graphene-gold (Au) hybrid nanoelectrode arrays (NEAs) modulated osteogenic differentiation of mesenchymal stem cells. This study aimed to uncover mechanistic of combined physicochemical and biophysical cues that modulate the signaling cascade for stem cell differentiation. Build upon the similar lithography technique and 2D graphene oxide nanomaterial, our biocompatible hybrid NEAs, have excellent electrochemical performance. The osteogenic differentiation of hMSCs was successfully monitored in both non-destructive and real-time manner. Since the destructive analysis process such as cell lysis and cell fixation are not necessary for assaying the osteogenic differentiation of hMSCs for transplantation, our developed combinatorial arrays and novel electrochemical detection method can bring a breakthrough in the preclinical investigation of differentiated osteoblasts. Collectively, this work will not only advance stem cell differentiation assays by providing a practical, non-destructive, real-time monitoring tool but also help scientists understand the fundamental interactions between nanostructures and stem cells better. More detailed mechanistic studies on how the combination of physicochemical and biophysical cues modulate the signaling cascades involved in stem cell can be investigated using this hybrid NEA platform for other exciting field of stem cell differentiation as well. In the last demonstration of this chapter, we developed an indirect method to characterize a heterogeneous population of cells using the concept of exosomes. We synthesized multifunctional magnetic-gold NRs by integrating the magnetic component of Ni and metal

enhanced fluorescence effect of Au to 1) target and magnetically extract and concentrate of extracellular vesicles and 2) sensitively detect miRNA expression of via MEF effect. Due to the excellent selectivity and sensitivity, the neuronal differentiation of hiPSC-NPC was successfully monitored in both non-destructive and real-time manner. The magnetic-gold NRs system also showed promise in characterizing heterogeneous population of brain tissue explants. This demonstration is pivotal as it represents the potential field of use application. For example, future exploration can be to analyst specific cell types for disease characterization and early detection. Moreover, by avoiding the destructive analysis process such as cell lysis and cell fixation, all of the three approaches brought breakthrough in the preclinical investigation such as the transplantation of differentiated stem cells. As shown, the wide range of nanomaterials will not only advance stem cell differentiation assays by providing a practical, non-destructive, real-time monitoring tool but also help to pursue the full potential of stem-cell based therapies.

More novel and robust research should stem from this thesis. With the advancement of nanotechnoloy in biomedical research, human can finally have precise control of every cell in their body. In the past couple decades, we have generated a myriad of tools in our toolbox. In the next two decades, we should focus on the next phase which is to manipulate our cellular component at the tissue level. As shown, current strategy still lacks clear understanding in mature functionality of tissues and organs. Going forward, the scientists in this field should focus on the translational therapeutic applications of nanotechnology. Good science comes from good citizens.

References

[1] I. J. Fox, G. Q. Daley, S. A. Goldman, J. Huard, T. J. Kamp, and M. Trucco, "Stem cell therapy. use of differentiated pluripotent stem cells as replacement therapy for treating disease," *Science*, vol. 345, no. 6199, p. 1247391, 2014.

[2] A. Solanki, J. D. Kim, and K. B. Lee, "Nanotechnology for regenerative medicine: nanomaterials for stem cell imaging," *Nanomedicine (Lond)*, vol. 3, no. 4, pp. 567–78, 2008.

[3] A. Solanki, J. D. Kim, and K. B. Lee, "Nanotechnology for regenerative medicine: nanomaterials for stem cell imaging," *Nanomedicine (Lond)*, vol. 3, no. 4, pp. 567–78, 2008.

[4] P. Prabhakaran, W. J. Kim, K. S. Lee, and P. N. Prasad, "Quantum dots (qds) for photonic applications," *Optical Materials Express*, vol. 2, no. 5, pp. 578–593, 2012.

[5] X. Michalet, F. F. Pinaud, L. A. Bentolila, J. M. Tsay, S. Doose, J. J. Li, G. Sundaresan, A. M. Wu, S. S. Gambhir, and S. Weiss, "Quantum dots for live cells, in vivo imaging, and diagnostics," *Science*, vol. 307, no. 5709, pp. 538–44, 2005.

[6] D. Bera, L. Qian, T. K. Tseng, and P. H. Holloway, "Quantum dots and their multimodal applications: A review," *Materials*, vol. 3, no. 4, pp. 2260–2345, 2010.

[7] D. J. Norris and M. G. Bawendi, "Measurement and assignment of the size-dependent optical spectrum in cdse quantum dots," *Phys Rev B Condens Matter*, vol. 53, no. 24, pp. 16338–16346, 1996.

[8] S. A. Kumar, A. A. Ansary, A. Ahmad, and M. I. Khan, "Extracellular biosynthesis of cdse quantum dots by the fungus, fusarium oxysporum," *Journal of Biomedical Nanotechnology*, vol. 3, no. 2, pp. 190–194, 2007.

[9] X. Michalet, F. F. Pinaud, L. A. Bentolila, J. M. Tsay, S. Doose, J. J. Li, G. Sundaresan, A. M. Wu, S. S. Gambhir, and S. Weiss, "Quantum dots for live cells, in vivo imaging, and diagnostics," *Science*, vol. 307, no. 5709, pp. 538–44, 2005.

[10] S. Lin, X. Xie, M. R. Patel, Y. H. Yang, Z. Li, F. Cao, O. Gheysens, Y. Zhang, S. S. Gambhir, J. H. Rao, and J. C. Wu, "Quantum dot imaging for embryonic stem cells," *BMC Biotechnol*, vol. 7, no. 1, p. 67, 2007.

[11] T. Torimoto, T. Adachi, K. Okazaki, M. Sakuraoka, T. Shibayama, B. Ohtani, A. Kudo, and S. Kuwabata, "Facile synthesis of zns-agins2 solid solution nanoparticles for a color-adjustable luminophore," *J Am Chem Soc*, vol. 129, no. 41, pp. 12388–9, 2007.

[12] M. Grzelczak, J. Perez-Juste, P. Mulvaney, and L. M. Liz-Marzan, "Shape control in gold nanoparticle synthesis," *Chem Soc Rev*, vol. 37, no. 9, pp. 1783–91, 2008.

[13] X. Zhang, "Gold nanoparticles: Recent advances in the biomedical applications," *Cell Biochem Biophys*, vol. 72, no. 3, pp. 771–5, 2015.

[14] P. M. Tiwari, K. Vig, V. A. Dennis, and S. R. Singh, "Functionalized gold nanoparticles and their biomedical applications," *Nanomaterials*, vol. 1, no. 1, pp. 31–63, 2011.

[15] D. Bobo, K. J. Robinson, J. Islam, K. J. Thurecht, and S. R. Corrie, "Nanoparticle-based medicines: A review of fda-approved materials and clinical trials to date," *Pharm Res*, vol. 33, no. 10, pp. 2373–87, 2016.

[16] M. C. Daniel and D. Astruc, "Gold nanoparticles: assembly, supramolecular chemistry, quantum-size-related properties, and applications toward biology, catalysis, and nanotechnology," *Chem Rev*, vol. 104, no. 1, pp. 293–346, 2004.

[17] X. H. Huang, P. K. Jain, I. H. El-Sayed, and M. A. El-Sayed, "Plasmonic photothermal therapy (pptt) using gold nanoparticles," *Lasers in Medical Science*, vol. 23, no. 3, pp. 217–228, 2008.

[18] X. Huang and M. A. J. J. o. a. r. El-Sayed, "Gold nanoparticles: optical properties and implementations in cancer diagnosis and photothermal therapy," *Journal of Advanced Research*, vol. 1, no. 1, pp. 13–28, 2010.

[19] L. Dykman and N. Khlebtsov, "Gold nanoparticles in biomedical applications: recent advances and perspectives," *Chem Soc Rev*, vol. 41, no. 6, pp. 2256–82, 2012.

[20] J. Gao, H. Gu, and B. Xu, "Multifunctional magnetic nanoparticles: design, synthesis, and biomedical applications," *Acc Chem Res*, vol. 42, no. 8, pp. 1097–107, 2009.

[21] G. Reiss and A. Hütten, *Magnetic nanoparticles*, pp. 28–40. CRC press, 2016.

[22] L. H. Reddy, J. L. Arias, J. Nicolas, and P. Couvreur, "Magnetic nanoparticles: design and characterization, toxicity and biocompatibility, pharmaceutical and biomedical applications," *Chem Rev*, vol. 112, no. 11, pp. 5818–78, 2012.

[23] J. Xie, G. Liu, H. S. Eden, H. Ai, and X. Chen, "Surface-engineered magnetic nanoparticle platforms for cancer imaging and therapy," *Acc Chem Res*, vol. 44, no. 10, pp. 883–92, 2011.

[24] A. J. Giustini, A. A. Petryk, S. M. Cassim, J. A. Tate, I. Baker, and P. J. Hoopes, "Magnetic nanoparticle hyperthermia in cancer treatment," *Nano Life*, vol. 1, no. 1n02, pp. 17–32, 2010.

[25] E. I. Galanzha, E. V. Shashkov, T. Kelly, J. W. Kim, L. Yang, and V. P. Zharov, "In vivo magnetic enrichment and multiplex photoacoustic detection of circulating tumour cells," *Nat Nanotechnol*, vol. 4, no. 12, pp. 855–60, 2009.

[26] M. F. Kircher, U. Mahmood, R. S. King, R. Weissleder, and L. Josephson, "A multimodal nanoparticle for preoperative magnetic resonance imaging and intraoperative optical brain tumor delineation," *Cancer Res*, vol. 63, no. 23, pp. 8122–5, 2003.

[27] M. Arruebo, R. Fernandez-Pacheco, M. R. Ibarra, and J. Santamaria, "Magnetic nanoparticles for drug delivery," *Nano Today*, vol. 2, no. 3, pp. 22–32, 2007.

[28] S. Miltenyi, W. Muller, W. Weichel, and A. Radbruch, "High gradient magnetic cell separation with macs," *Cytometry*, vol. 11, no. 2, pp. 231–8, 1990.

[29] I. A. Rahman and V. J. J. o. N. Padavettan, "Synthesis of silica nanoparticles by sol-gel: size-dependent properties, surface modification, and applications in silica-polymer nanocomposites—a review," *Journal of Nanomaterials*, vol. 2012, p. 8, 2012.

[30] A. Bitar, N. M. Ahmad, H. Fessi, and A. Elaissari, "Silica-based nanoparticles for biomedical applications," *Drug Discov Today*, vol. 17, no. 19-20, pp. 1147–54, 2012.

[31] A. Liberman, N. Mendez, W. C. Trogler, and A. C. Kummel, "Synthesis and surface functionalization of silica nanoparticles for nanomedicine," *Surf Sci Rep*, vol. 69, no. 2-3, pp. 132–158, 2014.

[32] M. Lin, Y. Zhao, S. Wang, M. Liu, Z. Duan, Y. Chen, F. Li, F. Xu, and T. Lu, "Recent advances in synthesis and surface modification of lanthanide-doped upconversion nanoparticles for biomedical applications," *Biotechnol Adv*, vol. 30, no. 6, pp. 1551–61, 2012.

[33] S. Shah, J. J. Liu, N. Pasquale, J. Lai, H. McGowan, Z. P. Pang, and K. B. Lee, "Hybrid upconversion nanomaterials for optogenetic neuronal control," *Nanoscale*, vol. 7, no. 40, pp. 16571–7, 2015.

[34] G. Chen, H. Qiu, P. N. Prasad, and X. Chen, "Upconversion nanoparticles: design, nanochemistry, and applications in theranostics," *Chem Rev*, vol. 114, no. 10, pp. 5161–214, 2014.

[35] M. Wang, G. Abbineni, A. Clevenger, C. Mao, and S. Xu, "Upconversion nanoparticles: synthesis, surface modification and biological applications," *Nanomedicine*, vol. 7, no. 6, pp. 710–29, 2011.

[36] D. Liang, B. S. Hsiao, and B. Chu, "Functional electrospun nanofibrous scaffolds for biomedical applications," *Adv Drug Deliv Rev*, vol. 59, no. 14, pp. 1392–412, 2007.

[37] Y. Zhang, C. T. Lim, S. Ramakrishna, and Z. M. Huang, "Recent development of polymer nanofibers for biomedical and biotechnological applications," *J Mater Sci Mater Med*, vol. 16, no. 10, pp. 933–46, 2005.

[38] A. K. Geim and K. S. Novoselov, *The rise of graphene*, pp. 11–19. World Scientific, 2010.

[39] Y. Zhu, S. Murali, W. Cai, X. Li, J. W. Suk, J. R. Potts, and R. S. Ruoff, "Graphene and graphene oxide: synthesis, properties, and applications," *Adv Mater*, vol. 22, no. 35, pp. 3906–24, 2010.

[40] C. Chung, Y. K. Kim, D. Shin, S. R. Ryoo, B. H. Hong, and D. H. Min, "Biomedical applications of graphene and graphene oxide," *Acc Chem Res*, vol. 46, no. 10, pp. 2211–24, 2013.

[41] V. C. Sanchez, A. Jachak, R. H. Hurt, and A. B. Kane, "Biological interactions of graphene-family nanomaterials: an interdisciplinary review," *Chem Res Toxicol*, vol. 25, no. 1, pp. 15–34, 2012.

[42] Y. Y. Shao, J. Wang, H. Wu, J. Liu, I. A. Aksay, and Y. H. Lin, "Graphene based electrochemical sensors and biosensors: A review," *Electroanalysis*, vol. 22, no. 10, pp. 1027–1036, 2010.

[43] C. H. Wang, W. J. Cherng, and S. Verma, "Drawbacks to stem cell therapy in cardiovascular diseases," *Future Cardiol*, vol. 4, no. 4, pp. 399–408, 2008.

[44] S. P. Medvedev, A. I. Shevchenko, and S. M. Zakian, "Induced pluripotent stem cells: Problems and advantages when applying them in regenerative medicine," *Acta Naturae*, vol. 2, no. 2, pp. 18–27, 2010.

[45] T. H. Kim, S. Shah, L. Yang, P. T. Yin, M. K. Hossain, B. Conley, J. W. Choi, and K. B. Lee, "Controlling differentiation of adipose-derived stem cells using combinatorial graphene hybrid-pattern arrays," *ACS Nano*, vol. 9, no. 4, pp. 3780–90, 2015.

[46] C. Liu, C. Zhu, J. Li, P. Zhou, M. Chen, H. Yang, and B. Li, "The effect of the fibre orientation of electrospun scaffolds on the matrix production of rabbit annulus fibrosus-derived stem cells," *Bone Res*, vol. 3, p. 15012, 2015.

[47] S. D. Chueng, L. Yang, Y. Zhang, and K. B. Lee, "Multidimensional nanomaterials for the control of stem cell fate," *Nano Converg*, vol. 3, no. 1, p. 23, 2016.

[48] S. Patel and K. B. Lee, "Probing stem cell behavior using nanoparticle-based approaches," *Wiley Interdiscip Rev Nanomed Nanobiotechnol*, vol. 7, no. 6, pp. 759–78, 2015.

[49] S. Pulavendran, M. Rajam, C. Rose, and A. Mandal, "Hepatocyte growth factor incorporated chitosan nanoparticles differentiate murine bone marrow mesenchymal stem cell into hepatocytes in vitro," *IET Nanobiotechnology*, vol. 4, no. 3, pp. 51–60, 2010.

[50] S. Pulavendran, C. Rose, and A. B. Mandal, "Hepatocyte growth factor incorporated chitosan nanoparticles augment the differentiation of stem cell into hepatocytes for the recovery of liver cirrhosis in mice," *J Nanobiotechnology*, vol. 9, p. 15, 2011.

[51] S. Patel, D. Jung, P. T. Yin, P. Carlton, M. Yamamoto, T. Bando, H. Sugiyama, and K. B. Lee, "Nanoscript: a nanoparticle-based artificial transcription factor for effective gene regulation," *ACS Nano*, vol. 8, no. 9, pp. 8959–67, 2014.

[52] A. Neumann, A. Christel, C. Kasper, and P. Behrens, "Bmp2-loaded nanoporous silica nanoparticles promote osteogenic differentiation of human mesenchymal stem cells," *Rsc Advances*, vol. 3, no. 46, pp. 24222–24230, 2013.

[53] A. E. Garcia-Bennett, M. Kozhevnikova, N. Konig, C. Zhou, R. Leao, T. Knopfel, S. Pankratova, C. Trolle, V. Berezin, E. Bock, H. Aldskogius, and E. N. Kozlova, "Delivery of differentiation factors by mesoporous silica particles assists advanced differentiation of transplanted murine embryonic stem cells," *Stem Cells Transl Med*, vol. 2, no. 11, pp. 906–15, 2013.

[54] J. Maia, T. Santos, S. Aday, F. Agasse, L. Cortes, J. O. Malva, L. Bernardino, and L. Ferreira, "Controlling the neuronal differentiation of stem cells by the intracellular delivery of retinoic acid-loaded nanoparticles," *ACS Nano*, vol. 5, no. 1, pp. 97–106, 2011.

[55] B. Shah, P. T. Yin, S. Ghoshal, and K. B. Lee, "Multimodal magnetic core-shell nanoparticles for effective stem-cell differentiation and imaging," *Angew Chem Int Ed Engl*, vol. 52, no. 24, pp. 6190–5, 2013.

[56] W. Chen, P. H. Tsai, Y. Hung, S. H. Chiou, and C. Y. Mou, "Nonviral cell labeling and differentiation agent for induced pluripotent stem cells based on mesoporous silica nanoparticles," *ACS Nano*, vol. 7, no. 10, pp. 8423–40, 2013.

[57] W. W. Yau, P. O. Rujitanaroj, L. Lam, and S. Y. Chew, "Directing stem cell fate by controlled rna interference," *Biomaterials*, vol. 33, no. 9, pp. 2608–28, 2012.

[58] S. Shah, A. Solanki, P. K. Sasmal, and K. B. Lee, "Single vehicular delivery of sirna and small molecules to control stem cell differentiation," *J Am Chem Soc*, vol. 135, no. 42, pp. 15682–15685, 2013.

[59] B. Leader, Q. J. Baca, and D. E. Golan, "Protein therapeutics: a summary and pharmacological classification," *Nat Rev Drug Discov*, vol. 7, no. 1, pp. 21–39, 2008.

[60] F. Spitz and E. E. Furlong, "Transcription factors: from enhancer binding to developmental control," *Nat Rev Genet*, vol. 13, no. 9, pp. 613–26, 2012.

[61] J. Park, I. Y. Kim, M. Patel, H. J. Moon, S. J. Hwang, and B. Jeong, "2d and 3d hybrid systems for enhancement of chondrogenic differentiation of tonsil-derived mesenchymal stem cells," *Advanced Functional Materials*, vol. 25, no. 17, pp. 2573–2582, 2015.

[62] S. Patel, T. Pongkulapa, P. T. Yin, G. N. Pandian, C. Rathnam, T. Bando, T. Vaijayanthi, H. Sugiyama, and K. B. Lee, "Integrating epigenetic modulators into nanoscript for enhanced chondrogenesis of stem cells," *J Am Chem Soc*, vol. 137, no. 14, pp. 4598–601, 2015.

[63] S. Patel, S. T. Chueng, P. T. Yin, K. Dardir, Z. Song, N. Pasquale, K. Kwan, H. Sugiyama, and K. B. Lee, "Induction of stem-cell-derived functional neurons by nanoscript-based gene repression," *Angew Chem Int Ed Engl*, vol. 54, no. 41, pp. 11983–8, 2015.

[64] L. J. Santos, R. L. Reis, and M. E. Gomes, "Harnessing magnetic-mechano actuation in regenerative medicine and tissue engineering," *Trends Biotechnol*, vol. 33, no. 8, pp. 471–9, 2015.

[65] M. J. Dalby, N. Gadegaard, and R. O. Oreffo, "Harnessing nanotopography and integrin-matrix interactions to influence stem cell fate," *Nat Mater*, vol. 13, no. 6, pp. 558–69, 2014.

[66] W. L. Murphy, T. C. McDevitt, and A. J. Engler, "Materials as stem cell regulators," *Nat Mater*, vol. 13, no. 6, pp. 547–57, 2014.

[67] L. Yuge, A. Okubo, T. Miyashita, T. Kumagai, T. Nikawa, S. Takeda, M. Kanno, Y. Urabe, M. Sugiyama, and K. Kataoka, "Physical stress by magnetic force accelerates differentiation of human osteoblasts," *Biochem Biophys Res Commun*, vol. 311, no. 1, pp. 32–8, 2003.

[68] J. Dobson, "Remote control of cellular behaviour with magnetic nanoparticles," *Nat Nanotechnol*, vol. 3, no. 3, pp. 139–43, 2008.

[69] B. D. Matthews, D. R. Overby, R. Mannix, and D. E. Ingber, "Cellular adaptation to mechanical stress: role of integrins, rho, cytoskeletal tension and mechanosensitive ion channels," *J Cell Sci*, vol. 119, no. Pt 3, pp. 508–18, 2006.

[70] S. Hughes, S. McBain, J. Dobson, and A. J. El Haj, "Selective activation of mechanosensitive ion channels using magnetic particles," *J R Soc Interface*, vol. 5, no. 25, pp. 855–63, 2008.

[71] J. R. Henstock, M. Rotherham, H. Rashidi, K. M. Shakesheff, and A. J. El Haj, "Remotely activated mechanotransduction via magnetic nanoparticles promotes mineralization synergistically with bone morphogenetic protein 2: Applications for injectable cell therapy," *Stem Cells Transl Med*, vol. 3, no. 11, pp. 1363–74, 2014.

[72] B. Hu, A. J. El Haj, and J. Dobson, "Receptor-targeted, magneto-mechanical stimulation of osteogenic differentiation of human bone marrow-derived mesenchymal stem cells," *Int J Mol Sci*, vol. 14, no. 9, pp. 19276–93, 2013.

[73] B. Hu, J. Dobson, and A. J. El Haj, "Control of smooth muscle alpha-actin (sma) up-regulation in hbmscs using remote magnetic particle mechano-activation," *Nanomedicine*, vol. 10, no. 1, pp. 45–55, 2014.

[74] A. K. Geim and K. S. Novoselov, "The rise of graphene," *Nat Mater*, vol. 6, no. 3, pp. 183–91, 2007.

[75] M. J. Allen, V. C. Tung, and R. B. Kaner, "Honeycomb carbon: a review of graphene," *Chem Rev*, vol. 110, no. 1, pp. 132–45, 2010.

[76] X. Sun, Z. Liu, K. Welsher, J. T. Robinson, A. Goodwin, S. Zaric, and H. Dai, "Nano-graphene oxide for cellular imaging and drug delivery," *Nano Res*, vol. 1, no. 3, pp. 203–212, 2008.

[77] D. Chimene, D. L. Alge, and A. K. Gaharwar, "Two-dimensional nanomaterials for biomedical applications: Emerging trends and future prospects," *Adv Mater*, vol. 27, no. 45, pp. 7261–84, 2015.

[78] S. Y. Park, J. Park, S. H. Sim, M. G. Sung, K. S. Kim, B. H. Hong, and S. Hong, "Enhanced differentiation of human neural stem cells into neurons on graphene," *Adv Mater*, vol. 23, no. 36, pp. H263–7, 2011.

[79] N. Li, X. Zhang, Q. Song, R. Su, Q. Zhang, T. Kong, L. Liu, G. Jin, M. Tang, and G. Cheng, "The promotion of neurite sprouting and outgrowth of mouse hippocampal cells in culture by graphene substrates," *Biomaterials*, vol. 32, no. 35, pp. 9374–82, 2011.

[80] Y. Wang, W. C. Lee, K. K. Manga, P. K. Ang, J. Lu, Y. P. Liu, C. T. Lim, and K. P. Loh, "Fluorinated graphene for promoting neuro-induction of stem cells," *Adv Mater*, vol. 24, no. 31, pp. 4285–90, 2012.

[81] T. Zhang, N. Li, K. Y. Li, R. F. Gao, W. Gu, C. C. Wu, R. G. Su, L. W. Liu, Q. Zhang, and J. Liu, "Enhanced proliferation and osteogenic differentiation of human mesenchymal stem cells on biomineralized three-dimensional graphene foams," *Carbon*, vol. 105, pp. 233–243, 2016.

[82] S. H. Ku and C. B. Park, "Myoblast differentiation on graphene oxide," *Biomaterials*, vol. 34, no. 8, pp. 2017–23, 2013.

[83] H. H. Yoon, S. H. Bhang, T. Kim, T. Yu, T. Hyeon, and B. S. Kim, "Dual roles of graphene oxide in chondrogenic differentiation of adult stem cells: Cell-adhesion substrate and growth factor-delivery carrier," *Advanced Functional Materials*, vol. 24, no. 41, pp. 6455–6464, 2014.

[84] J. Park, S. Park, S. Ryu, S. H. Bhang, J. Kim, J. K. Yoon, Y. H. Park, S. P. Cho, S. Lee, B. H. Hong, and B. S. Kim, "Graphene-regulated cardiomyogenic differentiation process of mesenchymal stem cells by enhancing the expression of extracellular matrix proteins and cell signaling molecules," *Adv Healthc Mater*, vol. 3, no. 2, pp. 176–81, 2014.

[85] W. C. Lee, C. H. Lim, H. Shi, L. A. Tang, Y. Wang, C. T. Lim, and K. P. Loh, "Origin of enhanced stem cell growth and differentiation on graphene and graphene oxide," *ACS Nano*, vol. 5, no. 9, pp. 7334–41, 2011.

[86] W. Guo, X. Zhang, X. Yu, S. Wang, J. Qiu, W. Tang, L. Li, H. Liu, and Z. L. Wang, "Self-powered electrical stimulation for enhancing neural differentiation of mesenchymal stem cells on graphene-poly(3,4-ethylenedioxythiophene) hybrid microfibers," *ACS Nano*, vol. 10, no. 5, pp. 5086–95, 2016.

[87] O. Akhavan and E. Ghaderi, "The use of graphene in the self-organized differentiation of human neural stem cells into neurons under pulsed laser stimulation," *Journal of Materials Chemistry B*, vol. 2, no. 34, pp. 5602–5611, 2014.

[88] O. Akhavan and E. Ghaderi, "Flash photo stimulation of human neural stem cells on graphene/tio2 heterojunction for differentiation into neurons," *Nanoscale*, vol. 5, no. 21, pp. 10316–26, 2013.

[89] T. H. Kim, K. B. Lee, and J. W. Choi, "3d graphene oxide-encapsulated gold nanoparticles to detect neural stem cell differentiation," *Biomaterials*, vol. 34, no. 34, pp. 8660–70, 2013.

[90] A. Solanki, S. T. Chueng, P. T. Yin, R. Kappera, M. Chhowalla, and K. B. Lee, "Axonal alignment and enhanced neuronal differentiation of neural stem cells on graphene-nanoparticle hybrid structures," *Adv Mater*, vol. 25, no. 38, pp. 5477–82, 2013.

[91] S. R. Shin, B. Aghaei-Ghareh-Bolagh, X. Gao, M. Nikkhah, S. M. Jung, A. Dolatshahi-Pirouz, S. B. Kim, S. M. Kim, M. R. Dokmeci, X. S. Tang, and A. Khademhosseini, "Layer-by-layer assembly of 3d tissue constructs with functionalized graphene," *Adv Funct Mater*, vol. 24, no. 39, pp. 6136–6144, 2014.

[92] T. Fujie, Y. Mori, S. Ito, M. Nishizawa, H. Bae, N. Nagai, H. Onami, T. Abe, A. Khademhosseini, and H. Kaji, "Micropatterned polymeric nanosheets for local delivery of an engineered epithelial monolayer," *Adv Mater*, vol. 26, no. 11, pp. 1699–705, 2014.

[93] F. Gattazzo, A. Urciuolo, and P. Bonaldo, "Extracellular matrix: a dynamic microenvironment for stem cell niche," *Biochim Biophys Acta*, vol. 1840, no. 8, pp. 2506–19, 2014.

[94] V. Leung and F. Ko, "Biomedical applications of nanofibers," *Polymers for Advanced Technologies*, vol. 22, no. 3, pp. 350–365, 2011.

[95] Z. Zhang, J. Hu, and P. X. Ma, "Nanofiber-based delivery of bioactive agents and stem cells to bone sites," *Adv Drug Deliv Rev*, vol. 64, no. 12, pp. 1129–41, 2012.

[96] K. S. Rho, L. Jeong, G. Lee, B. M. Seo, Y. J. Park, S. D. Hong, S. Roh, J. J. Cho, W. H. Park, and B. M. Min, "Electrospinning of collagen nanofibers: effects on the behavior of normal human keratinocytes and early-stage wound healing," *Biomaterials*, vol. 27, no. 8, pp. 1452–61, 2006.

[97] L. Jeong, I. S. Yeo, H. N. Kim, Y. I. Yoon, D. H. Jang, S. Y. Jung, B. M. Min, and W. H. Park, "Plasma-treated silk fibroin nanofibers for skin regeneration," *Int J Biol Macromol*, vol. 44, no. 3, pp. 222–8, 2009.

[98] Y. Zhou, D. Yang, X. Chen, Q. Xu, F. Lu, and J. Nie, "Electrospun water-soluble carboxyethyl chitosan/poly(vinyl alcohol) nanofibrous membrane as potential wound dressing for skin regeneration," *Biomacromolecules*, vol. 9, no. 1, pp. 349–54, 2008.

[99] B. Dhandayuthapani, U. M. Krishnan, and S. Sethuraman, "Fabrication and characterization of chitosan-gelatin blend nanofibers for skin tissue engineering," *J Biomed Mater Res B Appl Biomater*, vol. 94, no. 1, pp. 264–72, 2010.

[100] K. Ma, S. Liao, L. He, J. Lu, S. Ramakrishna, and C. K. Chan, "Effects of nanofiber/stem cell composite on wound healing in acute full-thickness skin wounds," *Tissue Eng Part A*, vol. 17, no. 9-10, pp. 1413–24, 2011.

[101] A. Mata, Y. Geng, K. J. Henrikson, C. Aparicio, S. R. Stock, R. L. Satcher, and S. I. Stupp, "Bone regeneration mediated by biomimetic mineralization of a nanofiber matrix," *Biomaterials*, vol. 31, no. 23, pp. 6004–12, 2010.

[102] H. Cui, M. J. Webber, and S. I. Stupp, "Self-assembly of peptide amphiphiles: from molecules to nanostructures to biomaterials," *Biopolymers*, vol. 94, no. 1, pp. 1–18, 2010.

[103] J. R. Venugopal, S. Low, A. T. Choon, A. B. Kumar, and S. Ramakrishna, "Nanobioengineered electrospun composite nanofibers and osteoblasts for bone regeneration," *Artif Organs*, vol. 32, no. 5, pp. 388–97, 2008.

[104] H. Yoshimoto, Y. M. Shin, H. Terai, and J. P. Vacanti, "A biodegradable nanofiber scaffold by electrospinning and its potential for bone tissue engineering," *Biomaterials*, vol. 24, no. 12, pp. 2077–82, 2003.

[105] G. Vunjak-Novakovic, G. Altman, R. Horan, and D. L. Kaplan, "Tissue engineering of ligaments," *Annu Rev Biomed Eng*, vol. 6, no. 1, pp. 131–56, 2004.

[106] Z. Yin, X. Chen, J. L. Chen, W. L. Shen, T. M. Hieu Nguyen, L. Gao, and H. W. Ouyang, "The regulation of tendon stem cell differentiation by the alignment of nanofibers," *Biomaterials*, vol. 31, no. 8, pp. 2163–75, 2010.

[107] C. H. Lee, H. J. Shin, I. H. Cho, Y. M. Kang, I. A. Kim, K. D. Park, and J. W. Shin, "Nanofiber alignment and direction of mechanical strain affect the ecm production of human acl fibroblast," *Biomaterials*, vol. 26, no. 11, pp. 1261–70, 2005.

[108] Z. Q. Feng, X. Chu, N. P. Huang, T. Wang, Y. Wang, X. Shi, Y. Ding, and Z. Z. Gu, "The effect of nanofibrous galactosylated chitosan scaffolds on the formation of rat primary hepatocyte aggregates and the maintenance of liver function," *Biomaterials*, vol. 30, no. 14, pp. 2753–63, 2009.

[109] A. Piryaei, M. R. Valojerdi, M. Shahsavani, and H. Baharvand, "Differentiation of bone marrow-derived mesenchymal stem cells into hepatocyte-like cells on nanofibers and their transplantation into a carbon tetrachloride-induced liver fibrosis model," *Stem Cell Rev*, vol. 7, no. 1, pp. 103–18, 2011.

[110] F. Gelain, D. Bottai, A. Vescovi, and S. Zhang, "Designer self-assembling peptide nanofiber scaffolds for adult mouse neural stem cell 3-dimensional cultures," *PLoS One*, vol. 1, no. 1, p. e119, 2006.

[111] G. A. Silva, C. Czeisler, K. L. Niece, E. Beniash, D. A. Harrington, J. A. Kessler, and S. I. Stupp, "Selective differentiation of neural progenitor cells by high-epitope density nanofibers," *Science*, vol. 303, no. 5662, pp. 1352–5, 2004.

[112] S. Shah, P. T. Yin, T. M. Uehara, S. T. Chueng, L. Yang, and K. B. Lee, "Guiding stem cell differentiation into oligodendrocytes using graphene-nanofiber hybrid scaffolds," *Adv Mater*, vol. 26, no. 22, pp. 3673–80, 2014.

[113] E. Beniash, J. D. Hartgerink, H. Storrie, J. C. Stendahl, and S. I. Stupp, "Self-assembling peptide amphiphile nanofiber matrices for cell entrapment," *Acta Biomater*, vol. 1, no. 4, pp. 387–97, 2005.

[114] L. S. Li and S. I. Stupp, "One-dimensional assembly of lipophilic inorganic nanoparticles templated by peptide-based nanofibers with binding functionalities," *Angew Chem Int Ed Engl*, vol. 44, no. 12, pp. 1833–6, 2005.

[115] M. V. Natu, H. C. de Sousa, and M. H. Gil, "Effects of drug solubility, state and loading on controlled release in bicomponent electrospun fibers," *Int J Pharm*, vol. 397, no. 1-2, pp. 50–8, 2010.

[116] K. Y. Baik, S. Y. Park, K. Heo, K. B. Lee, and S. Hong, "Carbon nanotube monolayer cues for osteogenesis of mesenchymal stem cells," *Small*, vol. 7, no. 6, pp. 741–5, 2011.

[117] S. Y. Park, D. S. Choi, H. J. Jin, J. Park, K. E. Byun, K. B. Lee, and S. Hong, "Polarization-controlled differentiation of human neural stem cells using synergistic cues from the patterns of carbon nanotube monolayer coating," *ACS Nano*, vol. 5, no. 6, pp. 4704–11, 2011.

[118] W. C. Lee, C. H. Lim, H. Shi, L. A. Tang, Y. Wang, C. T. Lim, and K. P. Loh, "Origin of enhanced stem cell growth and differentiation on graphene and graphene oxide," *ACS Nano*, vol. 5, no. 9, pp. 7334–41, 2011.

[119] S. Oh, K. S. Brammer, Y. S. Li, D. Teng, A. J. Engler, S. Chien, and S. Jin, "Stem cell fate dictated solely by altered nanotube dimension," *Proc Natl Acad Sci U S A*, vol. 106, no. 7, pp. 2130–5, 2009.

[120] K. Saha, A. J. Keung, E. F. Irwin, Y. Li, L. Little, D. V. Schaffer, and K. E. Healy, "Substrate modulus directs neural stem cell behavior," *Biophys J*, vol. 95, no. 9, pp. 4426–38, 2008.

[121] S. A. Ruiz and C. S. Chen, "Emergence of patterned stem cell differentiation within multicellular structures," *Stem Cells*, vol. 26, no. 11, pp. 2921–7, 2008.

[122] A. Solanki, S. Shah, K. A. Memoli, S. Y. Park, S. Hong, and K. B. Lee, "Controlling differentiation of neural stem cells using extracellular matrix protein patterns," *Small*, vol. 6, no. 22, pp. 2509–13, 2010.

[123] H. M. Geller and J. W. Fawcett, "Building a bridge: engineering spinal cord repair," *Exp Neurol*, vol. 174, no. 2, pp. 125–36, 2002.

[124] C. Miller, S. Jeftinija, and S. Mallapragada, "Synergistic effects of physical and chemical guidance cues on neurite alignment and outgrowth on biodegradable polymer substrates," *Tissue Eng*, vol. 8, no. 3, pp. 367–78, 2002.

[125] Y. D. Teng, E. B. Lavik, X. Qu, K. I. Park, J. Ourednik, D. Zurakowski, R. Langer, and E. Y. Snyder, "Functional recovery following traumatic spinal cord injury mediated by a unique polymer scaffold seeded with neural stem cells," *Proc Natl Acad Sci U S A*, vol. 99, no. 5, pp. 3024–9, 2002.

[126] B. Sandner, P. Prang, F. J. Rivera, L. Aigner, A. Blesch, and N. Weidner, "Neural stem cells for spinal cord repair," *Cell Tissue Res*, vol. 349, no. 1, pp. 349–62, 2012.

[127] M. Abematsu, K. Tsujimura, M. Yamano, M. Saito, K. Kohno, J. Kohyama, M. Namihira, S. Komiya, and K. Nakashima, "Neurons derived from transplanted neural stem cells restore disrupted neuronal circuitry in a mouse model of spinal cord injury," *J Clin Invest*, vol. 120, no. 9, pp. 3255–66, 2010.

[128] D.-H. Kim, P. P. Provenzano, C. L. Smith, and A. Levchenko, "Matrix nanotopography as a regulator of cell function," *The Journal of Cell Biology*, vol. 197, no. 3, pp. 351–360, 2012.

[129] G. Kumar, C. K. Tison, K. Chatterjee, P. S. Pine, J. H. McDaniel, M. L. Salit, M. F. Young, and J. Simon, C. G., "The determination of stem cell fate by 3d scaffold structures through the control of cell shape," *Biomaterials*, vol. 32, no. 35, pp. 9188–96, 2011.

[130] J. L. Li, H. C. Bao, X. L. Hou, L. Sun, X. G. Wang, and M. Gu, "Graphene oxide nanoparticles as a nonbleaching optical probe for two-photon luminescence imaging and cell therapy," *Angew Chem Int Ed Engl*, vol. 51, no. 8, pp. 1830–4, 2012.

[131] K. Yang, S. Zhang, G. Zhang, X. Sun, S. T. Lee, and Z. Liu, "Graphene in mice: ultrahigh in vivo tumor uptake and efficient photothermal therapy," *Nano Lett*, vol. 10, no. 9, pp. 3318–23, 2010.

[132] Y. W. Zhu, S. Murali, W. W. Cai, X. S. Li, J. W. Suk, J. R. Potts, and R. S. Ruoff, "Graphene and graphene oxide: Synthesis, properties, and applications (vol 22, pg 3906, 2010)," *Advanced Materials*, vol. 22, no. 46, pp. 5226–5226, 2010.

[133] S. Some, S. M. Ho, P. Dua, E. Hwang, Y. H. Shin, H. Yoo, J. S. Kang, D. K. Lee, and H. Lee, "Dual functions of highly potent graphene derivative-poly-l-lysine composites to inhibit bacteria and support human cells," *ACS Nano*, vol. 6, no. 8, pp. 7151–61, 2012.

[134] G. Y. Chen, D. W. Pang, S. M. Hwang, H. Y. Tuan, and Y. C. Hu, "A graphene-based platform for induced pluripotent stem cells culture and differentiation," *Biomaterials*, vol. 33, no. 2, pp. 418–27, 2012.

[135] N. A. Kotov, J. O. Winter, I. P. Clements, E. Jan, B. P. Timko, S. Campidelli, S. Pathak, A. Mazzatenta, C. M. Lieber, M. Prato, R. V. Bellamkonda, G. A. Silva, N. W. S. Kam, F. Patolsky, and L. Ballerini, "Nanomaterials for neural interfaces," *Advanced Materials*, vol. 21, no. 40, pp. 3970–4004, 2009.

[136] K. Kang, S. E. Choi, H. S. Jang, W. K. Cho, Y. Nam, I. S. Choi, and J. S. Lee, "In vitro developmental acceleration of hippocampal neurons on nanostructures of self-assembled silica beads in filopodium-size ranges," *Angew Chem Int Ed Engl*, vol. 51, no. 12, pp. 2855–8, 2012.

[137] M. T. Lam, S. Sim, X. Zhu, and S. Takayama, "The effect of continuous wavy micropatterns on silicone substrates on the alignment of skeletal muscle myoblasts and myotubes," *Biomaterials*, vol. 27, no. 24, pp. 4340–7, 2006.

[138] J. Zhang, F. Zhang, H. Yang, X. Huang, H. Liu, J. Zhang, and S. Guo, "Graphene oxide as a matrix for enzyme immobilization," *Langmuir*, vol. 26, no. 9, pp. 6083–5, 2010.

[139] D. F. Cooke, A. B. Goldring, I. Yamayoshi, P. Tsourkas, G. H. Recanzone, A. Tiriac, T. Pan, S. I. Simon, and L. Krubitzer, "Fabrication of an inexpensive, implantable cooling device for reversible brain deactivation in animals ranging from rodents to primates," *J Neurophysiol*, vol. 107, no. 12, pp. 3543–58, 2012.

[140] N. Hallfors, A. Khan, M. D. Dickey, and A. M. Taylor, "Integration of pre-aligned liquid metal electrodes for neural stimulation within a user-friendly microfluidic platform," *Lab Chip*, vol. 13, no. 4, pp. 522–6, 2013.

[141] S. Liu, Y. Qu, T. J. Stewart, M. J. Howard, S. Chakrabortty, T. F. Holekamp, and J. W. McDonald, "Embryonic stem cells differentiate into oligodendrocytes and myelinate in culture and after spinal cord transplantation," *Proceedings of the National Academy of Sciences of the United States of America*, vol. 97, no. 11, pp. 6126–6131, 2000.

[142] S. Pluchino, A. Quattrini, E. Brambilla, A. Gritti, G. Salani, G. Dina, R. Galli, U. Del Carro, S. Amadio, A. Bergami, R. Furlan, G. Comi, A. L. Vescovi, and G. Martino, "Injection of adult neurospheres induces recovery in a chronic model of multiple sclerosis," *Nature*, vol. 422, no. 6933, pp. 688–94, 2003.

[143] C. Zhao, A. Tan, G. Pastorin, and H. K. Ho, "Nanomaterial scaffolds for stem cell proliferation and differentiation in tissue engineering," *Biotechnol Adv*, vol. 31, no. 5, pp. 654–68, 2013.

[144] T. Shindo, Y. Matsumoto, Q. Wang, N. Kawai, T. Tamiya, and S. Nagao, "Differences in the neuronal stem cells survival, neuronal differentiation and neurological improvement after transplantation of neural stem cells between mild and severe experimental traumatic brain injury," *J Med Invest*, vol. 53, no. 1-2, pp. 42–51, 2006.

[145] H. Cao, T. Liu, and S. Y. Chew, "The application of nanofibrous scaffolds in neural tissue engineering," *Adv Drug Deliv Rev*, vol. 61, no. 12, pp. 1055–64, 2009.

[146] G. Orive, E. Anitua, J. L. Pedraz, and D. F. Emerich, "Biomaterials for promoting brain protection, repair and regeneration," *Nat Rev Neurosci*, vol. 10, no. 9, pp. 682–92, 2009.

[147] H. S. Keirstead, G. Nistor, G. Bernal, M. Totoiu, F. Cloutier, K. Sharp, and O. Steward, "Human embryonic stem cell-derived oligodendrocyte progenitor cell transplants remyelinate and restore locomotion after spinal cord injury," *J Neurosci*, vol. 25, no. 19, pp. 4694–705, 2005.

[148] A. Solanki, S. Shah, P. T. Yin, and K. B. Lee, "Nanotopography-mediated reverse uptake for sirna delivery into neural stem cells to enhance neuronal differentiation," *Sci Rep*, vol. 3, p. 1553, 2013.

[149] J. Takahashi, T. D. Palmer, and F. H. Gage, "Retinoic acid and neurotrophins collaborate to regulate neurogenesis in adult-derived neural stem cell cultures," *J Neurobiol*, vol. 38, no. 1, pp. 65–81, 1999.

[150] F. Sher, R. Rossler, N. Brouwer, V. Balasubramaniyan, E. Boddeke, and S. Copray, "Differentiation of neural stem cells into oligodendrocytes: involvement of the polycomb group protein ezh2," *Stem Cells*, vol. 26, no. 11, pp. 2875–83, 2008.

[151] F. Sher, V. Balasubramaniyan, E. Boddeke, and S. Copray, "Oligodendrocyte differentiation and implantation: new insights for remyelinating cell therapy," *Curr Opin Neurol*, vol. 21, no. 5, pp. 607–14, 2008.

[152] Y. Zhu, S. Murali, W. Cai, X. Li, J. W. Suk, J. R. Potts, and R. S. Ruoff, "Graphene and graphene oxide: synthesis, properties, and applications," *Adv Mater*, vol. 22, no. 35, pp. 3906–24, 2010.

[153] J. Xie, M. R. MacEwan, A. G. Schwartz, and Y. Xia, "Electrospun nanofibers for neural tissue engineering," *Nanoscale*, vol. 2, no. 1, pp. 35–44, 2010.

[154] A. Cipitria, A. Skelton, T. R. Dargaville, P. D. Dalton, and D. W. Hutmacher, "Design, fabrication and characterization of pcl electrospun scaffolds-a review," *Journal of Materials Chemistry*, vol. 21, no. 26, pp. 9419–9453, 2011.

[155] G. T. Christopherson, H. Song, and H. Q. Mao, "The influence of fiber diameter of electrospun substrates on neural stem cell differentiation and proliferation," *Biomaterials*, vol. 30, no. 4, pp. 556–64, 2009.

[156] Q. Shen, Y. Wang, E. Kokovay, G. Lin, S. M. Chuang, S. K. Goderie, B. Roysam, and S. Temple, "Adult svz stem cells lie in a vascular niche: a quantitative analysis of niche cell-cell interactions," *Cell Stem Cell*, vol. 3, no. 3, pp. 289–300, 2008.

[157] N. Baumann and D. Pham-Dinh, "Biology of oligodendrocyte and myelin in the mammalian central nervous system," *Physiol Rev*, vol. 81, no. 2, pp. 871–927, 2001.

[158] S. Lee, M. K. Leach, S. A. Redmond, S. Y. Chong, S. H. Mellon, S. J. Tuck, Z. Q. Feng, J. M. Corey, and J. R. Chan, "A culture system to study oligodendrocyte myelination processes using engineered nanofibers," *Nat Methods*, vol. 9, no. 9, pp. 917–22, 2012.

[159] D. R. Nisbet, K. E. Crompton, M. K. Horne, D. I. Finkelstein, and J. S. Forsythe, "Neural tissue engineering of the cns using hydrogels," *J Biomed Mater Res B Appl Biomater*, vol. 87, no. 1, pp. 251–63, 2008.

[160] H. Colognato and I. D. Tzvetanova, "Glia unglued: how signals from the extracellular matrix regulate the development of myelinating glia," *Dev Neurobiol*, vol. 71, no. 11, pp. 924–55, 2011.

[161] R. W. O'Meara, J. P. Michalski, and R. Kothary, "Integrin signaling in oligodendrocytes and its importance in cns myelination," *J Signal Transduct*, vol. 2011, p. 354091, 2011.

[162] R. W. O'Meara, J. P. Michalski, C. Anderson, K. Bhanot, P. Rippstein, and R. Kothary, "Integrin-linked kinase regulates process extension in oligodendrocytes via control of actin cytoskeletal dynamics," *J Neurosci*, vol. 33, no. 23, pp. 9781–93, 2013.

[163] D. J. Osterhout, A. Wolven, R. M. Wolf, M. D. Resh, and M. V. Chao, "Morphological differentiation of oligodendrocytes requires activation of fyn tyrosine kinase," *J Cell Biol*, vol. 145, no. 6, pp. 1209–18, 1999.

[164] C. S. Barros, T. Nguyen, K. S. Spencer, A. Nishiyama, H. Colognato, and U. Muller, "Beta1 integrins are required for normal cns myelination and promote akt-dependent myelin outgrowth," *Development*, vol. 136, no. 16, pp. 2717–24, 2009.

[165] A. D. Forrest, H. E. Beggs, L. F. Reichardt, J. L. Dupree, R. J. Colello, and B. Fuss, "Focal adhesion kinase (fak): A regulator of cns myelination," *J Neurosci Res*, vol. 87, no. 15, pp. 3456–64, 2009.

[166] Y. Zhang, T. R. Nayak, H. Hong, and W. Cai, "Graphene: a versatile nanoplatform for biomedical applications," *Nanoscale*, vol. 4, no. 13, pp. 3833–42, 2012.

[167] W. Reik, "Stability and flexibility of epigenetic gene regulation in mammalian development," *Nature*, vol. 447, no. 7143, pp. 425–32, 2007.

[168] M. Iwafuchi-Doi and K. S. Zaret, "Pioneer transcription factors in cell reprogramming," *Genes Dev*, vol. 28, no. 24, pp. 2679–92, 2014.

[169] S. Yamanaka, "Induced pluripotent stem cells: past, present, and future," *Cell Stem Cell*, vol. 10, no. 6, pp. 678–84, 2012.

[170] S. O. Choi, Y. C. Kim, J. W. Lee, J. H. Park, M. R. Prausnitz, and M. G. Allen, "Intracellular protein delivery and gene transfection by electroporation using a microneedle electrode array," *Small*, vol. 8, no. 7, pp. 1081–91, 2012.

[171] M. Yan, J. Du, Z. Gu, M. Liang, Y. Hu, W. Zhang, S. Priceman, L. Wu, Z. H. Zhou, Z. Liu, T. Segura, Y. Tang, and Y. Lu, "A novel intracellular protein delivery platform based on single-protein nanocapsules," *Nat Nanotechnol*, vol. 5, no. 1, pp. 48–53, 2010.

[172] R. J. Debs, L. P. Freedman, S. Edmunds, K. L. Gaensler, N. Duzgunes, and K. R. Yamamoto, "Regulation of gene expression in vivo by liposome-mediated delivery of a purified transcription factor," *J Biol Chem*, vol. 265, no. 18, pp. 10189–92, 1990.

[173] J. Futami, M. Kitazoe, T. Maeda, E. Nukui, M. Sakaguchi, J. Kosaka, M. Miyazaki, M. Kosaka, H. Tada, M. Seno, J. Sasaki, N. H. Huh, M. Namba, and H. Yamada, "Intracellular delivery of proteins into mammalian living cells by polyethylenimine-cationization," *J Biosci Bioeng*, vol. 99, no. 2, pp. 95–103, 2005.

[174] Y. Liu, H. Wang, K. Kamei, M. Yan, K. J. Chen, Q. Yuan, L. Shi, Y. Lu, and H. R. Tseng, "Delivery of intact transcription factor by using self-assembled

supramolecular nanoparticles," *Angew Chem Int Ed Engl*, vol. 50, no. 13, pp. 3058–62, 2011.

[175] S. S. Bale, S. J. Kwon, D. A. Shah, A. Banerjee, J. S. Dordick, and R. S. Kane, "Nanoparticle-mediated cytoplasmic delivery of proteins to target cellular machinery," *ACS Nano*, vol. 4, no. 3, pp. 1493–500, 2010.

[176] Z. Gu, A. Biswas, M. Zhao, and Y. Tang, "Tailoring nanocarriers for intracellular protein delivery," *Chem Soc Rev*, vol. 40, no. 7, pp. 3638–55, 2011.

[177] C. O. Fagain, "Understanding and increasing protein stability," *Biochim Biophys Acta*, vol. 1252, no. 1, pp. 1–14, 1995.

[178] T. K. Kim and J. H. Eberwine, "Mammalian cell transfection: the present and the future," *Anal Bioanal Chem*, vol. 397, no. 8, pp. 3173–8, 2010.

[179] C. E. Thomas, A. Ehrhardt, and M. A. Kay, "Progress and problems with the use of viral vectors for gene therapy," *Nat Rev Genet*, vol. 4, no. 5, pp. 346–58, 2003.

[180] M. G. Kaplitt, A. Feigin, C. Tang, H. L. Fitzsimons, P. Mattis, P. A. Lawlor, R. J. Bland, D. Young, K. Strybing, D. Eidelberg, and M. J. During, "Safety and tolerability of gene therapy with an adeno-associated virus (aav) borne gad gene for parkinson's disease: an open label, phase i trial," *Lancet*, vol. 369, no. 9579, pp. 2097–105, 2007.

[181] J. Pomerantz and H. M. Blau, "Nuclear reprogramming: a key to stem cell function in regenerative medicine," *Nat Cell Biol*, vol. 6, no. 9, pp. 810–6, 2004.

[182] M. A. Mintzer and E. E. Simanek, "Nonviral vectors for gene delivery," *Chemical reviews*, vol. 109, no. 2, pp. 259–302, 2008.

[183] A. Santel, M. Aleku, O. Keil, J. Endruschat, V. Esche, B. Durieux, K. Loffler, M. Fechtner, T. Rohl, G. Fisch, S. Dames, W. Arnold, K. Giese, A. Klippel, and J. Kaufmann, "Rna interference in the mouse vascular endothelium by systemic administration of sirna-lipoplexes for cancer therapy," *Gene Ther*, vol. 13, no. 18, pp. 1360–70, 2006.

[184] C. Wolfrum, S. Shi, K. N. Jayaprakash, M. Jayaraman, G. Wang, R. K. Pandey, K. G. Rajeev, T. Nakayama, K. Charrise, E. M. Ndungo, T. Zimmermann, V. Koteliansky, M. Manoharan, and M. Stoffel, "Mechanisms and optimization of in vivo delivery of lipophilic sirnas," *Nat Biotechnol*, vol. 25, no. 10, pp. 1149–57, 2007.

[185] J. C. Burnett, J. J. Rossi, and K. Tiemann, "Current progress of sirna/shrna therapeutics in clinical trials," *Biotechnol J*, vol. 6, no. 9, pp. 1130–46, 2011.

[186] K. K. Park, K. Liu, Y. Hu, P. D. Smith, C. Wang, B. Cai, B. Xu, L. Connolly, I. Kramvis, M. Sahin, and Z. He, "Promoting axon regeneration in the adult cns by modulation of the pten/mtor pathway," *Science*, vol. 322, no. 5903, pp. 963–6, 2008.

[187] J. Qiu, D. Cai, H. Dai, M. McAtee, P. N. Hoffman, B. S. Bregman, and M. T. Filbin, "Spinal axon regeneration induced by elevation of cyclic amp," *Neuron*, vol. 34, no. 6, pp. 895–903, 2002.

[188] Z. Ahmed, R. G. Dent, E. L. Suggate, L. B. Barrett, R. J. Seabright, M. Berry, and A. Logan, "Disinhibition of neurotrophin-induced dorsal root ganglion cell neurite outgrowth on cns myelin by sirna-mediated knockdown of ngr, p75ntr and rho-a," *Mol Cell Neurosci*, vol. 28, no. 3, pp. 509–23, 2005.

[189] B. Blits, M. Oudega, G. J. Boer, M. Bartlett Bunge, and J. Verhaagen, "Adeno-associated viral vector-mediated neurotrophin gene transfer in the injured adult rat spinal cord improves hind-limb function," *Neuroscience*, vol. 118, no. 1, pp. 271–81, 2003.

[190] W. T. Hendriks, M. J. Ruitenberg, B. Blits, G. J. Boer, and J. Verhaagen, "Viral vector-mediated gene transfer of neurotrophins to promote regeneration of the injured spinal cord," *Prog Brain Res*, vol. 146, pp. 451–76, 2004.

[191] C. Rathnam, S. D. Chueng, L. Yang, and K. B. Lee, "Advanced gene manipulation methods for stem cell theranostics," *Theranostics*, vol. 7, no. 11, pp. 2775–2793, 2017.

[192] A. M. Alkilany, S. E. Lohse, and C. J. Murphy, "The gold standard: gold nanoparticle libraries to understand the nano-bio interface," *Acc Chem Res*, vol. 46, no. 3, pp. 650–61, 2013.

[193] S. M. Lucas, N. J. Rothwell, and R. M. Gibson, "The role of inflammation in cns injury and disease," *Br J Pharmacol*, vol. 147 Suppl 1, no. S1, pp. S232–40, 2006.

[194] M. V. Rockman and L. Kruglyak, "Genetics of global gene expression," *Nat Rev Genet*, vol. 7, no. 11, pp. 862–72, 2006.

[195] V. M. Weake and J. L. Workman, "Inducible gene expression: diverse regulatory mechanisms," *Nat Rev Genet*, vol. 11, no. 6, pp. 426–37, 2010.

[196] A. K. Mapp, A. Z. Ansari, M. Ptashne, and P. B. Dervan, "Activation of gene expression by small molecule transcription factors," *Proc Natl Acad Sci U S A*, vol. 97, no. 8, pp. 3930–5, 2000.

[197] N. Reynolds, A. O'Shaughnessy, and B. Hendrich, "Transcriptional repressors: multifaceted regulators of gene expression," *Development*, vol. 140, no. 3, pp. 505–12, 2013.

[198] S. Patel, D. Jung, P. T. Yin, P. Carlton, M. Yamamoto, T. Bando, H. Sugiyama, and K. B. Lee, "Nanoscript: a nanoparticle-based artificial transcription factor for effective gene regulation," *ACS Nano*, vol. 8, no. 9, pp. 8959–67, 2014.

[199] J. M. Gottesfeld, L. Neely, J. W. Trauger, E. E. Baird, and P. B. Dervan, "Regulation of gene expression by small molecules," *Nature*, vol. 387, no. 6629, pp. 202–5, 1997.

[200] P. B. Dervan and B. S. Edelson, "Recognition of the dna minor groove by pyrrole-imidazole polyamides," *Curr Opin Struct Biol*, vol. 13, no. 3, pp. 284–99, 2003.

[201] C. H. Leung, D. S. Chan, V. P. Ma, and D. L. Ma, "Dna-binding small molecules as inhibitors of transcription factors," *Med Res Rev*, vol. 33, no. 4, pp. 823–46, 2013.

[202] S. Mertin, S. G. McDowall, and V. R. Harley, "The dna-binding specificity of sox9 and other sox proteins," *Nucleic Acids Res*, vol. 27, no. 5, pp. 1359–64, 1999.

[203] A. L. Fisher, S. Ohsako, and M. Caudy, "The wrpw motif of the hairy-related basic helix-loop-helix repressor proteins acts as a 4-amino-acid transcription repression and protein-protein interaction domain," *Mol Cell Biol*, vol. 16, no. 6, pp. 2670–7, 1996.

[204] A. J. Courey and S. Jia, "Transcriptional repression: the long and the short of it," *Genes Dev*, vol. 15, no. 21, pp. 2786–96, 2001.

[205] Z. Paroush, J. Finley, R. L., T. Kidd, S. M. Wainwright, P. W. Ingham, R. Brent, and D. Ish-Horowicz, "Groucho is required for drosophila neurogenesis, segmentation, and sex determination and interacts directly with hairy-related bhlh proteins," *Cell*, vol. 79, no. 5, pp. 805–15, 1994.

[206] Z. Krpetic, S. Saleemi, I. A. Prior, V. See, R. Qureshi, and M. Brust, "Negotiation of intracellular membrane barriers by tat-modified gold nanoparticles," *ACS Nano*, vol. 5, no. 6, pp. 5195–201, 2011.

[207] J. V. Jokerst, T. Lobovkina, R. N. Zare, and S. S. Gambhir, "Nanoparticle pegylation for imaging and therapy," *Nanomedicine (Lond)*, vol. 6, no. 4, pp. 715–28, 2011.

[208] M. Colombo, S. Carregal-Romero, M. F. Casula, L. Gutierrez, M. P. Morales, I. B. Bohm, J. T. Heverhagen, D. Prosperi, and W. J. Parak, "Biological applications of magnetic nanoparticles," *Chem Soc Rev*, vol. 41, no. 11, pp. 4306–34, 2012.

[209] F. Scherer, M. Anton, U. Schillinger, J. Henke, C. Bergemann, A. Kruger, B. Gansbacher, and C. Plank, "Magnetofection: enhancing and targeting gene delivery by magnetic force in vitro and in vivo," *Gene Ther*, vol. 9, no. 2, pp. 102–9, 2002.

[210] H. Hinterwirth, S. Kappel, T. Waitz, T. Prohaska, W. Lindner, and M. Lammerhofer, "Quantifying thiol ligand density of self-assembled monolayers on gold nanoparticles by inductively coupled plasma-mass spectrometry," *ACS Nano*, vol. 7, no. 2, pp. 1129–36, 2013.

[211] C. C. Stolt, P. Lommes, E. Sock, M. C. Chaboissier, A. Schedl, and M. Wegner, "The sox9 transcription factor determines glial fate choice in the developing spinal cord," *Genes Dev*, vol. 17, no. 13, pp. 1677–89, 2003.

[212] T. Vierbuchen, A. Ostermeier, Z. P. Pang, Y. Kokubu, T. C. Sudhof, and M. Wernig, "Direct conversion of fibroblasts to functional neurons by defined factors," *Nature*, vol. 463, no. 7284, pp. 1035–41, 2010.

[213] C. Grienberger and A. Konnerth, "Imaging calcium in neurons," *Neuron*, vol. 73, no. 5, pp. 862–85, 2012.

[214] T. Vierbuchen, A. Ostermeier, Z. P. Pang, Y. Kokubu, T. C. Sudhof, and M. Wernig, "Direct conversion of fibroblasts to functional neurons by defined factors," *Nature*, vol. 463, no. 7284, pp. 1035–41, 2010.

[215] Y. Li, M. Liu, Y. Yan, and S. T. Yang, "Neural differentiation from pluripotent stem cells: The role of natural and synthetic extracellular matrix," *World J Stem Cells*, vol. 6, no. 1, pp. 11–23, 2014.

[216] R. J. Dumont, D. O. Okonkwo, S. Verma, R. J. Hurlbert, P. T. Boulos, D. B. Ellegala, and A. S. Dumont, "Acute spinal cord injury, part i: pathophysiologic mechanisms," *Clin Neuropharmacol*, vol. 24, no. 5, pp. 254–64, 2001.

[217] M. B. Bracken, M. J. Shepard, T. R. Holford, L. Leo-Summers, E. F. Aldrich, M. Fazl, M. Fehlings, D. L. Herr, P. W. Hitchon, L. F. Marshall, R. P. Nockels, V. Pascale, J. Perot, P. L., J. Piepmeier, V. K. Sonntag, F. Wagner, J. E. Wilberger, H. R. Winn, and W. Young, "Administration of methylprednisolone for 24 or 48 hours or tirilazad mesylate for 48 hours in the treatment of acute spinal cord injury. results of the third national acute spinal cord injury randomized controlled trial. national acute spinal cord injury study," *JAMA*, vol. 277, no. 20, pp. 1597–604, 1997.

[218] C. H. Tator and M. G. Fehlings, "Review of the secondary injury theory of acute spinal cord trauma with emphasis on vascular mechanisms," *J Neurosurg*, vol. 75, no. 1, pp. 15–26, 1991.

[219] Q. Wang, T. Stacy, M. Binder, M. Marin-Padilla, A. H. Sharpe, and N. A. Speck, "Disruption of the cbfa2 gene causes necrosis and hemorrhaging in the central nervous system and blocks definitive hematopoiesis," *Proc Natl Acad Sci U S A*, vol. 93, no. 8, pp. 3444–9, 1996.

[220] X. Z. Liu, X. M. Xu, R. Hu, C. Du, S. X. Zhang, J. W. McDonald, H. X. Dong, Y. J. Wu, G. S. Fan, M. F. Jacquin, C. Y. Hsu, and D. W. Choi, "Neuronal and glial apoptosis after traumatic spinal cord injury," *J Neurosci*, vol. 17, no. 14, pp. 5395–406, 1997.

[221] S. L. Shuman, J. C. Bresnahan, and M. S. Beattie, "Apoptosis of microglia and oligodendrocytes after spinal cord contusion in rats," *J Neurosci Res*, vol. 50, no. 5, pp. 798–808, 1997.

[222] J. C. Gensel and B. Zhang, "Macrophage activation and its role in repair and pathology after spinal cord injury," *Brain Res*, vol. 1619, pp. 1–11, 2015.

[223] G. Yiu and Z. He, "Glial inhibition of cns axon regeneration," *Nat Rev Neurosci*, vol. 7, no. 8, pp. 617–27, 2006.

[224] J. L. Goldberg, "How does an axon grow?," *Genes Dev*, vol. 17, no. 8, pp. 941–58, 2003.

[225] D. J. Donnelly and P. G. Popovich, "Inflammation and its role in neuroprotection, axonal regeneration and functional recovery after spinal cord injury," *Exp Neurol*, vol. 209, no. 2, pp. 378–88, 2008.

[226] K. Liu, Y. Lu, J. K. Lee, R. Samara, R. Willenberg, I. Sears-Kraxberger, A. Tedeschi, K. K. Park, D. Jin, B. Cai, B. Xu, L. Connolly, O. Steward, B. Zheng, and Z. He, "Pten deletion enhances the regenerative ability of adult corticospinal neurons," *Nat Neurosci*, vol. 13, no. 9, pp. 1075–81, 2010.

[227] T. Kurimoto, Y. Yin, K. Omura, H. Y. Gilbert, D. Kim, L. P. Cen, L. Moko, S. Kugler, and L. I. Benowitz, "Long-distance axon regeneration in the mature optic nerve: contributions of oncomodulin, camp, and pten gene deletion," *J Neurosci*, vol. 30, no. 46, pp. 15654–63, 2010.

[228] F. Sun, K. K. Park, S. Belin, D. Wang, T. Lu, G. Chen, K. Zhang, C. Yeung, G. Feng, B. A. Yankner, and Z. He, "Sustained axon regeneration induced by co-deletion of pten and socs3," *Nature*, vol. 480, no. 7377, pp. 372–5, 2011.

[229] B. Shah, P. T. Yin, S. Ghoshal, and K. B. Lee, "Multimodal magnetic core-shell nanoparticles for effective stem-cell differentiation and imaging," *Angew Chem Int Ed Engl*, vol. 52, no. 24, pp. 6190–5, 2013.

[230] V. Stambolic, D. MacPherson, D. Sas, Y. Lin, B. Snow, Y. Jang, S. Benchimol, and T. W. Mak, "Regulation of pten transcription by p53," *Mol Cell*, vol. 8, no. 2, pp. 317–25, 2001.

[231] G. N. Pandian, Y. Nakano, S. Sato, H. Morinaga, T. Bando, H. Nagase, and H. Sugiyama, "A synthetic small molecule for rapid induction of multiple pluripotency genes in mouse embryonic fibroblasts," *Sci Rep*, vol. 2, p. 544, 2012.

[232] G. N. Pandian, K. Shinohara, A. Ohtsuki, Y. Nakano, M. Masafumi, T. Bando, H. Nagase, Y. Yamada, A. Watanabe, N. Terada, S. Sato, H. Morinaga, and H. Sugiyama, "Synthetic small molecules for epigenetic activation of pluripotency genes in mouse embryonic fibroblasts," *Chembiochem*, vol. 12, no. 18, pp. 2822–8, 2011.

[233] E. Harrison, J. R. Nicol, M. Macias-Montero, G. A. Burke, J. A. Coulter, B. J. Meenan, and D. Dixon, "A comparison of gold nanoparticle surface co-functionalization approaches using polyethylene glycol (peg) and the effect on stability, non-specific protein adsorption and internalization," *Mater Sci Eng C Mater Biol Appl*, vol. 62, pp. 710–8, 2016.

[234] E. Goncalves, E. Kitas, and J. Seelig, "Binding of oligoarginine to membrane lipids and heparan sulfate: structural and thermodynamic characterization of a cell-penetrating peptide," *Biochemistry*, vol. 44, no. 7, pp. 2692–702, 2005.

[235] P. Thomas and T. G. Smart, "Hek293 cell line: a vehicle for the expression of recombinant proteins," *J Pharmacol Toxicol Methods*, vol. 51, no. 3, pp. 187–200, 2005.

[236] O. H. Iwenofu, R. D. Lackman, A. P. Staddon, D. G. Goodwin, H. M. Haupt, and J. S. Brooks, "Phospho-s6 ribosomal protein: a potential new predictive sarcoma marker for targeted mtor therapy," *Mod Pathol*, vol. 21, no. 3, pp. 231–7, 2008.

[237] R. Wu, N. Hendrix-Lucas, R. Kuick, Y. Zhai, D. R. Schwartz, A. Akyol, S. Hanash, D. E. Misek, H. Katabuchi, B. O. Williams, E. R. Fearon, and K. R.

Cho, "Mouse model of human ovarian endometrioid adenocarcinoma based on somatic defects in the wnt/beta-catenin and pi3k/pten signaling pathways," *Cancer Cell*, vol. 11, no. 4, pp. 321–33, 2007.

[238] C. G. Geoffroy, B. J. Hilton, W. Tetzlaff, and B. Zheng, "Evidence for an age-dependent decline in axon regeneration in the adult mammalian central nervous system," *Cell Rep*, vol. 15, no. 2, pp. 238–46, 2016.

[239] C. L. Veenman, A. Reiner, and M. G. Honig, "Biotinylated dextran amine as an anterograde tracer for single-and double-labeling studies," *Journal of neuroscience methods*, vol. 41, no. 3, pp. 239–254, 1992.

[240] A. Reiner, C. L. Veenman, L. Medina, Y. Jiao, N. Del Mar, and M. G. Honig, "Pathway tracing using biotinylated dextran amines," *Journal of Neuroscience Methods*, vol. 103, no. 1, pp. 23–37, 2000.

[241] D. J. Finney, *Statistical method in biological assay*. Charles Griffin: London, 1952.

[242] G. P. Quinn and M. J. Keough, *Experimental design and data analysis for biologists*. Cambridge University Press, 2002.

[243] G. Dahlberg, "Statistical methods for medical and biological students," *Statistical methods for medical and biological students.*, 1940.

[244] D. A. Hosack, J. Dennis, G., B. T. Sherman, H. C. Lane, and R. A. Lempicki, "Identifying biological themes within lists of genes with ease," *Genome Biol*, vol. 4, no. 10, p. R70, 2003.

[245] J. Wen, D. Sun, J. Tan, and W. Young, "A consistent, quantifiable, and graded rat lumbosacral spinal cord injury model," *J Neurotrauma*, vol. 32, no. 12, pp. 875–92, 2015.

[246] E. R. Kandel, J. H. Schwartz, and T. M. Jessel, "Essentials of neural science and behavior," 1995.

[247] M. Sarter and V. Parikh, "Choline transporters, cholinergic transmission and cognition," *Nat Rev Neurosci*, vol. 6, no. 1, pp. 48–56, 2005.

[248] L. Backman, L. Nyberg, U. Lindenberger, S. C. Li, and L. Farde, "The correlative triad among aging, dopamine, and cognition: current status and future prospects," *Neurosci Biobehav Rev*, vol. 30, no. 6, pp. 791–807, 2006.

[249] V. N. Luine, S. T. Richards, V. Y. Wu, and K. D. Beck, "Estradiol enhances learning and memory in a spatial memory task and effects levels of monoaminergic neurotransmitters," *Horm Behav*, vol. 34, no. 2, pp. 149–62, 1998.

[250] G. Wenk, D. Hughey, V. Boundy, A. Kim, L. Walker, and D. Olton, "Neurotransmitters and memory: role of cholinergic, serotonergic, and noradrenergic systems," *Behav Neurosci*, vol. 101, no. 3, pp. 325–32, 1987.

[251] D. Ziavra, G. Makri, P. Giompres, S. Taraviras, D. Thomaidou, R. Matsas, A. Mitsacos, and E. D. Kouvelas, "Neural stem cells transplanted in a mouse

model of parkinson's disease differentiate to neuronal phenotypes and reduce rotational deficit," *CNS Neurol Disord Drug Targets*, vol. 11, no. 7, pp. 829–35, 2012.

[252] S. Park, E. Kim, S. E. Koh, S. Maeng, W. D. Lee, J. Lim, I. Shim, and Y. J. Lee, "Dopaminergic differentiation of neural progenitors derived from placental mesenchymal stem cells in the brains of parkinson's disease model rats and alleviation of asymmetric rotational behavior," *Brain Res*, vol. 1466, pp. 158–66, 2012.

[253] A. Bjorklund, "Use of stem cells for cell replacement in parkinson's disease," *Febs Journal*, vol. 278, pp. 51–51, 2011.

[254] R. A. Fricker-Gates and M. A. Gates, "Stem cell-derived dopamine neurons for brain repair in parkinson's disease," *Regen Med*, vol. 5, no. 2, pp. 267–78, 2010.

[255] S. U. Kim, J. K. Ryu, J. Kim, J. H. Bang, H. B. Choi, M. A. Lee, B. K. Jin, K. K. Cho, and E. Nakagawa, "Cell replacement therapy in parkinson disease: Transplantation of human neural stem cells.," *Journal of Neuropathology and Experimental Neurology*, vol. 60, no. 5, pp. 530–530, 2001.

[256] X. Z. Ai, Q. Ma, and X. G. Su, "Nanosensor for dopamine and glutathione based on the quenching and recovery of the fluorescence of silica-coated quantum dots," *Microchimica Acta*, vol. 180, no. 3-4, pp. 269–277, 2013.

[257] X. M. Cao, L. Q. Luo, Y. P. Ding, X. L. Zou, and R. X. Bian, "Electrochemical methods for simultaneous determination of dopamine and ascorbic acid using cetylpyridine bromide/chitosan composite film-modified glassy carbon electrode," *Sensors and Actuators B-Chemical*, vol. 129, no. 2, pp. 941–946, 2008.

[258] S. Casalini, F. Leonardi, T. Cramer, and F. Biscarini, "Organic field-effect transistor for label-free dopamine sensing," *Organic Electronics*, vol. 14, no. 1, pp. 156–163, 2013.

[259] R. Freeman, J. Elbaz, R. Gill, M. Zayats, and I. Willner, "Analysis of dopamine and tyrosinase activity on ion-sensitive field-effect transistor (isfet) devices," *Chemistry*, vol. 13, no. 26, pp. 7288–93, 2007.

[260] S. Liu, F. Shi, X. Zhao, L. Chen, and X. Su, "3-aminophenyl boronic acid-functionalized cuins2 quantum dots as a near-infrared fluorescence probe for the determination of dopamine," *Biosens Bioelectron*, vol. 47, pp. 379–84, 2013.

[261] S. M. Wabaidur, Z. A. Alothman, S. H. Lee, and S. M. Alam, "Sensitive determination of dopamine by its fluorescence enhancement on terbium(iii)-dipicolinic acid system," *Sensor Letters*, vol. 10, no. 1-2, pp. 92–95, 2012.

[262] J. W. Lim and I. J. Kang, "Chitosan-gold nano composite for dopamine analysis using raman scattering," *Bulletin of the Korean Chemical Society*, vol. 34, no. 1, pp. 237–242, 2013.

[263] W. A. El-Said, T. H. Kim, H. Kim, and J. W. Choi, "Detection of effect of chemotherapeutic agents to cancer cells on gold nanoflower patterned substrate

using surface-enhanced raman scattering and cyclic voltammetry," *Biosens Bioelectron*, vol. 26, no. 4, pp. 1486–92, 2010.

[264] S. Pande, S. Jana, A. K. Sinha, S. Sarkar, M. Basu, M. Pradhan, A. Pal, J. Chowdhury, and T. Pal, "Dopamine molecules on au-core-ag-shell bimetallic nanocolloids: Fourier transform infrared, raman, and surface-enhanced raman spectroscopy study aided by density functional theory," *Journal of Physical Chemistry C*, vol. 113, no. 17, pp. 6989–7002, 2009.

[265] M. Guvendiren and J. A. Burdick, "Stiffening hydrogels to probe short- and long-term cellular responses to dynamic mechanics," *Nat Commun*, vol. 3, p. 792, 2012.

[266] I. L. Weissman, "Translating stem and progenitor cell biology to the clinic: barriers and opportunities," *Science*, vol. 287, no. 5457, pp. 1442–6, 2000.

[267] A. M. Maroof, S. Keros, J. A. Tyson, S. W. Ying, Y. M. Ganat, F. T. Merkle, B. Liu, A. Goulburn, E. G. Stanley, A. G. Elefanty, H. R. Widmer, K. Eggan, P. A. Goldstein, S. A. Anderson, and L. Studer, "Directed differentiation and functional maturation of cortical interneurons from human embryonic stem cells," *Cell Stem Cell*, vol. 12, no. 5, pp. 559–72, 2013.

[268] F. Guilak, D. M. Cohen, B. T. Estes, J. M. Gimble, W. Liedtke, and C. S. Chen, "Control of stem cell fate by physical interactions with the extracellular matrix," *Cell Stem Cell*, vol. 5, no. 1, pp. 17–26, 2009.

[269] A. J. Engler, S. Sen, H. L. Sweeney, and D. E. Discher, "Matrix elasticity directs stem cell lineage specification," *Cell*, vol. 126, no. 4, pp. 677–89, 2006.

[270] V. Castiglioni, M. Onorati, C. Rochon, and E. Cattaneo, "Induced pluripotent stem cell lines from huntington's disease mice undergo neuronal differentiation while showing alterations in the lysosomal pathway," *Neurobiol Dis*, vol. 46, no. 1, pp. 30–40, 2012.

[271] P. T. Yin, S. Shah, M. Chhowalla, and K. B. Lee, "Design, synthesis, and characterization of graphene-nanoparticle hybrid materials for bioapplications," *Chem Rev*, vol. 115, no. 7, pp. 2483–531, 2015.

[272] M. Nikkhah, F. Edalat, S. Manoucheri, and A. Khademhosseini, "Engineering microscale topographies to control the cell-substrate interface," *Biomaterials*, vol. 33, no. 21, pp. 5230–46, 2012.

[273] D. W. Han, N. Tapia, A. Hermann, K. Hemmer, S. Hoing, M. J. Arauzo-Bravo, H. Zaehres, G. Wu, S. Frank, S. Moritz, B. Greber, J. H. Yang, H. T. Lee, J. C. Schwamborn, A. Storch, and H. R. Scholer, "Direct reprogramming of fibroblasts into neural stem cells by defined factors," *Cell Stem Cell*, vol. 10, no. 4, pp. 465–72, 2012.

[274] M. Bellin, M. C. Marchetto, F. H. Gage, and C. L. Mummery, "Induced pluripotent stem cells: the new patient?," *Nat Rev Mol Cell Biol*, vol. 13, no. 11, pp. 713–26, 2012.

[275] L. Qiang, R. Fujita, and A. Abeliovich, "Remodeling neurodegeneration: somatic cell reprogramming-based models of adult neurological disorders," *Neuron*, vol. 78, no. 6, pp. 957–69, 2013.

[276] M. Wernig, J. P. Zhao, J. Pruszak, E. Hedlund, D. Fu, F. Soldner, V. Broccoli, M. Constantine-Paton, O. Isacson, and R. Jaenisch, "Neurons derived from reprogrammed fibroblasts functionally integrate into the fetal brain and improve symptoms of rats with parkinson's disease," *Proc Natl Acad Sci U S A*, vol. 105, no. 15, pp. 5856–61, 2008.

[277] O. Lindvall, Z. Kokaia, and A. Martinez-Serrano, "Stem cell therapy for human neurodegenerative disorders-how to make it work," *Nat Med*, vol. 10 Suppl, pp. S42–50, 2004.

[278] J. H. Kim, J. M. Auerbach, J. A. Rodriguez-Gomez, I. Velasco, D. Gavin, N. Lumelsky, S. H. Lee, J. Nguyen, R. Sanchez-Pernaute, K. Bankiewicz, and R. McKay, "Dopamine neurons derived from embryonic stem cells function in an animal model of parkinson's disease," *Nature*, vol. 418, no. 6893, pp. 50–6, 2002.

[279] T. H. Kim, C. H. Yea, S. T. Chueng, P. T. Yin, B. Conley, K. Dardir, Y. Pak, G. Y. Jung, J. W. Choi, and K. B. Lee, "Large-scale nanoelectrode arrays to monitor the dopaminergic differentiation of human neural stem cells," *Adv Mater*, vol. 27, no. 41, pp. 6356–62, 2015.

[280] M. J. Biggs, R. G. Richards, N. Gadegaard, C. D. Wilkinson, R. O. Oreffo, and M. J. Dalby, "The use of nanoscale topography to modulate the dynamics of adhesion formation in primary osteoblasts and erk/mapk signalling in stro-1+ enriched skeletal stem cells," *Biomaterials*, vol. 30, no. 28, pp. 5094–103, 2009.

[281] K. R. Milner and C. A. Siedlecki, "Submicron poly(l-lactic acid) pillars affect fibroblast adhesion and proliferation," *J Biomed Mater Res A*, vol. 82, no. 1, pp. 80–91, 2007.

[282] R. J. McMurray, N. Gadegaard, P. M. Tsimbouri, K. V. Burgess, L. E. McNamara, R. Tare, K. Murawski, E. Kingham, R. O. Oreffo, and M. J. Dalby, "Nanoscale surfaces for the long-term maintenance of mesenchymal stem cell phenotype and multipotency," *Nat Mater*, vol. 10, no. 8, pp. 637–44, 2011.

[283] K. Kulangara, Y. Yang, J. Yang, and K. W. Leong, "Nanotopography as modulator of human mesenchymal stem cell function," *Biomaterials*, vol. 33, no. 20, pp. 4998–5003, 2012.

[284] W. Chen, L. G. Villa-Diaz, Y. Sun, S. Weng, J. K. Kim, R. H. Lam, L. Han, R. Fan, P. H. Krebsbach, and J. Fu, "Nanotopography influences adhesion, spreading, and self-renewal of human embryonic stem cells," *ACS Nano*, vol. 6, no. 5, pp. 4094–103, 2012.

[285] H. F. Cui, J. S. Ye, Y. Chen, S. C. Chong, X. Liu, T. M. Lim, and F. S. Sheu, "In situ temporal detection of dopamine exocytosis from l-dopa-incubated mn9d cells using microelectrode array-integrated biochip," *Sensors and Actuators B-Chemical*, vol. 115, no. 2, pp. 634–641, 2006.

[286] L. Amato, A. Heiskanen, C. Caviglia, F. Shah, K. Zór, M. Skolimowski, M. Madou, L. Gammelgaard, R. Hansen, and E. G. J. A. f. m. Seiz, "Pyrolysed 3d-carbon scaffolds induce spontaneous differentiation of human neural stem cells and facilitate real-time dopamine detection," *Advanced Functional Materials*, vol. 24, no. 44, pp. 7042–7052, 2014.

[287] M. B. Hariri, A. Dolati, and R. S. Moakhar, "The potentiostatic electrodeposition of gold nanowire/nanotube in haucl4 solutions based on the model of recessed cylindrical ultramicroelectrode array," *Journal of the Electrochemical Society*, vol. 160, no. 6, pp. D279–D288, 2013.

[288] M. Zhou, Y. Zhai, and S. Dong, "Electrochemical sensing and biosensing platform based on chemically reduced graphene oxide," *Anal Chem*, vol. 81, no. 14, pp. 5603–13, 2009.

[289] L. H. Tang, Y. Wang, Y. M. Li, H. B. Feng, J. Lu, and J. H. Li, "Preparation, structure, and electrochemical properties of reduced graphene sheet films," *Advanced Functional Materials*, vol. 19, no. 17, pp. 2782–2789, 2009.

[290] H. F. Cui, J. S. Ye, Y. Chen, S. C. Chong, and F. S. Sheu, "Microelectrode array biochip: tool for in vitro drug screening based on the detection of a drug effect on dopamine release from pc12 cells," *Anal Chem*, vol. 78, no. 18, pp. 6347–55, 2006.

[291] M. Abdul Kafi, W. A. El-Said, T. H. Kim, and J. W. Choi, "Cell adhesion, spreading, and proliferation on surface functionalized with rgd nanopillar arrays," *Biomaterials*, vol. 33, no. 3, pp. 731–9, 2012.

[292] G. Petit, T. Olsson, P. J. N. Brundin, and a. neurobiology, "The future of cell therapies and brain repair: P arkinson's disease leads the way," *Neuropathology and Applied Neurobiology*, vol. 40, no. 1, pp. 60–70, 2014.

[293] S. Pai, F. Verrier, H. Sun, H. Hu, A. M. Ferrie, A. Eshraghi, and Y. Fang, "Dynamic mass redistribution assay decodes differentiation of a neural progenitor stem cell," *J Biomol Screen*, vol. 17, no. 9, pp. 1180–91, 2012.

[294] R. Donato, E. A. Miljan, S. J. Hines, S. Aouabdi, K. Pollock, S. Patel, F. A. Edwards, and J. D. Sinden, "Differential development of neuronal physiological responsiveness in two human neural stem cell lines," *BMC Neurosci*, vol. 8, no. 1, p. 36, 2007.

[295] Z. L. Chaudhry and B. Y. Ahmed, "Caspase-2 and caspase-8 trigger caspase-3 activation following 6-ohda-induced stress in human dopaminergic neurons differentiated from renvm stem cells," *Neurol Res*, vol. 35, no. 4, pp. 435–40, 2013.

[296] M. Caiazzo, M. T. Dell'Anno, E. Dvoretskova, D. Lazarevic, S. Taverna, D. Leo, T. D. Sotnikova, A. Menegon, P. Roncaglia, G. Colciago, G. Russo, P. Carninci, G. Pezzoli, R. R. Gainetdinov, S. Gustincich, A. Dityatev, and V. Broccoli, "Direct generation of functional dopaminergic neurons from mouse and human fibroblasts," *Nature*, vol. 476, no. 7359, pp. 224–7, 2011.

[297] C. E. Muller-Sieburg, H. B. Sieburg, J. M. Bernitz, and G. Cattarossi, "Stem cell heterogeneity: implications for aging and regenerative medicine," *Blood*, vol. 119, no. 17, pp. 3900–7, 2012.

[298] P. Cahan and G. Q. Daley, "Origins and implications of pluripotent stem cell variability and heterogeneity," *Nat Rev Mol Cell Biol*, vol. 14, no. 6, pp. 357–68, 2013.

[299] P. S. Knoepfler, "From bench to fda to bedside: Us regulatory trends for new stem cell therapies," *Adv Drug Deliv Rev*, vol. 82-83, no. Supplement C, pp. 192–6, 2015.

[300] J. L. Sterneckert, P. Reinhardt, and H. R. Scholer, "Investigating human disease using stem cell models," *Nat Rev Genet*, vol. 15, no. 9, pp. 625–39, 2014.

[301] K. H. Narsinh, N. Sun, V. Sanchez-Freire, A. S. Lee, P. Almeida, S. Hu, T. Jan, K. D. Wilson, D. Leong, J. Rosenberg, M. Yao, R. C. Robbins, and J. C. Wu, "Single cell transcriptional profiling reveals heterogeneity of human induced pluripotent stem cells," *J Clin Invest*, vol. 121, no. 3, pp. 1217–21, 2011.

[302] U. Ben-David and N. Benvenisty, "The tumorigenicity of human embryonic and induced pluripotent stem cells," *Nat Rev Cancer*, vol. 11, no. 4, pp. 268–77, 2011.

[303] A. S. Lee, C. Tang, M. S. Rao, I. L. Weissman, and J. C. Wu, "Tumorigenicity as a clinical hurdle for pluripotent stem cell therapies," *Nat Med*, vol. 19, no. 8, pp. 998–1004, 2013.

[304] P. S. Knoepfler, "Deconstructing stem cell tumorigenicity: a roadmap to safe regenerative medicine," *Stem Cells*, vol. 27, no. 5, pp. 1050–6, 2009.

[305] M. J. Dalby, N. Gadegaard, and R. O. Oreffo, "Harnessing nanotopography and integrin-matrix interactions to influence stem cell fate," *Nat Mater*, vol. 13, no. 6, pp. 558–69, 2014.

[306] K. A. Kilian, B. Bugarija, B. T. Lahn, and M. Mrksich, "Geometric cues for directing the differentiation of mesenchymal stem cells," *Proc Natl Acad Sci U S A*, vol. 107, no. 11, pp. 4872–7, 2010.

[307] X. Wang, S. Li, C. Yan, P. Liu, and J. Ding, "Fabrication of rgd micro/nanopattern and corresponding study of stem cell differentiation," *Nano Lett*, vol. 15, no. 3, pp. 1457–67, 2015.

[308] R. McBeath, D. M. Pirone, C. M. Nelson, K. Bhadriraju, and C. S. Chen, "Cell shape, cytoskeletal tension, and rhoa regulate stem cell lineage commitment," *Dev Cell*, vol. 6, no. 4, pp. 483–95, 2004.

[309] J. H. Tsui, K. Janebodin, N. Ieronimakis, D. M. P. Yama, H. S. Yang, R. Chavanachat, A. L. Hays, H. Lee, M. Reyes, and D. H. Kim, "Harnessing sphingosine-1-phosphate signaling and nanotopographical cues to regulate skeletal muscle maturation and vascularization," *ACS Nano*, vol. 11, no. 12, pp. 11954–11968, 2017.

[310] T. R. Nayak, H. Andersen, V. S. Makam, C. Khaw, S. Bae, X. Xu, P. L. Ee, J. H. Ahn, B. H. Hong, G. Pastorin, and B. Ozyilmaz, "Graphene for controlled and accelerated osteogenic differentiation of human mesenchymal stem cells," *ACS Nano*, vol. 5, no. 6, pp. 4670–8, 2011.

[311] J. Yang, L. E. McNamara, N. Gadegaard, E. V. Alakpa, K. V. Burgess, R. M. Meek, and M. J. Dalby, "Nanotopographical induction of osteogenesis through adhesion, bone morphogenic protein cosignaling, and regulation of microrna," *ACS Nano*, vol. 8, no. 10, pp. 9941–53, 2014.

[312] H. S. Goodwin, A. R. Bicknese, S. N. Chien, B. D. Bogucki, C. O. Quinn, and D. A. Wall, "Multilineage differentiation activity by cells isolated from umbilical cord blood: expression of bone, fat, and neural markers," *Biol Blood Marrow Transplant*, vol. 7, no. 11, pp. 581–8, 2001.

[313] M. F. Pittenger, A. M. Mackay, S. C. Beck, R. K. Jaiswal, R. Douglas, J. D. Mosca, M. A. Moorman, D. W. Simonetti, S. Craig, and D. R. Marshak, "Multilineage potential of adult human mesenchymal stem cells," *Science*, vol. 284, no. 5411, pp. 143–7, 1999.

[314] P. M. Tsimbouri, P. G. Childs, G. D. Pemberton, J. Yang, V. Jayawarna, W. Orapiriyakul, K. Burgess, C. González-García, G. Blackburn, D. Thomas, C. Vallejo-Giraldo, M. J. P. Biggs, A. S. G. Curtis, M. Salmerón-Sánchez, S. Reid, and M. J. Dalby, "Stimulation of 3d osteogenesis by mesenchymal stem cells using a nanovibrational bioreactor," *Nature Biomedical Engineering*, vol. 1, no. 9, pp. 758–770, 2017.

[315] J. M. Kanczler and R. O. Oreffo, "Osteogenesis and angiogenesis: the potential for engineering bone," *Eur Cell Mater*, vol. 15, no. 2, pp. 100–14, 2008.

[316] J. Lee, H. K. Choi, L. Yang, S. D. Chueng, J. Choi, and K. Lee, "Nondestructive real-time monitoring of enhanced stem cell differentiation using a graphene-au hybrid nanoelectrode array," *Advanced Materials*, p. 1802762, 2018.

[317] M. P. Lutolf, P. M. Gilbert, and H. M. Blau, "Designing materials to direct stem-cell fate," *Nature*, vol. 462, no. 7272, pp. 433–41, 2009.

[318] W. Chen, Y. Shao, X. Li, G. Zhao, and J. Fu, "Nanotopographical surfaces for stem cell fate control: Engineering mechanobiology from the bottom," *Nano Today*, vol. 9, no. 6, pp. 759–784, 2014.

[319] T. Iskratsch, H. Wolfenson, and M. P. Sheetz, "Appreciating force and shape-the rise of mechanotransduction in cell biology," *Nat Rev Mol Cell Biol*, vol. 15, no. 12, pp. 825–33, 2014.

[320] D. Chen, H. Feng, and J. Li, "Graphene oxide: preparation, functionalization, and electrochemical applications," *Chem Rev*, vol. 112, no. 11, pp. 6027–53, 2012.

[321] M. Zhou, Y. Zhai, and S. Dong, "Electrochemical sensing and biosensing platform based on chemically reduced graphene oxide," *Anal Chem*, vol. 81, no. 14, pp. 5603–13, 2009.

[322] J. H. Lee, B. K. Oh, and J. W. Choi, "Electrochemical sensor based on direct electron transfer of hiv-1 virus at au nanoparticle modified ito electrode," *Biosens Bioelectron*, vol. 49, no. Supplement C, pp. 531–5, 2013.

[323] K. S. Kim, H. Jeong, M. S. Jeong, and G. Y. Jung, "Polymer-templated hydrothermal growth of vertically aligned single-crystal zno nanorods and morphological transformations using structural polarity," *Advanced Functional Materials*, vol. 20, no. 18, pp. 3055–3063, 2010.

[324] C. Selhuber-Unkel, M. Lopez-Garcia, H. Kessler, and J. P. Spatz, "Cooperativity in adhesion cluster formation during initial cell adhesion," *Biophys J*, vol. 95, no. 11, pp. 5424–31, 2008.

[325] X. H. Li, W. C. H. Choy, X. G. Ren, D. Zhang, and H. F. Lu, "Highly intensified surface enhanced raman scattering by using monolayer graphene as the nanospacer of metal film-metal nanoparticle coupling system," *Advanced Functional Materials*, vol. 24, no. 21, pp. 3114–3122, 2014.

[326] N. Yi, C. Zhang, Q. Song, and S. Xiao, "A hybrid system with highly enhanced graphene sers for rapid and tag-free tumor cells detection," *Sci Rep*, vol. 6, p. 25134, 2016.

[327] S. Stankovich, D. A. Dikin, R. D. Piner, K. A. Kohlhaas, A. Kleinhammes, Y. Jia, Y. Wu, S. T. Nguyen, and R. S. Ruoff, "Synthesis of graphene-based nanosheets via chemical reduction of exfoliated graphite oxide," *Carbon*, vol. 45, no. 7, pp. 1558–1565, 2007.

[328] S. Eigler, C. Dotzer, and A. Hirsch, "Visualization of defect densities in reduced graphene oxide," *Carbon*, vol. 50, no. 10, pp. 3666–3673, 2012.

[329] M. H. You, M. K. Kwak, D. H. Kim, K. Kim, A. Levchenko, D. Y. Kim, and K. Y. Suh, "Synergistically enhanced osteogenic differentiation of human mesenchymal stem cells by culture on nanostructured surfaces with induction media," *Biomacromolecules*, vol. 11, no. 7, pp. 1856–62, 2010.

[330] S. Khetan, M. Guvendiren, W. R. Legant, D. M. Cohen, C. S. Chen, and J. A. Burdick, "Degradation-mediated cellular traction directs stem cell fate in covalently crosslinked three-dimensional hydrogels," *Nat Mater*, vol. 12, no. 5, pp. 458–65, 2013.

[331] B. Geiger and A. Bershadsky, "Assembly and mechanosensory function of focal contacts," *Curr Opin Cell Biol*, vol. 13, no. 5, pp. 584–92, 2001.

[332] Q. Chen, P. Shou, C. Zheng, M. Jiang, G. Cao, Q. Yang, J. Cao, N. Xie, T. Velletri, X. Zhang, C. Xu, L. Zhang, H. Yang, J. Hou, Y. Wang, and Y. Shi, "Fate decision of mesenchymal stem cells: adipocytes or osteoblasts?," *Cell Death Differ*, vol. 23, no. 7, pp. 1128–39, 2016.

[333] C. Ge, Q. Yang, G. Zhao, H. Yu, K. L. Kirkwood, and R. T. Franceschi, "Interactions between extracellular signal-regulated kinase 1/2 and p38 map kinase pathways in the control of runx2 phosphorylation and transcriptional activity," *J Bone Miner Res*, vol. 27, no. 3, pp. 538–51, 2012.

[334] J. Wang, "Carbon-nanotube based electrochemical biosensors: A review," *Electroanalysis*, vol. 17, no. 1, pp. 7–14, 2005.

[335] A. M. Yu, Z. J. Liang, J. Cho, and F. Caruso, "Nanostructured electrochemical sensor based on dense gold nanoparticle films," *Nano Letters*, vol. 3, no. 9, pp. 1203–1207, 2003.

[336] Y. S. Fu, S. H. Ji, X. Chen, X. C. Ma, R. Wu, C. C. Wang, W. H. Duan, X. H. Qiu, B. Sun, P. Zhang, J. F. Jia, and Q. K. Xue, "Manipulating the kondo resonance through quantum size effects," *Phys Rev Lett*, vol. 99, no. 25, p. 256601, 2007.

[337] C. Zhu, G. Yang, H. Li, D. Du, and Y. Lin, "Electrochemical sensors and biosensors based on nanomaterials and nanostructures," *Anal Chem*, vol. 87, no. 1, pp. 230–49, 2015.

[338] A. Ambrosi, C. K. Chua, A. Bonanni, and M. Pumera, "Electrochemistry of graphene and related materials," *Chem Rev*, vol. 114, no. 14, pp. 7150–88, 2014.

[339] J. N. Beresford, J. H. Bennett, C. Devlin, P. S. Leboy, and M. E. Owen, "Evidence for an inverse relationship between the differentiation of adipocytic and osteogenic cells in rat marrow stromal cell-cultures," *Journal of Cell Science*, vol. 102, no. 2, pp. 341–351, 1992.

[340] G. R. Beck, E. C. Sullivan, E. Moran, and B. Zerler, "Relationship between alkaline phosphatase levels, osteopontin expression, and mineralization in differentiating mc3t3-e1 osteoblasts," *Journal of Cellular Biochemistry*, vol. 68, no. 2, pp. 269–280, 1998.

[341] N. Balis, E. Stratakis, and E. Kymakis, "Graphene and transition metal dichalcogenide nanosheets as charge transport layers for solution processed solar cells," *Materials Today*, vol. 19, no. 10, pp. 580–594, 2016.

[342] J. S. Yeo, R. Kang, S. Lee, Y. J. Jeon, N. Myoung, C. L. Lee, D. Y. Kim, J. M. Yun, Y. H. Seo, S. S. Kim, and S. I. Na, "Highly efficient and stable planar perovskite solar cells with reduced graphene oxide nanosheets as electrode interlayer," *Nano Energy*, vol. 12, pp. 96–104, 2015.

[343] H. Jiao, J. Chen, W. Li, F. Wang, H. Zhou, Y. Li, and C. Yu, "Nucleic acid-regulated perylene probe-induced gold nanoparticle aggregation: a new strategy for colorimetric sensing of alkaline phosphatase activity and inhibitor screening," *ACS Appl Mater Interfaces*, vol. 6, no. 3, pp. 1979–85, 2014.

[344] A. Safadi, E. Livne, M. Silbermann, and A. Z. Reznick, "Activity of alkaline phosphatase in rat skeletal muscle localized along the sarcolemma and endothelial cell membranes," *J Histochem Cytochem*, vol. 39, no. 2, pp. 199–203, 1991.

[345] A. Dellavalle, M. Sampaolesi, R. Tonlorenzi, E. Tagliafico, B. Sacchetti, L. Perani, A. Innocenzi, B. G. Galvez, G. Messina, R. Morosetti, S. Li, M. Belicchi, G. Peretti, J. S. Chamberlain, W. E. Wright, Y. Torrente, S. Ferrari, P. Bianco, and G. Cossu, "Pericytes of human skeletal muscle are myogenic precursors distinct from satellite cells," *Nat Cell Biol*, vol. 9, no. 3, pp. 255–67, 2007.

[346] Y. Shi, H. Inoue, J. C. Wu, and S. Yamanaka, "Induced pluripotent stem cell technology: a decade of progress," *Nat Rev Drug Discov*, vol. 16, no. 2, pp. 115–130, 2017.

[347] M. J. Workman, M. M. Mahe, S. Trisno, H. M. Poling, C. L. Watson, N. Sundaram, C. F. Chang, J. Schiesser, P. Aubert, E. G. Stanley, A. G. Elefanty, Y. Miyaoka, M. A. Mandegar, B. R. Conklin, M. Neunlist, S. A. Brugmann, M. A. Helmrath, and J. M. Wells, "Engineered human pluripotent-stem-cell-derived intestinal tissues with a functional enteric nervous system," *Nat Med*, vol. 23, no. 1, pp. 49–59, 2017.

[348] D. Dutta, I. Heo, and H. Clevers, "Disease modeling in stem cell-derived 3d organoid systems," *Trends Mol Med*, vol. 23, no. 5, pp. 393–410, 2017.

[349] A. Ascherio and M. A. Schwarzschild, "The epidemiology of parkinson's disease: risk factors and prevention," *Lancet Neurol*, vol. 15, no. 12, pp. 1257–1272, 2016.

[350] G. Logroscino, M. Piccininni, B. Marin, E. Nichols, F. Abd-Allah, A. Abdelalim, F. Alahdab, S. W. Asgedom, A. Awasthi, Y. Chaiah, A. Daryani, H. P. Do, M. Dubey, A. Elbaz, S. Eskandarieh, F. Farhadi, F. Farzadfar, S. M. Fereshtehnejad, E. Fernandes, I. Filip, K. J. Foreman, A. K. Gebre, E. V. Gnedovskaya, S. Hamidi, S. I. Hay, S. S. N. Irvani, J. S. Ji, A. Kasaeian, Y. J. Kim, L. G. Mantovani, T. P. Mashamba-Thompson, M. M. Mehndiratta, A. H. Mokdad, G. Nagel, T. H. Nguyen, M. R. Nixon, A. T. Olagunju, M. O. Owolabi, M. A. Piradov, M. Qorbani, A. Radfar, R. C. Reiner, M. A. Sahraian, S. Sarvi, M. Sharif, O. Temsah, B. X. Tran, N. T. Truong, N. Venketasubramanian, A. S. Winkler, E. M. Yimer, V. L. Feigin, T. Vos, C. J. L. Murray, and G. . M. N. D. Collabor, "Global, regional, and national burden of motor neuron diseases 1990-2016: a systematic analysis for the global burden of disease study 2016," *Lancet Neurology*, vol. 17, no. 12, pp. 1083–1097, 2018.

[351] A. Trounson and N. D. DeWitt, "Pluripotent stem cells progressing to the clinic," *Nat Rev Mol Cell Biol*, vol. 17, no. 3, pp. 194–200, 2016.

[352] I. Espuny-Camacho, A. M. Arranz, M. Fiers, A. Snellinx, K. Ando, S. Munck, J. Bonnefont, L. Lambot, N. Corthout, and L. Omodho, "Hallmarks of alzheimer's disease in stem-cell-derived human neurons transplanted into mouse brain," *Neuron*, vol. 93, no. 5, pp. 1066–1081. e8, 2017.

[353] P. J. Hallett, M. Deleidi, A. Astradsson, G. A. Smith, O. Cooper, T. M. Osborn, M. Sundberg, M. A. Moore, E. Perez-Torres, and A.-L. Brownell, "Successful function of autologous ipsc-derived dopamine neurons following transplantation in a non-human primate model of parkinson's disease," *Cell stem cell*, vol. 16, no. 3, pp. 269–274, 2015.

[354] A. Trounson and C. McDonald, "Stem cell therapies in clinical trials: Progress and challenges," *Cell Stem Cell*, vol. 17, no. 1, pp. 11–22, 2015.

[355] K. G. Chen, B. S. Mallon, R. D. McKay, and P. G. Robey, "Human pluripotent stem cell culture: considerations for maintenance, expansion, and therapeutics," *Cell Stem Cell*, vol. 14, no. 1, pp. 13–26, 2014.

[356] S. Dimmeler, S. Ding, T. A. Rando, and A. Trounson, "Translational strategies and challenges in regenerative medicine," *Nat Med*, vol. 20, no. 8, pp. 814–21, 2014.

[357] J. Ratajczak, K. Miekus, M. Kucia, J. Zhang, R. Reca, P. Dvorak, and M. Z. Ratajczak, "Embryonic stem cell-derived microvesicles reprogram hematopoietic progenitors: evidence for horizontal transfer of mrna and protein delivery," *Leukemia*, vol. 20, no. 5, pp. 847–56, 2006.

[358] A. V. Vlassov, S. Magdaleno, R. Setterquist, and R. Conrad, "Exosomes: current knowledge of their composition, biological functions, and diagnostic and therapeutic potentials," *Biochim Biophys Acta*, vol. 1820, no. 7, pp. 940–8, 2012.

[359] C. Thery, M. Ostrowski, and E. Segura, "Membrane vesicles as conveyors of immune responses," *Nat Rev Immunol*, vol. 9, no. 8, pp. 581–93, 2009.

[360] H. Im, H. Shao, Y. I. Park, V. M. Peterson, C. M. Castro, R. Weissleder, and H. Lee, "Label-free detection and molecular profiling of exosomes with a nanoplasmonic sensor," *Nat Biotechnol*, vol. 32, no. 5, pp. 490–5, 2014.

[361] X. Huang, T. Yuan, M. Tschannen, Z. Sun, H. Jacob, M. Du, M. Liang, R. L. Dittmar, Y. Liu, M. Liang, M. Kohli, S. N. Thibodeau, L. Boardman, and L. Wang, "Characterization of human plasma-derived exosomal rnas by deep sequencing," *BMC Genomics*, vol. 14, p. 319, 2013.

[362] E. Lund, S. Guttinger, A. Calado, J. E. Dahlberg, and U. Kutay, "Nuclear export of microrna precursors," *Science*, vol. 303, no. 5654, pp. 95–8, 2004.

[363] D. W. Greening, R. Xu, H. Ji, B. J. Tauro, and R. J. Simpson, *A protocol for exosome isolation and characterization: evaluation of ultracentrifugation, density-gradient separation, and immunoaffinity capture methods*, pp. 179–209. Springer, 2015.

[364] S. A. Melo, L. B. Luecke, C. Kahlert, A. F. Fernandez, S. T. Gammon, J. Kaye, V. S. LeBleu, E. A. Mittendorf, J. Weitz, N. Rahbari, C. Reissfelder, C. Pilarsky, M. F. Fraga, D. Piwnica-Worms, and R. Kalluri, "Glypican-1 identifies cancer exosomes and detects early pancreatic cancer," *Nature*, vol. 523, no. 7559, pp. 177–82, 2015.

[365] D. D. Taylor, W. Zacharias, and C. Gercel-Taylor, *Exosome isolation for proteomic analyses and RNA profiling*, pp. 235–246. Springer, 2011.

[366] S. A. Lee, L. Liu, S. K. Kim, and S. Park, "Tri-component gold–nickel–silver nanorods leading to multiple surface plasmon bands," *The Journal of Physical Chemistry C*, vol. 116, no. 34, pp. 18388–18393, 2012.

[367] A. K. Salem, P. C. Searson, and K. W. Leong, "Multifunctional nanorods for gene delivery," *Nat Mater*, vol. 2, no. 10, pp. 668–71, 2003.

[368] T. Papagiannakopoulos and K. S. Kosik, "Microrna-124: micromanager of neurogenesis," *Cell Stem Cell*, vol. 4, no. 5, pp. 375–6, 2009.

[369] K. Aslan, I. Gryczynski, J. Malicka, E. Matveeva, J. R. Lakowicz, and C. D. Geddes, "Metal-enhanced fluorescence: an emerging tool in biotechnology," *Curr Opin Biotechnol*, vol. 16, no. 1, pp. 55–62, 2005.

[370] S. Kuhn, U. Hakanson, L. Rogobete, and V. Sandoghdar, "Enhancement of single-molecule fluorescence using a gold nanoparticle as an optical nanoantenna," *Phys Rev Lett*, vol. 97, no. 1, p. 017402, 2006.

[371] Y. Chen, K. Munechika, and D. S. Ginger, "Dependence of fluorescence intensity on the spectral overlap between fluorophores and plasmon resonant single silver nanoparticles," *Nano Lett*, vol. 7, no. 3, pp. 690–6, 2007.

[372] X. Qiu and N. Hildebrandt, "Rapid and multiplexed microrna diagnostic assay using quantum dot-based forster resonance energy transfer," *ACS Nano*, vol. 9, no. 8, pp. 8449–57, 2015.

[373] R. M. Graybill and R. C. Bailey, "Emerging biosensing approaches for microrna analysis," *Anal Chem*, vol. 88, no. 1, pp. 431–50, 2016.

[374] M. Mahdiannasser and Z. Karami, "An innovative paradigm of methods in micrornas detection: highlighting dnazymes, the illuminators," *Biosens Bioelectron*, vol. 107, pp. 123–144, 2018.

[375] F. H. Gage, P. W. Coates, T. D. Palmer, H. G. Kuhn, L. J. Fisher, J. O. Suhonen, D. A. Peterson, S. T. Suhr, and J. Ray, "Survival and differentiation of adult neuronal progenitor cells transplanted to the adult brain," *Proc Natl Acad Sci U S A*, vol. 92, no. 25, pp. 11879–83, 1995.

[376] L. Cheng, W. Hu, B. Qiu, J. Zhao, Y. Yu, W. Guan, M. Wang, W. Yang, and G. Pei, "Generation of neural progenitor cells by chemical cocktails and hypoxia," *Cell Res*, vol. 24, no. 6, pp. 665–79, 2014.

[377] A. Jovicic, R. Roshan, N. Moisoi, S. Pradervand, R. Moser, B. Pillai, and R. Luthi-Carter, "Comprehensive expression analyses of neural cell-type-specific mirnas identify new determinants of the specification and maintenance of neuronal phenotypes," *J Neurosci*, vol. 33, no. 12, pp. 5127–37, 2013.

[378] V. T. Rao, S. K. Ludwin, S. C. Fuh, R. Sawaya, C. S. Moore, M. K. Ho, B. J. Bedell, H. B. Sarnat, A. Bar-Or, and J. P. Antel, "Microrna expression patterns in human astrocytes in relation to anatomical location and age," *J Neuropathol Exp Neurol*, vol. 75, no. 2, pp. 156–66, 2016.

[379] S. Herculano-Houzel, "The glia/neuron ratio: how it varies uniformly across brain structures and species and what that means for brain physiology and evolution," *Glia*, vol. 62, no. 9, pp. 1377–91, 2014.